TREATMENT OF NITROGENOUS AROMATIC COMPOUNDS CONTAMINATED WATER BY CATALYTIC WET PEROXIDE OXIDATION

Ph.D. THESIS

by

LOVJEET SINGH

**DEPARTMENT OF CHEMICAL ENGINEERING
INDIAN INSTITUTE OF TECHNOLOGY ROORKEE
ROORKEE – 247 667 (INDIA)
AUGUST, 2018**

TREATMENT OF NITROGENOUS AROMATIC COMPOUNDS CONTAMINATED WATER BY CATALYTIC WET PEROXIDE OXIDATION

A THESIS

Submitted in partial fulfilment of the requirements for the award of the degree

of

DOCTOR OF PHILOSOPHY
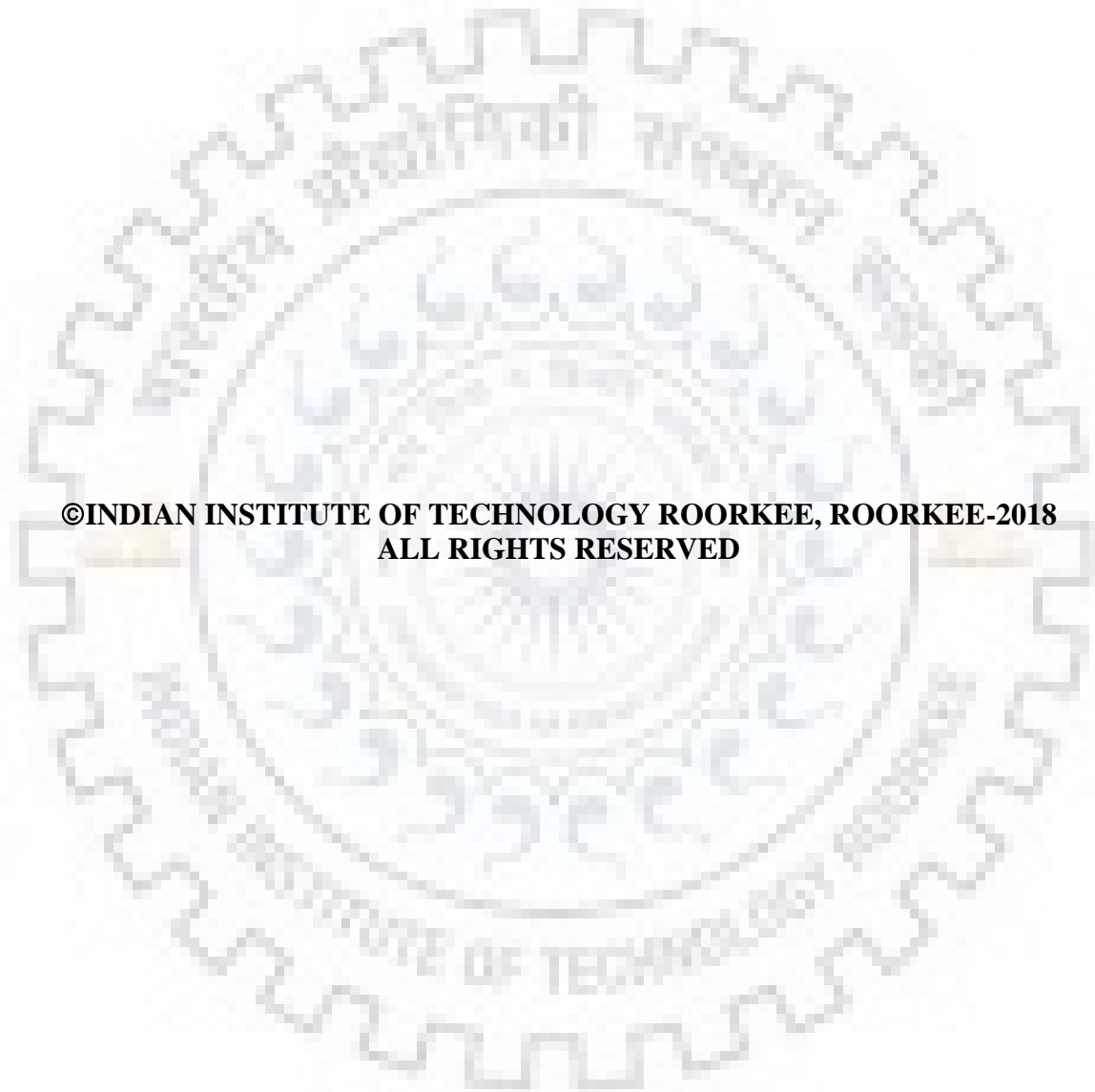
in

CHEMICAL ENGINEERING

by

LOVJEET SINGH

**DEPARTMENT OF CHEMICAL ENGINEERING
INDIAN INSTITUTE OF TECHNOLOGY ROORKEE
ROORKEE – 247 667 (INDIA)
AUGUST, 2018**

INDIAN INSTITUTE OF TECHNOLOGY ROORKEE
ROORKEE

CANDIDATE'S DECLARATION

I hereby certify that the work which is being presented in the thesis entitled **"TREATMENT OF NITROGENOUS AROMATIC COMPOUNDS CONTAMINATED WATER BY CATALYTIC WET PEROXIDE OXIDATION"** in partial fulfillment of the requirements for the award of the Degree of Doctor of Philosophy and submitted in the Department of Chemical Engineering of the Indian Institute of Technology Roorkee is an authentic record of my own work carried out during a period from July, 2012 to August, 2018 under the supervision of Prof. Shri Chand, Emeritus Fellow, Department of Chemical Engineering, Indian Institute of Technology Roorkee, Roorkee, India.

The matter presented in this thesis has not been submitted by me for the award of any other degree of this or any other Institute.

Signature of the Candidate

This is to certify that the above statement made by the candidate is correct to the best of my knowledge.

Signature of Supervisor

The Ph.D. Viva-Voce Examination of **Mr. Lovjeet Singh**, Research Scholar, has been held on_____.

Chairman, SRC   **Signature of External Examiner**

This is to certify that the student has made all the corrections in the thesis.

Signature of Supervisor   **Head of the Department**
Date:

ABSTRACT

Nitrogenous aromatic compounds such as Congo red, quinoline, aniline, etc. bearing wastewaters have attracted the attention of the scientific communities because of their potential eco-toxicological risks. Due to low nitrogenous pollutants removal efficiency of conventional wastewater treatment plants, worldwide concerns are raised for efficient and eco-friendly technologies. Advanced oxidation processes (AOPs), such as catalytic ozonation, photocatalysis, Fenton process and catalytic wet peroxide oxidation (CWPO)/heterogeneous Fenton-like processes have been investigated as promising technologies for the wastewater treatment. Among these AOPs, CWPO could achieve complete degradation of the pollutants into CO_2, N_2 and inorganic ions with the help of heterogeneous catalysts using hydrogen peroxide as oxidant under mild operating condition. The optimized catalyst design is still required to bring this technique to the forefront of the most efficient AOP technologies. In last years, copper containing heterogeneous catalysts have been reported suitable for industrial applications due to their wide working pH range as well as good redox properties. Particularly promising are copper incorporated zeolite Y and copper hydroxyl phosphate because of their high degradation efficiency. Although conventionally used, aqueous ion exchange (AIE) method for the preparation of Cu/zeolite Y, and hydrothermal method for the preparation of copper hydroxyl phosphate and copper phosphate are associated with various limitations. A further discussion is required in context of more advanced and green routes for their synthesis as well as evaluation of their catalytic performances in different type of reactors to increase their suitability for the large scale processes. Keeping in mind all the above discussed points, in the present research, wet-impregnation (IMP) and precipitation-impregnation (PI) for cu/zeolite Y and ultrafast sonochemical method for copper hydroxyl phosphate (CHP) and copper phosphate (CP) have been developed. Moreover, the catalytic activities of these catalysts have been tested in batch and continuous fixed-bed reactors. The IMP and PI methods not only overcome the limitations of AIE but also generate hierarchical mesoporosity in zeolite Y and increase surface area in considerable extent.

In present work, firstly, copper was incorporated on zeolite Y framework using IMP method with different targeted loading (1wt%, 2.5wt%, 5wt%, 7.5wt% and 10wt%) and tested for the degradation of Congo red in batch reactor. The maximum surface area of 667 m^2 g^{-1} and generation of mesoporosity was observed for 7.5wt% CuY (actual loading ~ 5wt%). The copper was present in well-dispersed monovalent and divalent states in this sample. The maximum degradation, decolorization and mineralization of 93.58%, 95.34% and 79.52% were exhibited by

Cu 7.5 wt% after optimum times of 2.5, 2 and 4 h, respectively. The optimized condition was observed at pH = 7, H_2O_2 concentration = 52.24 mM, catalyst concentration = 1 g L^{-1} and T = 60 °C. The kinetic studies revealed that the degradation and decolorization profiles for Congo red were well fitted to first-order kinetic model. Secondly, copper was incorporated on zeolite Y by three different methods (AIE, IMP and PI) and as-synthesized samples were tested for the CWPO of quinoline in continuous fixed-bed reactor. CuY_{AIE} promoted isolated species similar to CuY_{IMP}; however, large CuO crystallites of different sizes (4.7-6.1 nm) were present on the external surface of precipitation-impregnation (CuY_{PI}) catalysts depending upon the Cu loadings. The Langmuir surface area and pore volume (V_p) increase surprisingly from 567 to 909 m^2 g^{-1} and 0.26 to 0.51 cm^3 g^{-1}, respectively, for $5CuY_{PI}$. The mesoporosity generation in CuY_{PI} was result of higher desilication from zeolite framework due to synergetic effect of copper and NaOH. Almost comparable mineralization (61-65%) and H_2O_2 stoichiometric efficiencies (44.2-45.7%) were observed for CuY_{AIE} and CuY_{IMP} samples in continuous fixed-bed reactor. Higher catalytic activities of both catalysts in comparison to CuY_{PI} suggest that isolated sites are the most redox-active sites for H_2O_2 activation and play important role than high surface area, i.e., for CuY_{PI}. The optimised removal was observed at LHSV = 4 h^{-1}, particle size = 1.2-1.7 mm, H_2O_2/quinoline = 48 and T = 80 °C. The system followed Eley-Rideal mechanism and kinetic parameters were calculated using model based on this mechanism. Finally, copper hydroxyphosphate (CHP) and copper phosphate (CP) were synthesized using ultrafast sonochemical route and tested for the CWPO of aniline in aqueous solution. CHP was obtained at pH 5 in 2 h, and the formation of CP was noticed at pH = 3 and pH = 7. In CHP samples, small nanorods of size ~50 nm were self-assembled to larger nanospindles-like hierarchical architecture of size 500-700 nm. At low sonication energy, one dimensional nanorods was obtained. In CP samples, thin nanoflakes of size 100-200 nm were obtained. The *OH radicals generated through ultrasonic irradiation of water are thought to be responsible for formation of CHP phase. The optimized aniline degradation, TOC removal and H_2O_2 conversion of 99.86%, 74.73% and 68.84% were achieved for nanospindle-like architecture at pH = 7, H_2O_2 amount = 2.4 mL, catalyst concentration = 1 g L^{-1} and T = 80 °C. The recyclability up to five continuous cycles has shown a remarkable operational stability of CHP catalyst.

ACKNOWLEDGEMENTS

Words cannot completely express my love and gratitude to my family who have supported and encouraged me through this journey. I would like to thank my grandparents, Sardar Karam Singh, Mrs. Shan Kaur; parents, Sardar Manjeet Singh, Smt. Kuldeep Kaur; in-laws, Sh. Prem Lal, Smt. Nirmla Devi; caring brother, Mr. Jagjeet Singh; my sister, Jasmeet Kaur; brother-in-law, Mr. Madan Lal, Robin and Mr. Sanjay Sharma; sister-in-law, Mrs. Sapna Kumari and Meenakshi Dhiman; and all my relatives for their everlasting love and sacrifices, which sustained my interest in research and motivated me towards the successful completion of this study. Thanks to my cuties, Sahej and Saanvi who have given me much happiness and keep me hopping.

Finally, I thank the almighty God for providing me the passion, strength, diligence and the resources to complete this research.

(LOVJEET SINGH)

CONTENTS

LIST OF FIGURES

xi

LIST OF TABLES

AIE	Aqueous ion exchange
AAS	Atomic absorption spectroscopy
AC	Activated carbon
ACGIH TLV	American conference of governmental industrial hygienists threshold limit value
AOP	Advanced oxidation processes
BET	Brunauer-Emmett-Teller
BFA	Bagasse fly ash
BJH	Barrett-Joyner-Halenda
BOD	Biological oxygen demand
CHP	Copper hydroxyphosphate
CNS	Central nervous system
CNTs	Carbon nanotubes
COD	Chemical oxygen demand
CP	Copper phosphate
CPCB	Central pollution control board
CR	Congo red
CWPO	Catalytic wet peroxide oxidation
DFT	Density functional theory
DTG	Differential thermal gravimetry
EDTA	Ethylenediaminetetraacetic acid
EPS	Extracellular polymeric substances
FBR	Fixed-bed reactor
FESEM	Field emission scanning electron microscopy
FO	Forward osmosis
FTIR	Fourier transform infrared
GAC	Granular activated carbon
GO	Graphene oxide
HPLC	High performance liquid chromatography
HRTEM	High resolution transmission electron microscopy
HZM	Hierarchical porous ZnO microspheres
IC	Inorganic carbon
IC	Ion chromatography

ICDD	International center of diffraction data
ICP-MS	Inductively coupled plasma-mass spectroscopy
IDLH	Immediately dangerous to life or health
IMP	Wet impregnation
IUPAC	International union of pure and applied chemistry
K_{OC}	Organic carbon-water partition coefficient
K_{ow}	Octanol-water distribution coefficient
LHSV	Liquid hourly space velocity
MD	Membrane distillation
MOEFCC	Ministry of Environment, Forest and Climate Change
NDIR	Non-dispersive infrared detector
NF	Nanofiltration
OSHA PEL	Occupational safety and health administration permissible exposure limit
PAC	Poly aluminium chlorides
PAFSIC	Poly aluminium ferric silicate chloride
PAM	Polyacrylamide
PAN	Polyacrylonitrile
PI	Precipitation-impregnation
PMDA	Pyromellitic dianhydride
PSD	Pore size distribution
R^2	Correlation coefficient
RO	Reverse osmosis
RT	Room temperature
SAED	Selected area electron diffraction
S_{BET}	Specific surface area
SBR	Sequencing batch reactor
SCI	Science citation index
SDS	Sodium dodecyl sulfate
TC	Total carbon
TCA	Tricarboxylic acid cycle
TEM	Transmission electron microscopy

TFC	Thin film composite
TOC	Total organic carbon
TWA	Time weighted averages
UF	Ultrafiltration
UN	United Nations
USEPA	United States Environmental Protection Agency
UV-DRS	Ultra violet-visible diffused reflectance spectroscopy
UV-vis	Ultraviolet visible
WAO	Wet air oxidation
XPS	X-ray photoemission spectroscopy
XRD	X-ray diffraction
XRF	X-ray fluorescence
k_d	Rate constant
E_a	Activation energy
λ	Wavelength
d_P	Crystallites size
k_0	Frequency factor
β	Full width of the peak at half maximum
θ	Bragg's angle
S_{Lang}	Langmuir surface area
V_p	Pore volume
ε_L	Liquid holdup
C_o	Initial concentration
C_t	Final concentration
η	Stoichiometric efficiency
X	Conversion of pollutant
q_e	Adsorption capacity at equilibrium
q_{max}	Maximum adsorption capacity
R	Rejection capacity of membrane
t_R	Residence time
V_C	Catalyst bed volume
Q	Flow rate

PUBLICATIONS IN JOURNALS

1. **Singh L.**; Rekha P.; Chand S. Comparative evaluation of synthesis routes of Cu/zeolite Y catalysts for catalytic wet peroxide oxidation of quinoline in fixed-bed reactor, *J. Environ. Manag.* **215**, 1-12, 2018. (Impact factor: 4.005)

2. **Singh L.**; Rekha P.; Chand S. Cu-impregnated zeolite Y as highly active and stable heterogeneous Fenton-like catalyst for degradation of Congo red dye, *Sep. Purif. Technol.* **170**, 321-336, 2016. (Impact factor: 3.927)

3. **Singh L.**; Chand S. Ultrafast sonochemical synthesis of copper hydroxy phosphate and copper phsophate for catalytic wet peroxide oxidation of aniline in aqueous solution, *Ind. Eng. Chem. Res*. Communicated.

CONFERENCE PRESENTATIONS

1. **Singh L.**; Chand S. Cu-precipitated zeolite Y for degradation and mineralization of Congo red dye. International Conference on Energy, Functional Materials & Nanotechnology (ICEFN-2016), March 27-29 at kumaun university, Nanital, India. Got "Young Scientist Award for best poster presentation"

OTHERS PUBLICATIONS

1. Shankar R.; **Singh L**.; Mondal P.; Chand S. Removal of COD, TOC, and color from pulp and paper industry wastewater through electrocoagulation, *Desalin. Water Treat*. **52**, 7711-7722, 2014.

2. Shankar R.; **Singh L**.; Mondal P.; Chand S. Removal of lignin from wastewater through electro-coagulation, *World J. Environ. Eng*. **1**, 16-20, 2013.

1.1. GENERAL

The increasing pollution of water bodies is a serious global concern. The rapid industrialization and fast-growing population are major contributors of harmful contaminants into the ground as well as surface water. The pollution of these sources imposed negative impacts on the aquatic ecosystem, human health, countries' sustainable development and accessibility of potable water. According to the recent report of United Nations (UN), one-fourth population of the world is likely to live in the potable water-stressed area by 2050 [UN Report, 2018]. This calls for sincere efforts by different sectors to conserve the water resources in their pristine quality. In order to overcome the future challenges of clean water scarcity, highly efficient techniques of wastewater treatment and appropriate water management strategies for recycling of treated water have to be implemented on potential sources of contamination.

Chemical industry particularly organic chemical industry consumes large amount of fresh water during its wet processing operations and consequently discharges large volume of wastewater laden with toxic, carcinogenic and mutagenic contaminants. Nevertheless, increased attention is currently being paid to nitrogenous aromatic compounds designated as priority pollutants. In general, these contaminants can be characterized as persistent, ecotoxic, carcinogenic, mutagenic and repro-toxic. Direct discharge of these contaminants to water bodies creates severe environmental problems and causes hazardous health of living organisms. In the last years, European Union [European parliament, 2000] and USA [USEPA, 1996] have taken action to establish regulation to limit the nitrogenous aromatic compounds' concentrations in effluents to avoid environmental risks.

Conventional treatment systems have not been found suitable to remove these organic pollutants from wastewater, owing to their recalcitrant nature and low biodegradability. In order to meet the stringent water quality standards, it has become essential to remove these pollutants from wastewater before discharge into water bodies. This calls for the development of efficient and low cost treatment technologies. The efficient treatment technologies are also advantageous from two major water management aspects, recyclability of reclaimed water, and protection of fresh water sources. The recyclability of wastewater is a potential way to benefit industries economically and complements the image of corporate social responsibility and sustainable development. During the last few years, advanced oxidation processes (AOPs) have received the large attention to oxidize the hazardous organic contaminants. These processes generate *OH radicals, which are capable of oxidizing almost all the organic compounds in a

non-selective way. AOPs can oxidize the organic contaminants to non-toxic products. That is why they are called "the treatment processes of the 21st century" [Munter 2001].

1.2. NITROGENOUS AROMATIC COMPOUNDS

Azo dyes, heterocyclic aromatic compounds, and aromatic amines have been considered as the important members of nitrogenous aromatic compounds' family. Congo red, quinoline, and aniline belong to these categories of nitrogenous aromatic compounds and are well-known for variety of applications in different chemical industries as given in Table 1.1. These compounds are predominantly emitted by anthropogenic activities, which result into increase of their concentrations in the environment. Nitrogenous aromatic compounds laden wastewaters are commonly discharged from textile, pesticides, coal, petroleum, and pharmaceuticals industries.

Table 1.1: Applications and sources of discharge of Congo red, quinoline and aniline

Nitrogenous Pollutants	Application in industries	Source of pollutants	References
Congo red	Used in textile, paper, printing, leather and plastic industries; used as histological stain for amyloid and diagnosis of amyloidosis; used for testing of free HCl in gastric contents; as pH indicator and gelling agent for polyvinyl alcohol.	During Congo red manufacturing and application in chemical industries. Release in environment during medical applications.	Cheng et al. 2011; Shu et al. 2015
Quinoline	Serve as industrial solvent; used in manufacturing dyes such as quinoline yellow and cyanine dyes; as substrates in the production of fluoro-quinolone antibiotics; precursor for chelating agent 8-hydroxyquinoline; used to prepare precursor for "Assert" herbicide; used as parental compounds for the synthesis of anti-malarial and anti-microbial drugs; and used as wood treatment chemicals.	Retorting of oil shale to shale oil; coal carbonization and gasification; coal liquification; crude oil processing; chemical manufacturing industries.	Padoley et al. 2008; Zhu et al. 2008; Felczak et al. 2014; Saien et al. 2017
Aniline	Used to manufacture the precursors for polyurethane; aniline derivatives are used as antioxidants and accelerators for rubber industry; as a precursor to indigo dye to manufacture clothes such as jean; for production of drug such as paracetamol, sulpha drugs, etc.; its derivatives are used in manufacturing of explosives, herbicides, fungicides, plastics, and photographic.	Burning products of plastic and tobacco; degradation products of antipyrine, herbicides and azo dyes; during aniline manufacturing and applications.	Kirk & Othmer 1997; Exposito et al. 2017

Table 1.1 shows the industrial processes responsible for generation of these compounds in wastewater. The removal of these compounds from wastewater has recently received large attention because of their toxic, carcinogenic and mutagenic effect on human beings as well as aquatic organisms. Owing to their high aqueous solubility and persistence for long periods,

these compounds can easily get transported and pollute different water sources. Due to bio-recalcitrant and toxic nature of these compounds, the conventional biodegradation approach is not suitable. The scientific community is focusing on development of such technology which mineralizes these pollutants or at least degrades them into biodegradable products.

The elimination of these compounds has become compulsory because of increasing public awareness towards their toxic effects and government's stringent water quality standards. Central pollution control board (CPCB) under Ministry of Environment, Forest and Climate Change (MOEFCC), Government of India, has not fixed separate emission standards for these compounds. However, these compounds have been listed in category of hazardous materials by CPCB. In general, the maximum permissible limits of chemical oxygen demand (COD) of 250 mg L^{-1} and biochemical oxygen demand (BOD, 3 days, 27 °C) of 30 mg L^{-1} have been fixed for dye and dye intermediate industries [CPCB, 2018].

The concentration of aniline varies from 0.6 to 12 μg L^{-1} in surface water, from 0.48 to 14 μg L^{-1} in shale oil wastewater, and reaching a maximum concentration of 6000 μg L^{-1} in rubber industry wastewater [Reemtsma et al. 2006; Duran et al. 2018]. The water quality standards are very stringent for aniline in USA (< 6 μg L^{-1} in groundwater as defined by New Jersey Department of Environmental Protection) and China (< 1 mg L^{-1} in discharge effluent as issued by Chinese National Standard) [Wu et al. 2012]. The concentration of quinoline in industrial wastewater varies in range 6 to 500 mg L^{-1} [Jianlong et al. 2002; Bai et al. 2011].

1.3. CONGO RED, QUINOLINE AND ANILINE

Congo red (CR) is a benzidine-based anionic diazo dye having IUPAC name Disodium 3,3'-{[1,1'-biphenyl]-4,4'-diylbis[(E)diazene-2,1-diyl]}bis(4-amino naphthalene e-1-sulfonate). CR structure consists of one biphenyl group in centre which is linked to two symmetrical naphthalene rings through azo bonds (--N=N--) as shown in Fig. 1.1 [Shu et al. 2015]. Naphthalene rings also contain negatively charged sulfate group and polar amino groups [Wu et al. 2007]. It was first synthesized by German chemist Paul Böttiger in 1883 by coupling of bisdiazotised benzidine with two molecules of 4-sulfo-1-naphthylamine [Howie et al. 2009]. CR has wide applications in dyeing, paper, rubber and plastic industries. It has strong affinity towards cellulose fibers and majorly employed in textile industries. CR is a direct dye and does not require any mordant during dyeing of textile fibers [Cheng et al. 2011]. CR laden wastewater is commonly discharged during its manufacturing and application in chemical industries. It imparts dark colour to effluent and increase its COD. The conventional

remediation technologies for CR containing wastewater is difficult because of its complex aromatic structure which provide it physicochemical, thermal and optical stability.
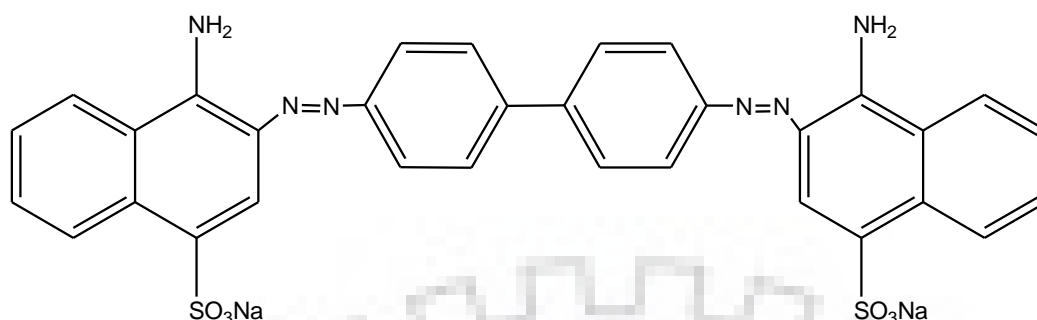
Fig. 1.1: Chemical structure of Congo red dye

Quinoline is one of the most important N-based heterocyclic compounds (Fig. 1.2). It has recently drawn the attention of researchers because of its wide applications in medical, bioorganic and organic chemistry. It was extracted for the first time in 1834 by Friedlieb Ferdinand Runge from coal tar and still exists as the principal source of quinoline [Bharate et al. 2015]. Quinoline and its derivatives naturally appear in plants, bacteria and fungi [Teichert et al. 2008]. Various naming reactions such as skraup, Friedlander, pfitzinger, and combes synthesis, have been conventionally used for the synthesis of quinoline ring [Prajapati et al. 2014]. Most of these reactions used o-substituted anilines as building blocks. It is used as parental molecule to synthesize compounds having large pharmacological activities including anticancer, anti-inflammatory, antifungal, antiprotozoal, and antipsychotics, etc [Bharate et al. 2015; Zheng et al. 2016]. Among various anthropogenic sources, coal processing contributes significantly for releasing of quinoline in environment [Fetzner et al. 1998]. Coal processing results into the production of tar and creosote which contain considerable amount of water-soluble quinoline [Blum et al. 2011]. Many reports indicate that quinoline compound has ecotoxic potential and can disturb the biological functions of living organism. A large amount of quinoline containing wastewater generated during its manufacturing and application. Due to its hazardous potential, the presence of quinoline in environment is a worldwide concern.
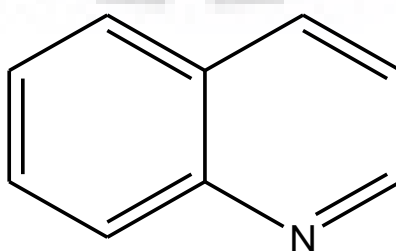
Fig. 1.2: Chemical structure of quinoline

Aniline comes into category of aromatic amine and considered a versatile raw material owing to its application in manufacturing of dyes, stabilizers for the rubber industry, pharmaceuticals, herbicides, antioxidants and explosive. Aniline was isolated for the first time in 1826 from natural dye indigo by German chemist Otto Unverdorben. The conventional process for aniline production is based on liquid phase or vapour phase hydrogenation of nitrobenzene using Pt, Pd, Cu and Ni as catalysts [Mohamed et al. 2014; Zhou et al. 2015]. The major amount of aniline is utilized as a raw material for the synthesis of polyurethane. In 2010, the global production of aniline was 23 million tons and 2/3 of it was employed for the synthesis of polyurethane [Daems et al. 2018]. The total amount of 30,000 tons of aniline is being introduced annually into the environment [Xiao et al. 2012]. This aromatic amine has recently drawn the attention of environmentalist because of its toxicity and wide distribution in water sources.

1.3.1. Toxicity of Congo red, quinoline and aniline

Table 1.2 describes the health effects and toxicity potential of these compounds. The metabolism process of body converts this dye into benzidine, a well-known human carcinogen [Chatterjee et al. 2009]. CR causes irritation to eyes and skin, and engenders drowsiness and respiratory complications [Mittal et al. 2009]. It exhibits mutagenic, blood clotting and reproduction effects [Mittal et al. 2009].

Quinoline shows cytotoxic activity by inhibiting topoisomerase II, an enzyme that disentangle the topological problems in DNA [Nitiss 2009a; 2009b)]. Since the mutagenic effects of nitrogenous heterocyclic compounds increase with increase in the number of rings, quinoline has been found more toxic than pyridine [Millemann et al. 1984]. Quinoline shows bio-recalcitrant behaviour due to steric hindrance of bicyclic fused structure [Zhu et al. 2012] The United States Environmental Protection Agency (USEPA) has declared it as priority organic pollutant [Wang et al. 2016]. Depending on evidence of tumors of liver and blood vessel in animals, quinoline has recently been classified as a GroupB2 *probable human carcinogen* by EPA [USEPA, 1996].

Aniline converts haemoglobin in blood to methemoglobin and cause cyanosis (reduce oxygen capacity of the blood) [Zhang et al. 2015]. Chronic exposure of aniline causes damage to cardiovascular system, bladder, liver and central nervous system (CNS). EPA has classified it as a GroupB2 *probable human carcinogen.* Aniline generates birth defects in animals, and causes irritation in mucous membranes and upper respiratory tract in human. The US Environmental Protection Agency and European Water Framework Directive 2000/60/EC have

listed aniline as a priority contaminant because of its toxic and mutagenic properties [USEPA, 1996; European parliament, 2000; Jurado-Sanchez et al. 2012].

1.3.2. Properties of Congo red, quinoline and aniline

Table 1.2 summarizes the physical and chemical properties of these compounds. Congo red is soluble in water and its solubility is high in organic solvents such as ethanol. The solution is orange in ethanol and blue in presence of acid in water. CR is non-volatile due to ionic state and does not volatilize from water to air. Low volatility can also be confirmed from low value of Henry's volatility constant ($1.83* 10^{-11}$ atm-m^3 mol^{-1}) [Mackay et al. 1999]. A Low K_{OC} (organic carbon-water partition coefficients) of 7 indicates towards the high mobility to pass through soil into groundwater; however, the ion exchange property prevents its leaching to ground water [Mackay et al. 1999]. Octanol-water partition coefficients (log K_{ow}) of 9.53 and bio-concentration factor of 1 confirm that this compound is mobile in aquifers and aquatic organisms cannot reduce CR by bioaccumulation [Lewis, 2004]. CR is highly soluble in water with solubility of 6.45 g L^{-1} at 25 °C. The sulfonate groups of CR are responsible for high aqueous solubility. US Food and Drug Administration (FDA) has estimated Maximum Recommended Therapeutic Dose value of 3.75 mg kg^{-1} day^{-1} for CR.

Quinoline and its derivatives are representatives of nitrogenous heterocyclic compounds in which one or more carbon atoms in the ring have been substituted by nitrogen atoms. This substitution of heteroatom influences their physical and chemical characteristics. For example, quinoline has higher aqueous solubility of 6.11 g L^{-1} at 25 °C than its homocyclic analogs [Jones et al. 2017]. Quinoline is miscible with polar organic solvents. Low value of Henry's volatility constant ($2.47* 10^{-7}$ atm-m^3 mol^{-1}) indicates that quinoline does not volatilize from water to air. Less K_{OC} of 79-205 signifies towards the low level sorption of released quinoline on sediments and particulates, and it is likely to partition into water. Bio-concentration factor of 21 and log K_{ow} of 2.03 confirm the low level of removal by bioaccumulation in aquatic organism and high mobility in aquifers [Sangster, 1989; Fischer et al. 2010].

Aniline is soluble in water having characteristics taste and rotten fish odour. Aniline characterizes moderate to high mobility in soil based upon K_{OC} values of 8-495 and may be adsorbed on sediments and suspended solids in water. Log K_{ow} of 0.90 confirm the negligible role of bioaccumulation in removal of aniline [Sangster, 1989]. Aniline has high aqueous solubility of 36 g L^{-1} at 25 °C. The reported value of Henry's volatility constant ($2.02* 10^{-6}$ atm-m^3 mol^{-1}) indicates that aniline is expected to volatilize from water surfaces [Lewis, 2004].

Table 1.2: Characteristics and toxicity of CR, quinoline and aniline [Mackay et al. 1999; Lewis, 2004]

Characteristics	Congo red powder	Quinoline	Aniline
Synonym	Direct red 28, cotton red	Benzopyridine	Aminobenzene, Aminophen, Benzenamine
Chemical formula	$C_{32}H_{22}N_6Na_2O_6S_2$	C_9H_7N	$C_6H_5NH_2$
Molecular weight (g mol^{-1})	696.67	129.16	93.13
Physical characteristics	colour depends on pH, Odourless	Colorless, pungent odour	Colorless, oily liquid, rotten fish odour
Density (kg m^{-3})	1640	1090.1	1021.6
Boiling point (°C) at 760 mmHg	383	237.7	184.1
Freezing point (°C)	360	-16.0	-6
Flash point (°C)		59	70
Solubility	Soluble in water, ethanol. Insoluble in diethyl ether.	Soluble in hot water, ethanol, carbon disulphide, acetone and ethyl ether	Soluble in water, methanol and diethyl ether
Reactivity	-	Turns yellow and later brown on exposure to light and air	Colour become yellow dark on exposure to light and air
LD$_{50}$ (oral) mg kg^{-1}	200 (rat)	331(rat)	952 (rat)
IDLH (mg m^{-3})	-	-	381
OSHA PEL (mg m^{-3})	-	-	TWA 19
ACGIH TLV (mg m^{-3})	-	-	TWA 7.6
Health risks	Acute effects involve allergic reaction, irritation in eyes, skin and gastrointestinal. Chronic exposure cause mutagenic for mammalian somatic cells, damage blood, cause drowsiness, and classified possible teratogenic for humans. Benzidine has been classified as Group 1 carcinogen.	Hazardous in case of contact with eyes and skin, toxic if inhaled or ingested. EPA classified it as Group B2, probable human carcinogen. Acute inhalation causes dizziness, headaches and nausea. Chronic exposure cause liver tumors, mutagenic and terotogenic effects on animals.	Acute exposure affects the liver. EPA Classified it as a Group B2, probable human carcinogen. Chronic exposure case conversion of hemoglobin to methahemoglobin. Mutagenic for all mammals, bacteria or yeasts. Cause damage to blood, cardiovascular system, bladder, liver and central nervous system (CNS).

OSHA PEL: Occupational Safety and Health Administration Permissible Exposure Limit, ACGIH TLV: American Conference of Governmental Industrial Hygienists Threshold Limit Value, TWA= Time Weighted Averages (on the basis of exposure of 8h day^{-1}), EPA: Environmental Protection Agency, IDLH: immediately dangerous to life or health.

1.4. TREATMENT METHODS FOR NITROGENOUS AROMATIC COMPOUNDS

Various methods have been reported for removal of Congo red, quinoline and aniline from wastewater. Based on existing literature, these methods can be broadly classified as: biological, physicochemical and advanced oxidation processes. Biological degradation refers to the removal process of organic pollutants from environment using metabolic activities of different microorganisms. Biological methods for wastewater treatment are more advantageous in comparison to physicochemical methods because of low cost, easy implementation in industry and less secondary pollution [Zhu et al. 2008]. Depending on the different metabolic strategies used by microorganism, the biological methods can be classified into aerobic (with molecular oxygen) and anaerobic (without molecular oxygen) categories. The biodegradation of nitrogenous aromatic compounds has been studied extensively in last decade under these metabolic conditions. It has generally been observed that these compounds resist degradation in conventional activated sludge units [Wang et al. 2004; Pereira et al. 2011]. Many studies have shown that these compounds are recalcitrant under anaerobic condition [Aislabie et al. 1990; Miethling et al. 1993; Pandey et al. 2007]. Recent reports show that these pollutants can be degraded using aerobic microorganisms. The main focus in these reports was to explore the degradation efficiency of an organism isolated from contaminated sites that had evolved to use these nitrogenous aromatic compounds as substrates for growth. Bacterial biodegradation can achieved higher degradation efficiency among these processes and has been reported faster than fungal biodegradation. However, the efficient bacteria are very less in number and are very specific towards that compound. Moreover, these biological methods are associated with several drawbacks such as requirement of long degradation time (2-7 days), the severe impacts of heavy metals, and rigidity towards fluctuation [Singh et al. 2011; Jin et al. 2012; Liu et al. 2013]. Higher concentration of these pollutants inhibits microorganism growth and causes negative effect on biological degradation [Zhu et al. 2008; Sun et al. 2009].

Physico-chemical method such as adsorption has attracted much attention of researchers for the removal of Congo red, quinoline and aniline from wastewater. Various adsorbent such as fibrous silicates, bagasse fly ash, metal oxide, zeolite, clay minerals and activated carbon have been used for the removal of nitrogenous organic pollutants [Burgos et al. 2004; Vico et al. 2006; Wang et al. 2010; Suresh et al. 2011; Ali et al. 2012; Rameshraja et al. 2012; Jadhav et al. 2013; Lei et al. 2017]. The most frequently employed adsorbent in removal of nitrogenous pollutants is activated carbon (AC). Different types of ACs have been used till now. These ACs are commonly prepared from agriculture and industrial wastes such as rubber tyre, sewage sludge, wood, olive stones, almond shells, coconut shell and bamboo culms [Ali et al. 2012].

The future of universal and inexpensive adsorption technology is bright in developing countries with the utilization of low cost adsorbents. However, this technique is associated with disadvantages of limited adsorption capacity, low selectivity, large contact time and poor performance at neutral pH. Management of spent adsorbents is required as adsorbed organic pollutants are hazardous to living beings [Ali et al. 2012].

Among others physicochemical techniques, coagulation is a widely used method for the treatment of wastewater in industries. However, this method is found inappropriate for the removal of nitrogenous organic compounds because of their high aqueous solubility and not much studied. Moreover, it generates large volume of sludge and transfers high concentration of toxic metals in treated effluents. On the other hand, the application of membrane process is limited due to its high cost and large volume of rejected residuals.
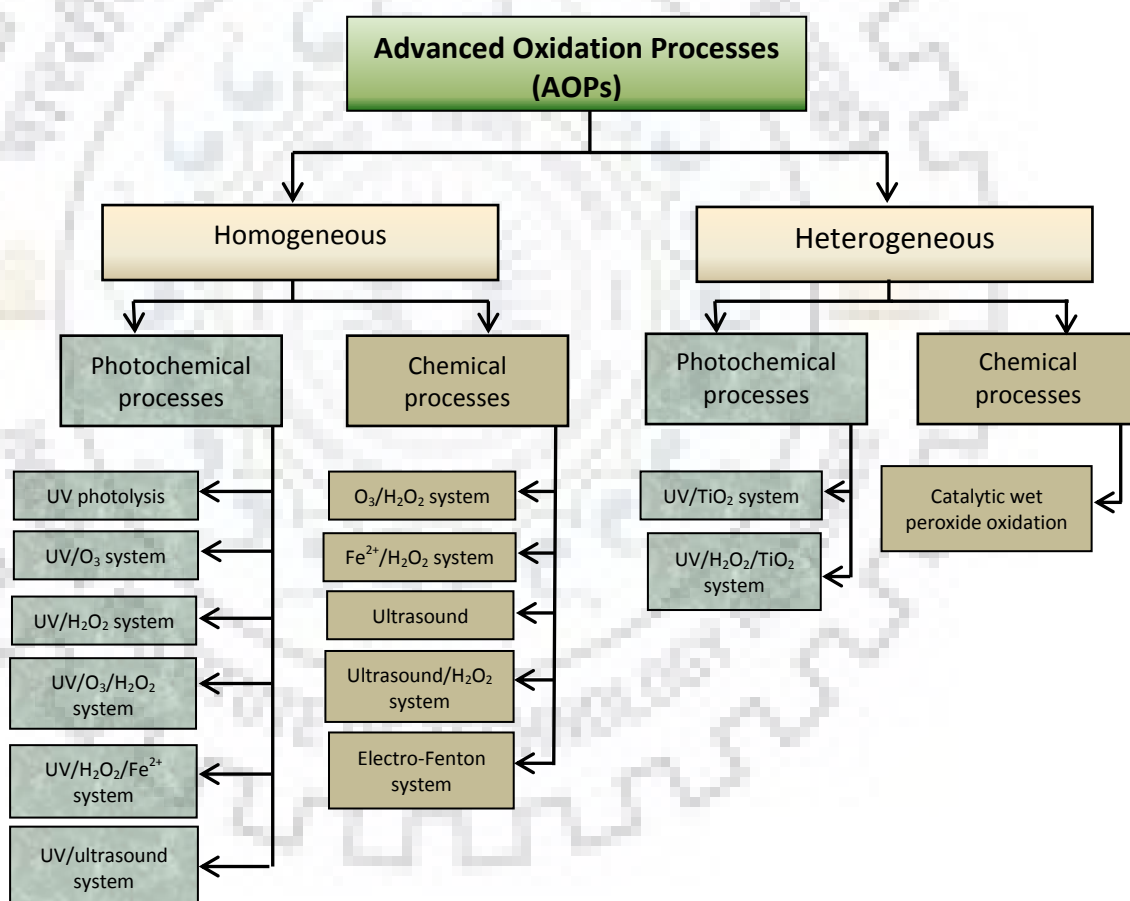
Fig. 1.3: Types of advanced oxidation processes

Keeping these facts in mind, the researchers are looking for alternative technologies which not only degrade but also mineralize these nitrogenous aromatic compounds present in water. Because of several limitations of biological and physicochemical treatment methods, the oxidative treatments of persistent organic pollutants have attracted the attention of researchers. Among different oxidative degradation techniques, advanced oxidation processes (AOPs)

which is capable of generating highly reactive oxidizing species, seen promising because of degradation of refractory pollutants at near-ambient condition. AOPs involves the sonochemical, electrochemical, catalytic ozonation, photocatalysis, Fenton process and catalytic wet peroxide oxidation (CWPO)/heterogeneous Fenton-like processes for the generation of oxidizing species hydroxyl radicals (*OH) (Fig. 1.3). These *OH radicals have high oxidation potential ($E° = 2.80$ eV vs. NHE) and can mineralize wide range of organic compounds to CO_2, H_2O and inorganic ions [Navalon et al. 2010]. The advantages and disadvantages of different processes have been discussed in detail in Chapter 2.

CWPO/heterogeneous Fenton-like process is a well-known process that can completely degrade the pollutants to CO_2, N_2 and inorganic ions using heterogeneous catalyst and H_2O_2 as oxidant at mild operating condition. CWPO offers numerous advantages over others AOPs in terms of wide range of pH, low energy consumption, limited transfer of metal cations into treated effluent, easy recoverability and reusability of catalyst. These facts make CWPO an economically viable option for wastewater treatment. Different transition metals (Fe, Cu, Mn, Zr) in different form (supported or unsupported catalysts) have been proposed for the degradation and mineralization of nitrogenous organic pollutants.

1.5. Cu/ZEOLITE Y AND COPPER HYDROXY PHOSPHATE AS CATALYSTS FOR CWPO

Recently, copper, which also behaves like a Fenton reagent, has been reported suitable for industrial applications due to its wide-working pH range as well as good redox properties [Xia et al. 2011; Bokare et al. 2014]. Unlike iron, copper does not form strong complexes with organic acid intermediates. Thus, it does not block the generation of hydroxyl radicals and can provide high mineralization [Nichela et al. 2013; Bokare et al. 2014]. Development of the highly active and stable copper containing catalyst has become a hot research topic in the field of CWPO of recalcitrant organic pollutants.

Zeolites are microporous crystalline materials and widely used in catalysis, adsorption, ion exchange and separation processes owing to their uniform pore size, large surface area and high thermal stability [Baroi et al. 2014; Ahmadi et al. 2015; Samanta et al. 2018]. Zeolite as catalyst support increase activity, selectivity and stability of active metallic species. Zeolite in pristine form does not exhibit considerable catalytic activity until appropriate active metal species are incorporated inside its framework [Carreon et al. 2008; Venna et al. 2009]. Several researchers have demonstrated the high catalytic activity and stability of metal-exchanged zeolites for the oxidative degradation of organic compounds [Hu et al. 2015; Samanta et al. 2018]. In recent years, copper containing zeolites have been used to activate hydrogen peroxide

to hydroxyl radicals and found suitable for industrial purpose due to high degradation efficiency as well as wide-working pH range [Wang et al. 2004; Dükkanci et al. 2010; Valkaj et al. 2011a]. Particularly promising is copper loaded zeolite Y, which shows higher activity than Cu/ZSM-5 in oxidation of toxic compound while exhibiting more efficient use of hydrogen peroxide [Valkaj et al. 2011b]. Aqueous ion exchange (AIE) has been used for both commercial and research purpose for the incorporation of copper metal in the zeolite Y. Many authors have prepared Cu-exchanged zeolite Y and employed this material for the applications, such as, formation of diethyl carbonate [Huang et al. 2014], degradation of atrazine [Hu et al. 2015], desulfurization of gasoline [Song et al. 2013] and antimicrobial activity [Ferreira et al. 2015]. Although conventionally used, AIE has been associated with various limitations; for example, requirement of high solvent volume, slow rate of metal loading, high metallic content in residual solvent and poor control of metal loading in framework [Mhamdi et al. 2009; Gao et al. 2015]. In order to overcome some of the drawbacks of the AIE, it has become necessary to developed more facile, green and environmentally-friendly approaches. Wet-impregnation and precipitation-impregnation can be developed as strategies to simultaneously remove the limitations of AIE as well as of microporosity in considerable extent. Moreover, the catalysts prepared by impregnation and precipitation-impregnation routes have never been studied for the CWPO of toxic nitrogenous aromatic compounds. Most of the CWPO studies have been carried out in batch reactors. The CWPO of nitrogenous aromatic compounds in continuous fixed bed reactor using Cu/zeolite Y has not been reported.

Cu_2OHPO_4 is receiving much attention because of its catalytic activity [Meng et al. 2003], magnetic properties [Belik et al. 2007], optical properties [Reddy et al. 1995] and electrochemical properties [Li et al. 2014]. Recently, it has also been investigated as a highly active Fenton-like catalyst. The presence of hydroxyl group in its crystalline structure plays a major role for selectively decomposing H_2O_2 to *OH radicals. In general, this material exhibit morphology and size-dependent properties. Various methods have been reported for the synthesis of micro- and nanostructured material including hydrothermal method [Xu et al. 20012], ionic liquid-assisted hydrothermal method [Duan et al. 2015], solvothermal route [Hu et al. 2017], dynamic template method [Guo et al. 2011] and microwave synthesis route [Hu et al. 2016]. However, these methods are associated with limitations of requirement of high temperature, long reaction time (6-72 h), environmentally hazardous raw materials, ligands-assisted fabrication, large number of influential parameters, and expensive reactors. Moreover, almost all above mentioned methods were reported to generate different architectures typically of micro-range. The synthesis of nanostructured Cu_2OHPO_4 has been rarely reported yet. We

have first time shown the ultra-rapid ultrasonic-assisted synthesis of Cu_2OHPO_4 and $Cu_3(PO_4)_2$ nanostructures at room temperature. In addition, the CWPO of aniline using Cu_2OHPO_4 has not been reported in previous literature.

1.6. OBJECTIVES OF THE PRESENT STUDY

The following objectives were fixed in view of research gaps, as discussed in detail in Chapter II of literature review.

➢ To synthesize the Cu/zeolite Y using aqueous ion-exchange, wet-impregnation and precipitation-impregnation routes.

➢ To synthesize different nano-architectures of copper hydroxyl phosphate and copper phosphate using ultrafast sonochemical route.

➢ To perform detailed characterization of the synthesized catalysts using ICPMS, N_2 sorption, XRD, FTIR, FE-SEM, UV-DRS, TEM, HRTEM and XPS techniques.

➢ To evaluate the catalytic activity of these materials for the CWPO of Congo red, quinoline and aniline in batch or/and continuous fixed-bed reactor.

➢ To optimize the operating parameters such as copper loading, catalyst dose, stoichiometric ratio of H_2O_2/pollutant, initial pH and temperature for the CWPO of individual components in aqueous solution.

➢ To determine kinetic and thermodynamic parameters, and to explore the possible reaction mechanism of mineralization of Congo red, quinoline and aniline by CWPO process.

➢ To explore catalytic stability and recyclability of the synthesized catalysts.

1.7. THESIS OUTLINE

The thesis is organized into seven chapters.

• *Chapter-I*

➢ This chapter first introduces the theme of the thesis, future challenges of clean water scarcity and requirement of efficient treatment technologies.

➢ Nitrogenous aromatic compounds such as Congo red, quinoline and aniline, their applications, sources of emission in water, physico-chemical properties and toxic effects on the living organisms have been discussed.

➢ The next sections of the chapter deal with the removal technologies and selection of suitable copper catalysts.

➢ The final section explains the objectives of the present research work.

• *Chapter-II*

➢ This chapter presents the detailed and critical literature review of various biological, physico-chemical and AOPs used for the treatment of Congo red, quinoline and aniline bearing wastewater.

➢ CWPO has been overviewed as prospective technology for the removal of recalcitrant organic pollutants.

➢ The available literature on synthesis and applications of copper containing zeolites Y and copper hydroxyl phosphate has been systematically discussed.

➢ The final section explains the research gaps on the basis of detailed literature review.

• *Chapter-III*

➢ This chapter deals with the experimental methodologies used for the synthesis of Cu/zeolite Y, Cu_2OHPO_4 and $Cu_3(PO_4)_2$ catalysts.

➢ Cu/zeolite Y samples were synthesized using aqueous ion exchange, wet impregnation and precipitation-impregnation routes.

➢ Cu_2OHPO_4 and $Cu_3(PO_4)_2$ samples were synthesized using ultrafast sonochemical method.

➢ The experimental procedures for evaluation of CWPO performance of synthesized catalysts have been explained for batch as well as continuous reactors.

➢ The working principles and experimental conditions of various analytical instruments, such as, XRF, XRD, surface area analyzer, FT-IR, UV-DRS, FE-SEM, TEM, HRTEM, HPLC, TOC, IC and AAS have been discussed in last two sections.

• *Chapter-IV*

➢ Detailed characterization of Cu-impregnated zeolite Y catalysts has been discussed in order to study the influence of copper loading on structure, texture and electronic states of copper.

➢ The catalysts were tested for the decolorization, degradation and mineralization of recalcitrant diazo dye (Congo red) in heterogeneous Fenton-like process.

➢ The effects of operating parameters, such as, copper loading, initial pH, H_2O_2 concentration, catalyst dose and temperature were studied for the optimization of Congo red degradation by heterogeneous Fenton-like process.

➢ The kinetics, thermodynamics and reusability of the catalyst have been discussed.

- *Chapter-V*

➢ This chapter provides the overview of copper immobilization on zeolite Y by different methods.

➢ Detailed characterization of as-synthesized materials has been discussed to understand the influence of these preparation methods on crystalline structure, hierarchical porosity and coordination environment of copper species.

➢ The catalysts prepared by different methods were tested for the oxidative degradation of quinoline in continuous fixed-bed reactor (FBR).

➢ The long term stability, kinetics and mechanism of CWPO of quinoline have been discussed in this chapter.

- *Chapter-VI*

➢ This chapter deals with the ultrafast sonochemical synthesis of Cu_2OHPO_4 and $Cu_3(PO_4)_2$ with different nanoarchitectures.

➢ Detailed characterization of as-synthesized materials has been discussed to evaluate the influence of pH, sonication energy and sonication time on purity of developed phases, particle size and their morphologies.

➢ The as-synthesized materials have been compared in terms of catalyst activity and stability for the catalytic wet peroxide oxidation (CWPO) of aniline in batch reactor.

➢ The kinetics, thermodynamics and reusability of the catalyst have been discussed in this chapter.

- *Chapter-VII*

➢ The detailed summary of the results and conclusions of this research work have been discussed in this chapter.

➢ The next section includes the key areas needed to be explored in near future for the improvement of this technology.

2.1. OVERVIEW

This chapter deals with the investigation of different treatment techniques for the removal of Congo red, quinoline and aniline from aqueous solution. Various biological and physico-chemical methods have been investigated for the treatment of nitrogenous aromatic pollutants. This chapter provides the critical review of various biological, physico-chemical, membrane based and advanced oxidation process used for the removal of nitrogenous aromatic pollutants. The detailed merits and de-merites of each process have also been discussed. The available literature on synthesis and applications of copper containing zeolites Y and copper hydroxyl phosphate has been systematically discussed.

2.2. BIOLOGICAL METHODS

These compounds resist degradation in conventional activated sludge units because of their low inherent biodegradability. The high solubility and high molecular weight impede their permeation through cell membranes. A brief overview of different biological methods used for the removal of nitrogenous aromatic compounds is given in Table 2.1.

Işik and Sponza [2003] studied the degradation of Congo red under anaerobic condition using microorganism *Pseudomonas* sp. and observed complete decolorization after 5 days of incubation. However, the mineralization efficiency was almost negligible. Other reports have also shown that azo bonds reduce to aromatic amines and these amines are bio-recalcitrant under anaerobic condition [Pandey et al. 2007]. On the contrary, the azoreductase enzymes of aerobic bacteria reductively cleave the azo bond of dyes to amines and can use these amines for their growth. In aerobic degradation of aromatic amines, the initial reactions involve the hydroxylation of the ring, followed by ring destruction by incorporating two oxygen atoms. Keeping this fact in mind, the major attention has been given on discussion of aerobic processes.

Chakraborty et al. [2013] studied the aerobic biodegradation of Congo red using white rot fungus *Alternaria alternata* CMERI F6 and measured the influence of different operating parameters. The maximum decolorization efficiency of 99.99% was observed at initial pH = 3-7, T = 25 °C, glucose = 27.75 mM, and dye = 0.86 mM after 48 h. Glucose was observed as more efficient substrates in comparison to beef extract, peptone, yeast extract and sugarcane bagasse. Congo red cannot be used as carbon source because azo bonds are electron deficient. A severe impact of heavy metals was also noticed on decolorization. The high cost of conventional carbon

substrates such as glucose, fructose and sucrose has limited their application [Zhao et al. 2012; Aljuboori et al. 2014].

Sadighi et al. [2013] synthesized the laccase-loaded chitosan nanoparticles and attached these particles on functionalized surface of glass beads. The surface functionalization of glass beads was carried out by three successive steps such as etching with NaOH, amino-functionalization using silane coupling agent such as 3-aminopropyltriethoxysilane and covalent attachment of glutaraldehyde. Higher enzymes immobilization efficiency was observed on functionalized glass beads using chitosan nanoparticles (40.1%) rather than direct immobilization without chitosan (32.2%). Laccase-entrapped chitosan nanoparticles on glass beads showed higher decolorization efficiency (100%) for Congo red in comparison to laccase immobilized on glass beads (43%) and free laccase (60%). Laccase-entrapped chitosan nanoparticles on glass beads showed higher reusability and retained 98% decolorization efficiency after 25 cycles. This immobilized bio-catalytic system has high thermal stability and improved life of enzyme substantially. However, the requirement of high cost surface modifying agents and redox mediator for high activity of enzymes can make this process uneconomical.

Ayed et al. [2010] optimized the different combination of three bacteria (*Sphingomonas paucimobilis, Bacillus* sp. and *Staphylococcus epidermidis*) for the maximum decolorization and COD removal efficiencies. The maximum decolorization (100%) and COD removal (98%) were obtained if *Sphingomonas paucimobilis, Bacillus* sp. and *Staphylococcus epidermidis* were in extent of 2.3%, 45.9% and 51.6%, and 0.6%, 98.5% and 0.8%, respectively. *Bacillus* sp. *and Staphylococcus epidermidis* majorly contributed in degradation of Congo red. Phytotoxicity studies showed that the degradation products were not toxic and treated effluent can be used for irrigation.

Gopinath et al. [2009] studied the assimilation of Congo red using *Bacillus* Sp. isolated from contaminated sites of tannery wastewater and observed complete degradation in aerobic condition within 24-27 h. In a different study [Gopinath et al. 2009], same group used random mutagenesis for genetic modification of *Bacillus* Sp. and observed higher degradation in comparison to wild strain. Ning et al. [2014] studied the performance of aerobic *Acitonetobacter baumannii* YNWH 226 bacteria for mineralization of Congo red and observed 93.72% TOC reduction. However, the severe impacts of heavy metals and long reaction time are major drawbacks of these processes [Singh et al. 2011].

Li et al. [2015] studied the capacity of *Acinetobacter baumannii* YNWH 226 to use Congo red as sole carbon source for the production of extracellular polymeric substances (EPS) which are used as bioflocculants. YNWH was isolated from sludge of dyeing wastewater treatment plant. The strain showed 98.60% decolorization efficiency and 94.02% TOC removal after 48 h. The results of different experimental study indicated that adsorption and degradation contribute simultaneously in dye removal. Bacterial strains retained stable decolorization (98.62-94.33%) up to 7 cycles. EPS contained polysaccharides and proteins in major proportion. The produced EPS has high flocculation activity and remarkable dewaterability. EPS combined with pollutants or sludge plays a significant role in adsorption and biodegradation.

Most of the previous studies have shown that quinoline is recalcitrant under anaerobic condition [Aislabie et al. 1990; Miethling et al. 1993]. Li et al. [2010] studied the degradation of quinoline using nitrate reducing anaerobic condition in acclimated activated sludge process. The sludge was obtained from anoxic tank of coking wastewater treatment plant. The complete degradation of quinoline and complete denitrification was observed at optimum $COD/NO_3-N = 7$ within 13 h. Nitrate rapidly reduced into nitrite, and this nitrite was used as electron acceptor in metabolic process until it is fully consumed. Quinoline transformed into 2 (1H)-quinolinone which mineralized more rapidly than quinoline. Therefore, quinoline degradation and mineralization efficiency profiles showed similar pattern with each other. Various isolated bacterial strains such as *Rhodococcus* sp. [Zhu et al. 2008] and Pseudomonas sp. BW003 [Sun et al. 2009] have shown quinoline degradation capability at lower concentration. Higher concentration (> 300) inhibits bacterial growth and causes negative effect on quinoline degradation.

Lin et al. [2010] isolated the quinoline-degrading bacterial strain *Pseudomonas putida* from municipal wastewater treatment plant sludge. A complete degradation of quinoline was observed within 3 h. Unlike most of bacteria, it can degrade quinoline at concentration higher than 3.87 mM. Therefore, this bacterium can be recognized as effective quinoline-degrading microorganism. However, the mineralization efficiency was almost negligible due to formation of recalcitrant intermediates.

Xu et al. [2015] studied the influence of glucose co-substrate on quinoline-degradation efficiency of mixed culture isolated from coal gasification treatment plant. *Pseudomonas* sp. was recognized as the predominant bacterial strain in this mixed culture. The presence of glucose accelerated the quinoline degradation. The time of complete removal of quinoline decreased from

30 to 18 h with increase in glucose concentration from 0 to 1000 mg L^{-1}. Additionally, lag time reduced from 7 to 2 h with increase in glucose concentration from 0 to 1000 mg L^{-1}. It increased the activity of monooxygenase which is responsible for quinoline degradation. Biodegradation kinetics of quinoline was best fitted with first-order model.

Zhuang et al. [2015] immobilized the quinoline-degrading bacterium *Streptomyces* sp. N01 over bamboo-carbon supported magnetite (Fe_3O_4/BC). The bacterium was isolated from coal gasification wastewater treatment plant. Unlike free cells, the immobilized cells could tolerate high concentration of quinoline, and found insensitive in a wide range of pH (5-10) and temperature (20-45 °C). The higher degradation efficiency of Fe_3O_4/BC was attributed to protection of cell from toxicity by BC, and improvement of cell permeability and enzyme activity by Fe_3O_4. The quinoline degradation followed first-order kinetics and immobilized cells show high reusability in 7 consecutive tests.

As discussed above, aromatic amine such as aniline compound is not degradable under anaerobic condition [Pereira et al. 2011]. De et al. [1994] reported that aniline concentration was constant for more than 6 months under methanogenic condition. Therefore, aerobic degradation methods have come into the prime focus of researchers. Many bacterial strains *Rhodococcus* sp. [Zhuang et al. 2007], *Candida tropicalis* [Wang et al. 2011], *Dietzia natronolimnaea* JQ-AN [Jin et al. 2012] and *Pseudomonas* spp. [Liu et al. 2013] have been reported for degradation of aniline in aerobic condition. However, the long degradation time (2-7 days), rigidity towards fluctuation and more resistant products with less toxicity has been reported.

Jin et al. [2012] isolated *Dietzia natronolimnaea* JQ-AN bacterium from aniline-containing industrial wastewater and studied its capability for aniline degradation in aerobic condition. The bacterium has high salinity tolerance and suitable for real aniline wastewater which usually have high salinity. Sodium acetate was used as co-substrates to improve microbial growth and aniline degradation. The maximum degradation of aniline was observed 87% at optimum condition T= 30 °C, pH= 8.0, sodium chloride= 3% (w/v), sodium acetate= 40 mM, aniline= 3.22 mM and time= 120 h. Catechol was identified as first intermediate in degradation of aniline and further degraded into small organic compounds such as succinic acid, citric acid, pyruvic acid and acetaldehyde. The major limitation of this bacterium was decrease in aniline degradation and microbial growth at concentration higher than 3.22 mM.

Table 2.1: A brief literature overview of biological methods for degradation of Congo red, quinoline and aniline

Target Compounds as substrates	Biological system	Optimized condition	Performance	Remarks	References
Congo red	White rot fungus in Erlenmeyer flask	$C_0 = 0.86$ mM $pH_0 = 3.0\text{-}7.0$ $T = 25\,°C$ glucose = 27.75 mM $t = 48$ h	Decolorization = 99.99%	• White rot fungus *Alternaria alternata* CMERI F6 was used for decolorization. • Congo red could not act as carbon source (electron donor). • Glucose was observed as the most efficient co-substrate for decolorization of Congo red. • Decolorization efficiency was insensitive of pH in range 3 to 7. • Decolorization efficiency decreased in presence of Hg, Cd and Pb.	Chakraborty et al. 2013
Congo red	Immobilized enzymes	$C_0 = 0.28$ mM $pH_0 = 5.0$ $T = 40\,°C$ 1-hydroxy benzotriazole = 0.5 mM Enzyme = 100 g L^{-1}	Decolorization (Immobilized enzymes)= 100.00% Decolorization (free enzymes)= 60.00%	• Laccase-loaded chitosan nanoparticles on glass beads (LCNG) showed higher decolorization efficiency in comparison to laccase immobilized on glass beads as well as free laccase. • The surface functionalization of glass beads was carried out using NaOH, 3-aminopropyltriethoxysilane and glutaraldehyde. • LCNG showed higher reusability and retained 98% decolorization efficiency up to 25 cycles. • Immobilization improved thermal stability and life of enzyme.	Sadighi et al. 2013
Congo red	Mixed culture in Erlenmeyer flask	$C_0 = 1.07$ mM $pH_0 = 7.0$ $T = 37\,°C$ glucose = 6.94 mM yeast = 3.0 g L^{-1}	Decolorization = 100.00% X_{COD}= 98.00%	• Optimization of different combination of three bacteria (*Sphingomonas paucimobilis, Bacillus* sp. *and Staphylococcus epidermidis*) was carried out for the maximum degradation of dye. • The maximum degradation was obtained	Ayed et al. 2010

Target Compounds as substrates	Biological system	Optimized condition	Performance	Remarks	References
		t = 10 h		when *Sphingomonas paucimobilis, Bacillus* sp. *and Staphylococcus epidermidis* were in extent (2.3%, 45.9% and 51.6%) and (0.6%, 98.5% and 0.8%). • *Bacillus* sp. *and Staphylococcus epidermidis* majorly contributed in degradation of Congo red. • Degradation products were non-toxic.	
Congo red	Liquid inoculum in Erlenmeyer flask	$C_0 = 0.14$ mM $pH_0 = 7.0$ T = 37 °C t = 48 h	Decolorization = 98.06%; X_{COD} = 94.02%	• *Acinetobacter baumannii* YNWH 226 used Congo red as sole carbon source for the production of extracellular polymeric substances (EPS) which worked as bioflocculants. • The strain showed 98.60% decolorization efficiency and 94.02% TOC removal after 48 h. • Bacterial strains retained stable decolorization (98.62-94.33%) up to 7 cycles. • EPS in combination with pollutants or sludge plays a significant role in adsorption and biodegradation.	Li et al. 2015
Quinoline	Acclimated activated sludge	$C_0 = 0.77$ mM T = 25 °C MLSS = 3 g L^{-1} COD/ NO_3-N = 7 t = 13 h	$X_{quinoline}$ = 100%, X_{TOC} = 100%	• The sludge was obtained from anoxic tank of coking wastewater treatment plant. • The complete degradation of quinoline and complete denitrification was observed at optimum COD/NO_3-N = 7 within 13 h. • Nitrite produced by reduction of nitrate was used as electron acceptor in metabolic process. • Quinoline converts into hydroxylated product 2 (1H)-quinolinone which mineralized more rapidly than quinoline.	Li et al. 2010

Target Compounds as substrates	Biological system	Optimized condition	Performance	Remarks	References
Quinoline	Immobilized over bamboo−carbon supported Fe_3O_4	$C_0 = 3.09$ mM pH = 5.0-10.0 T = 20-45 °C t = 16 h	$X_{quinoline}$ (immobilized cells) = 100% $X_{quinoline}$ (free cells) = 68.25%	• The bacterium *Streptomyces* sp. N01 was immobilized over Fe_3O_4/ bamboo carbon. • The immobilized system improved bacterium tolerance for high concentration of quinoline, and wide ranges of pH (5-10) and temperature (20-45 °C). • The quinoline degradation followed first order kinetics. • The degradation efficiency was constant for 7 cycles. • Fe_3O_4 was responsible for increasing cell permeability and enzyme activity.	Zhuang et al. 2015
Quinoline	Liquid inoculum in shake flasks	$C_0 = 3.87$ mM T = 30 °C t = 3 h	$X_{quinoline} = 100\%$	• The bacterium *Pseudomonas putida* was isolated from activated sludge of municipal wastewater. • Bacterium converted N−atoms into NH_3. • The bacterium was inefficient for mineralization of quinoline.	Lin et al. 2010
Quinoline	Free cells in shake flasks	$C_0 = 0.77$ mM T = 35 °C t = 18-30 h Glucose = 5.55 mM	$X_{quinoline} = 100\%$	• *Pseudomonas* sp. was isolated from coal gasification plant. • Glucose accelerated the quinoline degradation. • Glucose increased the activity of monooxygenase enzyme in bacterium. • The time of complete removal of quinoline decreased from 30 to 18 h with increase in glucose concentration from 0 to 5.55 mM.	Xu et al. 2015
Aniline	Cultured mycelial pellet as biomass	T = 30 °C $C_0 = 1.05$-1.54 mM air flow = 2 L h^{-1}	Aniline removal efficiency = 0.9 mg L^{-1} $MLSS^{-1}$ day^{-1}, COD	• The mycelial pellet was used in SBR instead of activated sludge. • The mycelial pellet contains aniline degrading microorganism *Acinetobacter*	Zhang et al. 2011

Target Compounds as substrates	Biological system	Optimized condition	Performance	Remarks	References
	carrier in SBR	HRT = 20 h SRT = 60 days pH_0 = 7.0-7.2 MLSS = 2364 mg L^{-1} t_{cycle} = 12 h	removal efficiency = 1.0 mg L^{-1} $MLSS^{-1}$ day^{-1}	*calcoaceticus* JH and the mineralization efficient mix culture of bacteria. • The mycelial pellet containing SBR was more efficient than SBR with activated sludge.	
Aniline	Adsorbed enzymes on carbon nanotubes (CNT)	C_0 = 5.36 mM T = 30 °C t = 24 h CNT = 0.2 g L^{-1}	$X_{aniline}$ (single wall CNTs) = 76.8% $X_{aniline}$ (multiple wall CNTs) = 41.6% $X_{aniline}$ (free cells) = 41.6%	• The bacterium was isolated from aniline wastewater treatment plant. • Higher efficiency of single wall CNTs was attributed to higher adsorption of enzymes on its surfaces.	Yan et al. 2011
Aniline	Liquid inoculum in shake flasks	C_0 = 3.22 mM pH = 8.0 T = 30 °C NaCl = 3% (w/v) sodium acetate = 40 mM t = 120 h	$X_{aniline}$ = 87%	• Isolated bacteriaum *Dietzia natronolimnaea* JQ-AN was used for aniline degradation in aerobic condition. • Sodium acetate as co-substrates improved microbial growth and aniline degradation. • This bacterium is suitable for real aniline wastewater which usually has high salinity. • Catechol, succinic acid, citric acid, pyruvic acid and acetaldehyde were major intermediates.	Jin et al. 2012
Aniline	Liquid inoculum in shake flasks	C_0 = 2.75 mM T = 10 °C t = 72 h	$X_{aniline}$ = 97%	• Cold tolerant isolated microbe *pseudomonas* sp. was used to degrade aniline and nitrobenzene. • Aniline at concentration higher than 2.75 mM was toxic to bacterial strain. • The biodegradation kinetics was best fitted with the zero order mohydel. • The main byproducts were azobenzene, azoxybenzene and acetanilide.	Liu et al. 2013

MLSS = mixed liquor suspended solids; HRT = hydraulic retention time; SRT = solids retention time; CNT = carbon nano tube

Zhang et al. [2011] used mycelial pellet as biomass carrier to immobilize the aniline degrading microorganism *Acinetobacter calcoaceticus* JH-9 and the mineralization efficient mix culture of bacteria. The mix culture contained *Bacillus* sp. F18, *Bacillus* sp. W5, *Acinetobacter* sp. F22 and *pseudomonas* sp. W2. This biomass carrier was used in SBR (sequencing batch reactor), and aniline removal efficiency was evaluated. The mycelial pellet containing-SBR showed high aniline degradation efficiency (0.9 mg L^{-1} $MLSS^{-1}$ day^{-1}) and higher COD removal efficiency (1.0 mg L^{-1} $MLSS^{-1}$ day^{-1}) as compare to SBR with JH and activated sludge system (0.6 mg L^{-1} $MLSS^{-1}$ day^{-1}). Ammonia was identified as major product and no nitrification of aniline was observed. The disadvantages associated with this system are requirement of higher level of sophisticated control, automated walls and higher level of maintenance.

Yan et al. [2011] studied the synergetic effect of carbon nanotubes (CNTs) and the enzymes of *Delftia* sp. XYJ6 in biodegradation of aniline. The aniline degrading bacterium was isolated from aniline wastewater treatment plant. Higher aniline biodegradation was observed using single wall carbon nanotubes (76.8%) in comparison to multiple walls carbon nanotubes (41.6%). The multiple walls CNTs showed degradation efficiency similar to free cell of bacterium (~41%). The higher efficiency of single wall CNTs was attributed to higher adsorption of enzymes on its surfaces.

Liu et al. [2013] isolated the cold-tolerant microbe *Pseudomonas* spp. from aniline contaminated sites and studied its aniline degradation efficiency in aerobic condition. Aniline degradation efficiency was 97% at 10 °C after 3 days. Aniline was toxic to bacterium at concentration higher than 2.75 mM. The generated by products were less toxic than aniline and required an alternative method for remediation.

Zhang et al. [2008] obtained a recombinant strain, *Escherichia coli* JM109-AN1 with aniline degrading gene cluster of 16 genes. This gene cluster contains aniline dioxygenase and catechol 2,3-dioxygenase in major extent. These genes facilitate the complete conversion of 3.22 mM aniline to TCA-cycle intermediates in 100 h.

2.2.1. Limitation of biological treatment methods

Biological degradation methods are very slow and take a lot of time [Zhu et al. 2008]. As mentioned above, the anaerobic treatments are not sufficient for mineralization of Congo red, quinoline and aniline. Aerobic cultures have ability to mineralize aromatic amines but these are also associated with certain drawbacks. White rot fungi need strict aerobic condition. The high cost

of conventional carbon substrates such as glucose, fructose and sucrose has limited their application. Only few aerobic strains can utilize these organic pollutants as sole carbon source and biodegradation is accomplished through specific enzymes. The availability of any nutrient (nitrogen, phosphorus and iron) could become the limiting factor and thus, affect the degradation process. The metabolic degradation of nitrogenous pollutants produce nitrate which can stimulate eutrophication. Their susceptibility to shock load and requirement of large area are major limitations associated with these methods. Less efforts have been made to explore the role of chemical composition, microbial ecology and geophysical properties of contaminates sites in evolution. This valuable information can be applied for the development of more effective methods for engineering strains with higher degradation capacity [Ju et al. 2010]. Since the biological methods are insufficient to degrade these nitrogenous aromatic pollutants completely, a chemical treatment prior to these methods can be a viable option to increase their biodegradability. Moreover, a tertiary treatment method can be used to reduce the toxicity of recalcitrant metabolic products.

2.3. PHYSICO-CHEMICAL METHODS

A number of physico-chemical methods such as adsorption, coagulation/flocculation and membrane technology have been investigated to treat dyes and nitrogenous pollutants. These treatment methods can be used singly or in combination for the removal of organic pollutants. They can be used in the form of pretreatment, main treatment or post treatment depending upon the quality of wastewater.

2.3.1. Adsorption

Adsorption is a widely used technology for wastewater treatment in various industries because of its high efficiency, low initial cost, universal nature and simple operation [Sharma et al. 2010; Devi et al. 2017]. Adsorption is commonly used to remove certain categories of organic pollutants which are difficult to degrade by conventional biological wastewater treatment methods. Therefore, it is commonly used as tertiary treatment method. The viability of adsorption technique mainly depends on the adsorbents characteristics. A brief overview of different adsorbents used for the removal of nitrogenous aromatic compounds is given in Table 2.2.

Li et al. [2015] prepared fibrous activated carbon (FCA) from silkworm cocoon waste and used it further for the adsorption of diazo Congo red dye. FCA was synthesized using two-step process of $(NH_4)_2HPO_4$ pretreatment followed by KOH activation. Both pretreatments led to

development of structure which has high porosity and high surface area. The highest surface area (2797 m^2 g^{-1}) was obtained with KOH activation treatment of 3 h. Adsorption capacity was observed to increase with surface area and highest adsorption capacity of 512 mg g^{-1} was obtained in acidic condition (pH =2). This was attributed to electrostatic interaction between the negatively charged SO$_3^{2-}$ anion and positively charged FCA surface. Adsorption of CR was best fitted with the pseudo-second order model. It was observed that adsorption rate was controlled by the intra-particle diffusion. Langmuir model was best fitted with the adsorption equilibrium data and the maximum adsorption capacity of 1100 mg g^{-1} was obtained. The formation of S-O and S=O bonds with the functional groups of FCA surface suggest the major role of chemical adsorption.

Lei et al. [2017] synthesized hierarchical porous ZnO microspheres (HZM) via a hydrothermal route and evaluated its performance for the adsorption of Congo red dye. Two dimensional nanosheets were arranged to establish the microsphere morphologies with diameters of 6-8 μm. HZM showed higher adsorption capacity in comparison to commercial ZnO at the same operating condition. The higher surface area and stronger electrostatic attraction (represented by higher zeta potential) were responsible factors for the large adsorption capacity. The pseudo-second order model was best fitted with the kinetic data. Langmuir model shows better fit with the adsorption equilibrium data in comparison to Freundlich model. The maximum adsorption capacity (334 mg g^{-1}) for HZM was much higher than commercial ZnO (72 mg g^{-1}). HZM showed good recyclability and possessed constant performance up to five cycles.

Vico et al. [2006] used Na-clay mineral such as sepiolite, palygorskite and saponite for the adsorption of quinoline from aqueous solution. Adsorption capacity was found to increase in the order of palygorskite (38.75 mg g^{-1}) < sepiolite (77.49 mg g^{-1}) < saponite (103.32 mg g^{-1}). The polar molecules adsorption mechanism between oxygen atoms of the basal plane and electron donor quinoline molecules was found responsible for the highest removal by saponite. Adsorption capacity increased with increase in pH and the contribution of ion exchange mechanism was negligible at pH > 6. High ionic strength shows little influence on adsorption capacity of saponite at all pH. The analysis of Na^{2+} and Mg^{2+} indicates that quinoline adsorption occur on broken edge sites and prevents their dissolution. The competitive adsorption of Mn^{2+} and quinoline shows that quinoline could be adsorbed on SiOH sites of tetrahedral sheets as well as MgOH and AlOH sites of octahedral sheets. A simultaneous pH increment was observed at initial stage of adsorption of

quinoline. This behavior was attributed to small contribution of hydroxyl ion displacement reaction in adsorption.

Rameshraja et al. [2012] used commercial grade coconut-based granular activated carbon (GAC) and bagasse fly ash (BFA) for the adsorptive removal of quinoline. GAC showed higher adsorption capacity in comparison to BFA. Higher performance of GAC as compare to BFA attributed to higher surface area of GAC. Adsorption data was best fitted with pseudo-second order model for both adsorbents. It was observed that adsorption process was controlled by more than two processes. Surface adsorption and intraparticle diffusion control the adsorption process of both the adsorbents. Adsorption process was endothermic in nature, which signified the simultaneous contribution of physisorption and chemisorption. It was observed that Redlich-peterson isotherm best fit the experimental data for both adsorbents at 45 °C. Negative values of thermodynamic factor ΔG^0 at all temperatures indicate the spontaneity of the quinoline adsorption on GAC and BFA. The thermodynamic parameters ΔH^0 and ΔS^0 were 12.64 kJ mol^{-1} and 112.96 J mol^{-1} K^{-1}, respectively.

Liao et al. [2013] synthesized mesoporous bamboo charcoal from moso bamboo by employing a sequence of heat treatment processes under N_2 atmosphere and used it for the adsorption of nitrogen heterocyclic compounds, viz. pyridine, indole and quinoline. The adsorption capacity of pyridine was lower than quinoline and indole due to relatively lower octanol-water distribution coefficient (log K_{ow}). Kinetic data was best fitted with pseudo-second order model and suggests that adsorption process is surface diffusion controlling in initial stage (1 h) and intraparticle diffusion controlling in later stages. Adsorption isotherms for all compounds were well fitted with Freundlich model. Adsorption capacity was increasing with temperature which may be attributed to involvement of not only physical adsorption but also chemical adsorption. Adsorption capacity of microwave regenerated material was higher as compared to fresh material. The regenerated adsorbent exhibited increase in mesoporous area and mesoporous volume. These mesopores were responsible for high capacity of regenerated adsorbent. The increase in hydrophobicity, graphitic content and π−π* content of regenerated adsorbent were also responsible for enhancement of adsorption capacity.

Burgos et al. [2002] employed kaolinite and montmorilonite for the adsorption of quinoline. In this study, the effect of operating parameters such as pH, ionic strength and quinoline concentration was measured. The adsorption capacity of montmorilonite was approximately 100

times of kaolinite due to higher charge density (charged siloxane sites). The selectivity for adsorption of cationic quinoline over Ca^{2+} was higher for montmorilonite in comparison to kaolinite. The highest adsorption capacity of 60.70 mg g^{-1} was observed for montmorilonite within pH range of 2.9-4.8 at ionic strength of 0.4 mM $CaCl_2$ and at quinoline concentration of 0.23 mM. The adsorption of quinoline was best fitted with the Langmuir isotherm.

Gao et al. [2015] prepared modified jute fiber using microwave heat treatment in presence of pyromellitic dianhydride (PMDA). The generation of carboxyl groups on the jute fibers was responsible for the increase in adsorption capacity. At pH below 7, the adsorption capacity decreased due to competition of protonated aniline with the H^+ ions to interact with functional group. The endothermic nature of adsorption was attributed to major role of chemisorption. The negative value of ΔG^0 (−18.05 kJ mol^{-1}) confirmed the thermodynamic feasibility of aniline adsorption. The positive values of ΔH^0 (8.88 kJ mol^{-1}) and ΔS^0 (0.029 kJ mol^{-1} K^{-1}) suggests the endothermic nature and affinity of adsorbent to aniline, respectively. The pseudo-second order kinetic model fitted well with the adsorption data. The adsorption equilibrium data are also well fitted with the Langmuir isotherm, which confirms the monolayer adsorption of aniline on modified jute fiber. The use of HCl solution was recognized as the best method for the regeneration of spent adsorbent. Adsorption mechanism was explained on the basis of electrostatic interaction, and formation of hydrogen bond between -OH of carboxyl group and amide group of aniline.

Hu et al. [2015] prepared g-C_3N_4 from pyrolysis of urea at 550 °C and employed it for the adsorption of aniline in aqueous solution. The effect of different variables such as contact time, pH, adsorbent dose, temperature, initial concentration and ionic strength was observed on removal efficiency. At pH above 5, the adsorption of aniline was attributed to π-π electron donor-acceptor mechanism. At pH < 5, electrostatic interaction between the protonated aniline and charged surface of g-C_3N_4 was a predominant mechanism. The adsorption equilibrium data of aniline was well described by the Langmuir isotherm. The adsorption kinetic data was well fitted with the pseudo-second order model. The independence of adsorption of aniline on ionic strength also indicates major contribution of π-π interaction. The negative value of ΔG^0 (−26.03 kJ mol^{-1}) confirmed that aniline adsorption is spontaneous. The positive values of ΔH^0 (12.42 kJ mol^{-1}) and ΔS^0 (113.71 J mol^{-1} K^{-1}) suggests the endothermic nature and affinity of adsorbent to aniline, respectively. G-

C$_3$N$_4$ was regenerated using alcohol solution and resulting material showed constant adsorptive capacity for large number of cycles.

Pardo et al. [2016] tested 11 different activated carbons (ACs) for the adsorptive removal of aniline. The main objective of the study was to observe the most dominant factor, textural properties or surface oxygen group, for the adsorption of aniline on ACs. The high adsorption capacity of ACs was recorded in correlation with the textural properties. Adsorption capacity was influenced by the textural properties in the following order: surface area > micropore volume > total pore volume > mesoporous volume. A negligible influence of high concentration of carboxylic and phenolic groups was observed on aniline adsorption irrespective of the high surface areas of many ACs. For most of the ACs, adsorption equilibrium and adsorption kinetics were best fitted with the Langmuir model and pseudo-second order model, respectively. The adsorption capacity decreased at pH below 7 because of electrostatic repulsion between deprotonated aniline and positive charged surface. The negative value of ΔG^0 (-19.04 kJ mol^{-1}) confirmed that aniline adsorption is spontaneous. The positive values of ΔH^0 (56.74 kJ mol^{-1}) and ΔS^0 (250 J mol^{-1} K^{-1}) indicates the major role of chemical adsorption and affinity of adsorbent to aniline, respectively.

Hu et al. [2014] synthesized sawdust-cyclodextrin (SD-β-CD) polymer using sonic oscillation for 20 minutes and used it for the removal of aniline from aqueous solution. β-CD layer on sawdust surface significantly increased the adsorption of aniline molecules. The adsorption capacity was found maximum within pH range of 4-8. The result may be attributed to higher stability of β-CD coating in this pH region. The pseudo-second order kinetic model was best fitted with the experimental adsorption data. The adsorption equilibrium data was best fitted with the Freundlich model at different temperatures and aniline concentrations. The adsorption capacity was found to decreases with increase in temperature, which indicates the exothermic nature of adsorption process. The negative value of ΔG^0 (-19.04 kJ mol^{-1}) showed that aniline adsorption is spontaneous on SD-β-CD. The adsorption mechanism was very much different from the porous materials because of its very low surface area. The major role was played by the electrostatic forces.

2.3.2. Coagulation-flocculation

Coagulation-flocculation is a widely used technology with the advantages of low cost and simple operation. Coagulation process is generally used as preliminary or tertiary step in wastewater treatment. The performance of coagulation process depends upon the chemical structure of organic

pollutants [Khandegar et al. 2013]. A brief overview of different types of coagulants used for the removal of nitrogenous aromatic compounds is given in Table 2.2.

Morshedi et al. [2013] produced the amyloid nanofibrils through incubation of hen egg-white lysozyme protein for 36 h at 57 °C and pH = 8.0. These protein fibrils were used as bio-coagulants for the removal of different dyes. The sulphate groups in the Congo red molecule induced negative charge and facilitated reaction with the basic residues of fibrils. This high molecular weight dye made big coagulates with the fibrils and precipitated out from the water. The coagulation process could also be attributed to hydrogen bonding between hydroxyl groups of amyloids and amine groups of the dye molecules. High dye removal efficiency was observed at high temperature due to well dispersion and high surface activity. The maximum dye removal of 95% was observed at pH = 7, T = 57 °C, fibrils = 30 mg L^{-1}, dye = 0.057 mM and NaCl = 500 mM. Higher removal efficiency was obtained in comparison to conventional activated carbon (6%). The treated decolorized effluent did not show any toxicity to living cells. However, the coagulation operation was pH sensitive. The lower efficiency at alkaline pH was due to aggregation of lysozyme protein.

Prajapati et al. [2016] compared the conventional coagulants such as aluminium sulfate, aluminium chloride, iron (III) chloride, poly aluminium chlorides (PAC) and poly diallydimethylammonium chloride (poly DADMAC) for the removal of Congo red at high concentration. Powder grade PAC SAB 18 was recorded with highest COD removal of 98.7% and decolorization efficiency of 99%. The use of PAC was also associated with advantages of less dosage requirement, less sludge and quick floc formation. The effectiveness of PAC was improved using physical blending with other inorganic or organic coagulants. The composite coagulant with 30% PAC and 70% iron chloride was best with COD removal of 99% at dosage of 250 mg L^{-1}. The maximum COD removal efficiency was observed at operating condition pH = 3-9, coagulant dose = 150 mg L^{-1}, T = 27 °C, Dye = 0. 71 mM and sedimentation time = 75 min. Above pH 9, COD removal efficiency decreases because of formation of $Al(OH)_4^-$ species. The negative charge of $Al(OH)_4^-$ flocs, due to presence of OH^- groups, repels the SO_3^- groups of the dye. The composite coagulant generates sludge with minimum sludge volume index of 50 mL g^{-1} which indicates towards the good settling characteristics.

Vijayaraghavan et al. [2016] studied the coagulation capacity of natural organic polymer extracted from algae *Sargassum* sp. for the Congo red dye removal. The extracted alginate was

basically a polysaccharide containing D-mannuronic acid and L-guluronic acids as monomer units. This alginate showed coagulant properties after conversion into insoluble polymers or gels in the presence of calcium ion. The maximum dye removal of 96% was observed at pH = 4, calcium dose = 6 g L^{-1}, coagulant dose = 60 mg L^{-1} and dye concentration = 0.36 mM. H^+ ions amount increased at pH = 4 and adsorbed on the alginate surface. The strong electrostatic attraction between positively charged alginate and negatively charged SO_3^- groups of dye was responsible for the maximum dye removal at pH = 4.

Li et al. [2018] recovered poly aluminium ferric silicate chloride (PAFSIC) from coal gangue waste and used as coagulant for treatment of coking wastewater. Acid and alkali leaching treatments were carried out to obtain PAFSIC coagulants of different composition. The coagulant was the mixture of crystalline and amorphous phases with majority of Si-O-Al and Si-O-Fe bonds. The maximum COD, color and natural organic matter removals were 70%, 75% and 62%, respectively, at T = 20 °C, Al/Fe = 3, (Al+Fe)/Si = 13 and coagulant dose = 125 mg L^{-1}. The organic removal through coagulation was ascribed to simultaneous effects of charge neutralization, adsorption to flocs and complexation interaction with active sites of metal hydroxides.

Wada et al. [1995] observed that aniline and other aromatic amines cannot be removed by synthetic polymer coagulants. A strategic combination of enzymatic reaction using tyrosinase and coagulation using synthetic polymers was explored in this study for the removal of aniline. Only 28% aniline removal was observed by incubation with tyrosinase. The removal of aniline increased from 28 to 97% in presence of 1.0 mM of phenol and this removal was attributed to cross-coupling reaction of aniline with quinones formed during incubation with tyrosinase. These water soluble cross-coupling products were precipitated out during treatment with cationic polymer coagulants (hexamethylenediamine-epichlorohidrin polycondensate, polyethleneimine or chitosan). The former two amino group containing coagulants exhibited the highest removal efficiency for aniline. The complete removal of aniline was observed with optimum coagulant dose of 30 mg L^{-1} and phenol concentration = 1.0 mM, within incubation time of 5 h. The combination of immobilized tyrosinase with polymeric coagulants has advantages of stable operation even after 10 cycles and requirement of low coagulant dose (4-12 mg L^{-1}).

Ahmadi et al. [2017] used the combination of coagulation/flocculation and flotation methods for the removal of aniline from aqueous solution. PAC was selected as coagulant because of advantages of low pH sensitivity, low temperature sensitivity, less dosage requirement, less

sludge and better sludge settling characteristics. The maximum aniline and COD removals of 95% and 89.6% was recorded at pH = 6, coagulation time = 10 min, PAC dosage = 20 mg L^{-1}, aniline = 2.147 mM, flotation time = 20 seconds, T = 20-23 °C and saturation pressure = 4 atm. A comparative study of the flotation and sedimentation methods indicate that the flotation method required less PAC dose to carry the flocs from bulk to surface. The aniline removal efficiency decreased after 10 min because of formation of large flocs. The effective average bubble diameter was measured 40 μm at saturation pressure of 4 atm for better contact with flocs.

2.3.3. Membrane technology

Membrane processes such as nanofiltration (NF), ultrafiltration (UF) and reverse osmosis (RO) have been employed as tertiary treatment method in industrial wastewater treatment operation. These processes are very efficient for nitrogenous aromatic pollutants removal and generate a pure permeate stream [Sinha et al. 2006; Ghosh et al. 2006; Maji et al. 2009]. A brief overview of different membrane used for the removal of nitrogenous aromatic compounds is given in Table 2.2.

Wang et al. [2012] synthesized inorganic-organic nanohybrid membrane for nanofiltration by assembling modified graphene oxide (GO) onto polyacrylonitrile (PAN) membrane and studied performance for the removal of Congo red and various dyes. GO incorporation exhibited positive effect on elasticity, hardness and thermal stability of the membrane. These membranes possessed excellent capacity for CR removal (99.5%). GO modified membrane showed higher rejection capacity in comparison to pure PAN membrane. The rejection capacity of CR improved from 91.5% to 99.5% after GO incorporation; however, the flux remained almost stable at 4.2 kg m^{-2} h^{-1} at pressure 500 kPa. The high rejection capacity was attributed to the electrostatic repulsion between the anionic dye molecules and negatively charged outer layer of GO.

Lin et al. [2016] studied the performance of tight ultrafiltration (UF) membrane for the removal and recovery of Congo red from pure aqueous solution and from solution with high salinity. The UF membrane provided high rejection for all direct dyes and high filtrate flux without rejecting Na_2SO_4. In pure solution, the rejection percentage decreased with increase in pressure which was attributed to enhanced adsorption on surface resulted into increase permeation of dye. On the other hand, higher rejection of CR was observed at high concentration. High removal percentage of 99.96% was observed at 400 kPa. The high rejection of CR was ascribed to synergetic effect of effective size increment due to aggregation of dye molecules and electrostatic repulsion from surface of membrane. The high rejection percentage of > 98.9% was obtained for

all dyes at a pressure of 400 kPa in the presence of 60 g L^{-1} Na$_2$SO$_4$. UF membrane possessed extraordinary operational stability for long run. An ultrafiltration-diafiltration method was used with desalination efficiency of 98% and dye rejection of 97%.

Liu et al. [2011] compared the performance of RO and NF membranes for the treatment of textile industry wastewater using response parameters of COD removal, flux and desalination efficiency. NF membrane (97%) showed higher COD removal in comparison to RO membrane (94%) which may be ascribed to sieving separation mechanism. Moreover, RO membrane showed higher desalination efficiency (99%) as compared to NF membrane (87%). It was also noticed that more severe flux reduction exhibited by RO membrane than NF membrane under the similar values of initial flux because of its more serious susceptibility to fouling. In particular, the permeate flux decreased from initial flux of 30 L m^{-2} h^{-1} to 21 L m^{-2} h^{-1} and 19 L m^{-2} h^{-1} for NF and RO membrane, respectively, within 0.5 h and thereafter remained stable. The higher COD removal efficiency of NF membrane was also ascribed to thicker layer of dye molecules on the NF membrane which was responsible for stronger Donnan effect between the layer and the charged dye molecules.

Li et al. [2016] developed a membrane distillation (MD) system for the treatment of real coking wastewater, while the influence of coagulation as pretreatment step was also explored. The membrane of MD system consisted of porous polytetrafluoroethylene film (35 μm) supported on polypropylene fabric layer (152 μm). It was observed that MD process had great potential to remove organic pollutants (> 97%) from coking wastewater. In coagulation pretreatment step, the performance of PAC and polyacrylamide (PAM) were compared. PAC as coagulant was observed to be efficient for the removal of organic pollutants (42%) from coking wastewater and reduced the possibility of membrane fouling. The use of PAM significantly enhanced the removal of organic contaminants (46%), but facilitated the deposition of aggregates on membrane surface which caused severe membrane fouling.

Cui et al. [2016] compared the performances of forward osmosis (FO) and RO techniques to check the suitability of FO as an alternative method to RO for the removal of aniline and other micro-pollutants. Three lab-made thin film composite (TFC) membranes with different porous substrates were used for the comparative evaluation. All TFC membranes showed higher rejection of aniline and other pollutants in FO mode. Aniline rejection remarkably improved to 90% in FO mode in comparison to 52.6-61.9% for RO mode in all membranes. Highest water flux (22 L m^{-2}

h^{-1}) and highest rejection (91.5%) was obtained for the membrane containing sulfonated polyphenylene sulfone as substrates. FO was observed with reasonable rejection at high concentration of aniline (21.47 mM).

Tanhaei et al. [2014] made an attempt to evaluate the performance of micellar-enhanced ultrafiltration for the removal of aniline using membranes with different pore sizes. An anionic surfactant sodium dodecyl sulfate (SDS) was used for the micelles formation in solution. The influence of nickel concentration, SDS concentration and presence of other surfactants was recorded on the micelles size and removal efficiency of aniline. The highest aniline rejection was observed for membrane with smallest pore size, but the SDS concentration was high. The rejection percentage of aniline increased from 47 to 64% with increase in SDS concentration from 20 mM to 80 mM and decreased slightly to 70% at SDS concentration of 160 mM. Aniline rejection improved in the presence of nickel metal ions but decreased slightly with increase in operating pressure from 200 to 500 kPa. SDS micelles become more compact at higher pressure and dissolve less number of aniline molecules. The presence of non-ionic surfactant (Brij35) has positive effect on aniline removal and aniline rejection increased with increase in Brij35/SDS molar ratio.

Hidalgo et al. [2014] compared the aniline removal efficiencies of NF and RO to find the better method. The performance of two NF membranes (both of polyamide) and three RO membranes (two of polyamide and one of polyether sulfone) was evaluated for this purpose. The rejection percentage of 79% and permeate flux of 100 kg h^{-1} m^{-2} were observed for NF membrane (NF97) with molecular cut-off of 200 g mol^{-1}. The aniline rejection percentage and permeate flux increased with increase in pressure. These results indicate that convective transport played major role in comparison to diffusion transport. The rejection and flux remained unaffected with increase in aniline concentration. The slight decrease in aniline rejection with increase in pH from 5 to 7 may be attributed to electrostatic interaction between neutral aniline and ionized carboxylate groups in membrane. The highest removal efficiency was observed for RO membrane with 86% rejection in comparison to 79% rejection for NF membrane at same experimental condition (pressure = 30 bar). The lowest value of ratio of permeability constants (B_s/A_w) also explained the best performance of RO membrane.

Table 2.2: Brief overview of studies related to adsorption, coagulation/flocculation, and membrane separation for removal of nitrogenous aromatic pollutants

Target Compounds	Adsorbent/ Coagulants/ Membrane	Optimized condition	Performance	Remarks	References
Adsorption					
Quinoline	Granular activated carbon (GAC) and bagasse fly ash (BFA)	pH_0 = 5.5 C_0 = 7.74 mM m = 5 g L^{-1} for GAC m = 10 g L^{-1} for BFA T = 45 °C t_e = 8 h	q_e = 77.82 mg g^{-1} for GAC; q_e = 32.67 mg g^{-1} for for BFA	• GAC showed higher adsorption capacity as compared to BFA. • Adsorption data was best fitted with pseudo-second order model for both adsorbents. • Surface adsorption and intraparticle diffusion control the adsorption process of both adsorbent. • Redlich-peterson isotherm best fit the experimental data for both adsorbents at 45 °C • The adsorption of quinoline was endothermic.	Rameshraja et al. 2012
Quinoline	Sepiolite, palygorskite, saponite	pH_0 = 6.7 C_0 = 20 mM m = 10 g L^{-1} T = 25 °C t_e = 12 h $NaClO_4$ = 0.1 M $Mn(ClO_4)_2$ = 1.5 mM	q_e = 103.32 mg g^{-1} for saponite; q_e = 77.49 mg g^{-1} for sepolite; q_e = 38.75 mg g^{-1} for palygorskite	• Adsorption capacity was highest for saponite. • Adsorption capacity increased with pH and the contribution of ion exchange mechanism was negligible at pH > 6. • High ionic strength shows little influence on adsorption capacity of saponite at all pH. • The competitive adsorption of Mn^{2+} and quinoline shows that quinoline could be adsorbed on SiOH sites of tetrahedral sheets as well as MgOH and AlOH sites of octahedral sheets.	Vico et al. 2006
Pyridine, indole and quinoline	Bamboo charcoal	pH_0 = 7.0 C_0 = 0.387 mM m = 2.5 g L^{-1} T = 25 °C t_e = 24 h $CaCl_2$ = 5 mM	q_e = 19.50 mg g^{-1} for indole q_e = 17.70 mg g^{-1} for quinoline q_e = 15.80 mg g^{-1} for pyridine	• Adsorption kinetic data was best fitted with pseudo-second order model. • Adsorption capacity of pyridine was lower than quinoline and indole because of relatively lower octanol-water distribution coefficient (log K_{ow}). • Adsorption isotherms for all compounds were well fitted with Freundlich model. • The negative ΔG^0 and positive ΔH^0 indicate that adsorption was spontaneous and endothermic in	Liao et al. 2013

Target Compounds	Adsorbent/ Coagulants/ Membrane	Optimized condition	Performance	Remarks	References
				nature. • The regenerated adsorbent exhibited increase in mesoporous area and mesoporous volume.	
Aniline	Modified jute fiber	$pH_0 = 7.0$ $C_e = 11.61$ mM $m = 3$ g L^{-1} $T = 45$ °C $t_e = 6$ h	$q_e = 146.00$ mg g^{-1}; $q_{max} = 169.49$	• The generation of carboxyl groups on the modified jute fibers was responsible for the higher adsorption capacity. • At pH below 7, the adsorption capacity decreased. • The pseudo-second order kinetic model fitted well with the adsorption data. • The adsorption equilibrium data were fitted with the Langmuir isotherm. • Adsorption is due to electrostatic interaction, and formation of hydrogen bond between –OH of carboxyl group and amide group of aniline.	Gao et al. 2015
Aniline	g−C$_3$N$_4$	$pH_0 = 4.0$ $C_e = 0.387$ mM $m = 0.2$ g L^{-1} $T = 65$ °C $t_e = 24$ h	$q_e = 80.00$ mg g^{-1} $q_{max} = 93.40$ mg g^{-1}	• The adsorption capacity of g-C$_3$N$_4$ was strongly influenced by pH, contact time, ionic strength and solid content. • The adsorption follows a pseudo second order kinetics and fitted well with the Langnuir adsorption model. • Thermodynamic analysis revealed a spontaneous exothermic adsorption process.	Hu et al. 2015
Aniline	11 different activated carbons	$pH_0 = 7.0$ $C_e = 0.774$ mM $m = 1.0$ g L^{-1} $T = 23$ °C $t_e = 1$ h	$q_e = 60.00$ mg g^{-1}; $q_{max} = 257.90$ mg g^{-1}	• Textural properties such as surface area and pore size have strong influence on the aniline adsorption. • For diluted aniline concentration, carbon with more oxygen moieties show less aniline adsorption. • Activated carbon shows better adsorption of aniline in alkaline solution.	Pardo et al. 2016
Aniline	sawdust−cyclo	$pH_0 = 4.0$-8.0	$q_e = 12.99$ mg g^{-1}	• Adsorption equilibrium is achieved in 30 min. at	Hu et al. 2014

35

Target Compounds	Adsorbent/ Coagulants/ Membrane	Optimized condition	Performance	Remarks	References
	dextrin polymer	$C_e = 0.658$ mM $m = 1.0$ g L^{-1} $T = 15$ °C $t_e = 0.5$ h	$q_{max} = 84.03$ mg g^{-1}	pH of 4-8. - Kinetic follows pseudo-second-order model. - Langmuir model shows better fit for adsorption process. - Possible mechanism involves the inclusion of aniline by β-CD through host-guest interactions	
Congo red	Activated carbon fibers	$pH_0 = 2.0$ $m = 0.2$ g L^{-1} $T = 25$ °C $t_e = 85$ h	$q_e = 512$ mg g^{-1}; $q_{max} = 1100$ mg g^{-1}	- Adsorption kinetics fitted well with the pseudo-second order kinetics. - Adsorption follows Langmuir adsorption model with monolayer adsorption on the surface of activated carbon fibers.	Li et al. 2015
Congo red	Hierarchical porous ZnO microspheres	$pH_0 = 2.0$ $C_e = 0.071$ mM $m = 0.1$ g L^{-1} $T = 30$ °C $t_e = 10$ h	$q_e = 262.10$ mg g^{-1}; $q_{max} = 334$ mg g^{-1}	- Porous ZnO exhibits higher adsorption capacity compared to commercial ZnO. - Overall adsorption process follows pseudo-second order kinetics. - Adsorption data were fitted best with Langmuir adsorption model. - Porous ZnO can be regenerated easily by calcination at 280 °C for 4 h.	Lei et al. 2017
Coagulation					
Congo red	Amyloid nanofibrils	$pH_0 = 7.0$ $C_0 = 0.057$ mM fibrils = 30 mg L^{-1} $T = 57$ °C NaCl = 500 mM	Decolorization = 95%	- The amyloid nanofibril was synthesized through incubation of hen egg-white lysozyme protein. - Decolorization efficiency increased with increase in temperature and ionic strength. - Higher decolorization was obtained in comparison to activated carbon (6%). - Lower efficiency at alkaline pH was due to aggregation of lysozyme protein.	Morshedi et al. 2013
Congo red	Aluminium sulfate, aluminium	$pH_0 = 3-9$ $C_0 = 0.71$ mM coagulant dose = 150	Decolorization = 99%; $X_{COD} = 99\%$	Powdered grade PAC SAB 18 shows highest COD removal of 98.7% and decolorization efficiency of 99%.	Prajapati et al. 2016

36

Target Compounds	Adsorbent/ Coagulants/ Membrane	Optimized condition	Performance	Remarks	References
	chloride, iron (III) chloride, poly aluminium chlorides (PAC) and poly diallydimethyl ammonium chloride (poly DADMAC)	$mg\ L^{-1}$ T = 27 °C $t_{sedimentation}$ = 1.25 h		• Removal efficiency of PAC was further improved by physical blending with other inorganic or organic coagulant. • 30% PAC and 70% iron chloride shows best COD removal of 99%. • The performance of composite coagulant was insensitive in broad range of pH = 3-9. • Low dose requirement and less sludge were observed during evaluation of PAC efficiency.	
Congo red	Alginate extracted from algae *Sargassum* sp.	pH_0 = 4 C_0 = 0.36 mM coagulant dose = 60 $mg\ L^{-1}$ calcium dose = 6 g L^{-1} $t_{sedimentation}$ = 0.5 h	Decolorization = 96%	• Alginate showed coagulant properties in the presence of calcium ion. • Natural polymer was consisted of D-mannuronic acid and L-guluronic acids as monomer units. • The strong electrostatic attraction between positively charged alginate and anions of dye was responsible for the decolorization.	Vijayaraghav an et al. 2016
Coking wastewater containing quinoline	Poly aluminium ferric silicate chloride (PAFSIC)	pH_0 = 7.8 C_0 (COD) = 146 mg L^{-1} coagulant dose = 125 $mg\ L^{-1}$ T = 20 °C $t_{sedimentation}$ = 0.5 h	X_{COD} = 70%	• Coagulant with molar ratios of Al/Fe = 3 and (Al + Fe)/Si = 13 exhibited the maximum COD removal efficiency. • Organics removal was attributed to combined effects of charge neutralization, adsorption to flocs and complexation interaction with metal hydroxides.	Li et al. 2018
Aniline	Hexamethylen e-diamine-epich-lorohidrin polycondensat e, polyethleneim i-ne or	pH_0 = 7.0 C_0 = 0.5 mM tyrosinase = 135.67 $mg\ L^{-1}$ phenol = 1.0 mM coagulant dose = 30 $mg\ L^{-1}$ T = 25 °C	$X_{aniline}$ = 100%	• The removal of aniline increased from 28 to 100% by free enzyme tyrosinase in presence of 1.0 mM of phenol. • The water soluble cross-coupling products of enzymatic degradation of aniline were precipitated out during treatment with cationic polymer coagulants.	Wada et al. 1995

Target Compounds	Adsorbent/ Coagulants/ Membrane	Optimized condition	Performance	Remarks	References
	chitosan			• The immobilized tyrosinase showed better performance in comparison to free tyrosinase.	
Aniline	Polyaluminium chloride (PAC)	$pH_0 = 6.0$ $C_0 = 2.147$ mM PAC = 20 mg L^{-1} T = 20-23 °C t = 0.16 h P = 4 atm	$X_{aniline} = 95\%$; $X_{COD} = 89.6\%$	• A combination of coagulation/flocculation and flotation methods was used. • Flotation process required less PAC dose in comparison to sedimentation process. • Flotation process also ne]eded small coagulation time. • Effective bubble diameter was 40 μm which gave better contact with flocs.	Ahmadi et al. 2017
Membrane processes					
Congo red	Graphene oxide (GO) incorporated polyacrylonitrile membrane (PAN)	$C_0 = 2.14$ mM effective area = 21 cm^2 T = 50 °C P = 500 kPa pH = 7	$R_{Congo\ red} = 99.5\%$	• GO incorporation exhibited positive effect on elasticity, hardness and thermal stability of the membrane. • The rejection capacity of PAN nanofiltration membrane improved from 91.5% to 99.5% after GO incorporation. • The flux remained almost stable at 4.2 kg m^{-2} h^{-1} at pressure 500 kPa after Gi9O incorporated. • The high rejection capacity was attributed to the electrostatic repulsion between the anionic dye molecules and negatively charged outer layer of GO.	Wang et al. 2012
Congo red	Hydrophilic poly ether sulfone membrane	$C_0 = 2.87$ mM effective area = 22.9 cm^2 T = 25 °C P = 400 kPa pH = 7.6 Na$_2$SO$_4$ = 422.4 mM	$R_{Congo\ red} = 99.96\%$ in pure solution; $R_{Congo\ red} = 99.75\%$ in solution with high salinity	• High rejection of ultrafiltration membrane was ascribed to synergetic effect of aggregation of dye molecules and electrostatic repulsion from surface of membrane. • The high rejection percentage of > 98.9% was obtained for all dyes in the presence of 60 g L^{-1} Na$_2$SO$_4$. • The membrane possessed extraordinary operational stability for long run.	Lin et al. 2016

Target Compounds	Adsorbent/ Coagulants/ Membrane	Optimized condition	Performance	Remarks	References
				• The rejection percentage decreased with increase in pressure and decrease with decrease in concentration of dye.	
Dye containing textile wastewater	Polyamide thin film composite (TFC) membrane	C_0 (COD) = 96−108 mg L^{-1} effective area = 140.6 cm^2 T = 25 °C P (RO) = 1.25 MPa P (NF) = 0.65 MPa pH = 6.7 NaCl = 17.24 mM	R_{COD} (NF) = 97%; R_{COD} (RO) = 94%	• NF membrane (97%) showed higher COD removal in comparison to RO membrane (94%). • Permeate flux decreased from initial flux of 30 L m^{-2} h^{-1} to 21 L m^{-2} h^{-1} and 19 L m^{-2} h^{-1} for NF and RO membrane, respectively. • RO membrane showed higher desalination efficiency (99%) as compared to NF membrane (87%). • Higher NF efficiency was attributed to stronger Donnan effect between the membrane layer and the charged dye molecules.	Liu et. al 2011
Quinoline containing coking wastewater	Polytetrafluoroe-thylene film supported on polypropylene fabric layer	C_0 (COD) = 315 mg L^{-1} effective area = 14.4 cm^2 T = 50 °C pH = 7.8 velocity = 0.3 m s^{-1}	R_{COD} = 99.7 %	• Membrane distillation coupled with coagulation pretreatment had great potential to remove organic pollutants (> 97%) from coking wastewater. • Polyaluminium chloride as coagulant removed 42% of organic pollutants from coking wastewater and reduced the possibility of membrane fouling. • Polyacrylamide removed 46% of organic contaminants, but caused severe membrane fouling.	Li et al. 2016
Aniline	Thin film composite (TFC) membrane	C_0 = 21.47 mM flow rate = 0.3 ml min^{-1} NaCl = 2 M effective area = 4 cm^2	$R_{aniline}$ (FO) = 91.5%; $R_{aniline}$ (RO) = 61.9%	• Aniline rejection remarkably improved to 90% in forward osmosis (FO) mode in comparison to 52.6-61.9% of reverse osmosis (RO) mode for all membranes. • Sulfonated polyphenylene sulfone membrane showed the highest water flux (22 L m^{-2} h^{-1}) and highest rejection (91.5%) for aniline. • The rejection percentage increased with increase of NaCl concentration in draw solution.	Cui et al. 2016

Target Compounds	Adsorbent/ Coagulants/ Membrane	Optimized condition	Performance	Remarks	References
				• FO has advantages of negligible operating pressure and low fouling tendency.	
Aniline	Commercial membrane Polyethersulfone	$C_0 = 0.05$ mM $Ni = 10$ ppm effective area = 40 cm^2 $T = 25$ °C $P = 200$ kPa pH = 7 SDS concentration = 160 mM	$R_{aniline} = 70.0\%$	• The performance of micellar-enhanced ultrafiltration (MEUF) was observed for the removal of aniline using membranes with different pore sizes. • The maximum removal was obtained for Polyethersulfone membrane with smallest pore size. • Aniline rejection improved in presence of nickel ions. • Mixed surfactant (SDS + Brij35) has higher rejection percentage in comparison to SDS alone. • Aniline rejection increased with increase in Brij35/SDS molar ratio.	Tanhaei et al. 2014
Aniline	Thin film composite (TFC) membrane	$C_0 = 2.14$ mM flow rate = 2502 ml min^{-1} effective area = 30 cm^2 $T = 20$ °C $P = 3000$ kPa pH = 5	$R_{aniline} = 79.0\%$	• Aniline removal efficiencies of nanofiltration and reverse osmosis were compared using two nanofiltration (NF) and three reverse osmosis (RO) membranes. • The rejection percentage of 79% was observed for NF membrane (NF97) at pressure 3000 kPa. • The highest removal efficiency was observed for RO membrane with 86% rejection percentage at pressure 3000 kPa. • The rejection percentage and permeate flux increased with increase in pressure.	Hidalgo et al. 2014

40

2.3.4. Drawbacks of the physico-chemical treatment methods

Adsorption process has been used widely for the removal of nitrogenous aromatic pollutants. Various new adsorbents have been developed and tested for this purpose. In spite of several studies for adsorption of aromatics, the exact mechanisms of interaction of nitrogenous organic pollutants with the complex surfaces of these adsorbents are still ambiguous [Apul et al. 2015]. The major issue related to adsorption is misunderstanding about the highly pH sensitive nature of functional group and active sites [Laszlo et al. 2007]. Many adsorbents do not work under natural condition. There is need to develop adsorbents which work at neutral pH and room temperature with short contact time [Ali et al. 2012]. The interaction between adsorbents and nitrogenous organic pollutants are complicated by presence of natural organic matter and inorganic ions. Low selectivity is also a serious issue in adsorption because these molecules compete with targeted pollutants to occupy active sites [Zhang et al. 2011; Pardo et al. 2016]. Regeneration of spent adsorbents is also an important issue because of its role in operation cost and waste disposal. Many thermo-chemical methods are commonly employed for its regeneration. The major drawbacks associated with these processes are that these are energy intensive and time consuming, and also deteriorate the adsorbent porosity. Organic matter containing waste adsorbent may cause damage to cells of plants and animals [Jing et al. 2011]. The safe disposal of adsorbent is still problematic.

Coagulation required high quantity of chemicals and subsequently generate large volume of sludge. The high concentration of metal cations in the treated effluent generates secondary pollution and thus, need a further treatment [Kimura et al. 2013]. The high production cost and negative impact on living organism is a major concern in use of polymeric coagulants [Vijayaraghavan et al. 2016]. Natural coagulants are low cost alternative but are limited to low concentration of nitrogenous pollutants [Patel et al. 2012; Prajapati et al. 2016].

Membrane processes are associated with several disadvantages such as membrane fouling and high membrane cost. Moreover, it is a non-destructive technique and generate retentate stream with high concentration of contaminants [Acero et al. 2016]. Therefore, further treatment is required to reduce the contaminants in retentate stream.

2.4. ADVANCED OXIDATION PROCESSES FOR THE TREATMENT OF NITROGENOUS AROMATIC COMPOUNDS

Because of several limitations of biological and physico-chemical treatment methods, a series of novel catalytic technologies have attracted the attention of researchers for oxidative treatment of

persistent nitrogenous organic pollutants. These oxidation techniques involve the catalytic wet air oxidation (CWAO), catalytic ozonation, photocatalysis, Fenton process, catalytic wet peroxide oxidation (CWPO)/heterogeneous Fenton-like processes [Arora et al. 1999; Ovejero et al. 2007; Yadav et al. 2017; 2018; Ghuge et al. 2018]. Among these techniques, advanced oxidation processes (AOPs) are promising catalytic technologies because of high degradation efficiency of refractory organic compounds at near-ambient condition [Kim et al. 2011]. Although these techniques involve different chemical system, all exhibited the similar feature of utilizing highly reactive oxidizing species hydroxyl radicals (*OH) [Oturan et al. 2014]. Depending on different processes, these *OH radicals can be either generated from water splitting or activation of chemical oxidants such as H_2O_2, O_3, etc. These *OH radicals have high oxidation potential (E° = 2.80 eV vs. NHE) and can mineralize wide range of organic compounds to CO_2, H_2O and inorganic ions [Navalon et al. 2010]. AOPs are comparatively more "environmental-friendly" than conventional methods because these techniques neither generate large amount of sludge (except Fenton process) nor transfer toxic pollutants from one phase to another.

Wet air oxidation (WAO) is a well-known technique for the treatment of effluent containing high organic load using pure oxygen or air as oxidant. Since WAO does not involve any hazardous chemical reactant and generates CO_2 and water as end products (on completion of oxidation), WAO is generally recognized as clean process. One major drawback of WAO is requirement of high temperature (125-320 °C) and high pressure (0.5-20 MPa) [Bhargava et al. 2006; Demire et al. 2012]. In addition, the end products such as low molecular weight acids and other ions (sulfate, chlorine) create corrosion problems. This process also generates gas containing harmful VOCs, NOx and offensive odor [Zhan et al. 2010].

Catalytic wet air oxidation (CWAO) requires milder operating condition and eliminates the more refractory contaminants in shorter time than WAO. Because of less severe operating condition, the capital and operating cost of CWAO are less than non-catalytic WAO. This process is applicable for those wastewaters which are too dilute for the thermal incineration and too concentrated for biological treatment. Various heterogeneous catalysts including noble metals (Ru, Rh, Pd, Pt, etc.), metal oxide (CuO, ZrO_2, Co_3O_4, TiO_2, CeO_2, etc.) and mixed metal oxide ($Ce_{1-x}Cu_xO_{2-\delta}$, $Ce_{1-x}Zr_xO_2$, Cu/Al_2O_3, etc.) have been synthesized and tested for the CWAO of nitrogenous aromatic compounds [Barbier et al. 2005; Garcia et al. 2005; Bhargava et al. 2006; Levi et al. 2008]. The removal efficiency of CWAO mainly depends on temperature, oxygen or air pressure, chemical properties of the pollutant and reaction time. The increasing pressure enhances

the oxygen solubility in water and increase the oxidation rate of CWAO. High temperature promotes the mineralization of organic pollutants to non-hazardous products. The fate of nitrogen atom is an important issue to be discussed because of toxicity of NH_3 and NO_3^-. The selectivity of catalyst for preferential molecular nitrogen (N_2) in CWAO of nitrogenous organic pollutants depends on the type of catalyst as well as reaction temperature and solution pH [Kim et al. 2011]. Table 2.3 summarized the performance of some catalysts for CWAO of nitrogenous aromatic pollutants. Barbier et al. [2005] studied the CWAO of aniline using noble metals (Ru, Rd and Pt) deposited on CeO_2. Ru showed the best activity for oxidation of aniline at 160-200 °C. Gomes et al. [2005] observed that Cu/MCM-41 manifested the high oxidation efficiency with the aniline conversion of 97% and mineralization efficiency of 73% at 200 °C and 0.69 MPa of oxygen. Pachupate and Vaidya [2018] recently reported low mineralization of quinoline (28%) using Ru/C catalyst at 220 °C and 690 kPa. Depending on the above mentioned parameters, CWAO can completely mineralize the organic contaminants into CO_2, H_2O and non-hazardous end products or oxidize them into biodegradable intermediates. However, CWAO is associated with disadvantages of energy intensive process and requirements of expensive reactors due to elevated temperature (90-250 °C) and pressure condition (0.1-3.0 MPa). Moreover, the low solubility of oxygen is responsible for gas liquid mass transfer resistance and can inhibit the catalytic activity [Bhargava et al. 2006]. Therefore, a low-cost alternative is necessary to be developed for the mineralization of nitrogenous aromatic compounds.

Photocatalysis appears to be a promising technology as semiconductors are inexpensive and capable of oxidizing various nitrogenous aromatic compounds. This process has other advantages such as no waste disposal issue, and requirement of mild temperature and pressure condition [Khataee et al. 2010; Park et al. 2014]. As shown in Fig. 2.1, the degradation of pollutants occurs by hydroxyl radicals generated from water splitting in presence of ultraviolet or visible light radiation. Several photo-catalysts including TiO_2, ZnO, $BiVO_4$, Bi_2O_3, SnO_2, CdO and WO_3 have been tested for the destruction of nitrogenous aromatic compounds [Bhatkhande et al. 2002; Ullah et al. 2008; Shang et al. 2009; Sajjad et al. 2010; Gulce et al. 2013]. Table 2.3 has illustrated the application of some photo-catalysts for the degradation of Congo red, quinoline and aniline. Among these photo-catalysts, TiO_2 is the most promising material because of its high photo-catalytic activity, low cost, biologically and chemically inert nature, and stable structure [Kumar et al. 2006; Erdemoglu et al. 2008; Oturan et al. 2014]. The photocatalytic degradation of nitrogenous aromatic compounds depends upon the chemical structure of compounds, nature of

functional groups as well as number and position of nitrogen atoms [Khataee et al. 2010; Jing et al. 2011]. The photo-catalytic activity of semiconductors can be further enhanced by metal doping, addition of chemical oxidants (H_2O_2 or ozone) and composite formation with organic materials, resulting improvement of separation of electron and holes [Sánchez et al. 1998; Guo et al. 2014; Jing et al. 2014]. The photodegradation efficiency depends on the catalyst properties, light intensity, light wavelength, pH, catalyst dose, temperature, initial concentration of pollutant and partial pressure of oxygen or air (if supplied) [Pera-Titus et al. 2004]. The photo-degradation technique is not suitable for the treatment of high strength wastewater. Moreover, a poor understanding about the reactor design for photo-catalytic operation has hindered its commercial application [Jing et al. 2011]. This technique is still under premature stage and need efforts to be fully applicable at large scale.
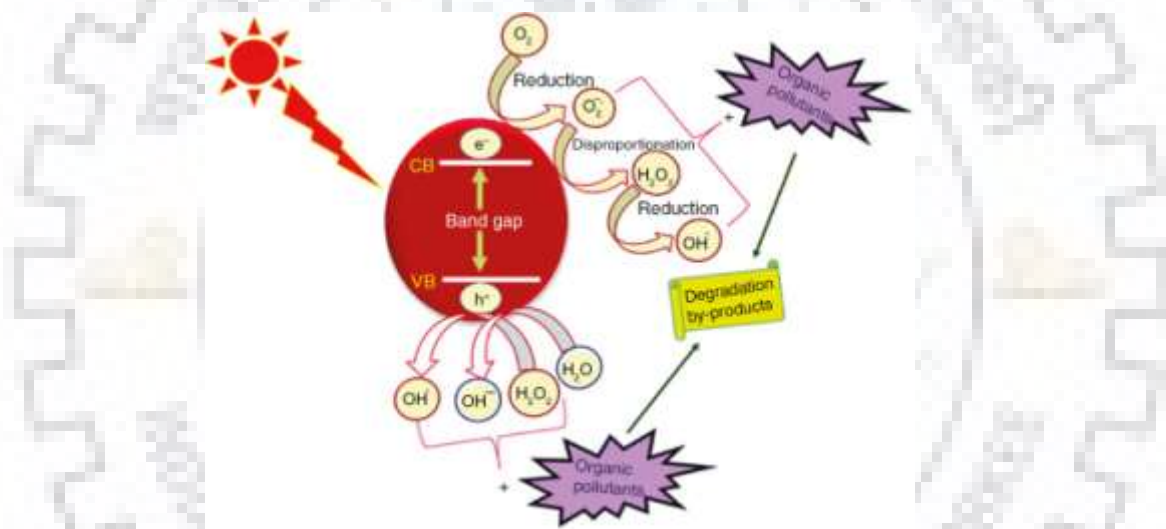
Fig. 2.1: Schematic representation for the basic process of photocatalysis [Mahopatra and Parida 2016]

Catalytic ozonation has been reported more efficient for mineralization in comparison to ozonation alone [Legube et al. 1999; Faria et al. 2009]. Hydroxyl radicals are generated by the decomposition of ozone in the presence of transition metal through electron transfer mechanism. Numerous metals (Fe, Ag, Cr, Ru, Cu, Co, Ce, Mn, TiO_2 and Ni) in different solid forms (metal oxides or deposited on supports) have been investigated as catalysts for the degradation as well as mineralization of nitrogenous aromatic compounds [Nawrocki et al. 2010; Zhu et al. 2017]. Table 2.3 has summarized the performance of some catalysts for oxidation of CR, quinoline and aniline. The mineralization efficiency of catalytic ozonation is influenced by catalyst nature, pH, catalyst dose, ozone dose, temperature and reaction time. The practical application of catalytic ozonation is

limited by several factors, such as low solubility of ozone in aqueous phase, strong influence of inorganic ions, and high energy consumption for ozone generation [Faria et al. 2009; Nawrocki et al. 2010; Zhu et al. 2017].

The classical Fenton reaction which involves electron transfer between Fe^{2+} and H_2O_2, has been extensively reported to generate *OH radicals for the elimination of refractory organic pollutants. The Fenton process possesses several advantages such as simple operation which enable easy implementation in existing wastewater treatment plants, use of inexpensive reagents, and feasibility at mild temperature ($\leq$ 353 K) and atmospheric pressure [Bautista et al. 2010]. The Fenton process efficiency depends on various factors such as pH, H_2O_2 concentration, Fe^{2+} concentration, initial concentration of pollutants, and temperature [Pera-Titus et al. 2004; Gupta et al. 2018]. Table 2.3 summarized the degradation and mineralization of CR, quinoline and aniline through Fenton process. Anotai et al. [2006] observed the aniline degradation and TOC removals of 30% and 24%, respectively, after 2 h of Fenton treatment in strong acidic condition (pH = 2). Su et al. [2013] have also reported the degradation efficiency of 24% for aniline within initial 5 min and no further increment was noticed due to deficiency of active ferrous ions. The oxidation efficiency of this method has been reported to be further improved under the assistance of UV light and ultrasonic waves [Nedoloujko et al. 1997]. However, the homogenous Fenton reaction is associated with many significant disadvantages such as requirement of low pH range (2-3), generation of large amount of iron sludge, deactivation of iron ion due to its complex formation ability with organic intermediates and requirement of high amount of chemicals for neutralizing treated effluents before the discharge [Navalon et al. 2010; Lyu et al. 2015].

Heterogeneous Fenton-like catalysis (catalytic wet peroxide oxidation) has been found more suitable than homogeneous Fenton process for practical applications because of several advantages, such as, broad range of pH, limited leaching of metal cations, easy recoverability and stable activity for many successive cycles [Ramirez et al. 2007; Garrido-Ramirez et al. 2010]. The term CWPO has been used here more frequently to differentiate between the typical Fenton process and the processes involving heterogeneous catalysts, since other transition metals also show activity for CWPO [Ribeiro et al. 2016; Rodrigues et al. 2017; Ou et al. 2018]. Heterogeneous catalysts also allow operation to be carried out in continuous flow reactor [Rodrigues et al. 2010; 2017; Singh et al. 2018; Ou et al. 2018]. Unlike CWAO, CWPO is a promising option because of its ability to completely degrade the pollutants to CO_2, N_2 and inorganic ions at mild operating condition (temperature <373 K and atmospheric pressure).

Table 2.3: Brief overview of studies related to catalytic wet air oxidation, catalytic ozonation, Fenton process and catalytic wet peroxide oxidation for removal of nitrogenous aromatic pollutants

Target pollutants	Catalyst	Reaction condition	Performance	Remarks	References
Catalytic wet air oxidation					
Azo dyes	Cu/carbon nanofibers (CNF)	$C_0 = 1.0\text{-}2.85$ mM T = 140 °C P = 800 kPa $pH_0 = 7$ catalyst dose= 0.1 g L^{-1} t = 3 h	$X_{decolorization} = 100\%$; $X_{TOC} = 6.8-71\%$	• The mineralization of dyes increase from (1-30%) to (6.8−71%) in presence of Cu/CNF catalyst with respect to wet oxidation. • The mineralization efficiency increased in the order of triazo < diazo < monoazo. • Cu/CNF catalyst oxidized undesirable byproducts and detoxified the treated effluent. • Cu/CNF showed stability in operation, and less copper leaching.	Rodriguez et al. 2009
Quinoline	Ru/C	$C_0 = 0.77$ mM T = 220 °C P = 690 kPa $pH_0 = 7$; t = 2 h catalyst dose= 0.1 g L^{-1}	$X_{quinoline} = 42.3\%$; $X_{TOC} = 28\%$	• TOC removal kinetics was best fitted with the two step first-order power law model. • TOC removal was surface reaction controlling.	Pachupate et al. 2018
Aniline	Cu/MCM-41, Cr/MCM-41, V/MCM-41	$C_0 = 21.47$ mM T = 200 °C P = 690 kPa $pH_0 = 7$ catalyst dose = 10.67 g L^{-1} t = 2 h	$X_{aniline} = 96\%$; $X_{TOC} = 73\%$	• Cu/MCM-41 showed the highest catalytic activity in terms of aniline conversion and selectivity for mineralization. • CuO was active species for CWAO of aniline. • Cu/MCM-41 showed stable performance for three consecutive runs. • Average copper leaching of 22 mg L^{-1} was observed after each cycle. The contribution of leached copper in catalytic activity was negligible.	Gomes et al. 2005
Aniline	Ru supported on multi-walled carbon nanotubes (MWCNT)	$C_0 = 21.47$ mM T = 200 °C P = 5000 kPa Ru loading = 0.65% $pH_0 = 7$ catalyst dose = 10.67 g L^{-1}, t = 0.75 h	$X_{aniline} = 100\%$; $X_{TOC} = 80.8\%$; $X_{aniline}$ (Non−catalytic) = 45%; X_{TOC} (Non−catalytic) = 30%	• Nitric acid oxidized MWCNT-COOH and showed higher oxidation efficiency as compared to ion exchanged MWCNT-COONa. • Incorporation of Na reduced the Ru leaching and improved the catalyst stability. • Ru/MWCNT led to higher aniline degradation and TOC	Garcia et al. 2006

Target pollutants	Catalyst	Reaction condition	Performance	Remarks	References
				removal as compared to Ru/activated carbon.	

Photocatalysis

Target pollutants	Catalyst	Reaction condition	Performance	Remarks	References
Congo red	Nanocrystalline TiO_2	$C_0 = 0.03$ mM $H_2O_2 = 17.6$ mM $T = 25$ °C $pH_0 = 2$-7 catalyst dose $= 3$ g L^{-1} $t = 0.5$ h visible light intensity $= 675$ W m^{-2}	$X_{decolorization} = 98\%$	• Nanocrystalline TiO_2 (anatase) was synthesized using hydrothermal method at 200 °C. • A complete degradation of dye was observed in visible light, whereas the mineralization efficiency was low. • Degradation of Congo red follows first order kinetics. • The degradation efficiency remained unaffected in presence of nitrate, sulphate and humic acid. • Nano-TiO_2 showed higher photo-degradation efficiency in comparison to Degussa P-25.	Erdemoglu et al. 2008
Congo red	3D flowerlike composite of TiO_2 with polyaniline (PAN);	$C_0 = 0.11$ mM $T = 25$ °C $pH_0 = 6$ catalyst dose (Ti/An $= 1/1$) $= 2.5$ g L^{-1} $t = 2$ h	$X_{degradation}$ (UV−light)$= 98\%$; $X_{degradation}$ (visible light)$= 96\%$	• Flowerlike TiO_2/PA composite was synthesized using sol-gel method. • Higher photocatalytic activity was obtained as compare to TiO_2 alone and Degussa P-25 in visible as well as UV-light. • The synergetic effect between hollow TiO_2 nanoparticles and PA reduce the electron-hole recombination rate. • Multiple reflections among PA nanoflakes were capable for the full use of UV-light and sunlight. • Photodegradation was in agreement with Langmuir-Hinshelwood mechanism.	Guo et al. 2014
Quinoline	TiO_2/graphene nanocomposite (TGC)	$C_0 = 0.55$ mM $T = 25$ °C $pH_0 = 6.0$ catalyst dose $= 1.5$ g L^{-1}, $t = 2$ h Intensity of visible light $= 20.5$ W m^{-2}	$X_{quinoline}$ (UV light) $= 100\%$; $X_{quinoline}$ (visible light) $= 75.56\%$	• Visible light driven photocatalytic degradation of nanocomposite was six time higher in comparison to P-25. • TGC showed stable performance after four times of repeated uses. • The high photocatalytic activity was attributed to effective electron-hole separation in presence of graphene. Graphene acted as electron acceptor.	Jing et al. 2014
Quinoline	Magnetically separable Fe_3O_4/TiO_2(FT)	$C_0 = 0.55$ mM $T = 80$ °C $pH_0 = 6.0$ catalyst dose $= 1.5$ g	$X_{quinoline} = 89.88\%$; $X_{quinoline}$ (P25) $= 79.58\%$	• Photocatalytic degradation of composite was 1.25 time higher in comparison to P-25. • The quinoline removal increased from 80.32% to 89.88% with decreasing the molar ratio of Fe_3O_4/TiO_2 from 1:10 to	Jing et al. 2013

Target pollutants	Catalyst	Reaction condition	Performance	Remarks	References
		L^{-1}, t = 2 h Intensity of visible UV light = 31.5 W m^{-2}		1:70. • FT showed constant performance up to three cycles of repeated uses.	
Aniline	TiO$_2$ (Degussa)	C$_0$ = 5.0 mM T = 25 °C pH$_0$ = 10.8 catalyst dose = 0.86 g L^{-1} Na$_2$CO$_3$ = 0.11 M t = 6 h	X$_{aniline}$ (with carbonate ions) = 100%; X$_{aniline}$ = 80%	• Aniline adsorption increased in presence of carbonate ions and resulted into high photo-degradation efficiency. • Photo-degradation was in agreement with Langmuir-Hinshelwood mechanism. • Azobenzene and nitrobenzene has been identified as major intermediates. • Both *OH and CO$^{*-}_3$ radicals were responsible for degradation in basic pH condition. • Photocatalytic activity decreased in presence of NO$^-_3$, SO$^{2-}_4$, PO$^{3-}_4$ and Cl$^-$.	Kumar et al. 2006
Aniline	TiO$_2$ (Degussa P−25)	C$_0$ = 3.76 mM T = 25 °C pH$_0$ = 3.0 ozone flow = 0.50 mmoles min^{-1} catalyst dose = 2.0 g L^{-1}, t = 2 h	X$_{TOC}$ (TiO$_2$ + O$_3$ + UV) = 96%	• Ozonation pretreatment integrated with photocatalysis provided higher TOC removal efficiency in comparison to ozonation or photocatalysis alone. • Photocatalysis followed by ozonation does not influence the aniline degradation. • Ozone transformed into ozonide anion radical which changed subsequently into hydroxyl radicals.	Sánchez et al. 1998
Catalytic ozonation					
Different azo dyes	CeO$_2$/AC	C$_0$ = 0.08-0.12 mM T = 25 °C pH$_0$ = 5.0-6.0 Ozone flow = 9.0 L h^{-1} catalyst dose = 0.5 g L^{-1}, t = 2.0 h	X$_{decolorization}$ = 100%; X$_{TOC}$ = 97−100%	• Catalytic ozonation was independent on the type of color solution. • CeO$_2$/AC composite exhibited the highest mineralization of dyes in comparison to CeO$_2$ and AC with ozone. • Catalytic activity decrease in presence of carbonate and bicarbonate ions due to scavenging of hydroxyl radicals. • Small chain carboxylic acids formed as end-products.	Faria et al. 2009
Quinoline in real coal gasification	CuO/AC	C$_0$ (COD) = 150 mg L^{-1} C$_0$ (quinoline) = 0.77	X$_{quinoline}$ = 92%; X$_{COD}$ = 69%	• CuO/AC provided higher quinoline degradation in comparison to AC and direct ozonation. • Hydroxyl radicals were identified as responsible species for	Han et al. 2013

48

Target pollutants	Catalyst	Reaction condition	Performance	Remarks	References
wastewater		mM; T = 25 °C pH$_0$ = 7.0, t = 1.0 h ozone flow = 60 L h^{-1} catalyst dose = 5.0 g L^{-1}		degradation. • CuO/AC possessed the constant activity for ten consecutive runs.	
Quinoline containing coal gasification wastewater	MnO$_x$/AC; FeO$_x$/AC	C$_0$ (COD) = 180 mg L^{-1} T = 22 °C, pH$_0$ = 6.5-7.5 ozone flow = 30.0 L h^{-1} catalyst dose = 1.0 g L^{-1} t = 1.0 h	X$_{COD}$ (MnO$_x$/AC) = 78.1%; X$_{COD}$ (FeO$_x$/AC) = 73.7%	• Activated carbon was prepared from sewage sludge using ZnCl$_2$ as activating agent. • COD removal was increasing in the order O$_3$ < O$_3$/SBAC < O$_3$/AC < FeO$_x$/AC < MnO$_x$/AC. • Biodegradability of effluent increased from 0.06 to 0.55 using MnO$_x$/AC. • Quinoline and iso-quinoline were totally removed. • MnO$_x$/AC possessed high stability up to tenth cycle.	Zhuang et al. 2014
Quinoline	Nano-MgO	C$_0$ = 0.15 mM T = 22 °C pH$_0$ = 7.2 ozone flow = 40 L h^{-1} catalyst dose = 0.2 g L^{-1} t = 0.25 h	X$_{quinoline}$ = 94.8%; X$_{TOC}$ = 45%	• MgO decomposed ozone into hydroxyl radicals, which played main role for degradation of quinoline. • The presence of phosphate inhibited the quinoline degradation. • Hydroxyquinoline and low molecular weight acids were identified as reaction intermediates. • Catalytic ozonation improve biodegradability index of treated effluent.	Zhu et al. 2017
Aniline	MgO from brucite mineral	C$_0$ = 2.15 mM T = 40 °C, pH$_0$ = 6.5 ozone flow = 18 mg h^{-1} catalyst dose = 4.16 g L^{-1}, t = 2.0 h	X$_{aniline}$ = 94.0%; X$_{TOC}$ = 70%	• Catalytic ozonation followed hydroxyl radical mediated degradation. • Aniline degradation rate was faster than nitrobenzene. • Mg^{2+} leaching does not create pollution problem because Mg^{2+} is an ion available in water.	Dong et al. 2007
Aniline	Ce based mixed oxides	C$_0$ = 1.0 mM T = 25 °C pH$_0$ = 6.5 ozone flow = 9 L h^{-1} catalyst dose= 0.14 g L^{-1} t = 3.0 h	X$_{aniline}$ = 100.0%; X$_{TOC}$ = 70%	• The mineralization efficiency of catalytic ozonation was higher than direct ozonation. • The highest TOC removal was achieved using CeO$_2$ and Ce$_{0.75}$Zr$_{0.25}$O$_2$. • The highest performance of Ce$_{0.75}$Zr$_{0.25}$O$_2$ was attributed to	Orge et al. 2012

Target pollutants	Catalyst	Reaction condition	Performance	Remarks	References
				high surface oxygen vacancies.	
				• Oxalic acid and oxamic acids were degradation by products.	
Fenton process					
Congo red	Iron salt	$C_0 = 0.33$ mM $H_2O_2 = 120$ mM $Fe^{2+} = 1.45$ mM $T = 25$ °C $pH_0 = 3$ $t = 0.25$ h	$X_{decolorization} = 100\%$; $X_{TOC} = 99\%$	• The optimization of decolorization and mineralization was carried out using Box-Behnken design and response surface analysis. • Dye mineralization increased with increase in H_2O_2 and Fe^{2+} concentration. • Fe^{2+} has more profound influence as compare to other parameters. • Two separate regression models were proposed which were in good agreement with experimental results.	Ay et al. 2009
Quinoline	Iron salt	$C_0 = 0.95$ mM $H_2O_2 = 12.7$ mM $Fe^{2+} = 1.5$ mM $T = 47$ °C, $pH_0 = 3$ $t = 1$ h, Intensity (solar) = 960 W m^{-2} Intensity (UV) = 2500 W m^{-2}	X_{TOC} (Fenton) = 10%; X_{TOC} (UV/Fenton) = 100%; X_{TOC} (solar/Fenton) = 80%	• No complex formation of quinoline and Fe^{2+} was observed in homogenous Fenton reaction. • High rate of photo-degradation was observed with Fe^{2+} rather than Cu^{2+}. • Photo-catalytic oxidation using TiO_2 was slower than light assisted homogenous Fenton reaction. • Carbon dioxide and nitrate were identified as end products.	Nedoloujko et al. 1997
Aniline	Iron salt	$C_0 = 10$ mM $H_2O_2 = 300$ mM $Fe^{2+} = 18.0$ mM $T = 90$ °C $pH_0 = 2$, $t = 1$ h	$X_{aniline} = 30\%$; $X_{TOC} = 24\%$; $X_{COD} = 14\%$	• The generation of phenol, nitrobenzene and oxalic acid confirm the radical-mediated oxidation pathway. • Aniline oxidized into either phenol or nitrobenzene and benzoquinonimine, which have equivalent COD/TOC ratio to aniline. • Fe^{3+}-oxalato complexes retard the regeneration of Fe^{2+} and stop the degradation. • Excessive amount of iron is required to provide free iron for redox reaction.	Anotai et al. 2006
Aniline	Iron salt	$C_0 = 5.37$ mM $H_2O_2/Fe^{2+} = 5/1$	$X_{aniline} = 100\%$	• Copper showed 50% aniline degradation at same experimental condition.	Gunale et al. 2007

Target pollutants	Catalyst	Reaction condition	Performance	Remarks	References
		$T = 30$ °C $pH_0 = 3$ $t = 2$ h		• The integration of Fenton oxidation with wet air oxidation found capable of reducing 82% COD. • The integrated system converted 78% of total nitrogen into N_2.	
Aniline	Iron salt	$C_0 = 10$ mM $H_2O_2 = 58$ mM $Fe^{2+} = 0.27$ mM $T = 27$ °C $pH_0 = 3.2$ $t = 1$ h	$X_{aniline} = 24\%$; $H_2O_2 = 28\%$	• Aniline degradation and H_2O_2 conversion stopped after 5 min because of complete conversion of Fe^{2+} to Fe^{3+}. • The availability of Fe^{2+} was limiting factor for aniline degradation. • Electro-Fenton provided higher efficiency (66%) because of regeneration of ferrous ion at cathode.	Su et al. 2013

Catalytic wet peroxide oxidation

Target pollutants	Catalyst	Reaction condition	Performance	Remarks	References
Congo red	Tourmaline	$C_0 = 0.07$ mM $H_2O_2 = 12.8$ mM $T = 25$ °C $pH_0 = 3$ catalyst dose=0.04 g L^{-1} $t = 25$ h	$X_{decolorization} = 56\%$	• Tourmaline possessed high adsorptive removal of 100% for Congo red dye at pH = 3. • Degradation of Congo red was lower than methylene blue and rhodamine B. • The degradation efficiency was pH-sensitive. It decreased with increase in pH. • Leached iron contributed significantly in degradation of dye.	Wang et al. 2013
Congo red	Fe/zeolite Y	$C_0 = 0.14$ mM $H_2O_2 = 17.6$ mM Fe loading = 1.53 wt% $T = 90$ °C $pH_0 = 7$ catalyst dose = 1 g L^{-1} $t = 4$ h	$X_{degradation} = 97\%$; $X_{decolorization}$ (0.75 h) = 100%; X_{COD} = 58%	• Fe was incorporated into zeolite Y by ion−exchange method. • The rate of dye degradation observed less in comparison to decolorization of dye. • Although acidic condition ($pH_0 = 2$) improved dye and COD removal, the leaching of Fe observed high in acidic condition.	Kondru et al. 2009
Congo red	Fe/CeO$_2$	$C_0 = 0.014$ mM $H_2O_2 = 0.02$ M Fe loading = 2 wt% $T = 35$ °C, catalyst	$X_{decolorization} = 96\%$	• CeO_2 was prepared by sol-gel method and Fe was incorporated by impregnation method. • Catalytic activity improved with increase in temperature. • The reusability experiments showed that catalyst possesses	Hu, 2014

Target pollutants	Catalyst	Reaction condition	Performance	Remarks	References
		dose = 1 g L^{-1}, t = 0.67 h		stable performance up to four cycles.	
Congo red	Cu/zeolite Y	C_0 = 0.143 mM H_2O_2 = 52.24 mM pH_0 = 7 Cu loading = 7.5 wt% T = 60 °C catalyst dose = 1 g L^{-1} t = 4.0 h	$X_{degradation}$ = 93.58%; $X_{decolorization}$ = 95.34%; X_{TOC} = 79.52%	• Particularly at Cu loading of 7.5 wt%, zeolite Y exhibited the highest surface area, hierarchical porosity and the highest amount of well dispersed $Cu^{1+/2+}$ species. • A strong influence of *pH* was noticed on leaching with maximum copper leaching of 13.85 mg L^{-1} at *pH* = 5. • Catalyst with 7.5 wt% copper loading showed reproducible activity upto 3rd cycle. • The best catalyst (7.5CuY) showed good catalytic activity as well as good framework stability during reusability test.	Singh et al. 2016
Quinoline	Cu/zeolite Y	C_0 = 3.87 mM T = 80 °C H_2O_2 = 52.24 mM pH_0 = 7 Cu loading = 7.5 wt% LHSV = 4 h^{-1} Particle size=1.2-1.7 mm t = 4.54 min	$X_{degradation}$ = 98%; X_{TOC} = 65%	• Almost comparable mineralization (61-65%) and H_2O_2 stoichiometric efficiencies (44.2-45.7%) were observed for ion-exchanged and impregnated samples. • Overall, Wet impregnation was found better than aqueous ion-exchange method. • Isolated sites are the most redox active sites for H_2O_2 activation and play more important role than high surface area. • The system was following Eley-Rideal mechanism and kinetic parameters were calculated using model based on this mechanism.	Singh et al. 2018
Aniline	Cu_2OHPO_4	C_0 = 1.07 mM T = 80 °C H_2O_2 = 17.12 mM pH_0 = 7 catalyst dose = 1 g L^{-1} t = 6 h	$X_{degradation}$ = 98%; X_{TOC} = 72%	• Cu_2OHPO_4 was first time synthesized by sonochemical method in less than 2 h. • Nano spindles showed higher activity in comparison to nanorods. • Hydroxyl radicals were found responsible for oxidation of aniline. • Aniline removal kinetics was best fitted with pseudo first order kinetic model.	Present work

The wide range of treatable pollutants concentration (0.2 mg L^{-1} to 5 g L^{-1}) indicates its suitability to treat the industrial effluents at low to high concentration [Ribeiro et al. 2016]. These facts make CWPO an economically viable option for wastewater treatment. In the CWPO process, hydroxyl radicals are generated by the set of redox processes between hydrogen peroxide and transition metal. These radicals are responsible for mineralization of refractory organic pollutants. Since H_2O_2 decomposes finally into oxygen and water, its environmental-friendly behavior rendered this technique attractive from environmental point of view. Different transition metals (Fe, Cu, Mn, Zr) in different form (supported or unsupported catalysts) have been studied for the degradation and mineralization of nitrogenous organic pollutants (Table 2.3). The performance depend on surface area, pore size, nature of active species, metal loading, pH, temperature, H_2O_2 concentration and catalysts dose [Singh et al. 2016]. However, further optimization of catalyst design is still required to bring this technique to the forefront of the most efficient AOP technologies.

The performance of heterogeneous catalysts should be evaluated in terms of substrate disappearance, stability, leached metal concentration and selectivity for H_2O_2 utilization in optimized conditions. The study should also include catalysts deactivation pathways and mechanistic view for confirmation of reaction end products.

2.5. LITERATURE REVIEW ON Cu/ZEOLITE Y SYNTHESIS AND ITS APPLICATION

International Union of Pure and Applied Chemistry (IUPAC) have classified porous materials into three main categories based on their pore size; (i) microporous, (ii) mesoporous, and (iii) macroporous [Haber et al. 1991]. Microporous materials have pore diameter less than 2 nm and various zeolites are typical examples of microporous materials. The pore diameters in mesoporous materials lie between 2 to 50 nm (examples: SBA-15, MCM-41, etc.). Porous materials with pore size larger than 50 nm are called macroporous materials. The applications of these porous materials as supports for active transition metallic species is the most straightforward tentative solution to overcome the previously described limitations of homogeneous Fenton process.

Supports improve significantly the activity, selectivity, and stability of active species [Anis et al. 2016; Liang et al. 2017]. Zeolites are mainly microporous in nature and have received large attention as suitable catalyst supports because of well-defined porous structure, high specific surface area and high thermal stability [Mouli et al. 2009]. Zeolites are crystalline aluminosilicates containing channel and cages as micropores that are open to the exterior surface of the particles and this open porosity is responsible for large surface area in comparison to non-porous materials

[Carreon et al. 2008; Moshoeshoe et al. 2017]. Zeolites possess ion-exchange properties because charge balancing alkali metals are bounded through ionic bond to zeolite framework and exchangeable with mono-, di- and trivalent inorganic cations without affecting zeolite framework. Several types of zeolites have been identified by researchers, and their pore structure and ion-exchange capacities depend upon Si/Al ratio of framework [Dalai et al. 1985]. Several authors have reported zeolites as excellent catalytic support for active metallic species and utilized for different applications such as adsorption, oxidation catalysis, chemical synthesis, etc [Wang et al. 2004; Dükkanci et al. 2010; Valkaj et al. 2011; Yaman et al. 2013].

Recently, copper, which also behaves like a Fenton reagent, has been reported suitable for industrial applications due to its wide working pH range as well as good redox properties [Dükkanci et al. 2010; Xia et al. 2011; Bokare et al. 2014]. Unlike iron, copper does not form strong complexes with organic acid intermediates. Thus, it does not block the generation of hydroxyl radicals and can provide high mineralization [Nichela et al. 2013; Bokare et al. 2014]. Designing a highly active and stable copper containing oxide catalyst has become a hotspot in the field of Fenton chemistry.

In recent years, copper containing zeolites have been used to activate hydrogen peroxide to hydroxyl radicals and found suitable for industrial purpose. Copper containing zeolites, such as Cu/13X [Valkaj et al. 2011], Cu/ZSM-5 [Wang et al. 2004], Cu-exchanged zeolite Y [Guzmán-Vargas et al. 2015] and CuFe/ZSM-5 [Dükkanci et al. 2010] have attracted the attention of researchers owing to their high catalytic activity and stability. Particularly promising is copper exchanged zeolite Y which exhibits better utilization of hydrogen peroxide than popular Cu/ZSM-5 and shows higher degradation of toxic compound [Valkaj et al. 2011]. A further discussion is required in context of more advanced preparation methods as well as use of continuous reactor to increase their suitability for the large scale processes.

Aqueous ion exchange (AIE) has been used for both commercial and research purpose for the incorporation of copper metal in the zeolite Y. This method works on the principle of balancing the negative charge appearing due to valency difference between Si and Al atoms in the framework [Macdonald et al. 2014]. For the AIE, zeolites are suspended several times in aqueous solution of copper salt at specified condition followed by filtration, washing, overnight drying and activation at high temperature (400-800 °C). The active copper species formed during AIE have been identified as isolated Cu^{2+} cations in several reports [Wang et al. 2004; Song et al. 2013]. Although conventionally used, AIE has been associated with various limitations; for example,

requirement of high solvent volume, slow rate of metal loading, high metallic content in residual solvent and poor control of metal loading in framework [Mhamdi et al. 2009; Gao et al. 2015]. In addition, ion exchange needs to be repeated several times in fresh solutions to obtain significant loading and also suffers from reproducibility problem to obtain desired metal content [Shwan et al. 2015]. Recently, Clemens et al. [2015] performed a solid state ion exchange method for Cu-SSZ-13 to circumvent the limitations of the AIE method and focused on characterizing copper species in the samples. In order to overcome some of the drawbacks of the AIE, it has become necessary to develop more facile, green and environmentally-friendly approaches.

Wet-impregnation is a popular method for the synthesis of supported catalysts. It is a methodology in which a solid support is mixed with small volume of metal salt solution (generally in water or ethanol) and solvent is continuously evaporated for substitution of metal ions into pores by capillary forces. Wet impregnation can overcome some of the above mentioned drawbacks of AIE due to faster processing time, no residual solvent, absence of additional filtration steps and better control over metal loading. Ucar et al. [2009] and Olivares-Marin et al. [2006] have reported that optimum loading of impregnated metal enlarged the pore size of carbon matrix from micropores to mesopores during activation stage and hence, increased its surface area. Precipitation is also a well-known method for the preparation of metal oxides. This method involves the addition of an alkaline compound for the precipitation of metallic species. In addition, alkaline treatment of zeolite is a popular post-synthetic approach for the generation of hierarchical porosity in microporous zeolite [Verboekend et al. 2011]. Furthermore, the combination of impregnation with precipitation can provide good control of metal loading without generating residual solvent. Therefore, precipitation-impregnation can be developed as strategy to simultaneously remove the limitations of AIE as well as of microporosity in considerable extent. Table 2.4 shows a comparison of recently reported copper containing zeolite Y on the basis of preparation methods, their characterization and application, which emphasizes the novelty of the current research. To the best of author's knowledge, the effect of copper impregnation and precipitation-impregnation have never been studied in term of its influence on crystalline structure, hierarchical porosity as well as coordination environment of copper species in zeolite Y matrix. Also, the effect of these routes has never been investigated for degradation of toxic nitrogenous aromatic compounds. Most of the CWPO studies have been carried out in batch reactors.

The fixed-bed reactor (FBR) allows catalyst reusability without need of filtration step and prevents unnecessary loss of catalyst.

Table 2.4: Recent studies of copper containing zeolites Y for different applications

System	reparation method	Activation method	Characterization techniques								Application Process	References
			XRD	N$_2$ sorption	FT-IR	UV-DRS	XPS	SEM/EDX	AAS/ICPMS	TPR		
Cu-Y	Mixing and heat treatment	Heating in muffle furnace	√				√		√	√	Oxidative carbonylation of methanol	Wang et al. 2015
CuNPs/Y	Mixing in suspension of zeolite	Reduction	√				√	√	√		Synthesis of propargylamines	Alonso et al. 2015
Cu(II)(salen)/Y	Ship-in-a-bottle and impregnation		√	√	√	√			√		Bleaching of pulp	Zhang et al. 2012
Cu(II)(Schiff ligand)/Y	Fixed ligand method		√	√	√	√	√	√	√		Oxidation of benzhydrol and degradation of rhodamine-B	Reddy et al. 2014
Cu/Y	Solid state Ion exchange	Heating in inert atmosphere	√	√	√				√		Propene adsorption	Benaliouche et al. 2012
Cu/Y	Ion exchange, precipitation	Heating in inert atmosphere	√	√	√		√		√		Diethyl carbonate by decarbonylation	Huang et al. 2014
Cu-Ag/Y or Cu-Zn/Y	Ion exchange	Calcination in muffle furnace	√		√			√	√		Antimicrobial Activity	Ferreira et al. 2015
Cu or Cu-Ce/Y	Ion exchange	Calcination in air	√	√	√		√	√	√	√	Desulfurization of gasoline	Song et al. 2013
Cu/dealuminated Y	Ion exchange	Calcination in air	√			√	√		√		Adsorption and microwave induced degradation of atrazine	Hu et al. 2015
Cu/Y	Wet impregnation	Calcination in air	√	√	√	√	√	√	√		Decolorization, degradation and mineralization of diazo dye	Singh et al. 2016

At the same time the higher treatable working volume, simple operation (no moving parts), less oxidant requirement, good catalyst stability, suitability for long-term operation (called workhorse of chemical industry) and short reaction time make it more economical than batch reactor [Halim et al. 2009; Tisa et al. 2014]. Few researchers have discussed the performance of FBR for treatment of wastewater [Botas et al. 2010; Mesquita et al. 2012; Satishkumar et al. 2013; Yan et al. 2014]. However, all of them use iron containing solid matrix as catalyst and phenol as a model pollutant. To the best of authors' knowledge, the CWPO of nitrogenous aromatic compounds in continuous FBR using Cu/zeolite Y has not been reported.

2.6. LITERATURE REVIEW ON COPPER HYDROXY PHOSPHATE SYNTHESIS AND ITS APPLICATION

Cu_2OHPO_4 is receiving much attention because of its catalytic activity [Meng et al. 2003], magnetic [Belik et al. 2007], optical [Reddy et al. 1995] and electrochemical properties [Li et al. 2014]. Recently, many researchers reported that Cu_2OHPO_4 could be used for oxidation of organic contaminants in wastewater under UV, visible and even near-infrared light [Xu et al. 2012; Wang et al. 2013; Zhao et al. 2015]. Copper hydroxyl phosphate is a highly active Fenton catalyst because of OH group between two Cu atoms, which play a major role for selectively decomposing H_2O_2 to *OH radicals. In general, this material exhibit morphology and size-dependent properties. Various methods have been reported for the synthesis of micro- and nanostructured material including hydrothermal method [Xu et al. 2006], ionic liquid-assisted hydrothermal method [Duan et al. 2015], solvothermal route [Hu et al. 2017], dynamic template method [Guo et al. 2011] and microwave synthesis route [Hu et al. 2016]. However, these methods are associated with limitations of requirement of high temperature, long reaction time (6-72 h), environmentally hazardous raw materials, ligands-assisted fabrication, large number of influential parameters, and expensive reactors. Moreover, almost all above mentioned methods were reported to generate different architectures typically of micro-range. The synthesis of nanostructured Cu_2OHPO_4 has been rarely reported yet. The development of a facile, fast and ligand-free synthesis route for fabrication of nano-architectures is still an important challenge.

In this study, we have explored the ultra-rapid ultrasonic-assisted synthesis of Cu_2OHPO_4 and $Cu_3(PO_4)_2$ nanostructures at room temperature. This route provides a novel strategy to control the morphology of both phases by varying sonication energy, and under the assistance of soft template.

Table 2.5: Recent studies on Cu$_2$OHPO$_4$ synthesis and applications

Catalyst	Preparation method (condition)	Application	Remarks	References
Cu$_2$OHPO$_4$	Hydrothermal (140-170 °C, 3 days) ethylenediamine, phosphoric acid, copper acetate	Hydroxylation of phenol	• The final product has crystal size of 100-2000 μm, S$_{BET}$ = 1.4 m^2 g^{-1} and thermal stability within range 25-650 °C. • Cu$_2$OHPO$_4$ (26.3%) showed higher phenol conversion in comparison to CuO (9.8%) and Cu$_4$O(PO$_4$)$_2$ (11.2%) at 80°C within 4 h. • Higher catalytic activity of Cu$_2$OHPO$_4$ than Cu$_4$O(PO$_4$)$_2$ could be attributed to OH species attached to copper atoms in structure. • Catalyst was easily regenerated by calcination in air at 550 °C. • Hydroxyl radicals were responsible for the high catalytic activity of Cu$_2$OHPO$_4$.	Xiao et al. 2001a
Cu$_2$OHPO$_4$	Hydrothermal (140-170 °C, 3 days) ethylenediamine, phosphoric acid, copper acetate	Hydroxylation of phenol	• The effect of different parameters such as temperature, catalyst size, catalyst dose, phenol to H$_2$O$_2$ molar ratio and reaction time was explored on phenol conversion. • Catalytic activity of CHP (28.3%) was similar to porous TS-1 zeolite (27.0%), which has been reported highly active for this application. • Phenol conversion and H$_2$O$_2$ efficiency increased with temperature and found maximum at 80 °C. However, selectivity for tar increased with temperature. • For similar catalytic activity, the reaction time decreased from 4 to 2 h with decrease in crystal size from 150 to 5 μm.	Xiao et al. 2001b
Cu$_2$OHPO$_4$	Hydrothermal (150 °C, 2 days) Diammonium hydrogen phosphate, copper chloride,	Catalytic wet peroxide oxidation of azo dye	• The morphology of products is elongated octahedral of size 50 μm. • Non-porous catalyst showed high activity for degradation of azo dye at pH=7. • The maximum degradation efficiency of 99.2% was observed at optimum condition of pH = 7, catalyst dose = 0.67 g L^{-1}, H$_2$O$_2$ = 0.2 mL (7 times of stoichiometric amount), dye = 0.026 mM and T = 60 °C within 2 h.	Zhan et al. 2010
Cu$_2$OHPO$_4$	Hydrothermal (180 °C, 6 h)	Photocatalytic degradation of azo dye	• Quadrangle star-like microcrystals of different size (2-15 μm) were obtained by adjusting the concentration of reactants. Moreover, bundles of microprisms were generated after decreasing NaOH amount or pH. • Bundles of microprisms showed the highest dye removal in visible light irradiation.	Xu et al. 2012
Cu$_2$OHPO$_4$/ g-C$_3$N$_4$	Hydrothermal (120 °C, 6 h, pH = 7)	Photo-Fenton photocatalytic	• Bundles of size 3 μm, consisted of small irregular microrods, were obtained. • The composite with 30% Cu$_2$OHPO$_4$ showed the highest photo-Fenton	Chen et al. 2015

Catalyst	Preparation method (condition)	Application	Remarks	References
	$CuNO3$, Na_2HPO_4	degradation of azo dye	photocatalytic activity (98%), which was higher than pure Cu_2OHPO_4 (24%) and g-C_3N_4 (78%) within 40 min. • Photo-Fenton photocatalytic degradation of dye followed pseudo-first order kinetics.	
Cu_2OHPO_4	Hydrothermal (140 °C, 24 h, concentration changed) KH_2PO_4, $CuCl_2$,	Photo-Fenton degradation of azo dye	• 1D and 3D hierarchical structures of Cu_2OHPO_4were prepared by changing the precursor concentrations. • Different hierarchical structures such as straw sheaves (60 μm), dumbbells (diameter 13-17 μm) and butterfly (27-35 μm) superstructures were prepared at 0.083 M, 0.033 M and 0.007 M precursor concentrations. • DFT theory showed that hydroxyl groups in its structure were responsible for high catalytic activity of dye removal under UV irradiation. • Cu_2OHPO_4 showed higher activity in comparison to Cu and CuO.	Zhao et al. 2015
Cu_2OHPO_4	Solvothermal route (120 °C, 6 h)	Photothermal performance	• Various morphologies such as multibranches-like (length = 5 μm), flower-like (dia = 3 μm), rod-like (length = 3 μm) and brick-like (length = 2-4 μm) were prepared using ethylene glycol (EG/water = 1/2), ethylene glycol (EG/water = 1/1), benzyl alcohol and ethanol, respectively, in the presence of PEG 2000. • Rod like structure showed the best photo-thermal efficiency which could be attributed to the high photo-absorption capacity induced by 1D structure.	Hu et al. 2017
$Cu_5(OH)_4(PO_4)_2$ on copper foil	Wet chemical method	Wide wavelength photocatalysis	• Various 3D flower-like and petal-like architectures were prepared. • Both architectures provided high efficiency for degradation of rhodamine 6G. • Catalyst with petal like morphology shows 97% degradation efficiency after 40 min whereas 95% efficiency was achieved with flower like morphology after 60 min.	Jiao et al. 2017
Cu_2OHPO_4, $Cu_3(PO4)_2$	Sonochemical synthesis (25 °C, 1-1.5 h)	Catalytic wet peroxide oxidation of Aniline	• Cu_2OHPO_4 and $Cu_3(PO4)_2$ are first time synthesized by sonochemical method at room temperature in less than 1.5 h. • Nano-spindles of Cu_2OHPO_4 showed higher activity in comparison to nano-flakes of $Cu_3(PO4)_2$. • Hydroxyl radicals were found responsible for oxidation of aniline. • Aniline removal kinetics was best fitted with pseudo first order kinetic model. • Catalyst showed higher stability and reusability.	Present study

The synthesized samples have been used for the CWPO of toxic and bio-recalcitrant compound aniline. To the best of authors' knowledge, the CWPO of aniline using Cu_2OHPO_4 has not been reported.

2.7. OVERVIEW OF LITERATURE SURVEY

The literature review illustrates the traditional and emerging technologies for the treatment of nitrogenous aromatic compounds polluted wastewater. The literature search in science citation index (SCI) database was carried out through Sci-Finder for studying the available reports on nitrogenous aromatic pollutants remediation techniques using keywords such as "Congo red, quinoline, aniline, biodegradation, advanced oxidation, coagulation/flocculation, membrane separation, adsorption, and physicochemical treatment". The conference publications were not included in the literature search. As shown in Fig. 2.2, Fig. 2.3 and Fig. 2.4, the numbers of research articles on applications of different technologies have substantially increased from 2000 to 2018. Adsorption and biological degradation methods are widely reported techniques for the removal of Congo red, quinoline and aniline. The increasing number of publications shows growing interest of researchers in the utilization of advanced oxidation processes (AOPs) for the treatment of nitrogenous aromatic compounds.
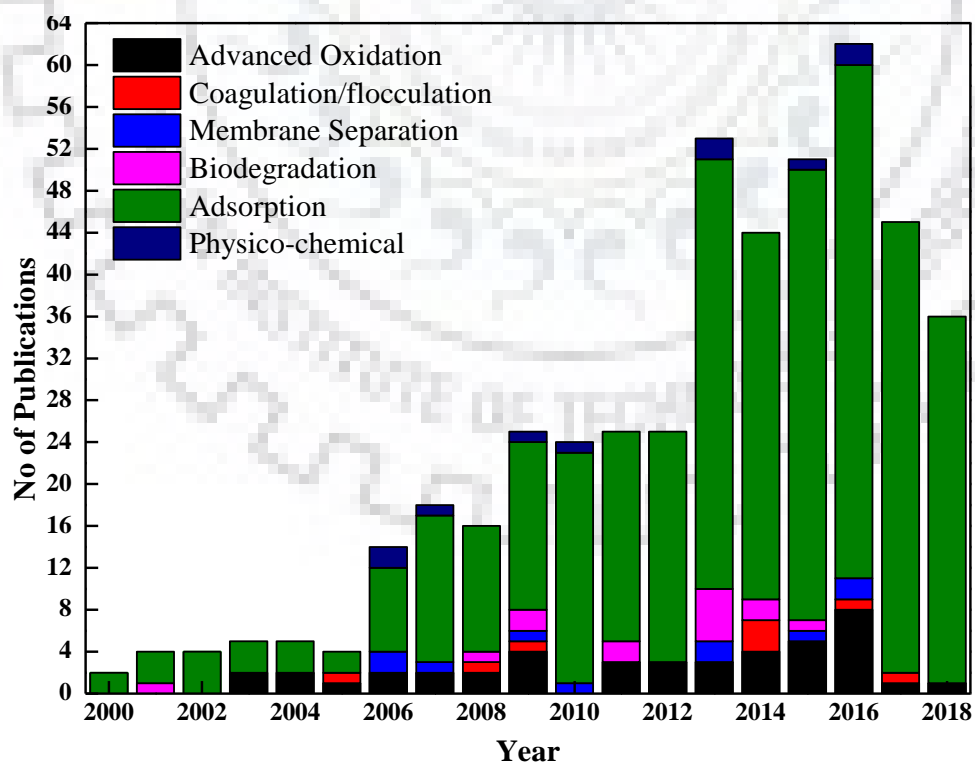
Fig. 2.2: Number of research articles published on applications of different treatment technologies for the removal of Congo red (Sci-Finder data base searched on July 5, 2018)
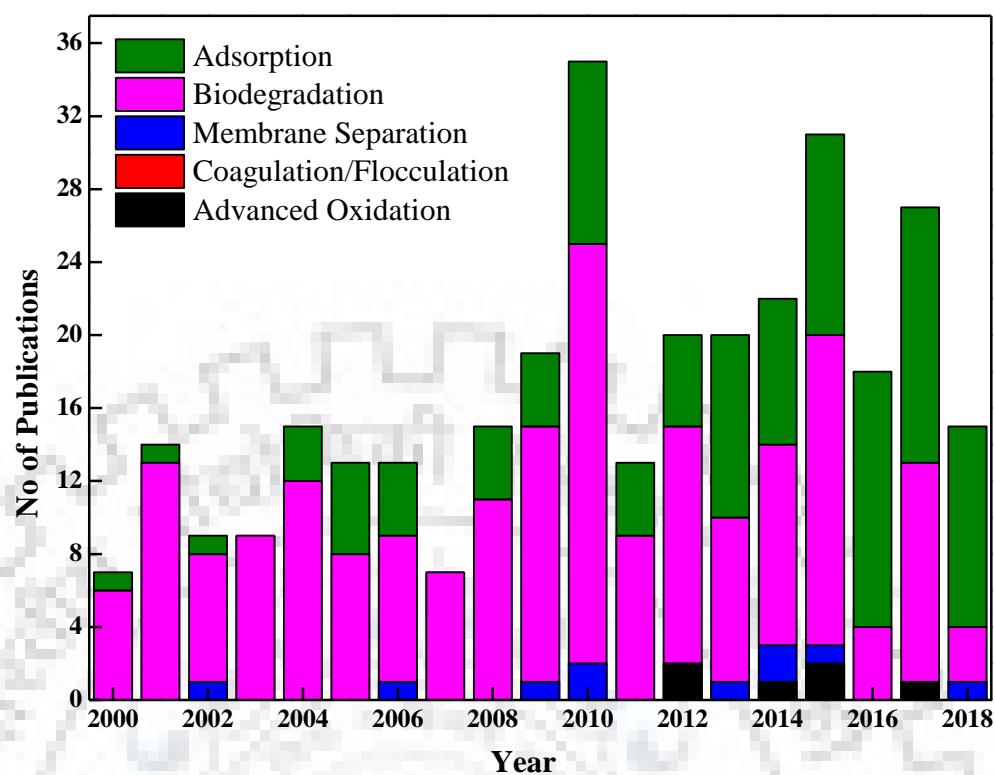
Fig. 2.3: Number of research articles published on applications of different treatment technologies for the removal of quinoline (Sci-Finder data base searched on July 5, 2018)
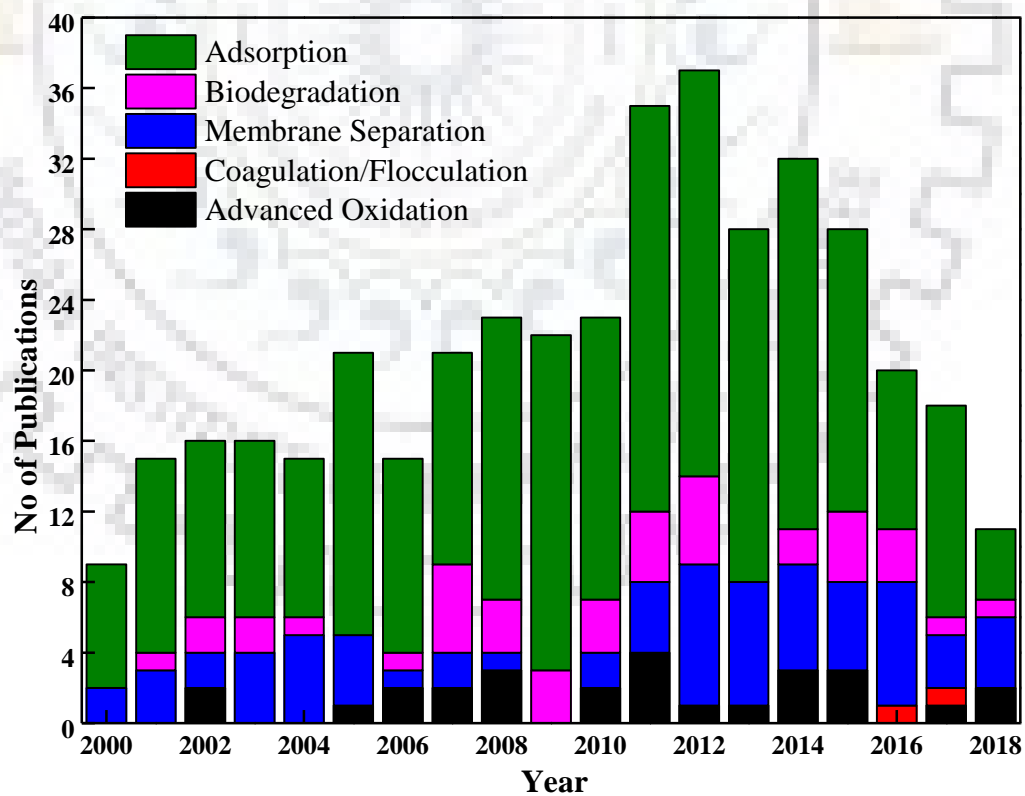
Fig. 2.4: Number of research articles published on applications of different treatment technologies for the removal of aniline (Sci-Finder data base searched on July 5, 2018)

2.8. RESEARCH GAPS

Literature review on treatment of Congo red, quinoline and aniline indicates that the maximum work has been carried out on the biological, adsorption and photocatalytic oxidation techniques. The following gaps have been noted in the removal/treatment of Congo red, quinoline and aniline from wastewater:

➤ The CWPO of Congo red and quinoline using Cu/zeolite Y as catalyst has not been reported.

➤ Most of the CWPO studies have been carried out in batch reactors. The CWPO of nitrogenous aromatic compounds in continuous FBR using Cu/zeolite Y has been rarely reported.

➤ AIE method is a conventional method to incorporate active metal in the zeolite Y. However, this method is associated with various limitations. There is a lack in research on developing more facile, green and environmentally-friendly alternative routes. Further, the post-synthetic approaches for the generation of hierarchical porosity in microporous zeolite Y have been investigated by a few researchers. Keeping this in view, wet-impregnation and precipitation-impregnation have been explored and developed as strategies to simultaneously remove the limitations of AIE as well as of microporosity in considerable extent.

➤ The influence of copper impregnation and precipitation-impregnation has never been studied in term of its influence on crystalline structure, hierarchical porosity as well as coordination environment of copper species in zeolite Y matrix. Moreover, the influence of these routes has never been investigated for degradation of toxic nitrogenous aromatic compounds.

➤ A number of studies are devoted to generate different architectures of Cu_2OHPO_4 and $Cu_3(PO_4)_2$; however, the fabrication of their nano-architectures using a facile, fast and ligand-free synthesis route has not been reported yet. In view of the above, a novel ultrasonic-assisted synthesis of Cu_2OHPO_4 and $Cu_3(PO_4)_2$ nanostructures have been developed.

➤ No study has been reported for the CWPO of aniline using different morphology of Cu_2OHPO_4 and $Cu_3(PO_4)_2$.

➤ The degradation mechanism, kinetics and reusability analysis is not much discussed in the case of CWPO of Congo red, quinoline and aniline.

The goals and objectives for the present work were fixed in view of the above as discussed in Chapter 1.

3.1. OVERVIEW

Experimental procedures for the synthesis, characterization and application of catalysts have been discussed in the present chapter. The chapter started with explanation of copper deposition on protonic form of zeolite Y (HY) using three different strategies, viz. aqueous ion exchange, wet impregnation and precipitation-impregnation. Thereafter, the experimental procedures for ultrafast sonochemical synthesis of copper hydroxy phosphate and copper phosphate have been explained. This is followed by discussion on experimental procedures for the catalytic wet peroxide oxidation (CWPO) of Congo red, quinoline and aniline in aqueous solution in batch and continuous fixed-bed reactors. The detailed information about the experimental conditions and data interpretation methods for various catalyst characterization techniques has been provided thereafter. The working principles and experimental conditions used in different analytical instruments for measurement of performance evaluating parameters (pollutant, TOC, anions) have been discussed in the end of this chapter.

3.2. EXPERIMENTAL DETAILS

3.2.1. Materials

The protonic form of zeolite (NaY, Si/Al = 2.83, procured from Sud Chemie Pvt. Ltd. India) was used as supporting material to synthesize CuY catalysts. The anionic diazo dye Congo red [C.I. = 22120, chemical formula = $C_{32}H_{22}N_6Na_2O_6S_2$, M.W. = 696.7 g mol^{-1}, λ_{max} = 497 nm] was supplied by Sigma-Aldrich and used without additional purification. Quinoline and aniline were purchased from Loba Chemie (India) and Merck (Germany), respectively. Other chemical used were 30 wt% hydrogen peroxide (Ranken, India), nitric acid (SD fine Chemicals, India), ammonium nitrate (Ranken, India), hydrogen chloride (Ranken, India), disodium hydrogen phosphate dihydrate (Himedia, India), manganese dioxide (Aldrich, Germany), sulphuric acid (Himedia, India) and sodium hydroxide (Ranken, India). The copper nitrate trihydrate salt (Himedia, India) was used as copper source in all the catalysts. The desired concentration of above mentioned chemicals was prepared by diluting with distilled water. Distilled water was obtained from a double distillation assembly.

Millipore water was used for the preparation of all analytical standards, eluents formation and sample dilution required for chromatography. All solvents employed in chromatography were of high performance liquid chromatography (HPLC) grade.

3.2.2. Synthesis methods

3.2.2.1. Preparation of HY sample

Ion exchange method was used to obtain the protonic form of zeolite (HY) from NaY. In a typical process, 15 g commercial zeolite (NaY) was mixed with 1500 mL of 0.1 M NH_4NO_3 solution, stirred for 5 h at 80 °C. The resulting sample was separated by centrifugation at 10000 RPM and washed several times by de-ionized water to remove nitrates. After washing, the sample was dried overnight in an oven at 110 °C. This process was repeated three times at same conditions and subsequently calcined at 550 °C in a muffle furnace for 5 h to decompose the ammonium ions. Finally, the HY zeolite was stored in a desiccator to avoid moisture adsorption due to its hygroscopic nature.

3.2.2.2. Preparation of Cu/zeolite Y catalysts

Copper was deposited over HY using three different routes, viz. aqueous ion exchange, wet impregnation and precipitation-impregnation.

3.2.2.2.1. Aqueous ion exchange (AIE)

For the synthesis of sample by AIE, 8 g of HY was mixed with 800 mL of 0.05M $Cu(NO_3)_2.3H_2O$ solution and stirred for 5 h at 80 °C. In order to avoid the formation of metal hydroxide, pH of the slurry was kept between 2 to 3 during exchange process [Song et al. 2013]. The solid sample was separated from slurry by centrifugation at 12000 RPM, washed several times with de-ionized water to remove nitrates and dried overnight in an oven at 120 °C. The process was repeated three times with the same sample using fresh copper nitrate solution each time to achieve complete ion exchange capacity, which has been represented as Cu/Al = 0.5 in this case due to divalent state of copper. Finally, the catalyst was activated by calcinations at 550±3 °C in a muffle furnace for 5 h.

3.2.2.2.2. Wet impregnation (IMP)

Wet impregnation method was used to prepare samples with different copper loading. To prepare these samples, required amount of copper nitrate trihydrate salt was dissolved in 30 mL double distilled water to which required amount of zeolite was added. In a typical synthesis, 1.43 g of $Cu(NO_3)_3.3H_2O$ salt was dissolved in 30 mL of double distilled water to obtain the copper loading similar to AIE and to which 4.75 g HY was added. The initial pH of the solution was adjusted to 4 using HNO_3 to prevent hydroxide precipitation and maintain zeolite structure stability. The sample was continuously stirred at 90 °C until all the water got evaporated and subsequently dried

overnight at 120 °C in an oven. The sample thus obtained was further washed with de-ionized water, dried overnight at 120 °C and calcined in muffle furnace at 550±3 °C for 5 h.

3.2.2.2.3. *Precipitation-impregnation (PI)*

Samples with different copper loadings were synthesized by dissolving required amount of $Cu(NO_3)_3.3H_2O$ in 50 mL of double distilled water followed by simultaneous addition of required amount of zeolite and NaOH. Sodium hydroxide was quickly added for the precipitation of $Cu(OH)_2$ and to avoid ion exchange which occurs at low pH (<4). The pH of the slurry was adjusted at 9.7-10. The resulting slurry was stirred for 1 h at 90 °C and kept for aging at the same temperature until all water evaporated. The samples were washed several times with de-ionized water, dried overnight at 120 °C and calcined at 550±3 °C for 5 h. A color change was observed from blue to dark grey after calcinations, which indicates conversion of $Cu(OH)_2$ to CuO.

3.2.2.3. *Preparation of Cu₂OHPO₄ and Cu₃(PO₄)₂*

All experiments were carried out in air atmosphere. In a typical experiment, 2.42 g $Cu(NO_3)_3.3H_2O$ was dissolved in 40 mL of double distilled water. Prior to the addition of copper salt, the initial pH of the water was adjusted to 2.5 using dilute nitric acid to prevent hydrolyzation of Cu^{2+} ions. The phosphate solution was prepared by dissolving 0.89 g $Na_2HPO_4.2H_2O$ in 40 mL double distilled water. This phosphate solution was added drop-wise to the copper nitrate solution which leads to the formation of blue precipitate. The final pH was adjusted to desired value using 0.1 M NaOH or 0.1 M HNO_3 solution. After stirred for 30 minutes, the final solution was irradiated with required amplitude of high intensity ultrasound (400 W, 24 kHz) using a probe sonicator at atmospheric condition for 2 h. During the synthesis, the colour of the suspension changed from blue to pale green and temperature of the solution increased to 60-70 °C. The precipitate was separated from slurry by centrifugation at 10000 RPM, washed several times with ethanol and dried overnight in an oven at 70 °C.

3.2.3. **Catalytic activity tests**

3.2.3.1. *Batch reactor*

All batch experiments were carried out in 100 mL three necked flat bottom flask equipped with heating system, pH electrode and magnetic stirrer. The simplified experimental set-up used for this study has been shown in Fig. 3.1. The reaction solution of nitrogenous aromatic compounds of desired concentration was freshly prepared in double distilled water and catalytic oxidation of this solution was performed under total reflux condition with continuous stirring at 600 RPM. In each

experiment, 100 mL solution was taken and the desired temperature of the reaction solution was maintained using a temperature controller. When thermal equilibrium reached, required amount of catalyst was added. The initial pH of the solution was adjusted at desired value by the addition of 0.1 M sulphuric acid or 0.1 M sodium hydroxide solution. Then, required amount of H_2O_2 was added and this time was considered as time zero (t = 0). The concentration of hydrogen peroxide was varied in multiples of stoichiometric amount, which is theoretically required to completely oxidize pollutants into CO_2, H_2O and mineral acids. The stoichiometric amounts of H_2O_2 for Congo red and aniline were calculated according to following stoichiometric equations Eq. 3.1 and Eq. 3.2. The operating conditions used for CWPO of Congo red and aniline have been summarized in Table 3.1.

$$C_{32}H_{22}N_6Na_2O_6S_2 + 91H_2O_2 \rightarrow 32CO_2 + 98H_2O + 6HNO_3 + 2NaHSO_4 \qquad (3.1)$$
$$2C_6H_5NH_2 + 35H_2O_2 \rightarrow 12CO_2 + 42H_2O + 2NO_2 \qquad (3.2)$$
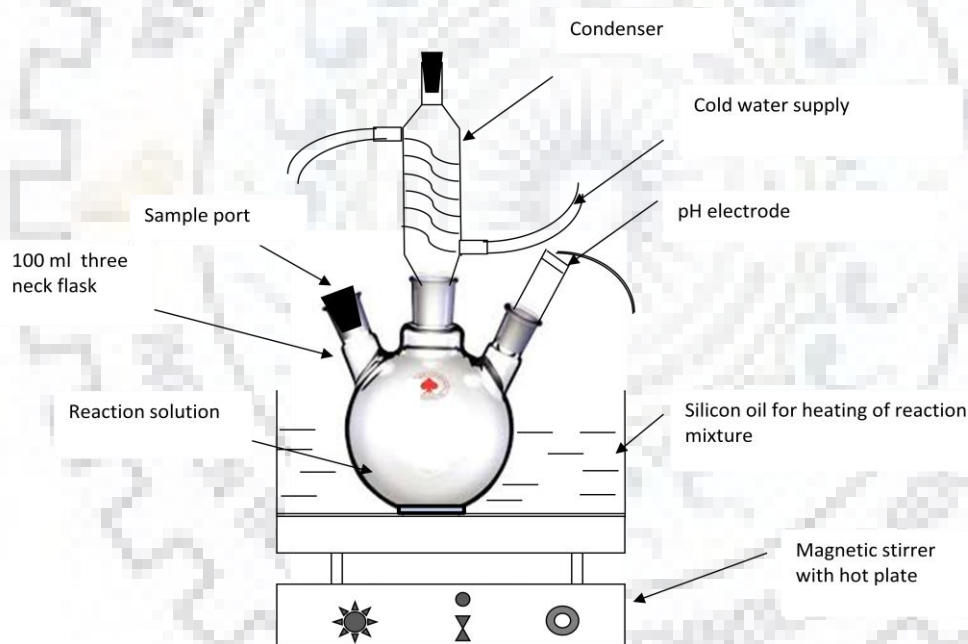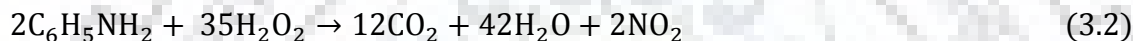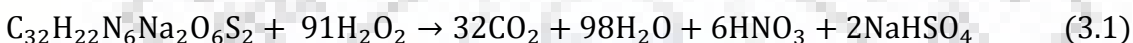
Fig. 3.1: Experimental set up to evaluate the catalytic activity of catalysts for CWPO

At regular time intervals, 1 mL of aliquot was sampled, diluted several times to bring concentration in calibrated data of instruments and the catalyst was separated by centrifuge. The extents of degradation of dye and aniline were measured immediately using UV-spectrophotometer (UV-1800, Shimadzu, Japan) and HPLC (Water, USA). TOC was determined by following method of combustion and quantification of generated CO_2 gas by non-dispersive infrared detector (NDIR) in a TOC analyzer (TOC-Vcph Shimadzu). The quenching of hydroxyl radicals was carried out before TOC measurement using solid MnO_2. The concentration of leached copper metal in final

effluent was measured using atomic absorption spectrophotometer (AAS, Varian Spectra-10 plus) for catalyst stability evaluation. Ion chromatography of the samples was conducted for confirmation of the mineralization as well as measurement of the inorganic ion concentrations. The basic principle and experimental condition used for these analytical techniques is explained in later sections.

Table 3.1: Operating conditions used for CWPO of Congo red and aniline in batch reactor

Experimental variables	Set parameters[a]	Set parameters[b]
Pollutant concentration, mM	0.143	1.07
H_2O_2 concentration, mM	13.06-156.72	9.36-74.88
Initial pH	5-11	5-11
Catalyst amount, g L^{-1}	0.5-2	0.3-2.0
Reaction temperature, °C	25-60	25-80
Stoichiometric amount of H_2O_2, mM	13.06	18.72

[a] CWPO of Congo red, [b] CWPO of aniline

3.2.3.2. Continuous up-flow fixed bed reactor

CWPO of quinoline aqueous solution (3.87 mM, pH 7.0) was carried out in an up-flow packed-bed glass column reactor. The catalyst in the form of spherical pellets was placed inside the bed and a layer of inert glass beads was placed at top and bottom of this bed for uniform liquid distribution. The glass tube was surrounded by jacketed annular tube, where hot silicone oil was circulated at high flow rate to heat the catalyst bed. The specifications of the packed-bed reactor and operating condition of CWPO experiments have been listed in Table 3.2. The column diameter/particle diameter ratio was kept larger than 8 to avoid the wall effect. The temperature of the packed-bed (40-80 °C) was maintained by circulating oil in outer jacket. The quinoline and H_2O_2 mixture was kept in storage tank, which was placed in oil bath to keep the whole system at isothermal condition. The initial pH of the mixture was set using 0.1 M sulphuric acid or 0.1 M sodium hydroxide solution. The concentration of H_2O_2 was kept in multiples of its stoichiometric amount, which is theoretically required for the complete mineralization of quinoline solution as per Eq. 3.3). The stoichiometric amount of H_2O_2 is 92.88 mM.

$$C_9H_7N + 24 H_2O_2 \rightarrow 9CO_2 + 27 H_2O + HNO_3 \qquad (3.3)$$
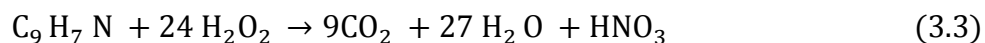
The reactants mixture was fed to the reactor using a peristaltic pump (Gilson, USA) at the different space velocities, corresponding to flow rates (Q) = 0.97-3.89 cm^3 min^{-1}. These space

velocities were varied to evaluate the influence of residence time (t_R) on performance of the reactor. The residence time (t_R) of liquid feed over the catalyst bed was calculated by Eq. 3.4 [Martinez et al. 2007];

$$t_r = \frac{\varepsilon_L V_c}{Q} \tag{3.4}$$

where, liquid holdup (ε_L) was calculated from excel flooded-bed simulator developed by Larachi and Grandjean (source: www.gch.ulaval.ca/). This simulator involves the feed solution, physical properties, operating parameters, particle and bed properties, and properties of the CO_2 gas generated during mineralization of quinoline.

Table 3.2: Reactor dimension and operating conditions used in CWPO experiments

Specification	Operating conditions
Internal diameter of reactor, cm	1.30
Column height, cm	20
Catalyst weight, g	9.31
Particle size of catalyst, mm	0.4-1.7 (40-12 mesh)
Catalyst bed volume (V_C), cm^3	13.4-14.6
Bed porosity	0.37-0.42
Particle density, g cm^{-3}	1.1
Quinoline concentration, mM	3.87
H_2O_2 concentration, mM	46.44-278.64
LHSV, h^{-1}	4-16
Residence time (t_R), min	1.11-4.54
Reaction temperature, °C	40-80

Aliquots were regularly taken from the treated effluent to examine percent removal of quinoline as well as total organic carbon (TOC), H_2O_2 consumption, final pH and leached copper concentration. Prior to analysis, all samples were filtered through millipore filters (pore size 0.2 µm). The concentration of quinoline in aqueous solution was measured using HPLC (HPLC) (Water, USA). TOC of all the treated samples was measured using TOC Vcph-Shimadzu spectrophotometer for the determination of degree of mineralization. H_2O_2 conversion was estimated using iodometric titration method. In order to evaluate the efficiency of catalytic activity, the removals of quinoline and TOC, and H_2O_2 conversions were calculated according to Eq. 3.5;

$$\text{Quinoline or TOC removal (\%)} = \left(\frac{C_o - C_t}{C_o}\right) \times 100 \qquad (3.5)$$

where, C_o is the initial concentration (mg L^{-1}) in feed and C_t is the final concentration (mg L^{-1}) in treated effluent. The concentration of leached copper was determined by ICP-MS (Perkin Elmer ELAN DRC-e, USA). The H$_2$O$_2$ stoichiometric efficiency (η) was calculated according to Eq 3.6;

$$\eta = \frac{\text{Theoretical amount of oxidant required for the desired TOC removal}}{\text{Actual amount of } H_2O_2 \text{ consumed in reactor}} \times 100 \qquad (3.6)$$

The basic principle and experimental condition used for these analytical techniques have been explained in subsequent sections.

3.3. CHARACTERIZATION

3.3.1. X-ray fluorescence (XRF)

XRF is a non-destructive analytical technique used for the determination of elemental composition of materials. It is an excellent technology for qualitative and quantitative analysis of material composition. It works on the principles of wavelength dispersive spectroscopy in which sample is excited with primary X-ray source and emitted fluorescent X-rays from the sample were measured [Beckhoff et al. 2006; Jenkins 2012]. Characteristic fluorescent X-rays of particular wavelength emitted from sample after excitation is unique for the specific element.

In the present research, XRF (*Bruker, S4 Poinner*) was used to determine the chemical composition and Si/Al ratio of parent zeolite (Na-Y) in elemental form.

3.3.2. X-ray diffraction (XRD)

X-ray diffraction is widely used non-destructive analytical technique used for phase identification, stress properties, crystal structure determination, quality control and can provide information about unit cell dimensions [Hanawalt et al. 1938; Bertin et al. 1978; Tsuji et al. 2004; Toma et al. 2012]. It is also used for variable temperature studies to determine phase diagrams, thermal expansion, and material stability. The use of XRD is limited to crystalline materials as amorphous materials do not give useful diffraction pattern due to overlapping of peaks. It works on the principle of constructive interference produced by interaction of monochromatic X-ray with crystalline sample when conditions satisfy Bragg's law (nλ=2d sinθ).

In the present research work, XRD was used for the analysis of crystallographic phases of the catalysts. The XRD pattern was recorded on *Rigaku Ultima IV diffractometer* using monochromatic Cu-Kα radiation (λ = 1.542Å) at 40 kV and 40 mA. The patterns were collected in

2θ range of 5-80° with step size 0.02°. The materials were ground and homogenized prior to analysis. Scherrer's equation given in Eq. 3.7 was implemented for the estimation of average crystallites size.

$$d_P = \frac{K\lambda}{\left(\beta_{Sample} - \beta_{standard}\right)\cos\theta} \tag{3.7}$$

where, d_P is the crystallites size, λ is wavelength of X-ray radiation, K is Scherrer's constant (0.94), β is the full width of the peak at half maximum (FWHM) and θ is Bragg's angle. The instrumental broadening ($\beta_{standard}$) was measured using pure silicon powder as standard sample.

Data interpretation was carried out using X'pert high score plus and the powder diffraction database of the International Center of Diffraction Data (ICDD).

3.3.3. Surface area analyzer

Surface area analysis is a well-established technique for investigating the textural properties such as specific surface area, pore volume and pore size distribution of the materials [Gregg et al. 1982; Rouquerol et al. 1999; Thommes et al. 2015]. Typically, inert gas such as N_2 or Ar is adsorbed over the surface of solid at cryogenic temperature (77 or 87 K) and the adsorbed amount is measured on the solid materials at different pressure. Langmuir's model and Brunauer-Emmett-Teller (BET) equation are generally used to estimate the specific surface area of microporous and mesoporous materials, respectively. The BET equation is the most widely used method and can be represented as;

$$\frac{1}{v\left[\left(\frac{p_0}{p}\right)-1\right]} = \frac{c-1}{v_m c}\left(\frac{p}{p_0}\right) + \frac{1}{v_m c} \tag{3.8}$$

where, v is the adsorbed gas quantity, v_m is the monolayer adsorbed gas quantity, p_0 and p are the saturation and equilibrium pressure of adsorbate at the temperature of adsorption and c is the BET constant. The BET equation is used to calculate v_m. v_m is further used to calculate the total surface area (S_{total}) and specific surface area (S_{BET}) using given equations (Eq. 3.9 & 3.10);

$$S_{total} = \frac{(v_m N s)}{V} \tag{3.9}$$

$$S_{BET} = \frac{S_{total}}{a} \tag{3.10}$$

where, N is Avogadro's number, V is the molar volume of adsorbate gas, s is the adsorption cross section of the adsorbing species and a is the mass of solid adsorbent.

In the present research, surface area analyzer was used to evaluate the porous nature of samples. N_2 sorption isotherm was recorded at −196 °C using *Autosorb-iQ2, Quantachrome*

Instruments, USA. Before the analysis, Cu/zeolite Y samples were degassed at 150 °C for 6 h under vacuum. Langmuir model was fitted using adsorption data of isotherms between relative pressure ranges of $P/P_0 = 0.05\text{-}0.3$ to determine the surface area of Cu/zeolite Y samples. The average pore size was determined using density functional theory (DFT) method. On the other hand, Cu_2OHPO_4 and $Cu_3(PO_4)_2$ samples were degassed at 90 °C for 6 h under vacuum. The surface area was obtained using BET model in relative pressure ranges of $P/P_0 = 0.05\text{-}0.3$. The average pore size was calculated using Barrett-Joyner-Halenda (BJH) method in desorption range of isotherm. Total pore volume was estimated using N_2 adsorption data of isotherm at relative pressure $P/P_0 = 0.99$.

3.3.4. Fourier transform infrared (FTIR) spectroscopy

FTIR is versatile analytical technique used to analyze the functional groups in the organic, inorganic and bio-molecules. It can be employed for quantitative and qualitative estimation of solid, liquid or gaseous samples [Fayer et al. 2001; Tolstoy 2003; Stuart 2004; Silverstein et al. 2005]. It monitors the vibrations of functional groups present in the samples and provides the data for identification of compounds. It is very popular to explain the hydrogen bonding, and electrostatic interaction between nanoparticles and support materials in composite.

In the present research, FTIR was used to investigate the structure of catalyst in more detail. *Nicolet Avatar 370 CSI spectrometer* was used to analyze the functional groups of the synthesized materials. For the analysis, 2-3 mg of sample was mixed with 200 mg of KBr powder and grounded into fine powder using mortar pastel. Finely grounded powder was pressed into transparent pellet of 1 to 1.5 mm thickness in a hydraulic press at a pressure range of 150 psi for 30 sec. The transparent pellet was then scanned in the range of 400 to 4000 cm^{-1} at a resolution of 4 with 32 scans per spectrum.

3.3.5. Ultra violet-visible diffused reflectance spectroscopy (UV-DRS)

UV-vis DRS, a type of spectroscopy in which diffuse reflection of radiation in UV-vis range (190-800 nm) is measured as light interact with the sample. It is an important technique for studying heterogeneous catalysts, as both d-d and charge transfer transitions of solid samples can be explored [Perkampus et al. 1992; Owen 1996; Tsuchiya 2001]. Therefore, it provides information about oxidation state and coordination environment of metal ions. The basic principle of this technique is based on the absorption, scattering, specular reflection and diffuse reflection of incident monochromatic light. The reflected light returns in the air and measured relative to the

non-absorbing standard (BaSO4, NaF, MgO) by spectrophotometer [Sassaroli et al. 2004]. In order to reduce the proportion of specular reflection in reflected light, the particle size of powder must be reduced to a size equivalent to wavelength. In the present study, UV-DRS were recorded with UV-visible spectrophotometer (*UV-2450 Shimadzu*) using $BaSO_4$ as reference material in the range 200-600 nm. A reliable evaluation of diffuse reflectance spectra requires the calculation of the Kubelka-Munk spectra from the absolute reflectance of the sample. Kubelka munk function for active phase was calculated after deducting the influence of support HY from all Cu-Y samples, as shown in Eq. 3.11 below, since zeolite Y show absorption in the same region (200-250nm) as copper species.

$$F(R)_{Cu\ species} = F(R)_{sample} - F(R)_{HY} \tag{3.11}$$

3.3.6. X-ray photoemission spectroscopy (XPS)

XPS is a surface sensitive spectroscopic technique that provides the information regarding atomic composition, chemical environment and electronic state of elements present within the sample [Wagner et al. 1979; Suga et al. 2014]. It is a qualitative as well as quantitative analysis. The basic principle of this technique is based on photoelectric effect. The electrons are released from the shells when photons of known energy (X-rays) strike on the material surface and kinetic energy of these electrons is measured by spectrometer. The spectrum is defined in number of electrons that escape from the top 0 to 10 nm of the material surface versus binding energy. Binding energy is a unique characteristic of element and can be estimated from following equation:

$$B.E. = h\vartheta - K.E. - W \tag{3.12}$$

Where, *hv* = energy of incident photons, *K.E.* = kinetic energy of released electrons and *W* = work function.

In the present research, *PHI versaprobe II, FEI inc.,USA* was used to recognize the atomic composition of catalysts and nature of different atoms such as Cu, O, Al, Si, and P. The analysis was performed at room temperature in ultra-high vacuum of 10^{-9} mbar using microfocused (100 μm, 100 W) monochromatic Al-Kα radiation source (*hv* = 1,486.6 eV). High-resolution spectra were recorded at the step size of 0.025 eV and an Ar+ ion gun was used. All spectra were measured with respect to energy reference of C1s peak at 284.6 eV.

3.3.7. Field emission scanning electron microscopy (FESEM)

FESEM is powerful version of microscope which uses high energy electron beam instead of light to generate variety of signals such as secondary electrons, X-rays and reflected electrons from the

surface of solid samples. In FESEM, the electrons are generated from thin and sharp tungsten needle under electric field. The voltage requirements between the tungsten cathode and anode are 0.5-30 kV in the presence of high vacuum (10^{-8} Torr). The focused and accelerated electrons bombard the surface of the sample and secondary electrons are generated from sample. These secondary electrons are caught by detector and generate an electronic signal. These signals provide information about external morphology, crystalline structure, chemical composition and orientation of the material [Haine et al. 1961; Wischnitzer 1962; Wells 1974]. The researchers from different fields such as biology, chemistry and physics utilize this technique to study structures that may be as small as 10-20 nm.

In the present research, *FE-SEM, Quanta 200 FEG, USA* at an acceleration voltage 20 kV was used for microstructure analysis of the catalysts and their distribution on the surface of support. Prior to analysis, the samples were coated with gold to render them conductive by standard sputtering technique.

3.3.8. Transmission electron microscopy (TEM)

TEM is a very powerful technique for material science in which a high energy electron beam is transmitted through very thin sample. The transmitted portion is focused by the objective lens into an image on phosphor screen. The interactions of electrons with the atoms of the sample are used for the analysis of crystal structure and various features in the structure like dislocations, defects, grain boundaries and composition [Graef et al. 2003; Williams et al. 2009]. It can also be used to characterize the shape, size, quality, and density of quantum wells, wires and dots.

In the present research, TEM was used to study the morphology and size. Sample preparation is very important for high quality image. The samples were prepared by dispersing small amount of sample in ethanol using ultrasonicator for 15 min. The suspended particles were placed on carbon coated copper grid (200 mesh). The grid was air dried, followed by examination in the TEM. Analysis was done using *TECNAI G^2S* at an operating voltage of 200 kV. High resolution transmission electron microscopy (HRTEM) was also used for in-depth study of the crystalline nature of the particles. The samples were prepared by the same method as discussed above.

3.3.9. Inductively coupled plasma mass spectrometry (ICP-MS)

ICP-MS is an important analytic technique used for the detection of elements at very low concentrations (part per quadrillion, ppq). It is combination of high energy inductively coupled

plasma and mass spectrometer for separation and quantification of ions [Nelms et al. 2009; Thomas et al. 2013]. In the present research, copper content of samples was estimated using ICP-MS (*Perkin Elmer ELAN DRC-e, USA*) by following acid digestion technique. This instrument was also used to measure the concentration of leached copper metal in final effluent.

3.4. ANALYTICAL METHODS

3.4.1. Ultraviolet-visible (UV-Vis) spectroscopy

UV-Vis spectroscopy refers to absorption spectroscopy in which light is absorbed by molecules in the UV-vis region (200-800 nm) of electromagnetic spectrum and results in the excitation of electron from ground state to higher energy state [Settle, 1997; Owen, 1996]. It is very often used for quantitative determination of transition metal ions and conjugated organic compounds using the principle of Beer-Lambert's law [Tsuchiya, 2001; Sassaroli and Fantini 2004]. In the present research, the extents of decolorization and degradation of Congo red dye were measured immediately at 495 and 343 nm, respectively, using UV-spectrophotometer (UV-1800, Shimadzu, Japan). The degradation and decolorization degree of Congo red were calculated according to Eq. 3.13:

$$\text{Degradation or Decolorization degree}(\%) = \left(\frac{A_i - A_t}{A_i}\right) * 100 \qquad (3.13)$$

where, A_i is the absorbance value at respective band for untreated Congo red dye solution (100 mg L^{-1}) and A_t is absorbance value at treatment time t (min).

3.4.2. High pressure liquid chromatography (HPLC)

HPLC is a powerful analytical tool used to identify and quantify the various components in the mixture. It is one type of column chromatography and compounds are identified on the basis of time taken by them to pass through column to the detector [Hamilton et al. 1982; Brown et al. 1989]. The small particles size of column packing material exhibit high surface area which allows high interaction between the stationary phase and mobile phase molecules. Reversed phase HPLC is most commonly used category of HPLC in which long hydrocarbon chains (C$_8$ or C$_{18}$) are deposited on the silica column to make it non-polar. Polar solvents such as alcohols and water mixture are used. The non-polar compounds in the mobile phase are attracted by hydrocarbon chains because of Van der Waals dispersion forces and they have more retention time in

comparison to polar compounds. The concentration of different organic compounds (leaving column at different retention times) can be measured using UV-detector. In this work, the concentration of quinoline, aniline and their intermediates species formed during the CWPO were measured through HPLC instrument (*Water, USA*). The instrument was equipped with a C18 reverse phase column, single-piston reciprocating pumps and a UV detector. The concentration of quinoline was measured using mobile phase (methanol/water = 80/20 (v/v)), detector wavelength of 275 nm with flow rate of 1 mL min^{-1} in isocratic mode. Likewise, the concentration of aniline was measured using mobile phase (methanol/water = 60/40 (v/v)), detector wavelength of 280 nm with flow rate of 0.5 ml min^{-1}. The mobile phase and aliquots were filtered through 0.2 µm pore size PTFE membrane filter before inserting in HPLC instrument. A calibration curve was prepared through plotting area of peak vs. different concentration of nitrogenous aromatic compound. This calibration curve was used to evaluate the final concentration of pollutants in aqueous solution after CWPO reaction.

3.4.3. Total organic carbon (TOC) analyzer

TOC was determined by following method of combustion. The quantification of generated CO_2 gas was carried out by non-dispersive infrared detector (NDIR) in a TOC analyzer (TOC-Vcph Shimadzu). The instrument directly measured the total carbon (TC) and inorganic carbon (IC). TOC was calculated by subtracting IC from TC results.

In TOC analyzer, the combustion reactor consists of quartz tube packed with platinum catalyst. High purity zero air was supplied as carrier gas into the reactor and temperature of reactor was maintained at 680 °C. The injected sample oxidized in the reactor and transformed into CO_2. The carrier gas flows in reactor at volumetric flow rate of 150 mL min^{-1} and carries the combustion products into dehumidifier for cooling and dehydration. The chlorine compounds were removed through halogen scrubber. The generated CO_2 is analyzed through NDIR detector. The measured amount of CO_2 was utilized to observe the TC concentration using the TC calibration curve by potassium hydrogen phthalate as standard [Bisutti et al. 2004; El-Haloty et al. 2013]. Inorganic carbon (IC) includes carbonates and bicarbonates present in water. IC was measured by sparging CO_2 gas through a liquid sample at pH = 3 by using 25% H_3PO_4 solution. IC was analyzed in the form of CO_2 using NDIR detector. The calibration curve for IC measurement was plotted using Na_2CO_3 and $NaHCO_3$ solutions as standards.

3.4.4. Ion chromatography (IC)

Ion chromatography is generally used to quantify the inorganic ions and low molecular weight organic acids in aqueous solutions [Weiss et al. 2016]. In the present work, IC (*Metrohm, USA*) was used to measure nitrite, nitrate, ammonium, and sulfate ions to confirm the mineralization of nitrogenous aromatic compounds. IC instrument was equipped with an isocratic pump, dialysis system, stationary phase column, and conductivity detector. The stationary phase column *Metrosep A Supp 5* (4×250) contains polymeric substrate functionalized with quaternary ammonium groups which can interact with different anions and separate them. The concentration of anions was measured using conductivity detector. The total injected volume of sample was 20 µL, and the aqueous solution containing sodium carbonate (3.2 mmol L^{-1}) and sodium bicarbonate (1 mmol L^{-1}) was used as the eluent at flow rate of 0.7 ml min^{-1}. The background conductivity of the eluent was decreased using 100 mmol L^{-1} sulfuric acid solution as anionic suppressor.

3.4.5. Atomic absorption spectroscopy (AAS)

Atomic absorption spectroscopy is a commonly used technique to measure the concentration of metals with good accuracy and high selectivity. This technique is based on the principle that free atoms in the gaseous state can absorb radiation at specific resonance wavelength and the amount of absorption is proportional to concentration of the atom [Welz 1999]. The stability of the catalyst can be evaluated by measuring the concentration of leached copper metal in final effluent using AAS (*Varian Spectra-10 plus*). The instrument was equipped with hollow cathode lamp as light source, nebulizer, flame atomizer, monochromator, and detector. Concentration of the samples is usually determined from calibration curve which is generated from standards of known concentration. Air-acetylene mixture was used as fuel gas using detector wavelength of 324.75 nm. In the present research, copper loading on zeolite Y was measured using this instrument after following acid digestion method. In the present research, the analysis results of ICPMS and AAS are almost comparable. However, Atomic absorption spectroscopy is very easy to use and of low cost. ICPMS is found more suitable for multiple elements analysis, free from chemical interferences but not easy to operate and is very costly to run.

4.1. OVERVIEW

This chapter provides a detailed discussion on the influence of incorporation of different copper loadings over zeolite Y via wet impregnation technique. The detailed experimental procedure has been given in *Chapter-III*. The synthesized catalysts were characterized by using XRD, N_2 sorption, FESEM, FTIR, UV-DRS and XPS techniques in order to study the influence of copper loading on structure, texture and electronic states of copper. Furthermore, the catalysts have been tested for the decolorization, degradation and mineralization of recalcitrant diazo dye (Congo red) in heterogeneous Fenton-like process. The effects of operating parameters, such as, copper loading, initial pH, H_2O_2 concentration, catalyst dose and temperature were studied for the optimization of Congo red degradation by heterogeneous Fenton-like process. The effects of various operating parameters on copper leaching from catalyst were also observed. The kinetics, thermodynamics and reusability of the catalyst have also been discussed.

4.2. LOADING OF COPPER ON ZEOLITE Y

As discussed earlier in *Section 3.2.2* of *Chapter III*, copper was loaded on zeolite Y by wet impregnation technique.

4.2.1. Chemical composition

In order to study the control of copper loading obtained by impregnation method on zeolite Y, a series of samples with different copper loading were prepared. Table 4.1 summarizes the theoretically targeted and experimentally obtained copper content (before and after washing step), Cu/Al ratios and nomenclature of respective samples. As observed for samples before washing, this method provides good control over metal loading with good reproducibility. A small difference has been observed between targeted and actual copper content after washing in view of the subsequent loses of copper during washing step of catalyst preparation. Moreover, the impregnation route facilitated higher deposition of copper than the traditional ion exchange method [Komatsu et al. 1994; Hernández-Maldonado et al. 2003]. Ideally, the maximum copper content obtained by ion exchange is Cu/Al = 0.5 because each Cu^{2+} ion can balance the negative charge on two framework aluminums. However, this loading cannot be obtained due to competition of other impurities with copper for occupying the aluminum sites [Sobalík et al. 1998; Takahashi et al. 2001]. The high Cu/Al ratio for impregnation may be associated with the major deposition of metal in supercages and easily accessible external sites as well as small deposition in sodalite cages

[Campos-Martín et al. 1996]. Thus, the impregnation method has shown to be better than the conventional AIE which works on the principle of charge neutralization and cannot be controlled to achieve targeted metal content. Furthermore, a significant difference was observed in colors of different samples. The color varied from light blue to light gray with increase in copper loading from 1 to 10 wt%. The gray color of the sample 10CuY confirmed the formation of CuO [Kim et al. 2007].

Table 4.1: Targeted and experimentally obtained copper content on zeolite Y, Cu/Al ratios, and nomenclature of respective samples

Targeted Cu content (wt %)	Cu (wt%) (acid digestion before washing step)	Cu (wt%) (acid digestion after washing step)	Cu (wt%) (EDX)	Cu/Al content (after washing step)	Sample name
1.00	1.00	1.00	1.00	0.10	1CuY
2.50	2.38	1.95	2.33	0.18	2.5CuY
5.00	4.82	2.83	3.56	0.26	5CuY
7.50	7.37	4.87	4.93	0.46	7.5CuY
10.00	9.76	7.46	7.92	0.73	10CuY

4.2.2. X-ray diffraction

X-ray diffraction patterns (XRD) of NaY, HY and CuYs were recorded with the aim of noticing the effects of protonization and copper loading on crystalline nature of catalyst. Fig. 4.1a depicts that all CuY samples (except 10CuY) exhibit diffraction pattern similar to the diffractogram of crystalline aluminosilicate material: Zeolite Y (in sodium form $Na_2Al_2Si_{4.5}O_{13} \cdot xH_2O$, PDF card-430168). For all CuY samples (except 10CuY), these results are attributed to well-dispersed Cu species interacting with zeolite framework and no new phase formation is observed despite of high temperature treatment at 550 °C [Sagar et al. 2006]. However, two weak XRD diffraction peaks of NaY zeolite corresponding to (222) and (422) planes disappear in the patterns of HY and CuY. The disappearance of these peaks may be ascribed to local defects sites and hydrolysis of small fraction of Al-O bonds during sudden exposure of calcined samples to air [Saceda 2011]. Beside the diffractogram of the zeolite Y, the diffraction pattern of 10CuY also display low intensity peaks at diffraction angles 35.5° and 38.7° corresponding to [1,1,-1] and [1,1,1] planes, respectively, of monoclinic CuO crystallite (PDF files 48-1548). These low intensity peaks and their large FWHM suggest the presence of small copper oxide particles inside the pores of zeolite. It was found that intensity of all peaks decreased with metal loading, which occurred due to

absorption of X-ray by layer of copper species [Kim et al. 2007]. Armengol et al. [1999] also observed decrease in intensity of diffraction pattern of Y faujasite as Na^{1+} ions exchange with Cu^{2+} ions.
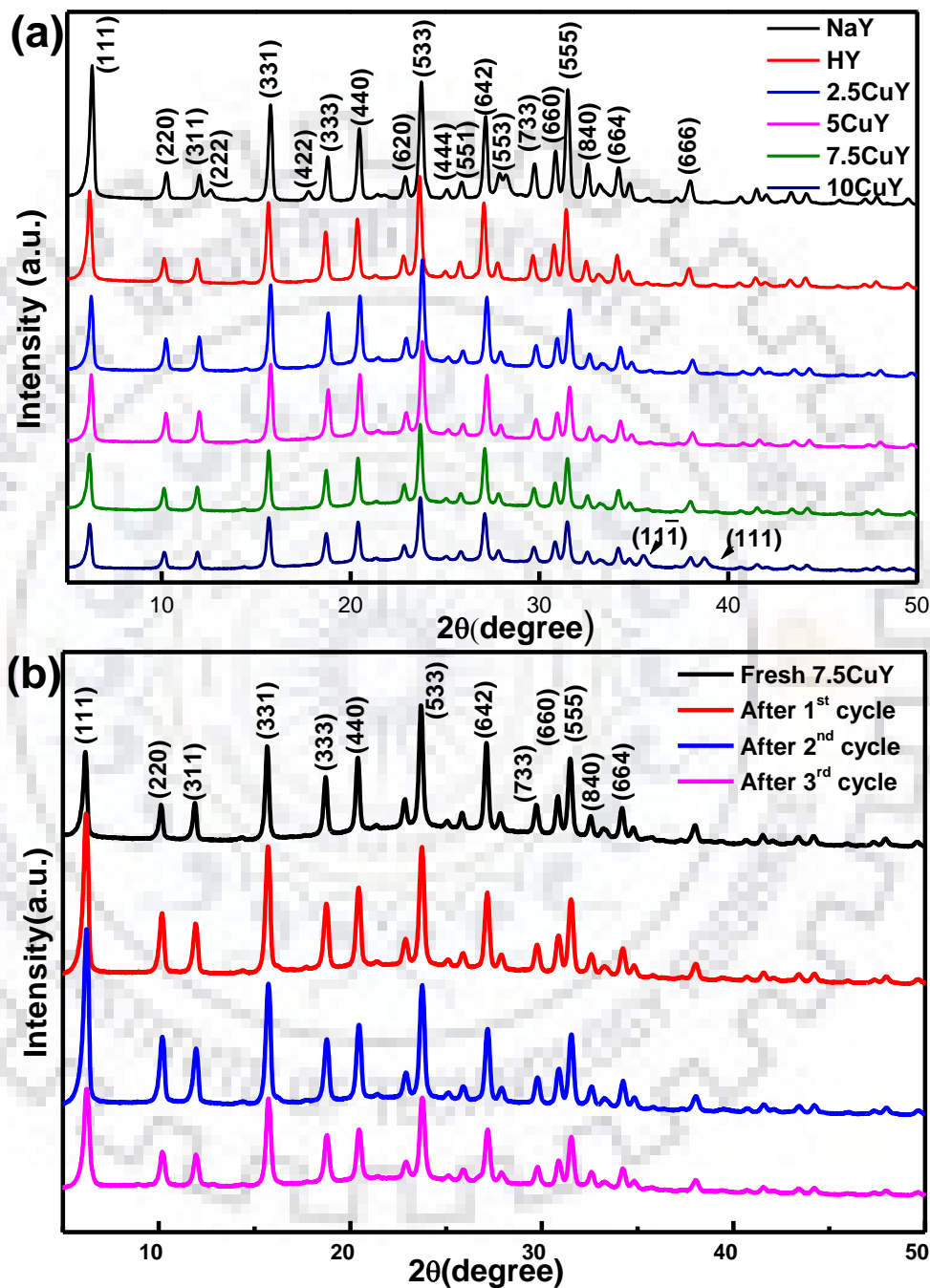
Fig. 4.1: (a) XRD patterns for fresh CuY zeolite with different loading (b) XRD pattern for used catalyst up to 3rd cycle

However, in the present case, the decrement in intensity was found more significant in the most prominent diffraction line (111) and thus, proved the highest effect of metal loading on that

plane. The relative intensity of (111) peak reduced from 100% to 72% after protonization of zeolite NaY (Table 4.2). As expected, the increase of copper loading from 2.5 to 10 wt% resulted into further diminishing of relative intensity from 63.47 to 43.34%. Moreover, the shift in 2θ value was observed after transition of NaY to HY and subsequent copper loading. This shift presents change of inter-planar spacing and unit cell size (Table 4.2). The change in unit cell size depends on the concept of ionic radius. During protonization of NaY, replacement of Na^{1+} (ionic radius 116 pm) with NH^{4+} ions (ionic radius 143 pm) occurs. Thus, the expansion of the unit cell may be attributed to mixed NH_4-H form after thermal treatment at 550 °C [Kaduk et al. 1995]. Similarly, the contraction of unit cell after wet impregnation with Cu (<5 wt%) may be ascribed to smaller ionic radius of Cu^{2+} (72 pm) than NH^{4+} ions. However, the unit cell size increase with increase in copper loading. Richter and co-worker [2007] observed similar unit cell expansion with increase in copper content using precipitation method followed by heat treatment in inert atmosphere. As shown in Fig. 4.1b, no change in zeolite structure was observed after three consecutive cycles of CuY zeolite in heterogeneous Fenton-like reaction. This result indicates high framework stability of zeolite Y under extreme oxidizing condition.

Table 4.2: Effect of copper loading on intensity of (111) peak and unit cell parameters

Sample name	Zeolite (NaY)	Zeolite HY)	2.5CuY	5CuY	7.5CuY	10CuY
Relative intensity (%)	100	71.78	63.47	58.14	50.54	43.34
Bragg's angle (2θ)	6.32	6.18	6.26	6.26	6.18	6.18
Inter planar spacing (Å)	13.99	14.30	14.12	14.12	14.30	14.30
Unit cell Parameter (Å)	24.22	24.77	24.46	24.46	24.77	24.77

4.2.3. Textural properties

The nitrogen sorption isotherms of all samples have been presented in Fig. 4.2 and the resulting textural properties are summarized in Table 4.3. All samples exhibit a rapid uptake of N_2 at low relative pressure range, which indicates the presence of micro pores in all samples [Dükkanci et al. 2010]. Higher N_2 adsorption volume for 7.5CuY at low relative pressure suggests higher and stable crystallinity. The presence of H_4 type hysteresis loop in the higher N_2 volume curve signifies the formation of mesopores [Huang 2010]. The Langmuir surface areas (S_{Lang}) and pore volumes (V_p) have not been affected up to copper loading of 5 wt%, which reflect the stable framework of zeolite Y and uniform dispersion of copper atoms [Klaas et al. 1997]. However, both increase surprisingly from 567 to 667 m^2 g^{-1} and 0.26 to 0.34 cm^3 g^{-1}, respectively, for 7.5CuY. These

improvements may be caused by higher crystallinity and mesopores formation, as discussed above. To further confirm the mesopores formation in 7.5CuY, the pore size distribution for all samples was compared using DFT model (Fig. 4.3). Interestingly, the generation of hierarchical porosity, characterized with mesopores (in range 3-10 nm) in small extent and intrinsic micropores (about 0.98 nm) in major extent, were observed.
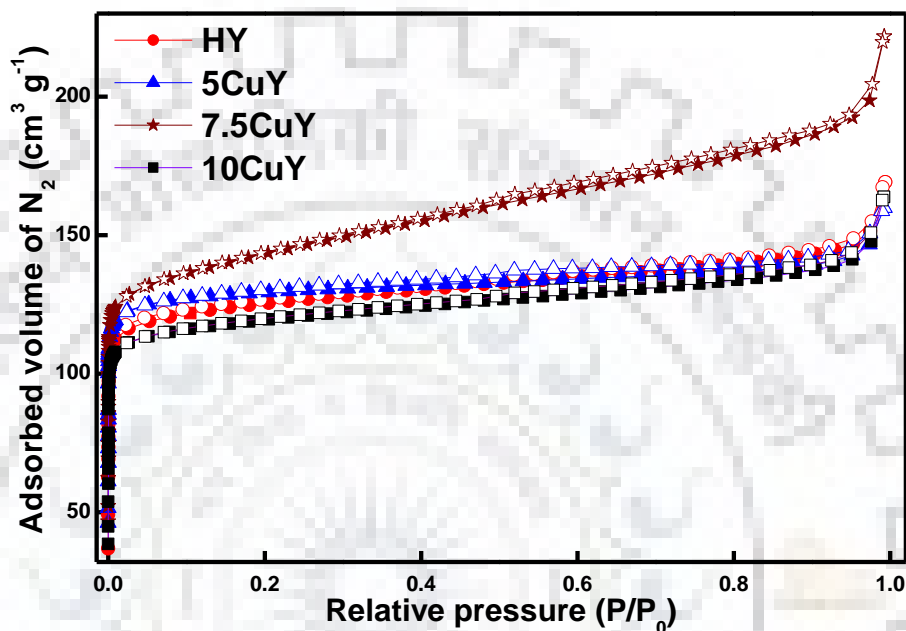
Fig. 4.2: N₂ sorption isotherms of CuY zeolites with different Cu loadings
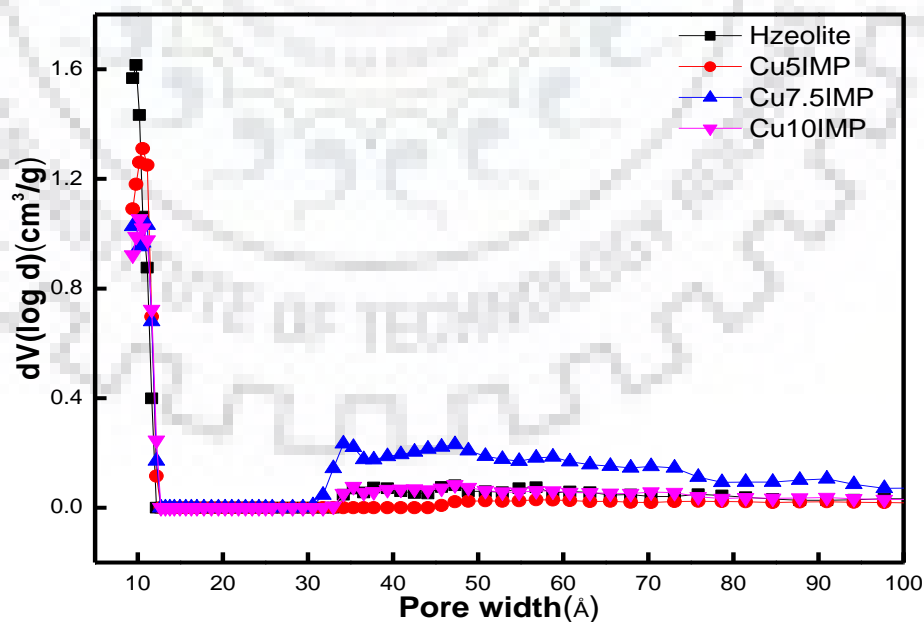
Fig. 4.3: Pore size distribution of CuY zeolites with different Cu loadings (DFT model)

In contrast to aforementioned results, the substantial decrease in S_{Lang}, V_p and d of 10CuY could be attributed to the deposition of copper species into pores and/or external surface sites of support. This deposition of copper species onto external sites further facilitates the grain agglomeration and leads to the formation of copper oxides which has low surface area [Garcia et al. 2011]. The formation of CuO was also supported by XRD studies. Table 4.3 summarizes the change in surface area and pore volume during three consecutive cycles of the best catalyst (7.5CuY). The increase in the surface area is substantial, however, the decrease in the pore volume is very less (decreased from 0.34 to 0.33 cc g^{-1}). The leaching of copper during reaction could easily make the comparatively smoother surface rougher which in turn could increase the specific surface area. Furthermore, a little pore collapse could be the probable reason for the decrease in pore volume.

Table 4.3: Textural parameters of different CuY zeolites with different Cu loadings

Sample name	S_{Lang} (m^2 g^{-1})	V_p (cm^3 g^{-1})	d (Å)
H-Y	567	0.26	9.82
2.5CuY	563	0.24	10.20
5CuY	574	0.24	10.61
7.5CuY	667	0.34	9.80,10-30
10CuY	539	0.25	9.16
7.5CuY(1st cycle)	701	0.33	9.80
7.5CuY(3rd cycle)	702	0.31	9.80

4.2.4. FESEM/EDAX analysis

Fig. 4.4 shows the FESEM images of HY and CuY catalysts. Zeolite appears as agglomerate of irregular polyhedra of size 392-675 nm. No dissimilarity is detected between surface morphologies of HY and CuYs. The surface is smooth without any deposition of copper particles. This implies that copper particles are dispersed homogenously throughout the zeolite samples. As shown in Fig. 4f, EDAX analysis shows the presence of silica, aluminum, oxygen and sodium in different concentration with the largest content of silica.

4.2.5. FTIR analysis

Fig. 4.5 illustrates the FTIR spectra of all the samples in the range 1400-350 cm^{-1}. As reported earlier for rare earth metals [Sousa-Aguiar 1998], impregnation of copper metals brings only small changes in the structure of zeolite Y. The insertion of cations leads to small change of band located

around 900-1130 cm^{-1}, which correspond to asymmetric stretching of Si-O(Al) vibration in tetrahedra or alumino- and silico-oxygen bridges [Garcia et al. 2011].
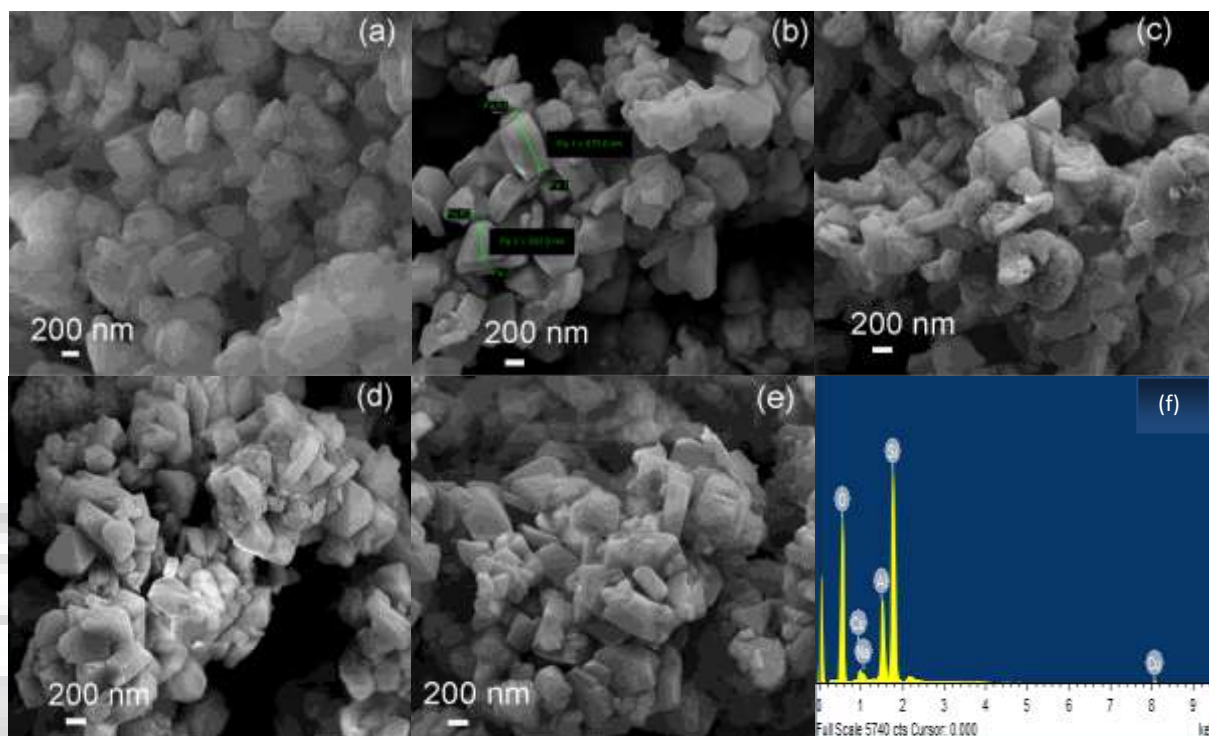
Fig. 4.4: SEM images of (a) HY, (b) 1CuY, (c) 5CuY, (d) 7.5CuY, (e) 10CuY and (f) EDAX of 7.5CuY

This change can be clearly observed in the present case with the shift of this band from 1018 to 1043 cm^{-1} after exchange of sodium form to protonic form. This shift characterized the partial dealumination of framework which is also supported by XRD analysis. Similar effects, i.e., change in intensity or broadening of this band can also be observed as copper content increases. There is minute shift in framework sensitive double ring vibration band, which appear around 577 cm^{-1}. The wavelength of this band can be correlated with framework Si/Al ratio [Peter et al. 2012] and small change in this wavelength signifies small dealumination occurring due to incorporation of copper and calcination at high temperature. The band of Si-OSi bending and symmetrical stretching of $(Si,Al)O_4$ building units have been observed in between 400-550 and 660-860 cm^{-1}, respectively [Wang et al. 2005]. The later band exhibit overlapping and decrease in intensity with increase of copper loading, which signify the interaction of Cu with the external linkage of tetrahedral building units. The bands at 400, 510 and 600 cm^{-1} are attributed to CuO [Andas et al. 2013] and cannot be distinguished in copper containing zeolite due to overlapping with other bands. Further, it may also be observed that zeolite framework remain intact in spite of its use in

three consecutive cycles for heterogeneous Fenton-like reaction. These results were also supported by XRD and N_2 sorption analysis.
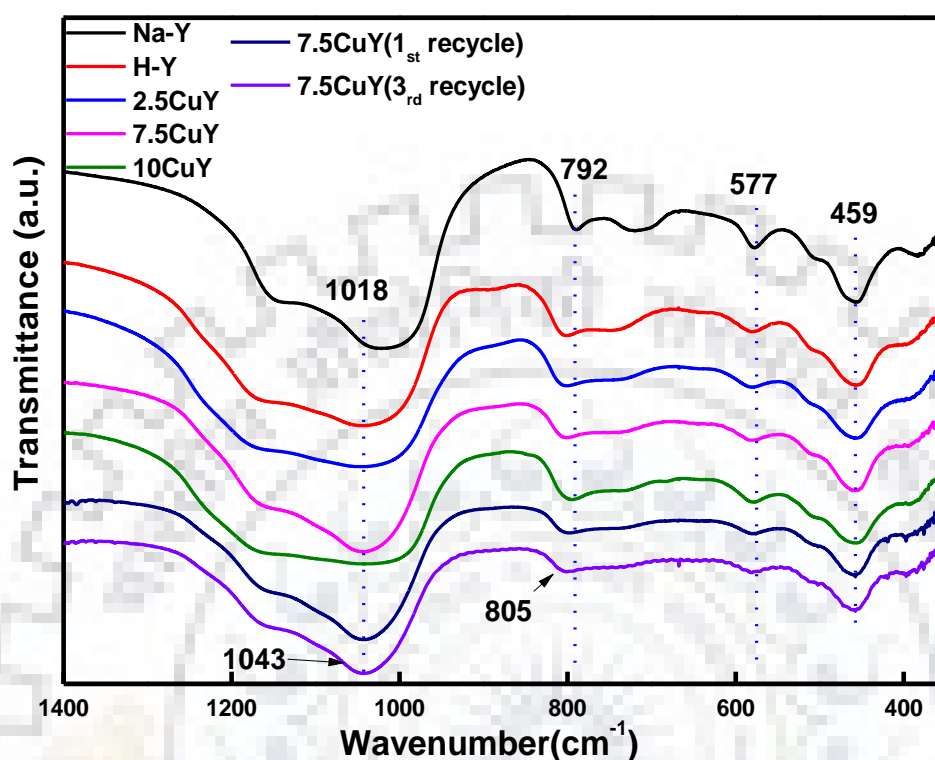
Fig. 4.5: FTIR spectra of all CuY catalysts with different Cu loadings

4.2.6. UV/DRS analysis

Diffuse reflectance UV-vis spectra were recorded to characterize the coordination environment of copper element with zeolite Y. These spectra of copper species were evaluated in term of Kubelka-munk function and shown in Fig. 4.6. Deconvolution of characteristic peak for 7.5CuY (inset of Fig. 4.6) reveals that each spectrum consists of three bands, which represent three types of copper species. The band in low wavelength region (< 250 nm) can be attributed to Cu^{1+} species on the surface [Carvalho et al. 2000]. The most intense band is centered at 270 nm and can be assigned to charge transfer between mononuclear Cu^{2+} and oxygen atoms, where Cu^{2+} only occupy the isolated sites [Kustrowski et al. 2005]. Moreover, a very weak band was found in high wavelength region (>330nm), which suggest the presence of $[Cu-O-Cu]_n$–type cluster differing from bulk CuO [Mendes et al. 1997]. The absorption spectra are marginally dominating into low wavelength region for copper loading ≤ 5 wt% and thus, indicate that Cu^{1+} species are present in a somewhat greater extent. On the other hand for 7.5CuY, the domination of band centered at 270 nm explains a little majority of isolated Cu^{2+} ions. Furthermore, the band intensity increases with increases in

metal loading from 2.5 to 7.5 wt%. This increment is associated with increase of highly disperse copper species which strongly interacts with zeolite Y [Hu et al. 2001]. For further increase in copper loading (>7.5 wt%), band intensity starts decreasing because of the formation of CuO which has weak interaction with zeolite Y and could not be characterized by UV-DRS technique.
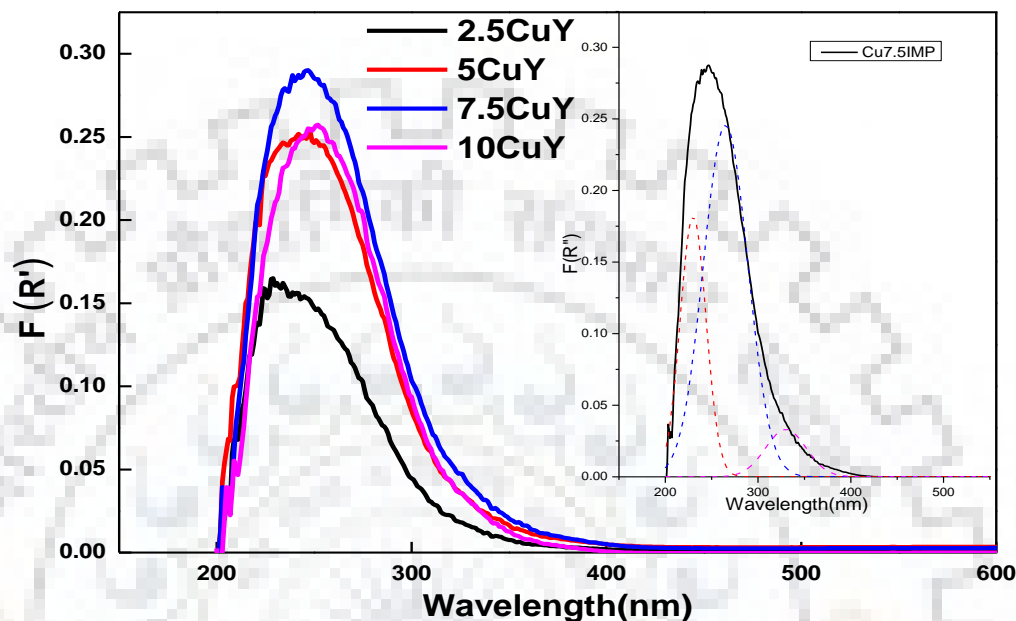
Fig. 4.6: Normalized UV-vis DRS spectrum of copper species on zeolite Y with different Cu loadings and deconvolution of the 7.5CuY peak (inset)

4.2.7. XPS analysis

XPS spectra of CuY reveal the presence of different oxidation states of copper element on the surface of support depending upon the shape and position of Cu 2p peaks, shown in Fig. 4.7. It should be noted that no Cu peaks were observed for loading content < 5 wt% due to low concentration of copper on the zeolite surface. The two peaks at 952.2 and 932.4 eV are due to Cu $2p_{1/2}$ and Cu $2p_{3/2}$, respectively. The energy difference between these two peaks is 19.8 eV, which agrees well with the reported value of 19.8 eV [Ye et al. 2012]. The main peak of Cu $2p_{3/2}$ photoelectron of both samples comprises from overlapping of two maxima at binding energies 932.6 eV and 933.4 eV which can be attributed to Cu^{1+} and Cu^{2+} states, respectively [Zhang et al. 2007]. These results are in good agreement with UV-vis DRS technique, which also reveal co-existence of both states. The formation of Cu^{1+} species occurs due to auto-reduction of Cu^{2+} to Cu^{1+} during heat treatment. The shape of photoelectron spectrum of 10CuY can be attributed to CuO being in agreement with previous reported literature [Espinos et al. 2002]. The presence of CuO has already been observed using XRD. Moreover, peaks at energy values 940.87 and 942.85 eV can be

assigned to shake up satellites, which characterize the d^9 configuration in the ground state, i.e., Cu^{2+} [Karthikeyan et al. 2016]. The slightly higher coverage area of Cu $2p_{3/2}$ photoelectron peak and satellite peaks indicate the presence of Cu^{2+} species in major extent for 10CuY samples [Espinos et al. 2002]. For sample 7.5CuY, Cu^{1+} and Cu^{2+} states have been observed in equal extent because of absence of satellite peaks.
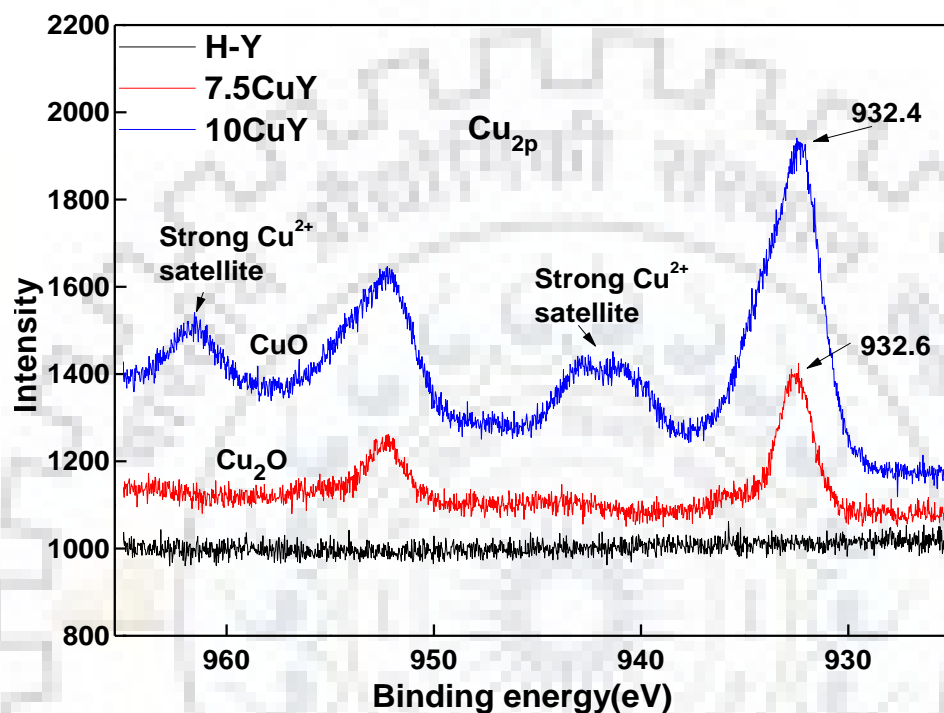
Fig. 4.7: XPS data of copper species on zeolite Y with different Cu loadings

4.3. CATALYTIC ACTIVITY STUDIES

4.3.1. Role of different mechanisms

In order to explain the roles of different non-catalytic and catalytic mechanisms in the degradation of Congo red, various experiments were designed as highlighted in Fig. 4.8. As shown in figure, H_2O_2 alone could not remove the color significantly because of its low oxidation potential ($E_0 = 1.78$ V vs. NHE) [Hassan et al. 2011]. The effect of adsorption of dye was observed by running an experiment at the same condition with 7.5CuY but without H_2O_2. The color removal is about 28%. This behavior may be attributed to hierarchical porosity which allows large molecules of Congo red dye to enter into pores of zeolite. Furthermore, catalytic activity of HY was observed due to the presence of iron (0.65 wt%, XRF analysis), which could also contribute into catalytic activity. A slightly higher removal (4%) was observed as compare to H_2O_2 alone. This inefficiency might be due to presence of extra-lattice iron (III) oxide cluster, which are inactive

towards H_2O_2 to generate hydroxyl radicals [Taran et al. 2013]. The contribution of homogenous Fenton-like reaction has been explained in terms of catalytic activity of leached Cu ions (8.67 mg L^{-1}), which were detected in filtered solution after first run of fresh catalyst. The decolorization efficiency of leached copper ions was only 20% after 120 min which is very less as compared to 98% decolorization efficiency of heterogeneous copper catalyst. Fig. 4.8 clearly depicts that heterogeneous system (CuY + H_2O_2) is much faster than the homogenous system. Thus, the higher catalytic activity might be attributed to the synergic effect between adsorption and Fenton-like catalysis. The low activity of homogenous system might be due to leaching of those copper species, which are inactive towards activation of H_2O_2. Hence, it can be concluded that the key role in overall degradation of Congo red is played by the adsorption of dye and reaction of H_2O_2 with the copper species available on the surface of zeolite Y.
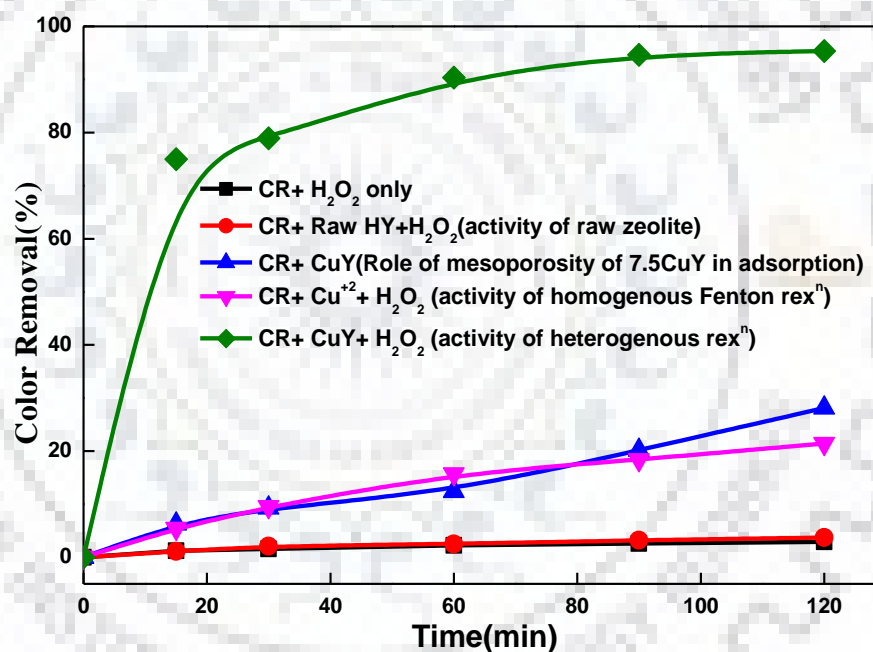
Fig. 4.8: Contribution of various mechanisms in catalytic activity of 7.5CuY at pH = 7, [H_2O_2] = 52.24 mM, Catalyst = 1 g L^{-1}, T = 60 °C, and dye = 0.143 mM

4.3.2. Mechanistic view of the mineralization of congo red dye

The reaction path for the generation of reactive species and mineralization of dye has been discussed in this section. As depicted in Fig. 4.9, the reaction majorly proceeds *via* one electron transfer from the reduced form of copper to oxidant and oxidant to the oxidized form of copper with simultaneous generation of hydroxyl radical (*OH) and perhydroxyl radical (HO_2*) [Liang et al. 2010]. Thus, hydrogen peroxide participates as an oxidizing agent as well as reducing agent

(Eq. 4.1 and 4.2). It is well reported that *OH radical is the responsible species for the mineralization of organic pollutant [Hassan et al. 2011]. HO_2* does not play significant role in degradation of organic pollutant due to its lower oxidation potential than *OH [Dantas et al. 2006].

$$Cu^{1+}/zeolite\ Y + H_2O_2 \rightarrow Cu^{2+}/zeolite\ Y + OH^* + OH^- \tag{4.1}$$

$$Cu^{2+}/zeoliteY + H_2O_2 \rightarrow Cu^{1+}/zeoliteY + HO_2^* + H^+ \tag{4.2}$$
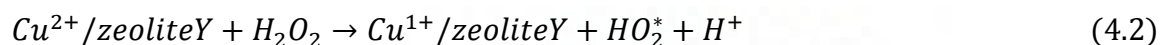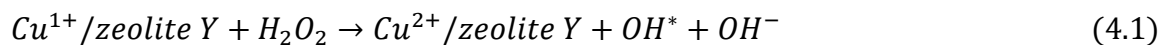
Hydroxyl radical, formed during the above reactions, further attack the azo group (-N=N-) and naphthalene rings, and finally mineralize it into CO_2, H_2O and mineral acid.
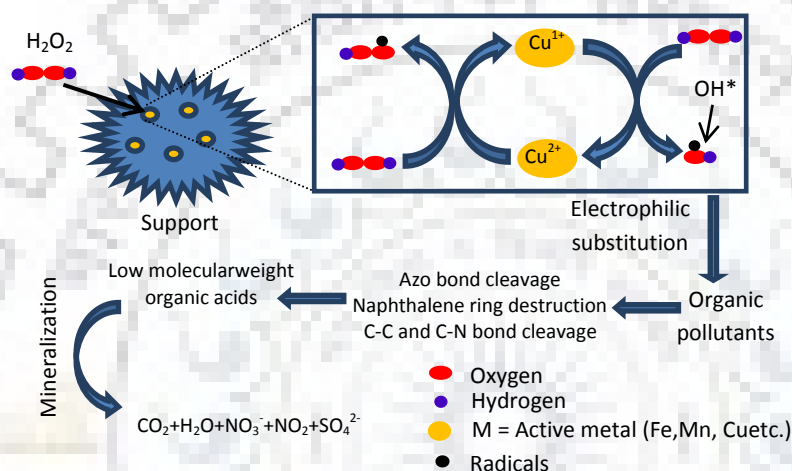
Fig. 4.9: Schematic diagram of catalytic activity of copper impregnated zeolite Y for mineralization of Congo red dye

In order to identify the different intermediate products, the HPLC analysis was performed at 497 and 343 nm. As shown in Fig. 4.10 and 4.11 for HPLC chromatograms, the peak for Congo red emerge at 6.15 min. Characteristics peaks for both bands diminish with increase in reaction time and thus, signify rapid degradation of dye molecule. A faster cleavage of azo bond in comparison to degradation of naphthalene rings can also be clearly observed. However, no intermediate products were identified. In order to further confirm the mineralization of dye molecules, the concentration of NO_2^-, NO_3^- and SO_4^- were measured by ion chromatography (Fig. 4.12). After 4 h of reaction time, the concentrations of NO_2^-, NO_3^- and SO_4^{2-} were measured 3.2, 7.4 and 6.9 mg L^{-1}, respectively. According to nitrogen balance, approximately 70% of total nitrogen converted into N_2 gas.
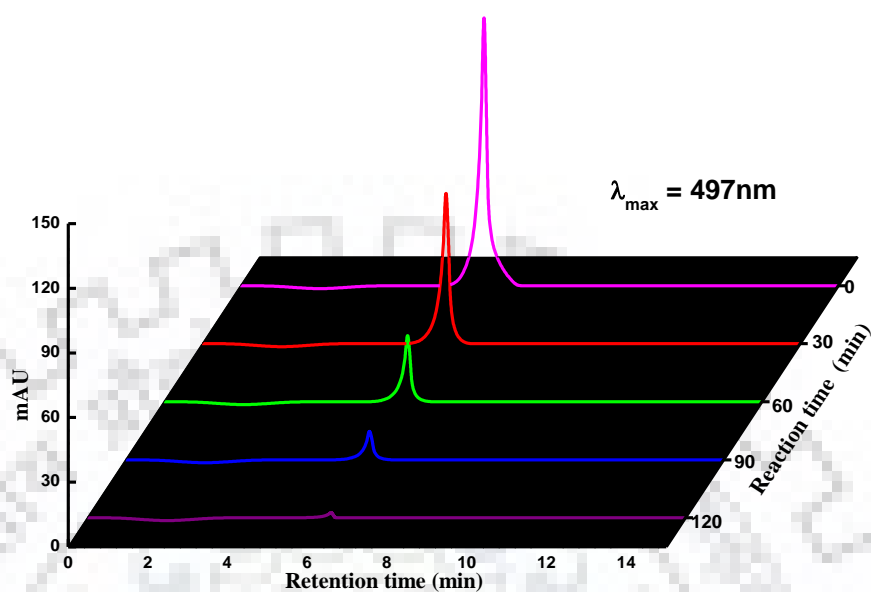
Fig. 4.10: HPLC chromatogram for identification of degradation product at 497 nm (λ$_{max}$)
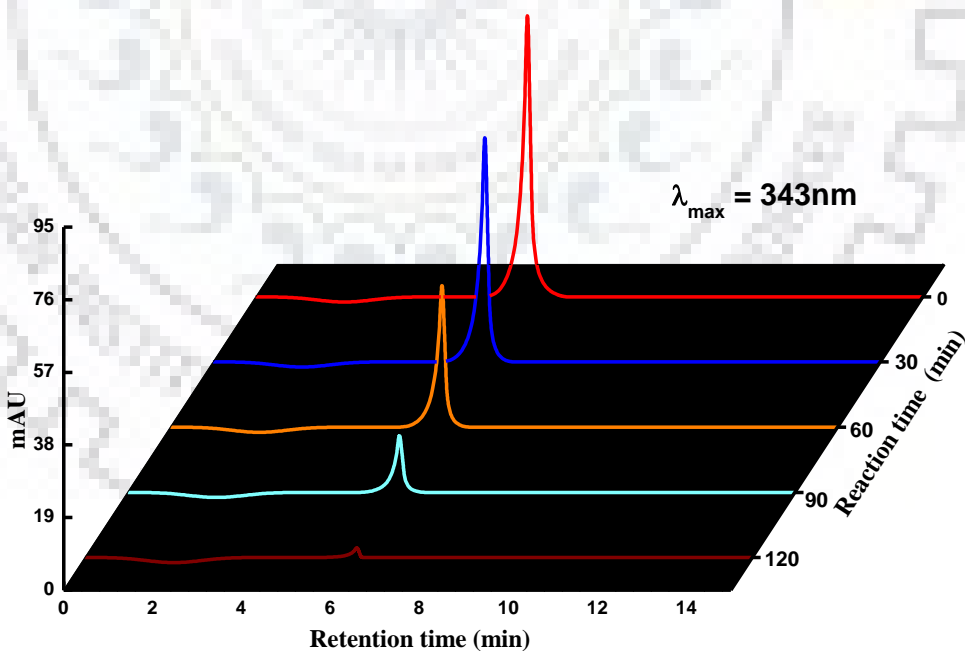
Fig. 4.11: HPLC chromatogram for identification of degradation product 343 nm (λ$_{max}$)

Various side reactions occur simultaneously during activation of H_2O_2. These reactions influence degradation efficiency depending upon several reaction parameters, such as, active phase

concentration, oxidant concentration and pH. A clear insight about complexity of side reactions has been presented *via* Eq 4.3-4.7. A detail study of effects of abovementioned parameters on decolorization, degradation and mineralization has been shown in forthcoming sections.

$$OH^* + 2OH^- \quad \rightarrow \quad HO_2^* + H_2O \tag{4.3}$$

$$OH^* + OH^* \quad \rightarrow \quad 2OH^- \tag{4.4}$$

$$H_2O_2 + OH^* \quad \rightarrow \quad HO_2^* + H_2O \tag{4.5}$$

$$Cu^{y+} + OH^* \quad \rightarrow \quad Cu^{(y+1)+} + OH^- \tag{4.6}$$

$$2H_2O_2 \quad \rightarrow \quad O_2 + 2H_2O \tag{4.7}$$
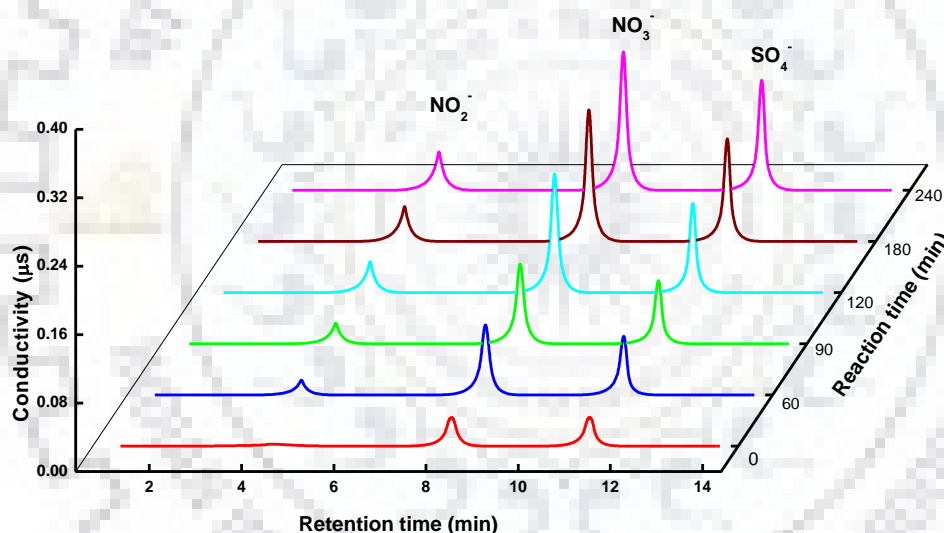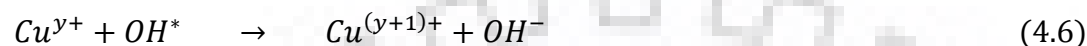
Fig. 4.12: Ion chromatogram for measurement of mineralize products

4.3.3. Effect of copper loading

As shown in previous sections, the copper species provide active centers for the activation of H_2O_2 and consequently degradation of dye. In this section, the influence of Cu loading (1-10 wt%) on catalytic activity as well as stability has been studied using 1 g L^{-1} of the catalyst. Dye degradation has been found to increase up to 7.5CuY with the maximum dye degradation of 93.58% at 150 min (Fig. 4.13a). However, dye removal decreases with further increase in copper loading. In general, the dye degradation occurs at faster rate up to 90 min and thereafter, become slower during 90 to 150 min. During the course of reaction, the color of solution changed from its initial dark red to

fuchsia and finally the fuchsia color disappeared into colorless solution. The degree of decolorization increases from 89% to 99% with an increase in copper loading from 1 to 5 wt% and decreases for Cu loadings greater than 7.5 wt% (Fig. 4.13b). Interestingly, no induction period was noticed and high initial oxidation rate was observed.

Fig. 4.13: Effect of copper loading on (a) dye degradation, (b) color removal, and (c) TOC, leached copper concentration and copper extent at pH = 7, [H₂O₂]= 52.24 mM, catalyst = 1 g L⁻¹, T = 60 °C, and [dye] = 0.143 mM

Several researchers have reported induction period, which was the result of time needed for surface activation of metal species (reduction to lower oxidation state) and/or for dissolution of enough metal for starting of homogenous reaction [Park et al. 2002; Luo et al. 2009]. This result

further supports that the CuY contains sufficient quantity of active sites (Cu^{1+}) for the quick generation of highly reactive hydroxyl radical and thus the heterogeneous Fenton like reaction majorly contribute to catalytic activity. Moreover, higher activity has been found as compared to CuFeZSM-5, which provided 45% degradation and 34% TOC removal from dye solution after 2 h at neutral condition [Dükkanci et al. 2010].

As can be seen from Fig. 4.13c, TOC removal increases with Cu concentration up to 7.5CuY and decreases for 10CuY. A maximum TOC removal of 79.52% has been obtained for 7.5CuY at 4 h. The maximum overall catalytic activity of 7.5CuY can be attributed to well disperse $Cu^{1+/2+}$ species, the highest surface area (667 m^2 g^{-1}) and hierarchical porosity. These properties are responsible for effective generation of highly reactive hydroxyl radicals (*OH) from hydrogen peroxide. However, 10CuY contains CuO phase in major extent, which is responsible for the blockage of pores of zeolite and lesser activity of catalyst [Dükkanci et al. 2010]. Due to highest catalytic activity, 7.5CuY was selected as optimum loading for oxidation of congo red dye and used for further studies of the optimization of operating parameters. As shown in Fig. 4.13c, leaching of copper increased with increase in metal loading. However, copper extent in aqueous solution decreases with metal loading. Kim et al. [2007] reported similar behavior for copper content. At the end of experiments (4 h), final pH of treated solutions was also measured and found varying in the range 5.2 to 5.8 for different catalysts.

4.3.4. Effect of pH

The influence of initial pH (5-11) on dye degradation and decolorization degree is presented in Fig. 4.14a and 4.14b, respectively. The maximum dye degradation of 93.58% has been observed at neutral condition within 150 min. The dye removals at pH 5, 9 and 11 are 83.58%, 89.56% and 35.46%, respectively. For pH = 5, the dye degradation occurs at fastest rate up to 45 min but surprisingly become slower after that as compared to other pH conditions. Similar trend has been observed for decolorization rate at pH 5 up to 30 min which become slow from 30 to 120 min. This behavior can be explained by the consideration of point of zero charge (pH_{pzc}), measured in the range 6-8. At pH < pH_{pzc}, surface become more acidic due to presence of protons which result into fast formation of *OH [Valkaj et al. 2011] and thus, exhibited fast catalytic activity up to 30 min. However, excessive leaching of active species might occur after 30 min due to continuous decrement in pH and result into slow rate of degradation from 30 to 150 min. In contrast to it, fast degradation has been found at initial pH = 9 after 60 min. It may occur due to shifting in pH of the

reaction solution towards neutral condition (inset of Fig. 4.14c). The maximum color removal of 95.34% is noticed for neutral pH at 120 min. It has been observed that color removal is more than degradation of naphthalene rings.

Fig. 4.14: Effect of initial pH on (a) dye degradation, (b) color removal, and (c) TOC, leached copper concentration and copper extent of 7.5CuY at [H$_2$O$_2$] = 52.24 mM, catalyst = 1 g L^{-1}, T = 60 °C, and [dye] = 0.143 mM. Final pH at different initial pH values have been shown in inset of Fig. 4.14c

Fig. 4.14c shows that the TOC removal increases from 53.46 to 79.52% with increase in pH from 5 to 7 and a further increase in pH results in significant decrease in TOC removal from

70.35 to 25.84. Similar results were also reported by other researchers using copper in homogenous Fenton-like reaction [Lin et al. 2005; Zhana et al. 2010]. The decrement in catalytic activity at higher alkaline condition can be explained on the basis of two aspects. First, OH^- reacts with *OH to form HO_2, which has very low reactivity with organic contaminants (Eq. 4.3) [Nezamzadeh-Ejhieh et al. 2011]. Second, H_2O_2 decompose into H_2O and O_2 at higher pH (Eq. 4.7) [Ahmed et al. 2015]. Leaching of copper species was mainly influenced by initial pH as compared to other operating variables. The catalyst shows lowest stability towards leaching at pH ≤ 5 (Fig. 4.14c). Leached copper concentration (mg L^{-1}) and copper extent (%) decreased from 13.85 mg L^{-1} to 2.73 mg L^{-1} and 28.49% to 5.60% with increase in initial pH from 5 to 9, respectively. However, a small increment of leached copper concentration at highly alkaline condition (pH = 11) can be attributed to exchange of copper with sodium due to addition of high amount of NaOH to increase the pH. The final pH of reaction solution was also measured at different initial pH conditions and a decrement was noticed for all values (inset of Fig. 4.14c). This decrement can be attributed to the formation of organic acid intermediates, HNO_3 or H_2SO_4 from sulfonate groups of dye [Karkmaz et al. 2004]. Considering high mineralization, low leaching and final pH obtained near neutralized conditions, initial pH = 7 was used in subsequent studies. To further check the effect of different intermediates, experiments were run at initial pH = 7 without adding dye. A negligible copper concentration (0.34 mg L^{-1}) was found in aqueous solution after 4 h. This experiment has made clear that the intermediates of reaction exhibit major contribution to copper leaching.

4.3.5. Effect of H_2O_2 concentration

H_2O_2 is the source of reactive *OH radicals in the heterogeneous Fenton-like reaction and thus, directly control the concentration of radicals for the degradation of the dye molecules. The concentration of H_2O_2 has been varied in multiples of stoichiometric amount, which is required for the complete mineralization of 0.143 mM solution of Congo red (Eq. 4.8).

$$C_{32}H_{22}N_6Na_2O_6S_2 + 91H_2O_2 \rightarrow 32CO_2 + 98H_2O + 6HNO_3 + 2NaHSO_4 \qquad (4.8)$$
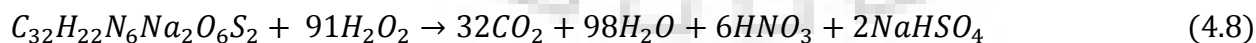
Fig. 4.15a depicts that the dye degradation increases from 81.47 to 93.58% with increase in H_2O_2 concentration from 13.06 to 52.24 mM. Similarly, degree of decolorization increases from 85.38 to 95.34% with an increase in H_2O_2 from 13.06 to 52.24 mM H_2O_2 (Fig. 4.15b). However, a negative

effect has been observed on degradation and decolorization degree with further increase in H_2O_2 concentration.

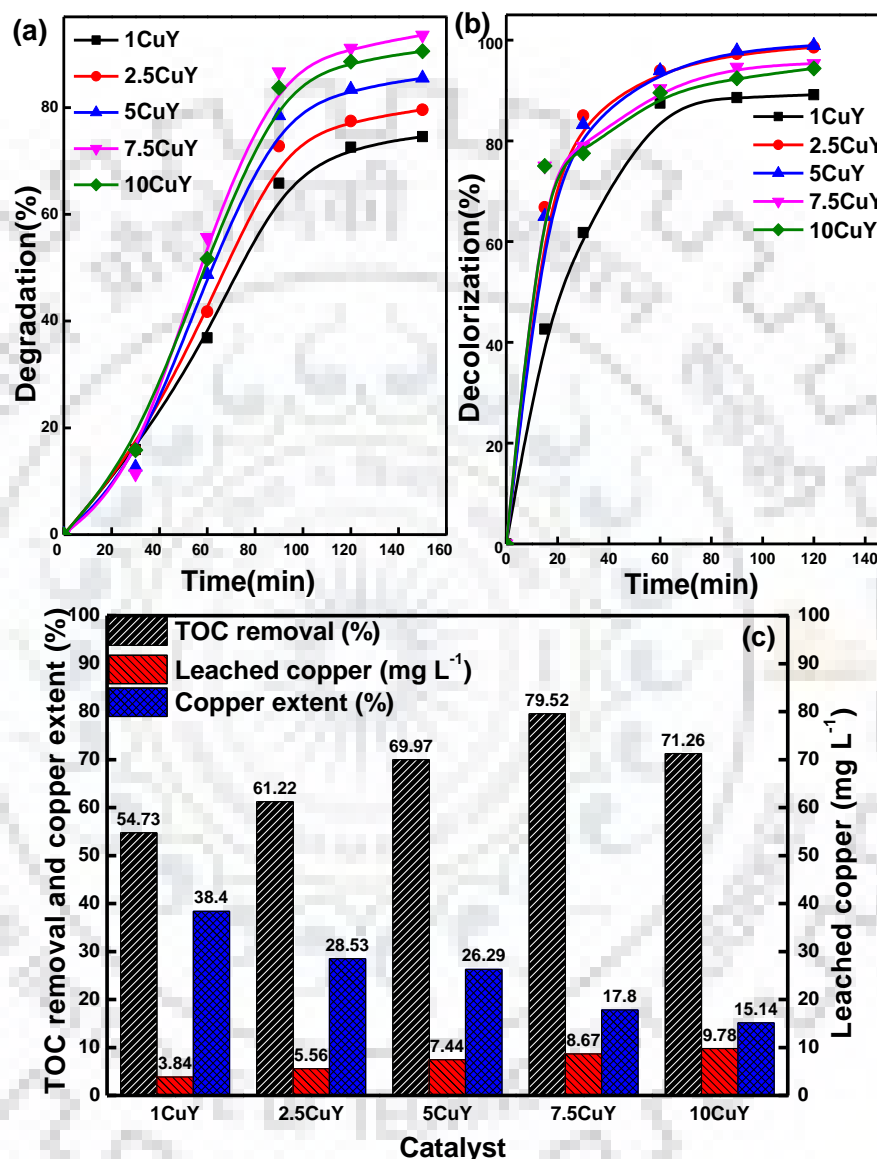**Fig. 4.15: Effect of H_2O_2 concentration on (a) dye degradation, (b) color removal, and (c) TOC, leached copper concentration and copper extent of 7.5CuY at pH = 7, catalyst = 1 g L^{-1}, T = 60 °C and [dye] = 0.143 mM**

As observed in Fig. 4.15c, the TOC removal increases gradually from 59.29 to 79.52% with an increase in H_2O_2 concentration from 13.06 to 52.24 mM which become constant with further increment up to 104.48 mM and thereafter starts decreasing. This decrease in catalytic activity for $H_2O_2 > 104.48$ mM can be attributed to undesirable scavenging of *OH radicals with

itself (Eq. 4.4) or by the excessive H_2O_2 (Eq. 4.5) [Zhana et al. 2010]. The excess quantity of H_2O_2 results into formation of HO_2*, which has low oxidation potential [Zhana et al. 2010]. Thus, H_2O_2 molar concentration of 52.24 mM has been considered as optimum reaction condition. Fig. 4.15c also depicts the leached copper concentration, copper extent and final pH as a function of H_2O_2 dosages. Unexpectedly, a lesser influence of H_2O_2 concentration has been observed as compared to other operating parameters. Leached copper concentration and copper extent has been found to vary in the range 7.25–9.42 mg L^{-1} and 14.88–19.34%, respectively, even after using H_2O_2 concentration 12 times of stoichiometric amount. Similar results were also observed by Melero et al. [2007] and Herney-Ramirez et al. [2010] in case of Fe_2O_3 supported over SBA-15 and clay, respectively. The final pH was observed closer to initial pH for 52.24 mM H_2O_2, which might be attributed to higher mineralization of acidic intermediates.

4.3.6. Effect of catalyst concentration

Experiments were conducted with different amount of 7.5CuY catalyst to obtain optimum catalyst concentration (to get maximum catalytic activity). The effect of catalyst concentration (varied in the range 0.5–2 g L^{-1}) on dye degradation and decolorization has been shown in Fig. 4.16a and 4.16b, respectively. It can be seen that dye degradation increases from 79.11 to 91.13% (in 2 h) with increase in catalyst concentration from 0.5 g L^{-1} to 1 g L^{-1} and further increase in loading result in decrease in degradation to 81%. On the other hand, the degree of decolorization decreases continuously with increase in catalyst concentration from 0.5 g L^{-1} to 2.0 g L^{-1}. Similar results for decolorization has been mentioned at high copper loading (≥5 wt%) and thus, it can be concluded that low copper loading favor the high decolorization degree. TOC removal increases from 58.48 to 79.52% with increase in catalyst concentration from 0.5 to 1 g L^{-1} (Fig. 4.16c). This behavior can be attributed to increased availability of active sites on zeolite Y for the activation of H_2O_2 [Ramirez et al. 2007]. The TOC removal, however, started decreasing with further increase in catalyst amount (>1 g L^{-1}), which is attributed to increase in rate of decomposition of H_2O_2 to O_2 due to thermodynamic and mass transfer factors [Andas 2013]. Moreover, quenching of *OH radicals with excess Cu ions may also be responsible for such trend (Eq. 4.6) [Lyu et al. 2015]. Thus, catalyst concentration of 1 g L^{-1} was taken as optimum value. As expected, the leached copper concentration increases from 7.52 to 12.81 mg L^{-1} with increase in catalyst concentration from 0.5 g L^{-1} to 2.0 g L^{-1}. However, the copper extent decreases (Fig. 4.16c). The final pH (t = 4

h) was measured to be more acidic for catalyst concentration of 0.5 and 2.0 g L^{-1} due to incomplete mineralization of acidic intermediates in reaction solution.
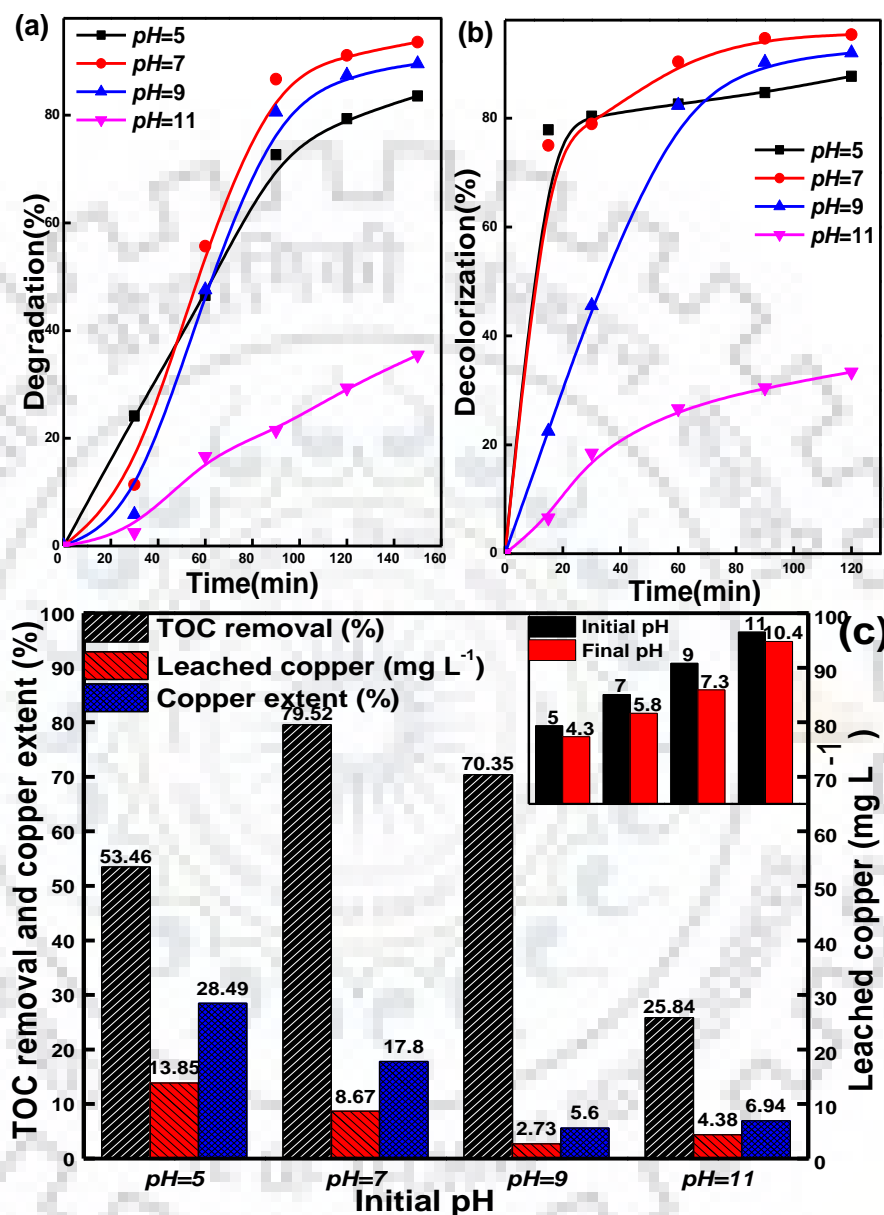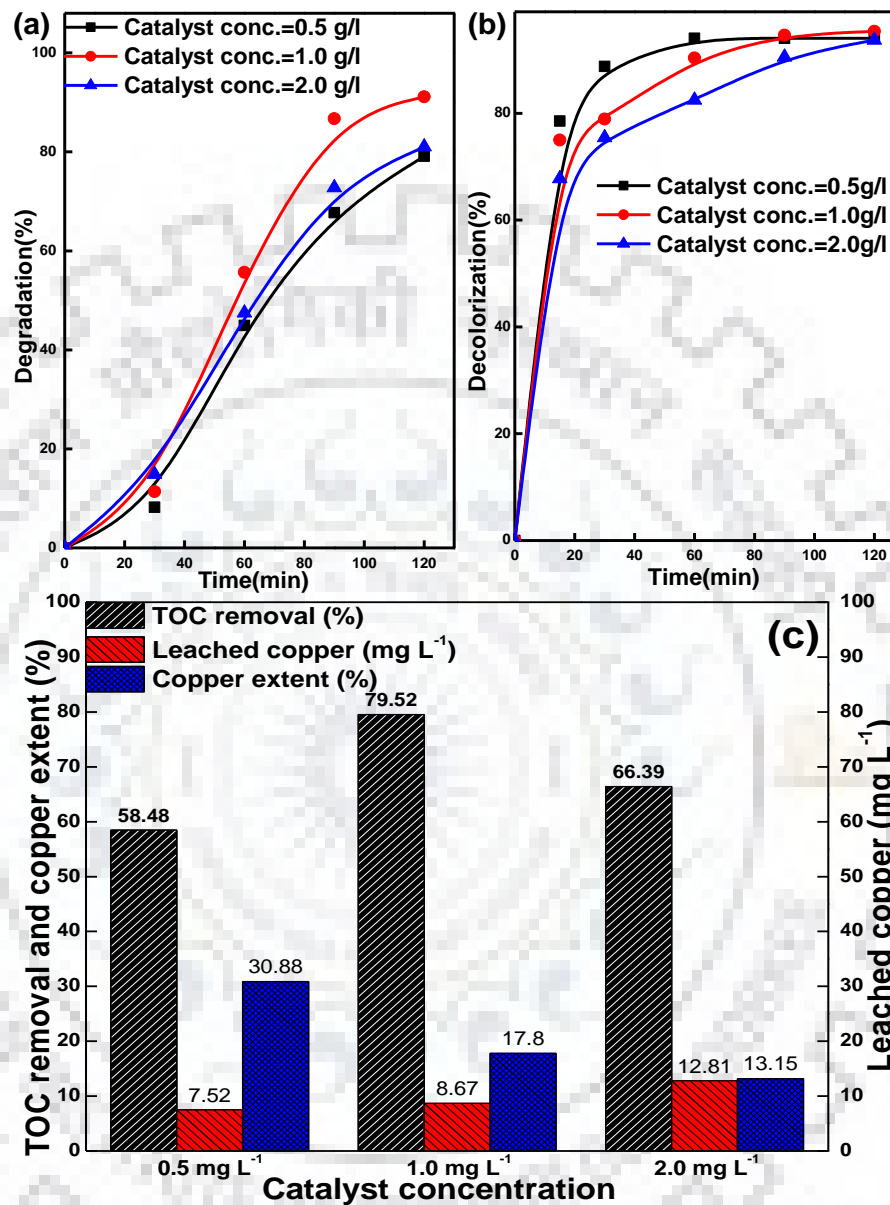

Fig. 4.16: Effect of catalyst concentration on (a) dye degradation, (b) color removal, and (c) TOC, leached copper concentration and copper extent of 7.5CuY at pH = 7, [H$_2$O$_2$] = 52.24mM, T = 60°C and [dye] = 0.143 mM

4.3.7. Effect of reaction temperature

Fig. 4.17a and 4.17b presents the plot of degradation and decolorization of Congo red as a function of temperature in the range 25–60 °C, respectively. Dye degradation increases proportionally with increase in temperature. Dye degradation of 55.42, 79.02 and 93.58% has been measured at 25, 40

and 60 °C, respectively. Similar trend is also followed by decolorization degree with maximum value of 95.34% at 60 °C. This phenomenon can be attributed to increase in decomposition of H_2O_2 into highly reactive *OH radicals with increase in temperature [Rusevova et al. 2014]. Fig. 4.17c depicts that the TOC removal has increased drastically from 37.42 to 79.52% with increase in temperature from 25 to 60 °C. Higher catalytic activity with mild rise in temperature suggests suitability of this catalyst for practical applications. As expected, leaching of copper species was also affected with reaction temperature.
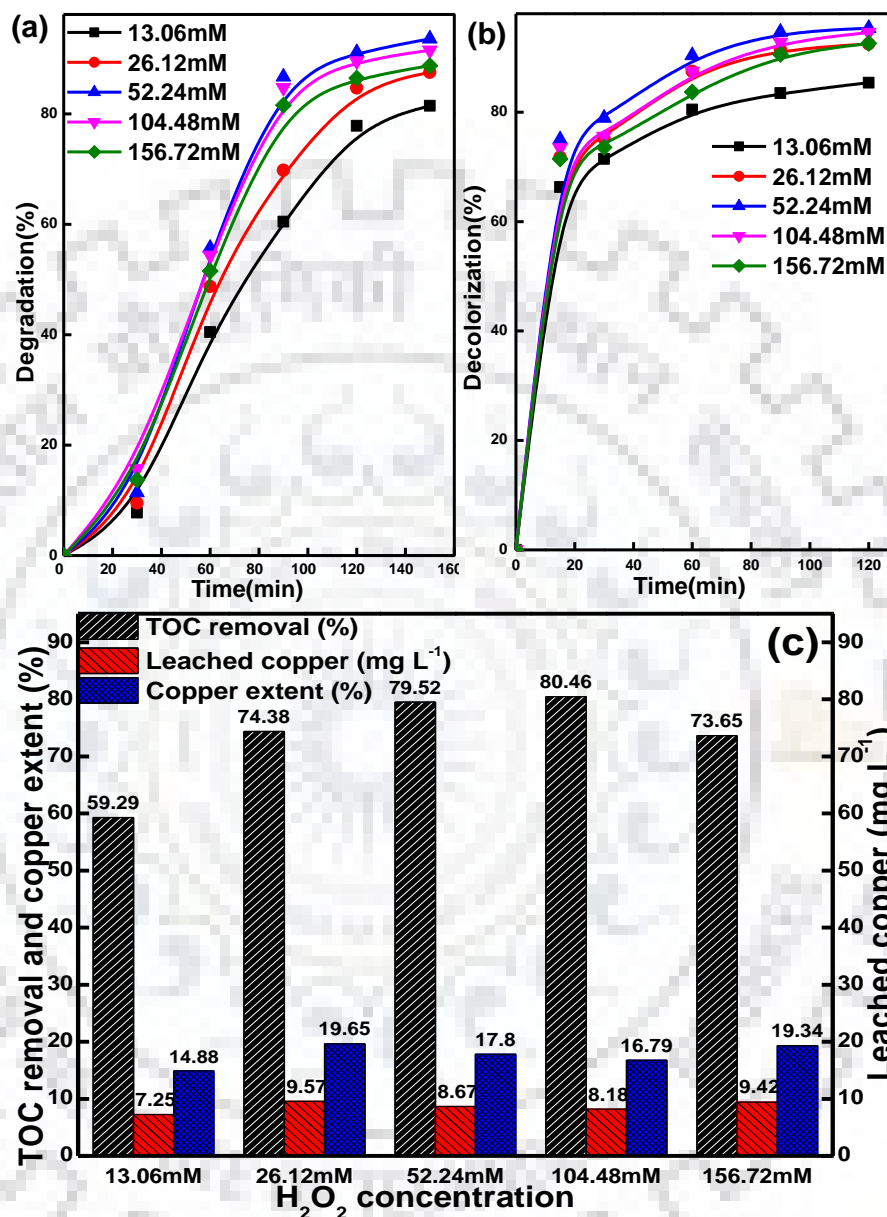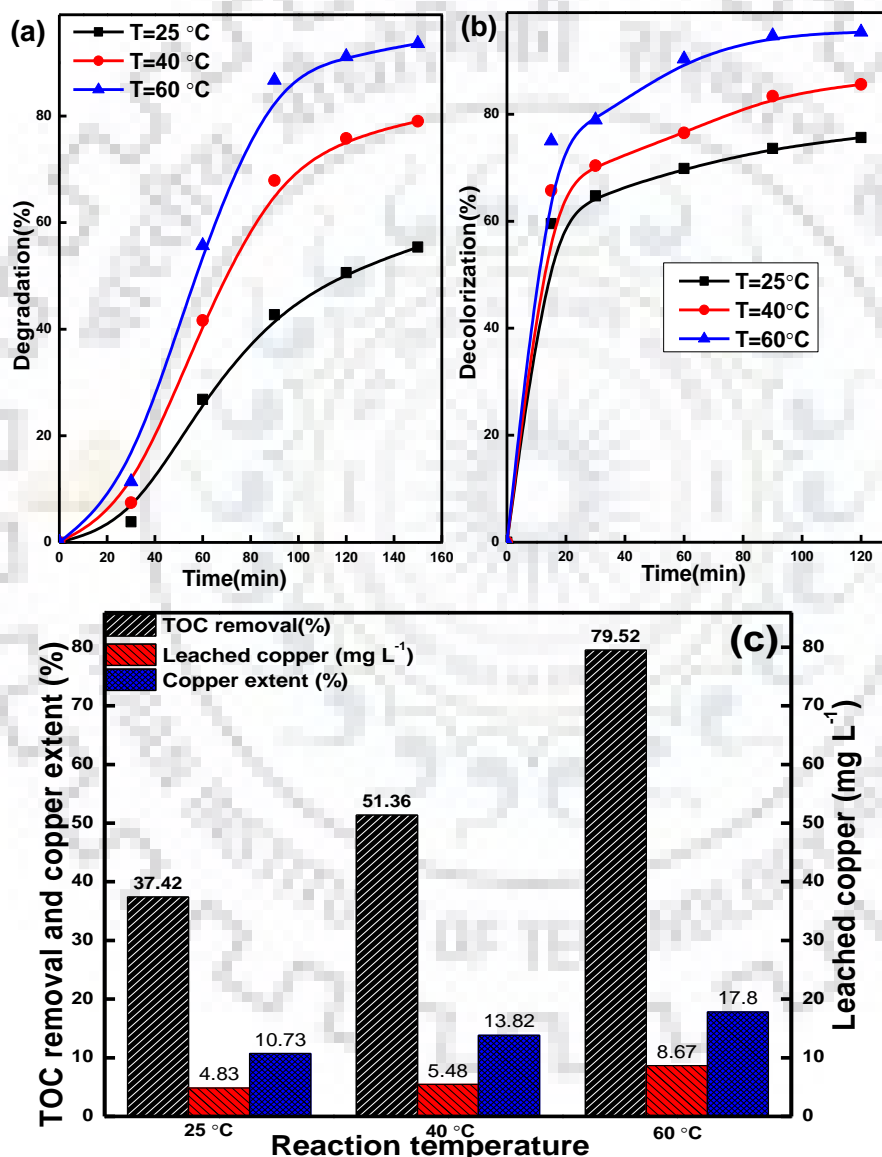

Fig. 4.17: Effect of temperature on (a) dye degradation, (b) color removal, (c) TOC, leached copper concentration and copper extent of 7.5CuY at initial pH = 7, [H₂O₂] = 52.24 mM, catalyst = 1 g L⁻¹ and [dye] = 0.143 mM

As shown in Fig. 4.17c, leached copper concentration (mg L^{-1}) and copper extent (%) increase from 4.83 mg L^{-1} to 8.67 mg L^{-1} and 10.73% to 17.80% with increase in temperature from 25 to 60 °C, respectively. The final pH of reaction solution was also measured at different temperature and a decrement was noticed from 6.2 to 5.3 with increase in temperature from 25 to 40 °C. Large decrement in final pH at 40 °C indicates high concentration of acidic intermediates. However, final pH at 60 °C was observed more close to initial neutral condition due to higher mineralization of the acidic intermediates. Due to high mineralization and final pH obtained near neutral pH condition, all experiments were carried out at 60 °C.

4.3.8. Kinetic studies

In order to examine the kinetic behavior of reaction, degradation and decolorization profiles have been fitted to a first order kinetic model [ln(1/(1 − x)) vs. time], where x is degradation or decolorization fraction. As shown in Fig. 4.18a and 4.18b, this model fitted well to both the profiles with $R^2 > 0.94$. Rate constants are estimated from the slope of straight lines as a function of temperature and value of fitting parameters (R^2) are given in Table 4.4. Rate constant (k_d) for dye degradation increases with increase in temperature and exhibited maximum value of rate constant 0.01892 min^{-1} at 60 °C. Decolorization shows two stage first order kinetics for all temperature conditions [Xu et al. 2011]. The decolorization rate was found to be very fast for the initial 15 min followed by slower rate from 15 to 120 min. Rate constants and R^2 for both steps are shown in Table 4.4. Assuming the slowest step of reaction as the rate determining step, activation energies of dye degradation and decolorization were calculated from Arrhenius equation (plots of ln k vs. 1/T) (Fig. 4.18c and 4.18d).

Table 4.4: Kinetic parameters for degradation and decolorization of dye at different temperatures

| Temperature (°C) | Degradation | | Decolorization | | | |
| | | | Fast step | | Slow step | |
	k_d (min^{-1})	R^2	k_{c1} (min^{-1})	R^2	k_{c2} (min^{-1})	R^2
25	0.0056	0.98	0.0564	0.98	0.0054	0.95
40	0.0109	0.97	0.0671	0.98	0.0080	0.98
60	0.0189	0.96	0.0886	0.99	0.0170	0.94

Activation energy (E_a) and frequency factor (k_0) obtained for dye degradation were 28.64 kJ mol^{-1} and 608.70 min^{-1}, respectively. However, activation energy and frequency factor for

decolorization were 27.21 kJ mol^{-1} and 303.20 min^{-1}. These values of E_a are similar to E_a of oxidation of azo dyes, i.e., 35.9 kJ mol^{-1}for decolorization over Fe^0 and 25.2 kJ mol^{-1} for decolorization in homogenous Fenton reaction [Xu et al. 2008; Fan et al. 2009].
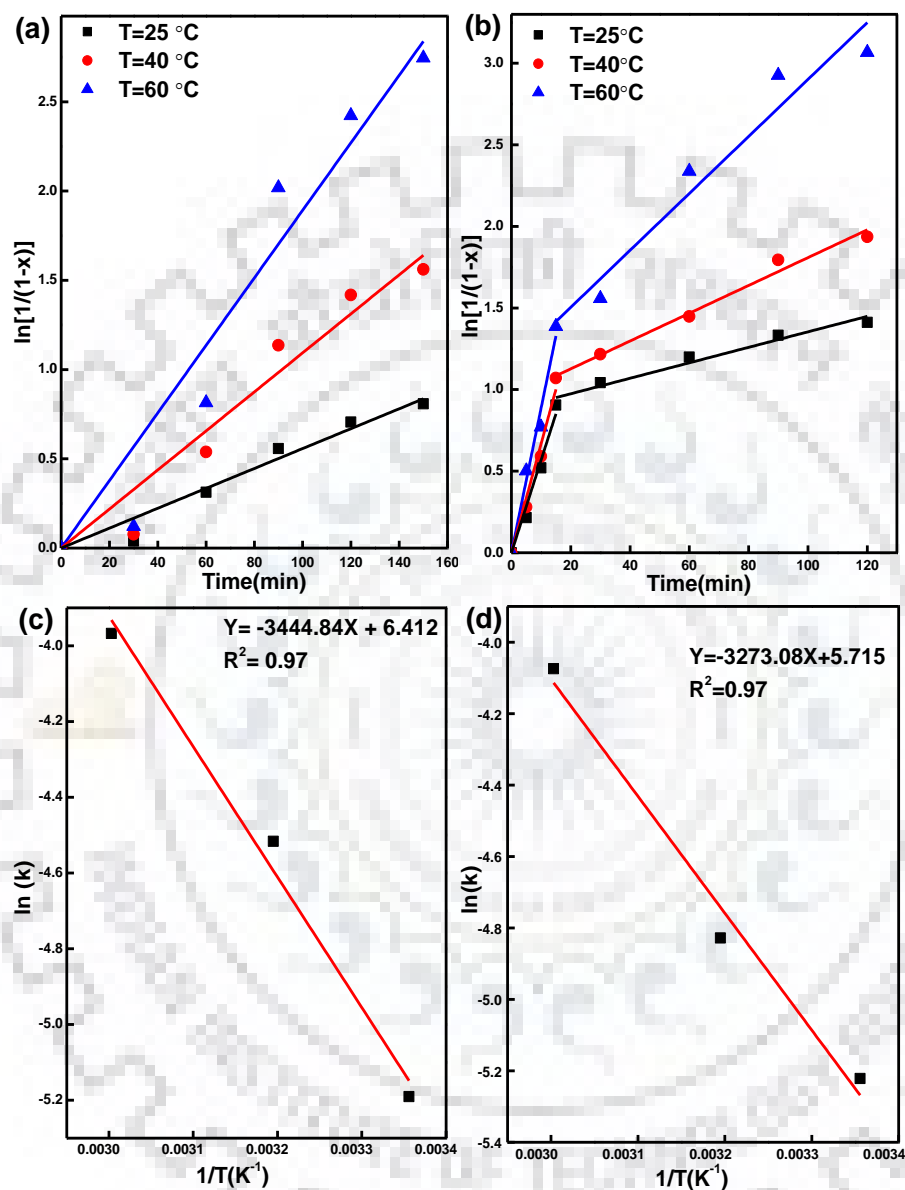
Fig. 4.18: Kinetic study plots of degradation and decolorization of Congo red dye

4.3.9. Reusability of catalyst

The reusability of catalyst is a parameter of vital importance from industrial perspective. The reusability potential of CuY has been evaluated on the basis of catalytic performance as well as stability of framework during three consecutive cycles. As illustrated in Fig. 4.19 and Table 4.5, the catalyst during its second cycle has higher catalytic activity as compared to fresh catalyst with maximum degradation, decolorization and mineralization of 97.85, 98.57 and 83.26%,

respectively. This higher catalytic efficiency may be due to removal of framework impurities during first cycle. However, the catalytic efficiency slightly decreases in third cycle. Stability of framework has been tested in term of leaching of copper species, stability of crystal structure and pore blockage. The concentration of leached copper in solution was 8.67 mg L^{-1} after first run of catalyst (Table 4.5). The pH of effluent was 5.8 and required neutralization before discharge in reservoirs. As per the Eh-pH diagram, the copper ion precipitates out at pH = 7 with copper solubility is <1 mg L^{-1}at pH = 7. The precipitated copper was easily separated out and thus, the copper concentration was obtained below permissible limit of Indian Standard (3 mg L^{-1}) [CPCB 2018].
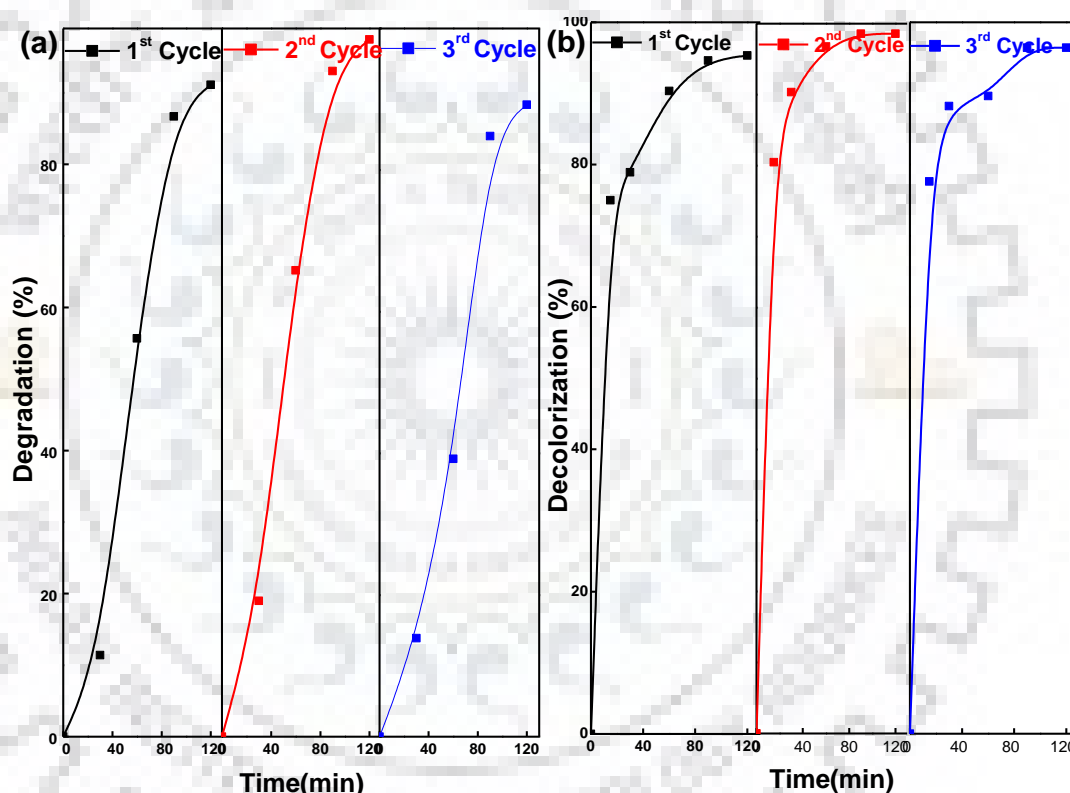
Fig. 4.19: Reusability test of 7.5CuY catalyst at optimized condition

Table 4.5: TOC removal, leached copper content, copper extent and final pH up to 3rd cycle of catalyst

No. of cycles	TOC removal (%)	Leached copper concentration (mg L^{-1})	Copper extent (%)	Final pH
1$_{st}$ cycle	79.52	8.67	17.80	5.8
2$_{nd}$ cycle	83.26	6.69	16.72	5.9
3$_{rd}$ cycle	73.48	4.93	14.80	5.7

As shown earlier in XRD and FTIR studies (Fig. 4.1b and 4.5), no change were observed in zeolite framework during multiple uses. The surface area, pore volume and pore size were almost similar to fresh catalyst during its repeated use (Table 4.3). These results reveal high catalytic performance as well as high stability of copper impregnated zeolite Y in degradation of toxic pollutants.

4.4. SUMMARY

A facile wet impregnation method was used for the synthesis of copper-containing zeolite Y. Zeolite Y immobilized with different concentrations of copper showed promising catalytic activity for the degradation and mineralization of recalcitrant diazo dye (Congo red) in heterogeneous Fenton-like process. Different characterization techniques (XRD, N_2 sorption, FTIR, FESEM/EDAX, UV-DRS and XPS) reveal the successful incorporation of well dispersed copper species (Cu^{1+} and Cu^{2+}) on the surface of zeolite Y. The synergic effect between adsorption and Fenton-like catalysis was responsible for the higher catalytic activity. The maximum degradation, decolorization and mineralization of 93.58%, 95.34% and 79.52% were achieved after 2.5, 2 and 4 h, respectively, under the following optimized condition: copper loading of 7.5 wt %, initial pH 7, H_2O_2 concentration of 52.24 mM, catalyst concentration of 1 g L^{-1} and temperature of 60 °C. Leaching of copper species was majorly influenced by initial pH as compared to other operating variables. The catalyst 7.5CuY showed good catalytic activity as well as good framework stability during reusability test. This study showed that strategic operation of the Cu impregnated zeolite Y can be a practical option for effective mineralization of a complex organic substrate.

COMPARATIVE EVALUATION OF SYNTHESIS ROUTES OF Cu/ZEOLITE Y CATALYSTS FOR CATALYTIC WET PEROXIDE OXIDATION OF QUINOLINE IN FIXED-BED REACTOR

5.1. OVERVIEW

This chapter provides the overview of copper immobilization on zeolite Y by different methods. The resulting Cu/zeolite Y were characterized for in-depth understanding of the influence of these preparation methods on crystalline structure, hierarchical porosity and coordination environment of copper species. The performance of catalysts prepared by these methods have been examined and compared in terms of catalyst activity and stability for the continuous oxidative degradation of quinoline in fixed-bed reactor (FBR). The best catalyst is identified and the effects of different operating conditions (liquid hourly space velocity (LHSV), particle size, H_2O_2/quinoline molar ratio and temperature) were measured on mineralization efficiency (total organic carbon degradation), H_2O_2 conversion and leaching of active species. Moreover, the long term stability, kinetics and mechanism of CWPO of quinoline have been discussed.

5.2. LOADING OF COPPER ON ZEOLITE Y

In order to find a better alternative of conventional aqueous ion-exchange method, several Cu/zeolite Y samples were synthesized by three different routes, viz. aqueous ion exchange (AIE), wet impregnation (IMP) and precipitation-impregnation (PI). The detailed experimental procedure is given in *Section 3.2.2* of *Chapter III*.

5.2.1. Influence of preparation methods on copper loading

To understand the control over copper loading attained by different routes, samples with different copper loading were synthesized. The copper loading has also been presented in Cu/Al ratio as copper content by AIE method depends on Al content (Table 5.1). The maximum possible copper loading by AIE can be expressed as Cu/Al= 0.5 because each Cu^{2+} ion can neutralize the opposite charge on two aluminums atoms of the framework. However, in the present case, the maximum actual Cu/Al ratio for AIE was 0.48 (~5 wt%). This difference of theoretical and actual loading may be attributed to the competition between copper and other cationic impurities to occupy the aluminum sites (Takahashi et al. 2001). Furthermore, this loading was observed higher than popular ZSM-5 (generally 2-3 wt%) because zeolite Y has higher Al content (low Si/Al ratio) than ZSM-5. AIE provides poor control over metal loading as a high initial copper amount (10.9 g copper nitrate) was used and the process had to be repeated three times for the above mentioned

loading. On the contrary, the IMP and PI methods facilitate good control over copper loading with good reproducibility. The actual and initial copper loadings were slightly different on account of subsequent loss of the copper during washing steps (Table 5.1). Moreover, it has been observed that both methods (IMP and PI) can provide higher Cu/Al ratio as compared to traditional AIE method; however, the nature and location of copper species are different (vide infra). Thus, both methods have shown to be better than the ion exchange in terms of control over copper loadings. Both methods also require less volume of solvent, less time, no filtration, no residual solvent, which are good from the industrial perspectives. In order to obtain a clear insight into the influence of preparation methods, samples with copper loading of 5wt % (equivalent to copper loading by AIE method) has been considered.

Table 5.1: Initial and actual copper loading over zeolite Y, Cu/Al ratios, and nomenclature of specimens

Cu incorporation methodologies	Actual Cu content[a] (wt.%)	Initial Cu amount (wt.%)	Cu/Al (wt. ratio)[a]	Crystallite size (nm)[b]	Sample ID
Ion exchange	5.03	--	0.48	ND	$5CuY_{AIE}$
Impregnation	4.87	7.50	0.46	ND	$5CuY_{IMP}$
Impregnation	7.46	10.00	0.73	ND	$7CuY_{IMP}$
Precipitation	2.98	5.00	0.28	4.7	$3CuY_{PI}$
Precipitation	5.04	7.50	0.44	5.6	$5CuY_{PI}$
Precipitation	6.94	10.00	0.68	6.1	$7CuY_{PI}$

[a] Measured by ICP-MS using acid digestion technique, ND = not detected

[b] Calculated using scherrer equation

5.2.2. Structural properties

The influence of protonization and preparation methods on crystalline nature of zeolite Y as well as structure of copper species was investigated by XRD analysis and shown in Fig. 5.1. Two small peaks (222, 422) of NaY were absent in diffractogram of protonized zeolite (HY). The disappearance of these peaks may be attributed to hydrolysis of Al-O bonds in small extent during calcination of samples (Saceda et al. 2011). Both $5CuY_{AIE}$ and $5CuY_{IMP}$ samples exhibit diffraction pattern typical of zeolite HY structure and CuO phase cannot be detected. The absence of CuO crystallites in $5CuY_{AIE}$ and $5CuY_{IMP}$ indicates that both methods facilitate well-dispersed or isolated copper species attached with Al sites (Wang et al. 2012). Beside the diffractogram of HY,

5CuY$_{PI}$ displays two peaks of monoclinic CuO crystallite (PDF files 48-1548) of significant intensities at angle 35.5° and 38.7° (inset of Fig. 5.1). These peaks were further used for the estimation of crystallite size of CuO using scherrer equation (Eq. 5.1) and calculated to be around 5.6 nm for 5CuYPI catalyst (Table 5.1). This size of crystallites are too large to enter into the pores of zeolite and thus, it can be deduced that copper oxide locate on the external surface of CuY$_{PI}$. Detailed information about nature of copper species has been provided in UV-DRS and XPS techniques section.

$$d_P = \frac{K\lambda}{\left(\beta_{Sample} - \beta_{standard}\right)\cos\theta}$$

(5.1)

Where, d_P is the crystallites size, λ is wavelength of X-ray radiation, K is Scherrer's constant (0.94), β is the full width of the peak at half maximum (FWHM) and θ is Bragg's angle. The instrumental broadening ($\beta_{standard}$) was measured using pure silicon powder as standard sample.
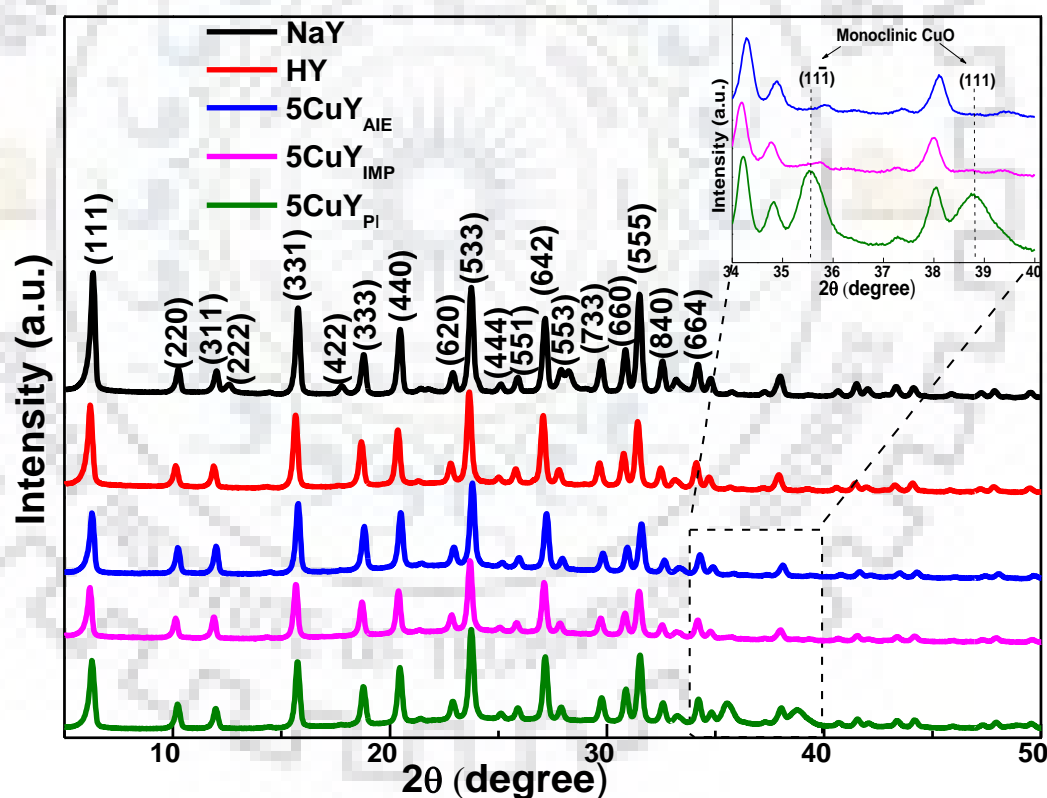
Fig. 5.1: X-ray diffraction pattern of NaY, HY and Cu-containing samples

5.2.3. Textural investigations of copper containing zeolite Y (CuY)

The individual influence of each preparation method on the pore structure of CuY was investigated by N$_2$ sorption measurements at 77 K. As shown in Fig. 5.2a and 5.2b, the resulting isotherms of

all specimens display a sharp sorption of N_2 in low relative pressure range, which specifies the existence of microporosity in all specimens [Dükkanci et al. 2010b]. $5CuY_{AIE}$ displayed type-I isotherm similar to pure zeolite HY and textural properties were not affected (Table 5.2). This reflects the intact framework of zeolite Y after AIE method. On the other hand, H_4 type hysteresis loop was observed in $5CuY_{IMP}$ and $5CuY_{PI}$ isotherms which indicate the formation of mesopores [Huang et al. 2010]. The higher uptake for $5CuY_{PI}$ than $5CuY_{IMP}$ between middle to high relative pressure reveals the higher extent of mesoporosity generated by precipitation method as compared to impregnation method. The Langmuir surface area (S_{Lang}) and pore volume (V_p) increase surprisingly from 567 to 909 m^2 g^{-1} and 0.26 to 0.51 cm^3 g^{-1}, respectively, for $5CuY_{PI}$. Additionally, the t-plot method reveals development of substantial mesoporosity with surface area (S_{meso}) = 276 m^2 g^{-1}. This represents a 6-fold increase in external surface area without affecting its microporosity (V_{micro}, S_{micro}). Recently, Verboekend et al. [2012] reported combinations of acid and base treatments to prepare hierarchical Y zeolite and observed similar trend of modification of textural properties. To further verify the mesoporosity generation in $5CuY_{PI}$, the pore size distribution for all specimens was evaluated using DFT model (Fig.5.3).
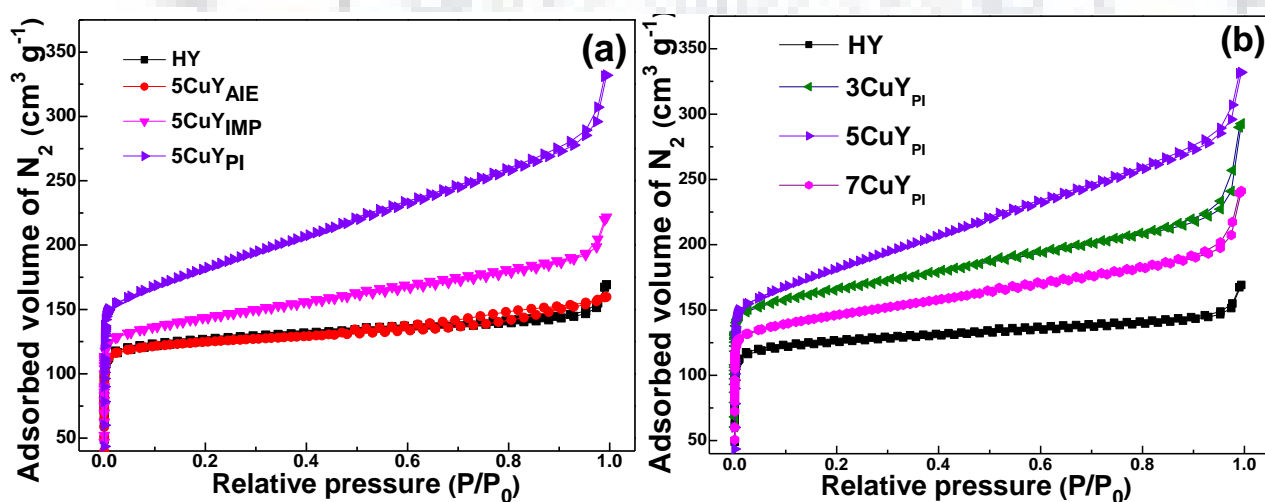
Fig. 5.2: N_2 sorption isotherms of (a) samples with copper loading 5 wt.% and (b) samples prepared by PI method having different copper loadings

Interestingly, the generation of hierarchical porosity, characterized with mesopores (in range 2.5-6 nm) in considerable extent and intrinsic micropores (about 0.78 nm) in major extent, was observed. Qin et al. [2011]] obtained limited mesoporosity S_{meso}= 60 m^2 g^{-1} by the NaOH treatment (368 K, 1-3 h) on prisitine zeolite Y. The above discussion implies that the introduction of mesoporosity is due to synergetic effect of copper and base NaOH. To further confirm the role of copper loading, different experiments were performed and the observed isotherms have been illustrated in Fig.5.2b.

The figure shows that a critical loading exists and further increment in it results in reduction of mesopore surface area. The substantial reduction in S_{Lang}, V_p and S_{meso} of $7CuY_{PI}$ could be ascribed to significance of a particular molar ratio of copper and NaOH for the generation of substantial mesoporosity. The lower surface area of CuO in comparison to zeolite Y as well as blockage of the pores by its large crystallites may have small influence [Garcia et al. 2011]. The introduction of mesoporosity in $5CuY_{PI}$ was result of efficient desilication, which has been proved through XPS analysis (*vide infra*).

Table 5.2: Textural properties of CuY zeolites

Samples ID	S_{Lang} $(m^2\,g^{-1})^a$	V_p $(cm^3\,g^{-1})$	V_{micro} $(cm^3\,g^{-1})^b$	S_{micro} $(m^2\,g^{-1})^b$	S_{meso} $(m^2\,g^{-1})^b$
HY	567	0.26	0.171	343	54
$5CuY_{AIE}$	563	0.24	0.173	355	47
$5CuY_{IMP}$	667	0.34	0.164	329	134
$3CuY_{PI}$	772	0.45	0.192	380	151
$5CuY_{PI}$	909	0.51	0.163	317	276
$7CuY_{PI}$	677	0.37	0.169	341	131

^{a} Calculated by fitting Langmuir model

^{b} Calculated by t-plot method
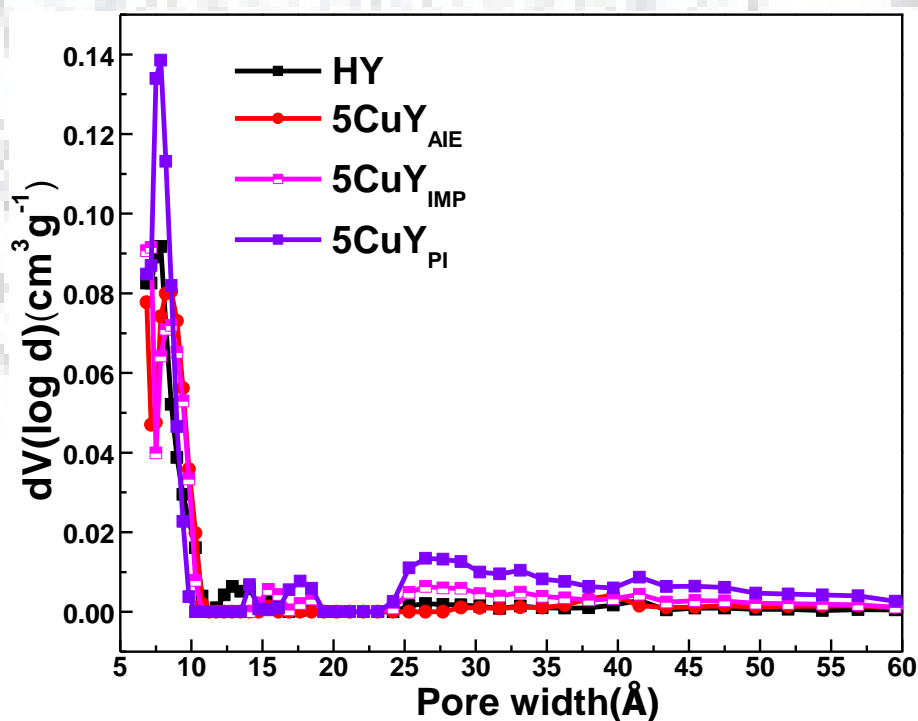
Fig. 5.3: Pore size distribution using DFT model

5.2.4. FESEM analysis

FESEM images shown in Fig. 5.4 depict that zeolite Y crystallites were in shape of irregular polyhedra and the average particle size was about 400-700 nm. Interestingly, $5CuY_{AIE}$ and $5CuY_{IMP}$ exhibit smooth surface similar to HY. This result evidences that copper species are dispersed uniformly over the support. However, the CuO cluster can be clearly observed in $5CuY_{PI}$ samples. The presence of CuO is in good agreement with observations of XRD analysis.
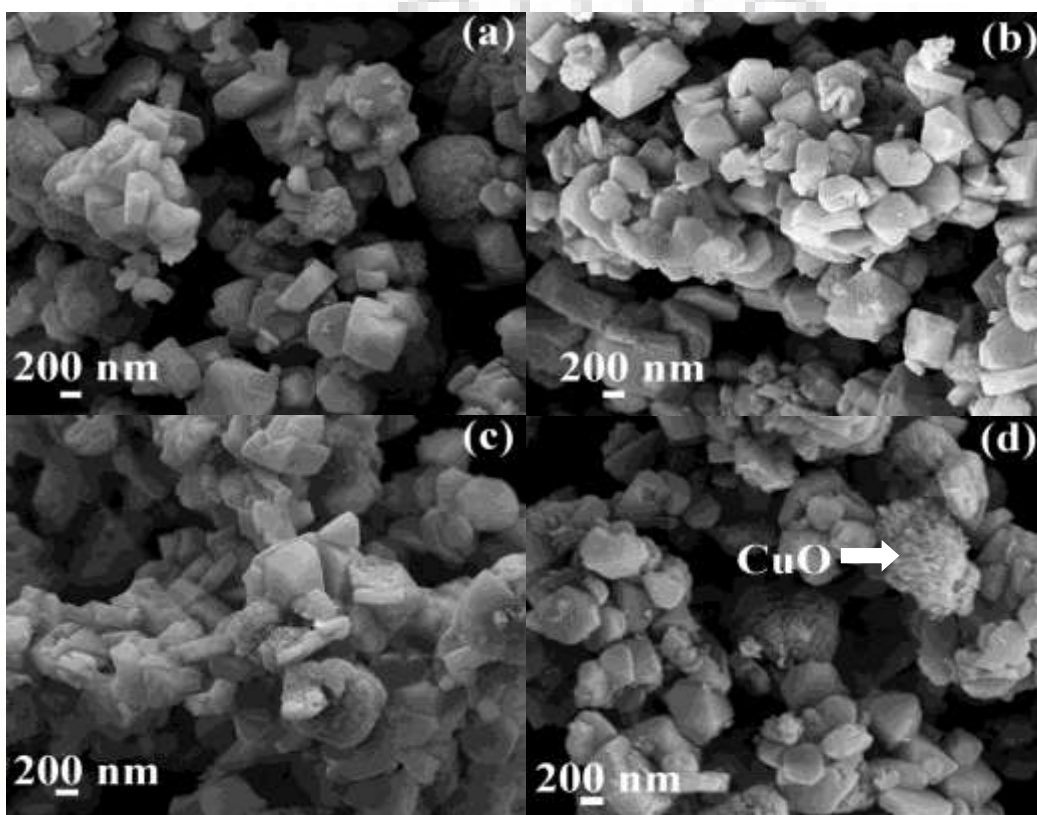
Fig. 5.4: FESEM images of (a) HY, (b) $5CuY_{AIE}$, (c) $5CuY_{IMP}$, (d) $5CuY_{PI}$

5.2.5. Coordination environment of Cu using UV-vis DRS analysis

UV-vis DRS spectra were investigated in term of Kubelka-Munk function of pure copper phase (F(R')) and depicted in Fig. 5.5. The F(R') was calculated after excluding the influence of zeolite HY from CuY samples, since zeolite HY owns a band in the region of copper species (200-250 nm). Each spectrum comprised of most relevant charge transfer (CT) and d-d transition bands. The CT band was further fitted with three subcomponents at wavelengths 227, 263 and 335 nm, which can be ascribed to three different types of copper species (inset of Fig. 5.5). The band centered at 227 and 263 nm can be assigned to charge transfer from framework oxygen to isolated Cu^{1+} and

Cu^{2+} sites, respectively [Carvalho et al. 2000; Kuśtrowski et al. 2005]. The weak band at 335 nm corresponds to dimeric $(Cu-O-Cu)^{2+}$ bridges, whose oxygen is not associated with zeolite framework [Mendes et al. 1997]. For $5CuY_{AIE}$, the domination of band centered at 263 nm indicates that ion exchange facilitates higher extent of isolated Cu^{2+} species as compared to other preparation methods. The isolated species Cu^{2+} were also observed for $5CuY_{IMP}$ and in a little majority than Cu^{1+} sites. Conversely, the isolated Cu^{2+} species and $(Cu-O-Cu)^{2+}$ dimers were absent for $5CuY_{PI}$, since no corresponding band were observed at 263 and 335 nm. Their absence clearly describes the remarkable effect of preparation methods on Cu^{2+} speciation. However, the domination of CT band towards low wavelength region (< 230) confirms the presence of Cu^{1+} species in considerable amount. These results corroborate the observation of isolated species in $5CuY_{IMP}$ as well as availability of Cu^{1+} sites in $5CuY_{PI}$ through XPS analysis (*vide infra*).
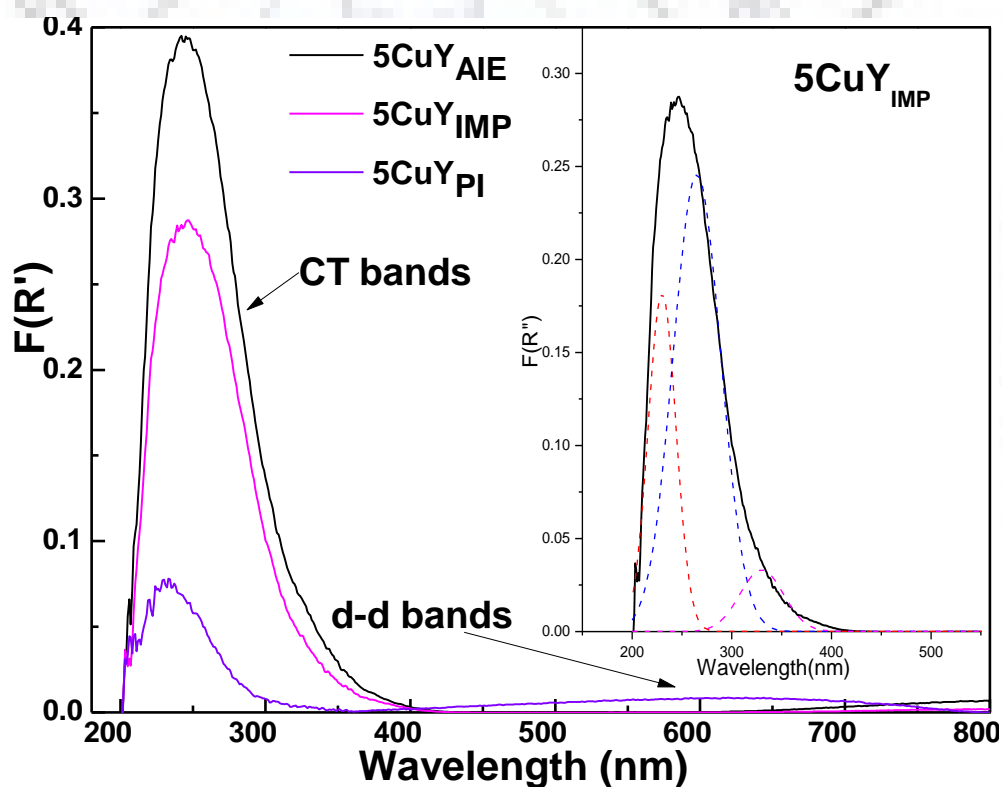
Fig. 5.5: UV-vis DRS spectra in term of Kubelka-Munk function

In addition, the d-d transition bands were found for all samples in wavelength region (500-800 nm), which indicates only the Cu^{2+} species, since Cu^{1+} has fully filled d orbital ($3d^{10}$). Both $5CuY_{AIE}$ and $5CuY_{IMP}$ samples exhibit the d-d transition band centered at 800 nm, which signify isolated highly distorted Cu^{2+} sites [Giordanino et al. 2013]. A broad d-d transition band in visible range for $5CuY_{PI}$ can be assigned to Cu^{2+} in octahedrally coordinated CuO particles [Klaas et al.

1997; Cao et al. 2015; Li et al. 2016]. This finding of availability of CuO is in good agreement with XRD, SEM and XPS analysis.

5.2.6. Coordination environment of copper using XPS analysis

The chemical composition and electronic structures of all samples were examined using XPS analysis. The XPS survey scan spectra present peaks of different elements (Fig. 5.6a), such as Si, Al, O and/or Cu. Fig. 5.6b shows the narrow scan spectra of Cu2p of $5CuY_{PI}$ and $5CuY_{IMP}$ samples. To have a clear insight about the location of copper species obtained by different methods, one has to keep in mind that XPS is a surface analysis technique and has average depth of analysis for a few nanometres. The high intensity signal for $5CuY_{PI}$ reveals the presence of major amount of copper on the surface of the catalyst. For $5CuY_{IMP}$, the intensity of the signal is low because small extent of copper was present on the surface and copper in major proportion was present in pores of the catalyst. The two peaks at 952.2 and 932.24 eV represent Cu $2p_{1/2}$ and Cu $2p_{3/2}$, respectively. It is worth noting that binding energy of the $Cu2p_{3/2}$ core level of $5CuY_{IMP}$ (932.56 eV) is slightly higher than $5CuY_{PI}$ (932.24 eV). It has earlier been reported for different zeolites (X, SSZ-13) that isolated copper ions in zeolite pores have higher $Cu2p_{3/2}$ binding energies than bulk oxides [Clemens et al. 2015; Romero et al. 2015]. Hence, impregnation method promotes insertion of isolated copper ions into pores of zeolite. The shape of the Cu2p spectrum of $5CuY_{PI}$ may be ascribed to copper oxide and found in agreement with previous published literature [Espinos et al. 2002]. The existence of CuO was also supported by XRD. The main peak Cu $2p_{3/2}$ core level of both samples can be best fitted with two components at binding energies 932.4 and 933.5 eV, which can be attributed to Cu^{1+} and Cu^{2+} states, respectively [Wu et al. 2006]. The additional peaks around 941 eV result from the shake-up satellite, which characterize the $3d^9$ configuration (paramagnetic nature) of Cu^{2+} species. The relative amount Cu^{2+}/Cu^{1+} for $5CuY_{PI}$ and $5CuY_{IMP}$ samples were 2.30 and 0.97, respectively, calculated from ratio of sum of area of Cu^{2+} peaks to that of Cu^{1+} peaks (Table 5.3).

Fig. 5.6c, 5.6d and 5.6e illustrate the core level spectra of Si2p, O1s and Al2p, respectively. For $5CuY_{IMP}$, the intensity of Si2p peak slightly decreased from the intensity of HY; however, the peak intensity of $5CuY_{PI}$ decreased significantly. These results attributed to desilication of zeolite Y and also show the synergetic effect of copper and NaOH for silica removal. The quantitative results also verify these findings. The decrements in O1s intensity and increment in Al2p intensity

also indicate the effective desilication or decrease in Si/Al ratio [Barr et al. 1990]. The progressive decrements in binding energy for all elements also signify that aluminate units are increasing in tetrahedral environments [Herreros et al. 1994].
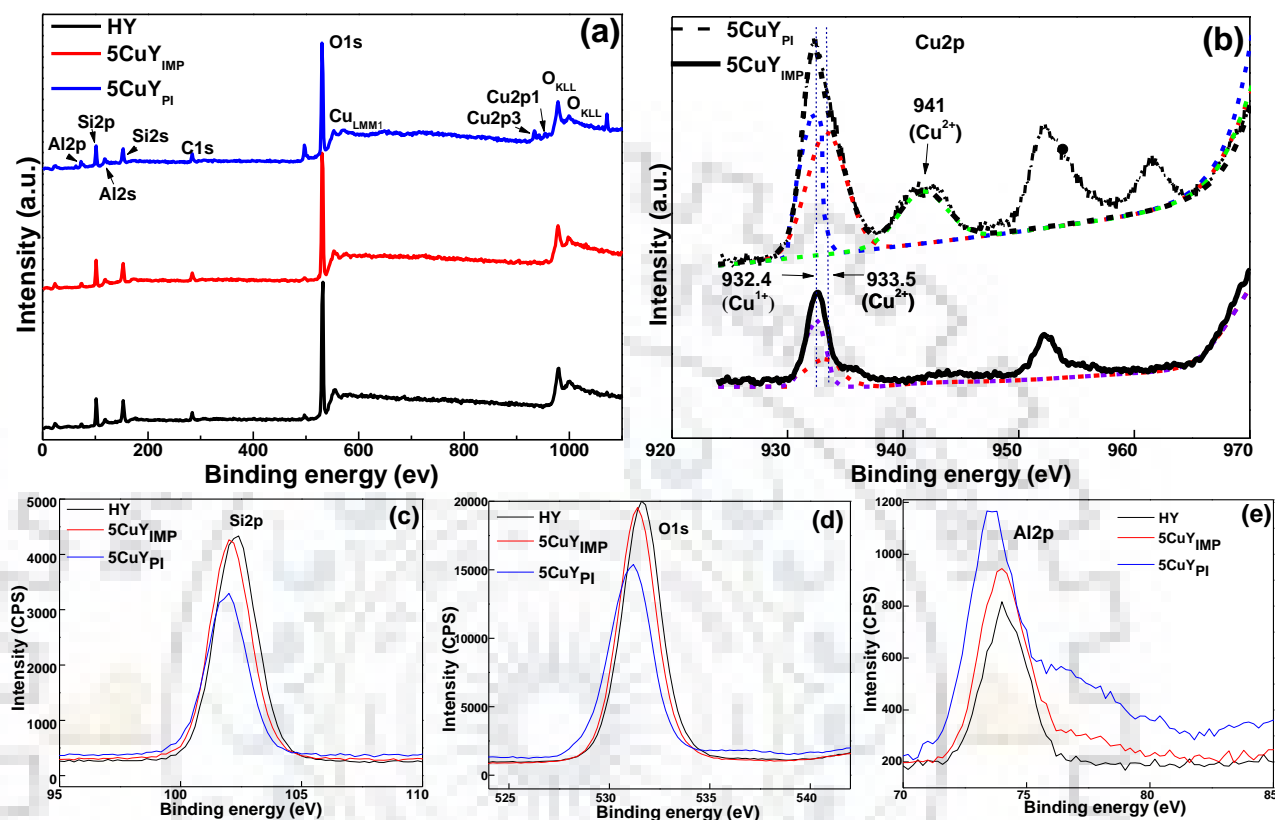
Fig. 5.6: XPS analysis of HY, 5CuY$_{IMP}$ and 5CuY$_{PI}$ samples (a) survey scan, (b) high resolution spectra of Cu2P, and core level spectra of (c) Si2p, (d) O1s and (e) Al2p

Table 5.3: Comparison of atomic composition and Cu^{2+}/Cu^{1+} ratio of samples

Sample ID	Binding energy Cu2p$_{3/2}$ (eV)	Atomic composition (%)					Cu^{2+}/Cu^{1+}
		Si2p	Al2p	O1s	Cu2p3	Si/Al	
HY	-	26.51	6.58	66.91	-	3.87	-
5CuY$_{IMP}$	932.56	25.68	7.98	65.40	<1	3.21	0.97 (40.53)[a] (8.90)[b] (50.57)[c]
5CuY$_{PI}$	932.24	21.90	13.27	63.38	1.45	1.65	2.30 (45.49)[a] (24.23)[b] (30.27)[c]

[a] area % of Cu^{2+} peak at 933.5 eV
[b] area % of Cu^{2+} peak around 941 eV
[c] area % of Cu^{1+} peak at 932.4 eV

5.3. CATALYTIC ACTIVITY OF Cu/ZEOLITE Y IN FIXED BED REACTOR

5.3.1. Effect of preparation method on catalytic activity

Fig. 5.7 compares the CWPO performance of all CuY catalysts in terms of conversions of quinoline, TOC, H_2O_2 and final pH as a function of time in fixed bed reactor. Each catalyst possesses transient period of different length of time (2-4 h) in the beginning of the run. After that period, quinoline, TOC and H_2O_2 conversions reach to steady-state. The length of period increased in the order of $5CuY_{IMP} < 5CuY_{AIE} < 5CuY_{PI}$. Botas et al. [2010] assumed this period on the basis of diffusional constraints associated with accessibility of supported iron particles. In order to obtain some information about this phenomenon, experiments were performed in batch reactors with powdered catalysts at high stirring speed (Fig. 5.8). The purpose of setting this condition was to avoid the diffusional resistances. As observed in continuous reactor a slower rate period was also noticed for $5CuY_{PI}$ as compare to $5CuY_{IMP}$ and $5CuY_{AIE}$ in batch reaction. Likewise, $5CuY_{IMP}$ exhibits the fastest removal in the beginning; however, the final conversion was less than that of $5CuY_{AIE}$. These results confirm the major influence of nature of active species in the present case. The shortest transient period for $5CuY_{IMP}$ may be ascribed to greater extent of Cu^{1+} active sites (from XPS analysis), which have extra electrons for the rapid production of highly reactive *OH radical from H_2O_2. The longest period for $5CuY_{PI}$ could be ascribed to slow pre-conditioning (reduction to lower oxidation state) of copper oxide species.

At steady state (after 100 min reaction time), similar quinoline conversions (> 98%) were obtained for both $5CuY_{IMP}$ and $5CuY_{AIE}$ catalysts. However, a significant reduction of quinoline conversion was observed for $5CuY_{PI}$. TOC results reveal that $5CuY_{AIE}$ attains the highest catalytic activity with constant conversion (~65.4%) up to 8 h. $5CuY_{IMP}$ demonstrates almost similar TOC conversion. Conversely, $5CuY_{PI}$ exhibits the lowest TOC conversion. Fig. 5.7 depicts that H_2O_2 conversion proceeds synchronously with the quinoline degradation. Both $5CuY_{AIE}$ and $5CuY_{IMP}$ catalysts manifest trend of H_2O_2 conversion similar to trend of quinoline and TOC conversions. However, no such correlation was observed between H_2O_2 conversion and pollutant removal by $5CuY_{PI}$. It shows highest activity for H_2O_2 conversion but it exhibits lowest activity for degradation of pollutant.

In order to elucidate H_2O_2 decomposing route and corresponding catalytic performance of catalysts, the H_2O_2 stoichiometric efficiency was calculated. The H_2O_2 stoichiometric efficiencies

were observed as 44.2% and 45.7% for $5CuY_{AIE}$ and $5CuY_{IMP}$, respectively. The H_2O_2 stoichiometric efficiency of $5CuY_{PI}$ was low (21.6%).
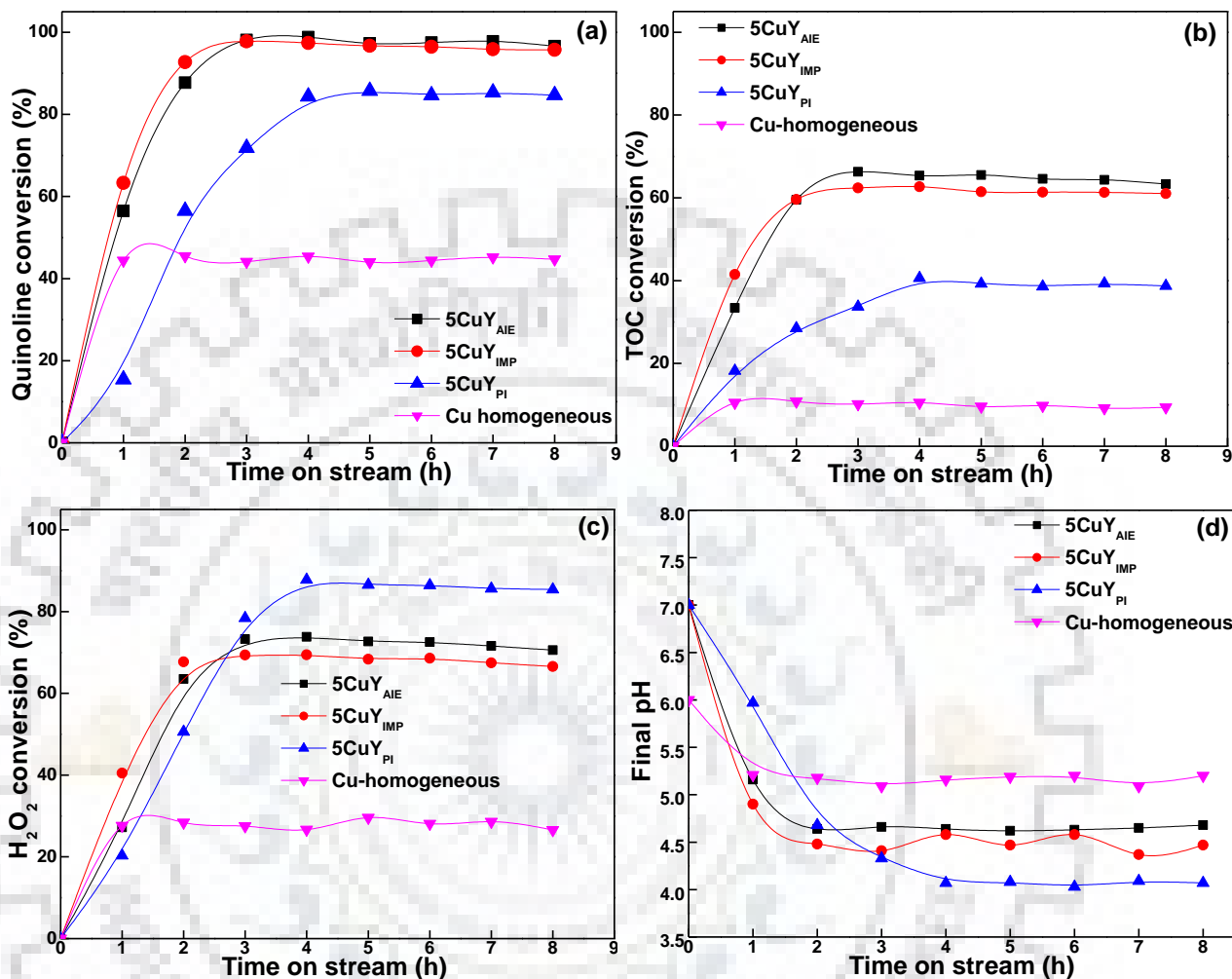
Fig. 5.7: Influence of preparation method on (a) Quinoline conversion (b) TOC conversion (c) H_2O_2 conversion and (d) Final pH in a fixed bed reactor. LHSV = 4 h^{-1}, T = 80 °C, pH$_0$ = 7, [Quinoline] = 3.87 mM, [H_2O_2] = 185 mM and particle size = 1.2-1.7 mm

High stoichiometric efficiencies for the former catalysts confirm that both catalysts promote catalytic conversion of H_2O_2 into *OH radicals [Satishkumar et al. 2013]. High selectivity towards *OH generation was result of high redox activity of well-dispersed isolated species as well as their properties of high mobility of charge carriers within the zeolite framework (UV-*vis* DRS analysis). On the contrary, the low H_2O_2 stoichiometric efficiency of $5CuY_{PI}$ indicates non-selective decomposition of H_2O_2 to inactive O_2 and H_2O species [Nie et al. 2009]. The low stoichiometric efficiency of $5CuY_{PI}$ may be ascribed to the presence of large crystallites of CuO particles on the

catalyst surface. The low activity behavior of CuO is in agreement with the previous reports for oxidation of organic pollutant through different processes [Kim et al. 2007; Nie et al. 2009].
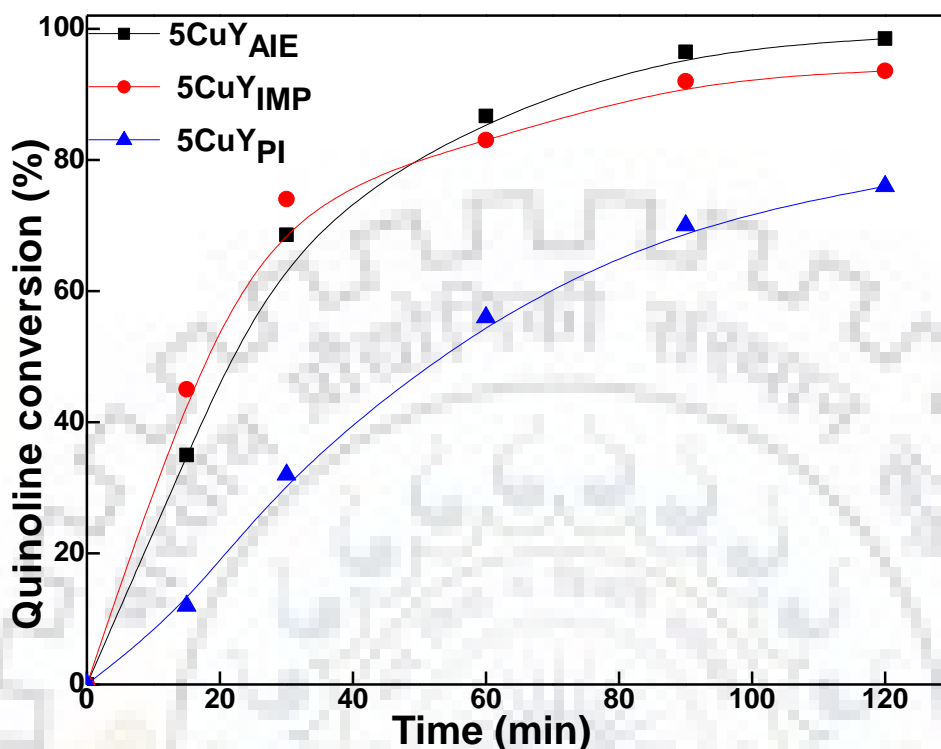
Fig. 5.8: Influence of preparation methods on catalytic activity of powdered catalysts in batch reactor. T = 80 °C, pH$_0$ = 7, [H$_2$O$_2$] = 185 mM, [Quinoline] = 3.87 mM, [catalyst] = 0.3 g L^{-1} and stirring speed = 800 RPM

5CuY$_{AIE}$ and 5CuY$_{IMP}$ catalysts are more active than the precipitated catalyst, even though later sample have hierarchical porosity as well as higher surface area. One can ascertain from these results that high surface area is not an essential parameter to obtain high catalytic activity in CWPO, and isolated copper species (Cu^{2+} and/or Cu^{1+}) are the most redox-active species for CWPO. Recently, Tang et al. [2014] observed that isolated Ti sites on microporous beta-zeolite were more active than Ti sites located at external surface of mesoporous MCM-41 in epoxidation of 2-cyclohexen-1-one by H$_2$O$_2$. Thus, it can be concluded that location and electronic state of active phase play more important role than textural properties.

With neutral pH of reaction mixture, all samples show high resistance towards leaching. 5CuY$_{PI}$ showed the lower copper concentration (<4 mg L^{-1}) within the treated effluent as compared to copper concentration of 6 mg L^{-1} and 14-15 mg L^{-1} for 5CuY$_{AIE}$ and 5CuY$_{IMP}$, respectively. The leached copper extents were 0.6 and 1.5% for 5CuY$_{AIE}$ and 5CuY$_{IMP}$,

respectively, for 8 h operation. These results corroborate the observation of Santos et al. [2005] of negligible leaching from Cu-based catalysts at pH >5 in catalytic wet air oxidation (CWAO) of phenol. The pH decrement from 7 to 4.7 at the outlet of reactor for $5CuY_{AIE}$ and $5CuY_{IMP}$ confirms the formation of organic acids. The presence of acetic acid and formic acid was also confirmed by HPLC analysis. The lowest final pH (~4) was recorded for $5CuY_{PI}$ due to low mineralization of organic acids. The incapability of copper to form complex with residuals organic intermediates (acetic acid, formic acid) can also be responsible for negligible lixiviation. In order to check the contribution of homogeneous reaction, copper containing reaction solution ($[Cu^{2+}] = 15$ mg L^{-1}) was fed in the reactor packed with zeolite HY pellets. Low copper concentration cause less H_2O_2 conversion and subsequently less pollutant removal (9% TOC). Experiments were also carried out to confirm the role of homogeneous reaction using glass beads in the reactor at same condition. As expected, less TOC removal (7.7%) was obtained. Thus, the activity of species on catalyst surface is high and reaction is following heterogeneous pathway. As shown in Fig. 5.8, the homogeneous reaction starts quickly and the presence of transient period in presence of catalysts indicates that reaction starts by heterogeneous pathway.

5.3.2. Long term activity

The long term activity of catalyst is a key parameter in practical application. Fig. 5.9 illustrate the long term catalytic performances of two better catalysts, $5CuY_{AIE}$ and $5CuY_{IMP}$ at the experimental condition that provide high oxidation of quinoline. $5CuY_{AIE}$ exhibits constant TOC removal of 65.4% with copper leaching of approximately 6 mg L^{-1} up to reaction period of 50 h. After that period, the TOC removal and copper leaching gradually decreased from 65.4 to 60% and 6 to 1.5 mg L^{-1}, respectively. The leached copper extent was approximately 7.6% after 250 h. $5CuY_{IMP}$ also display TOC removal of 61% that remained unchanged up to 100 h and decreases slightly up to 250 h. The measurement of the leached copper concentration in effluent shows that the copper content was 14-15 mg L^{-1} for 10 h, reduce to 8 mg L^{-1} in next 30 h and remain less than 5 mg L^{-1} up to 250 h. The total leached copper amount was 14.4% of initial copper content. The constant TOC removal for long time and high reluctance towards leaching signify that a strong interaction exists between copper species and zeolite Y support in both samples (also observed in XPS analysis). In addition, the treated effluent required neutralization before discharge in reservoirs. As per the Eh-pH diagram, the copper ion precipitates out at pH = 7 with copper solubility is <1 mg L^{-1} at pH = 7. The precipitated copper was easily separated out and thus, the copper concentration was obtained below permissible limit of Indian Standard (3 mg L^{-1}) [CPCB 2018].
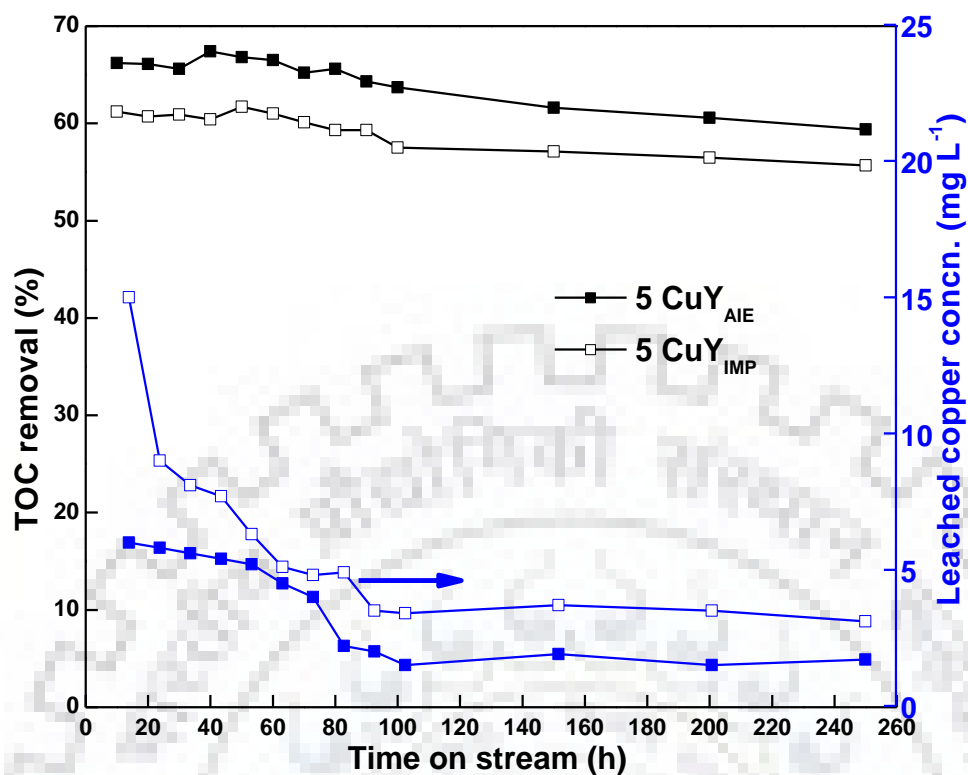
Fig. 5.9: Long term activity of 5CuY$_{AIE}$ and 5CuY$_{IMP}$ at T = 80 °C, pH$_0$ = 7, LHSV = 4 h^{-1}, [H$_2$O$_2$] = 185 mM, [Quinoline] = 3.87 mM and particle size = 1.2-1.7 mm

As depicted in Fig. 5.10a, no new phase was formed during catalytic run in both samples. FTIR spectrum of fresh and used samples indicates that long term operation does not bring any changes to band located at 457, 580, 803 and 1039 cm^{-1}(Fig. 5.10b). These bands correspond to the Si-O-Si bending, double ring vibration, Si-Al(O) symmetrical stretching and asymmetric stretching of tetrahedral building units, respectively [Garcia et al. 2011; Singh et al. 2016]. Thus, it can be concluded that Cu/zeolite framework remained intact. Previous studies have shown that carbonaceous deposits accumulated on active sites may also contribute in catalyst deactivation [Luca et al. 2014]. However, no carbonaceous residues were observed by FTIR analysis in the present case. The characteristics peaks of quinoline in IR spectrum, predominantly exist in range 1500-500 cm^{-1}, were absent in spectra of both catalysts [Zhang et al. 2014]. Furthermore, negligible changes in textural properties also confirmed the absence of these deposits. Thus, slow leaching could be the only responsible factor for decay of catalyst activation at the end. These results reveal high operational stability (up to 250 h) of both catalysts for degradation of toxic pollutants.
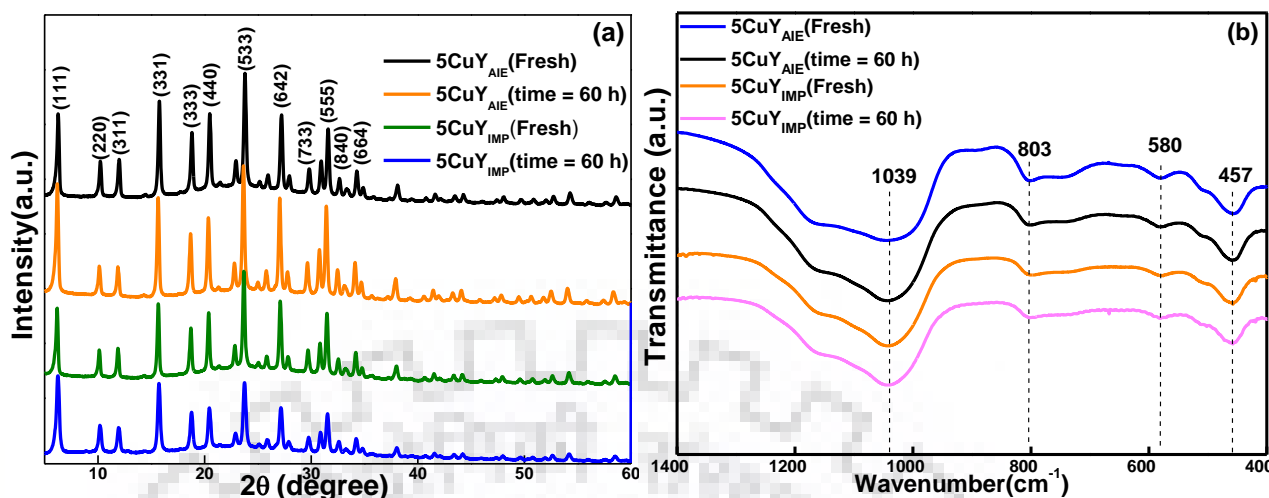
Fig. 5.10: (a) XRD and (b) FTIR analysis of used samples to show structural changes and carbonaceous deposits on catalyst surface

5.3.3. Exclusion of mass-transfer resistances and effect of reaction parameters

In view of the objectives to find the better alternative to the complex ion exchange method, the impregnation method has been found suitable from every aspect. Because of high environmental benignity, greater control over copper loading and comparable catalytic activity performance, the wet impregnation method has been selected as a better alternative to complex ion-exchange method and used for further studies on the effect of process parameters and kinetics of the mineralization process, as will be shown later. It is well known that mass-transfer limitations must be eliminated before measurement of the kinetic data. After exclusion of limitation of external and internal diffusion, the effect of the process variables has also been shown in the selected range.

5.3.4. Effect of liquid hourly space velocity (LHSV) or residence time

Fig. 5.11 illustrates the variation in conversion with space time (W/Q) for runs having two different weight of catalyst. The external diffusion resistance can be neglected when same conversion achieved for different weighted system at the fixed value of space time [Liu et al. 2006; Xiao et al. 2010]. When W/Q < 21.24 kgcat h L^{-1}, the two lines of both system almost coincide and thus, the resistance of external diffusion may be ignored. Therefore, All the experiments were carried out in the region of W/Q < 21.24 kgcat h L^{-1} (corresponding to LHSV > 3 h^{-1}). The lack of particle size effect also supports this fact since the conversion of external diffusion limited reaction varies inversely with particle size (*vide infra*).

LHSV (defined as feed flow rate/ catalyst bed volume) is a scale-up variable and can be used directly for further testing in large scale equipment. Fig. 5.12a presents the influence of LHSV on the TOC conversion after reaching the steady-state. It can be seen that the TOC removal decreases from 61 to 20% with an increase in LHSV from 4 to 16 h^{-1}. The increase in LHSV from 4 to 16 h^{-1} lead to decrease in residence time (t_r) of reactants from 4.54 to 1.11 min (Fig. 5.12a), resulting in less conversion. Similar influence of LHSV was also noticed on H_2O_2 conversion and stoichiometric efficiency (Fig. 5.12b). Both parameters decrease from 66.6% to 36.3% and 45.7% to 28%, respectively, with the increase in LHSV from 4 to 16 h^{-1}. The role of longer residence time to higher conversion and yield has been reported for different types of processes [Erjavec et al. 2013; Sheydaei et al. 2014; Miladinovic et al. 2015]. In addition, contrary to our expectation of higher leaching due to higher shear forces, a decrement of copper leaching (15.2 to 3.7 mg L^{-1}) was observed with increase in LHSV. Beside low conversions, a high LHSV would increase the pressure drop inside packed bed reactor and thereby cause the unstable operation of the system. Due to the highest removal and stable operation, LHSV 4 h^{-1} was selected as optimum parameter.
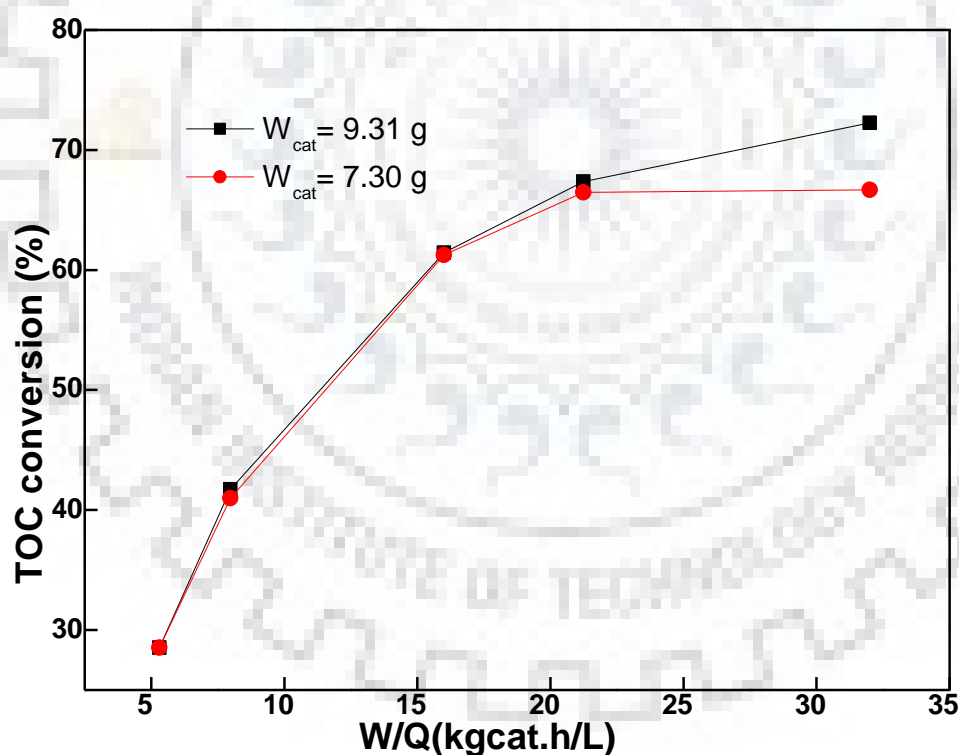
Fig. 5.11: Effect of space time on TOC removal at T = 80 °C, pH$_0$ = 7, [Quinoline] = 3.87 mM, [H$_2$O$_2$] = 185 mM and particle size = 1.2-1.7 mm

Fig. 5.12: Effect of LHSV on (a) TOC removal, and (b) H$_2$O$_2$ conversion, stoichiometric efficiency and copper leaching of 5CuY$_{IMP}$ at T = 80 °C, pH$_0$ = 7, [Quinoline] = 3.87 mM, [H$_2$O$_2$] = 185 mM and particle size = 1.2-1.7 mm

5.3.5. Effect of particle size

The internal diffusion resistance can be neglected when conversion of the reactant does not change with the particle size [Fogler 2006]. In order to assess the contribution of internal diffusion, some experiments were carried out with selected range of particle size 0.4-0.8, 0.8-1.2 and 1.2-1.7 mm. Fig. 5.13a shows that slightly higher TOC conversions were obtained with increase in average particle size from 0.6 to 1.45 mm. Likewise, H$_2$O$_2$ conversion increase slightly from 56.5 to 66.6% (Fig. 5.13b). These results indicate that the influence of internal diffusion may be ignored in the selected range of particle size.

In order to find plausible explanation of unexpected slight increment of TOC conversion with increase in particle size, a study was carried out with a different point of view. The impact of the particles size was observed on bed properties such as bed volume, void space and flow characteristics (Table 5.4). Bed volume and bed porosity decrease with decrease in particle size. Liquid hold-up, a factor to measure actual liquid amount present in voids by taking into account different properties of liquid and gas phases (explained in catalytic activity test procedure), also decrease with decrease in porosity and result into decrease of residence time of reactant mixture. The large residence time for large particles may be responsible for slightly higher catalytic activity. However, a significant influence of particle size was observed on copper leaching. Copper leaching decreases from 28 to 15 mg L^{-1} with increase in average particle size from 0.6 to 1.45

mm (Fig. 5.13b). Small particles led to higher leaching which affect the long term stability of the catalyst. These results are in agreement with the observations in previous reports of CWAO [Suwanprasop et al. 2005]. Due to higher removal and low leaching, the particles of 1.2-1.7 mm size were selected for further study. The results of both sections indicate that residence time is a performance controlling factor for the continuous CWPO in fixed bed reactor and offset the external and internal diffusional limitations.
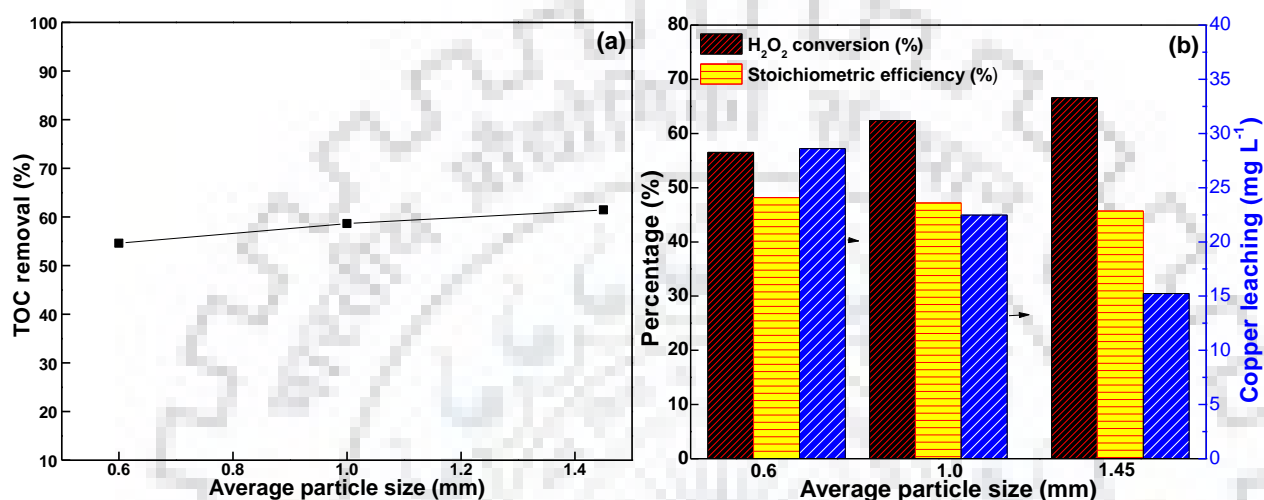
Fig. 5.13: Effect of particle size on (a) TOC removal, and (b) H_2O_2 conversion, stoichiometric efficiency and copper leaching of $5CuY_{IMP}$ at T = 80 °C, $pH_0 = 7$, LHSV = 4 h^{-1}, [Quinoline] = 3.87 mM, $[H_2O_2]$ = 185 mM

Table 5.4: Influence of particle size on bed properties

Particle size (mm)	Bed volume (cm³)	Bed porosity (void fraction)	LHSV (h⁻¹)	Liquid hold-up	Residence time (min)
1.2-1.7	14.6	0.42	4	0.303	4.54
0.8-1.2	14.1	0.40	4	0.290	4.20
0.4-0.8	13.4	0.37	4	0.262	3.60

5.3.6. Influence of H_2O_2/quinoline molar ratio

H_2O_2 is the source of *OH radicals on catalyst surface and directly control the degradation of the quinoline molecules. H_2O_2 concentration was varied in inlet stream from 46.44 to 278.64 mM to keep H_2O_2/quinoline molar ratio in range 12 to 72 (stoichiometric ratio = 24, according to Eq. 5.2).

$$C_9 H_7 N + 24 H_2O_2 \rightarrow 9CO_2 + 27 H_2 O + HNO_3 \qquad (5.2)$$

Fig. 5.14a illustrates that the TOC removal increases from 36.47% to 61.35% with increase in H_2O_2/quinoline molar ratio from 12 to 48. However, an adverse effect has been observed on TOC

120

removal on further increasing the reactants molar ratio to 72. At very high concentration, H_2O_2 begin to scavenge *OH radicals on catalyst surface and inhibit its reaction with quinoline molecules in the solution [Xia et al. 2011]. This indicates that rate of quinoline mineralization is between zero order and first order with respect to concentration of H_2O_2. At higher concentration of H_2O_2, rate is independent on its concentration. The highest TOC removal was observed at molar ratio 48. As expected, Fig. 5.14b depicts that H_2O_2 conversion and stoichiometric efficiency decreases with increase in H_2O_2 dosage. The decreasing stoichiometric efficiency indicates towards poor utilization of oxidant. A balance in H_2O_2 conversion and stoichiometric efficiency has been observed for molar ratio 48 with the highest TOC removal. Surprisingly, a negligible influence of H_2O_2 concentration has been observed on copper leaching. Copper leaching was varying between 12.7 to 17.5 mg L^{-1}, even after increasing oxidant concentration from 0.5 to 3 times of stoichiometric dose. Similar behavior has also been reported by Herney-Ramirez et al. [2010] and Melero et al. [2007] in batch reactor using Fe_2O_3 supported over SBA-15 and clay, respectively.
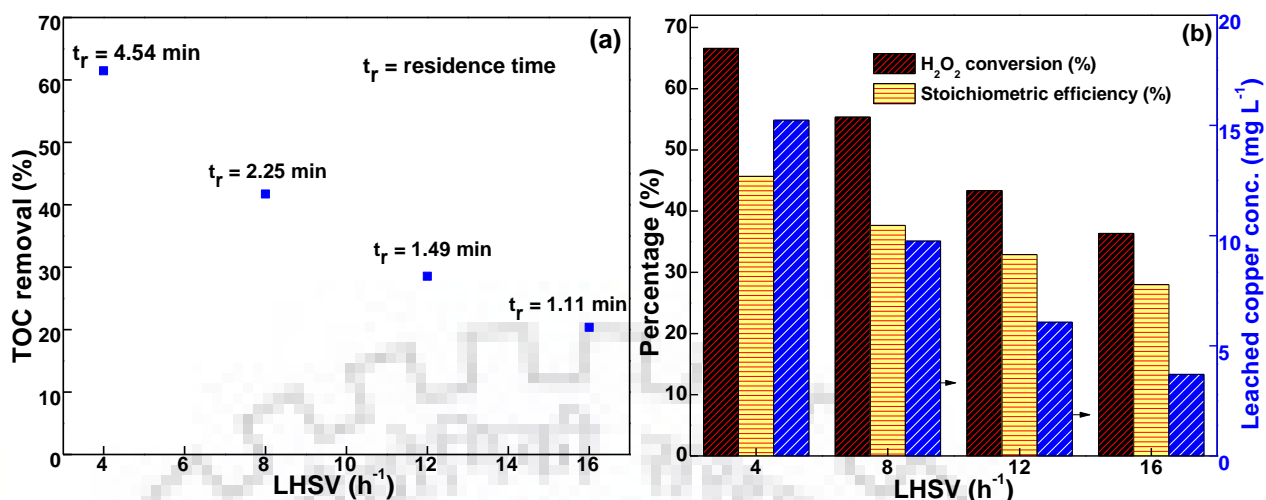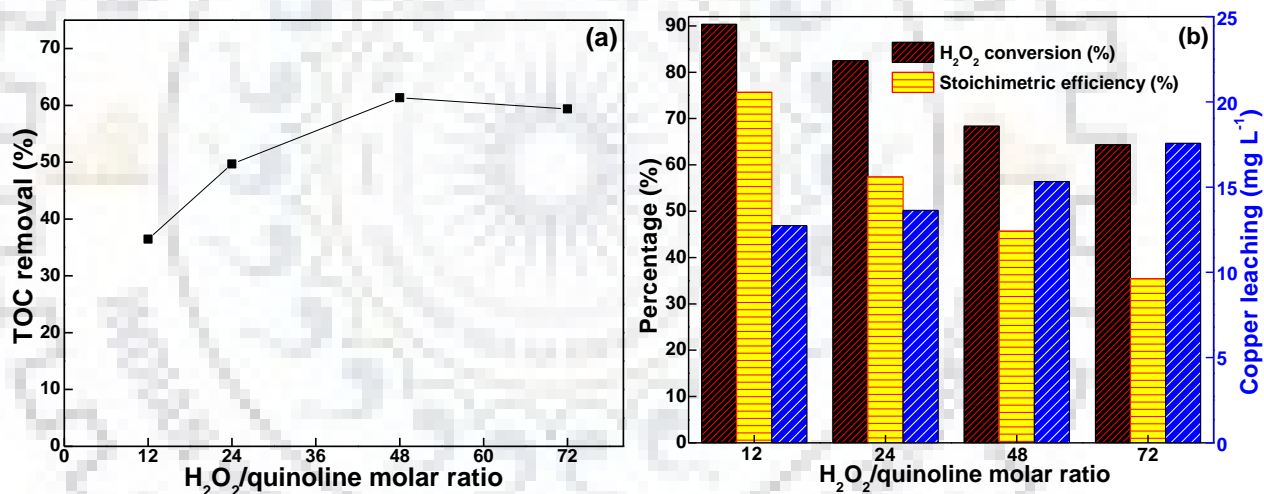

Fig. 5.14: Effect of reactants molar ratio on (a) TOC removal, and (b) H_2O_2 conversion, stoichiometric efficiency and copper leaching of 5CuY$_{IMP}$ at T = 80 °C, pH$_0$ = 7, [Quinoline] = 3.87 mM, LHSV = 4 h^{-1} and particle size = 1.2-1.7 mm

5.3.7. Effect of reaction temperature

Fig. 5.15a illustrates TOC removal as a function of reaction temperature and LHSV during the oxidation of quinoline over 5CuY$_{IMP}$ catalyst. Variation of temperature from 40 to 80 °C at a higher LHSV slightly influences the oxidation of quinoline. Conversely, a large increase in TOC removal was observed for similar increase in temperature at a lower LHSV. For example, at the

low LHSV of 4 h^{-1}, TOC removal enhanced from 27 to 61% when reaction temperature increased from 40 to 80 °C, while TOC removal barely increased with temperature at high LHSV of 16 h^{-1}. Fig. 5.15b depicts that H_2O_2 conversion and stoichiometric efficiency increases from 36.6 to 66.6% and 37.4 to 45.7% with increase in temperature from 40 to 80 °C at LHSV of 4 h^{-1}. Thus, higher rate of decomposition of H_2O_2 into *OH at 80 °C is responsible for the higher TOC removal [Yan et al. 2016]. A fluctuation was noticed as well as low TOC conversion on increasing the temperature above 80 °C. The vapor phase formation and thermal decomposition of H_2O_2 into inactive species (O_2 and H_2O) may be ascribed to this behavior. As shown in Fig. 5.15b, temperature does not significantly affect copper leaching. At low LHSV, the effect of temperature is dominant over mass transfer and thus, it may be concluded that the system is working under chemical kinetic control [Guo et al. 2005; Miladinović et al. 2015]. In contrast to high temperature requirement (> 130 °C) in conventional catalytic wet air oxidation (CWAO), CWPO can be carried out at lower temperature [Valkaj et al. 2011; Esteves et al. 2016], which is in agreement with our findings using Cu/zeolite Y catalyst.
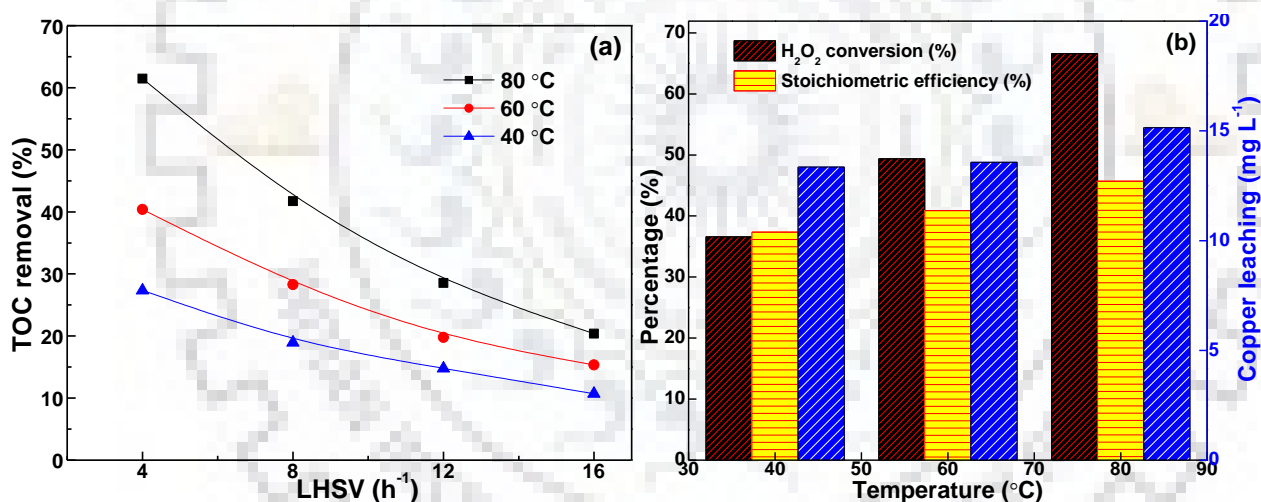
Fig. 5.15: Influence of LHSV and temperature on (a) TOC removal, and (b) H_2O_2 conversion, stoichiometric efficiency and copper leaching of 5CuY$_{IMP}$ at pH$_0$ = 7, [Quinoline] = 3.87 mM, [H_2O_2] = 185 mM and particle size = 1.2-1.7 mm

5.3.8. Mechanistic view and kinetics of the CWPO process

Several experiments were performed at optimized condition to elucidate the contribution of various non-catalytic and catalytic mechanisms in oxidation of quinoline. As shown in Table 5.5, H_2O_2 solely could not degrade quinoline due to its low oxidation potential (E^0 = 1.78 V vs. NHE) [Hassan et al. 2011]. As observed from conversions of both reactants, the role of thermal

decomposition was insignificant at 80 °C. The catalytic activity of supporting material (HY) was examined, which showed almost negligible contribution in H_2O_2 activation and quinoline removal. The quinoline removal by adsorption was very small and in agreement with the finding of no carbonaceous deposits on surface of $5CuY_{AIE}$ and $5CuY_{IMP}$ (*vide supra*). This result may be attributed to similarity between pore size of catalyst (0.78 nm) and kinetic diameter of quinoline (0.65 nm). $5CuY_{PI}$ has shown slightly higher removal by adsorption and may occur due to hierarchical porosity, which enables quinoline molecules to diffuse into pores. The decomposition of hydrogen peroxide was not significantly affected due to addition of quinoline. Relatively less concentration of quinoline compared to that of H_2O_2 may be responsible for this behavior. The contribution of leached Cu ions on catalytic activity has been evaluated and it was shown to be very less for $5CuY_{AIE}$ and $5CuY_{PI}$, whereas $5CuY_{IMP}$ has shown slightly higher quinoline removal of 44.2% (9% TOC) up to 10 h. The removal decreased thereafter because of less leaching (*vide supra*). Hence, it can be deduced that the major role in oxidation of quinoline is played by reaction of H_2O_2 with the copper species immobilized over the surface of zeolite Y, i.e., the heterogeneous mechanism. Homogeneous phase reaction also play minor role in degradation of quinoline in case of $5CuY_{IMP}$.

Table 5.5: Role of different mechanisms in term of quinoline conversion (%) and concentration of mineralized products

Sample ID	Quinoline + H_2O_2	Quinoline + H_2O_2 +HY	Quinoline + catalyst (without H_2O_2)	H_2O_2 + catalyst (without quinoline)	Quinoline + H_2O_2 + leached copper	NO_2^- (mg L^{-1})	NO_3^- (mg L^{-1})	NH_3 (mg L^{-1})
$5CuY_{AIE}$	1.8(3.5)[a]	2.4(4.1)	5.4	(68.7)	25.4(15.3)	22.46	34.25	13.66
$5CuY_{IMP}$	-	-	6.7	(65.3)	44.2(26.4)	19.27	31.51	11.45
$5CuY_{PI}$	-	-	15.9	(78.5)	10.8(6.4)	13.65	26.77	6.74

[a] H_2O_2 conversion (%) is given in brackets ( ). All experiments were carried out at T = 80 °C, pH_0 = 7, [Quinoline] = 3.87 mM, [H_2O_2] = 185 mM, LHSV = 4 h^{-1}, Catalyst = 9.31 g and particle size = 1.2-1.7 mm.

It was observed that the major role in oxidation of quinoline is played by reaction of H_2O_2 with the copper species immobilized over the surface of zeolite Y, i.e., the heterogeneous mechanism. Based on this discussion, a reaction path has been proposed for the generation of reactive species and mineralization of quinoline for $5CuY_{IMP}$ catalyst (Fig. 5.16). Lousada et al. [2012] explain that H_2O_2 adsorption occurs on transition metal oxide prior to its decomposition into adsorbed *OH radical based on experimental and DFT calculation. The catalytic decomposition of hydrogen peroxide proceeds *via* reduction-oxidation inter-conversion of isolated

copper species (Cu^{2+} or Cu^{1+}) on catalyst surface with simultaneous production of surface-bound *OH radical and perhydroxyl radical (HO_2*) [Lousada et al. 2012]. It is well-known fact that *OH radical is the responsible species for the oxidation of organic contaminants [Xu et al. 2012]. However, experiments were carried out to identify the reactive species using tert-butyl alcohol (TBA) as adsorbed *OH probe compound [Lousada et al. 2012; Guan et al. 2013]. As shown in Fig. 5.16, TBA restrained the quinoline degradation and it decreases with increase in the TBA concentration. The inhibition of quinoline degradation verified the generation of *OH radicals in system. The oxidation potential of HO_2* is much lower than *OH and does not contribute in oxidation [Massa et al. 2011]. Since the role of adsorption of quinoline is negligible and *OH radical is highly reactive, quinoline loss would occur at solid-liquid interface.
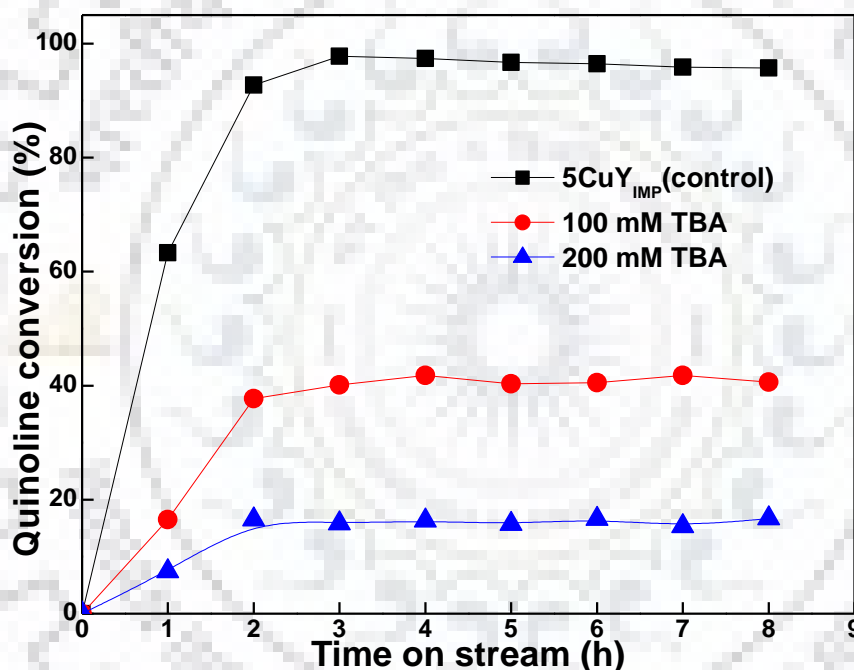
Fig. 5.16: Inhibition effect of radical scavenger on quinoline degradation at T = 80 °C, pH_0 = 7, [Quinoline] = 3.87 mM, [H_2O_2] = 185 mM, LHSV = 4 h^{-1} and particle size = 1.2-1.7 mm

As shown in Fig. 5.17, highly oxidizing adsorbed hydroxyl radicals react with C-C and C-N bonds of rings, break quinoline into low molecular weight organic acids (detected by HPLC analysis), and finally mineralize it into CO_2, N_2 and inorganic ions. Oxalic acid was found in trace amount in liquid. Copper oxalate was not present on surface of catalyst (from XRD analysis), probably because the high temperature promotes the mineralization of oxalic acid to CO_2. To further verify the mineralization of quinoline, the concentrations of NH_3, NO_2^- and NO_3^- were measured by ion chromatography (Table 5.5). According to mass balance on nitrogen atom, around

54-61% of total nitrogen transformed into N_2 gas. The formation of N_2 gas has also been reported by other researchers during CWPO of nitrogenous pollutants [Zoha et al. 2002; Subbaramaiah et al. 2013,].

As discussed earlier, the TOC removal increases with temperature and concentration of reactants. The influence of internal and external diffusions may be ignored in the selected range of parameters. It was also observed that the adsorption of quinoline on $5CuY_{IMP}$ is negligible and a strong interaction (chemisorption) exists between the catalyst and H_2O_2. FTIR analysis is in agreement with it due to finding of no carbonaceous deposits on surface of used $5CuY_{IMP}$ catalyst.
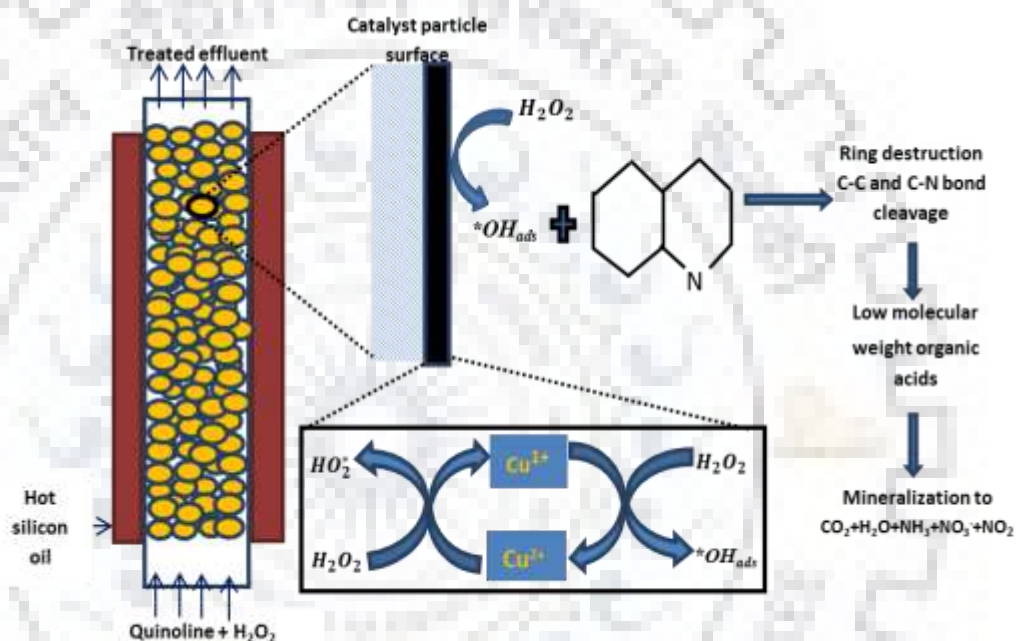
Fig. 5.17: Proposed mechanism of CWPO of quinoline on 5CuY$_{IMP}$

Recently, DFT study suggests that *OH radicals remain adsorbed on catalyst surface by forming bonds with metal cations [Lousada et al. 2012]. Since *OH radicals are highly reactive (life is in nanoseconds), they must be completely reacted with H_2O_2 and organic species on catalyst surface prior to diffusing into liquid phase. According to these experimental results, it may be assumed that mineralization of quinoline is surface reaction controlling. It follows Eley-Rideal mechanism, in which the reaction occurs between adsorbed *OH radical and quinoline molecule in liquid phase. Since quinoline is not adsorbing onto surface of catalyst, the degradation of quinoline should not follow Langmuir-Hinshelwood mechanism. The proposed mechanism for quinoline mineralization may be represented as follows:

$$[CuY] + H_2O_2 \overset{K_1}{\leftrightarrow} [CuY.HO^*] \quad (Fast) \tag{5.i}$$

$$[CuY.HO^*] + Q(l) \overset{k}{\rightarrow} [CuY.Prod] \quad (Slow) \tag{5.ii}$$

$$[CuY.Prod] \overset{K_2}{\leftrightarrow} [CuY] + Prod \quad (Fast) \tag{5.iii}$$
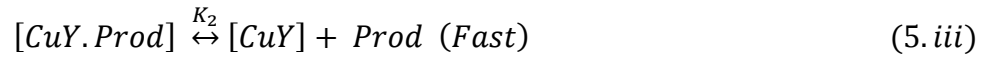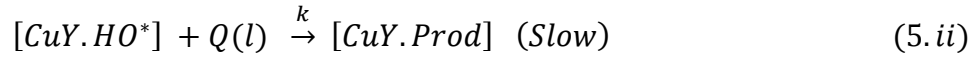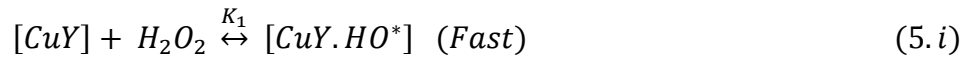
Here, [CuY] represents the concentration of vacant active sites of catalyst; [CuY.HO*] and [CuY.Prod] represents the sites adsorbed by HO* and products, respectively; K_1 and K_2 signify the adsorption and desorption equilibrium constants, respectively, and k represents the surface reaction constant. The HO* associated with active sites has also been shown by Liang et al. [2012]. The rate law for mineralization of quinoline, assuming Eley-Rideal mechanism, can be expressed as

$$r = \frac{kK_1 C_{H_2O_2} C_Q}{1 + K_1 C_{H_2O_2} + K_2 C_{Prod}} \tag{5.3}$$

As observed from the experimental results, the adsorption of products is negligible and thus, $K_2 C_{Prod}$ can be ignored. The above rate law can be reduced as

$$r = \frac{kK_1 C_{H_2O_2} C_Q}{1 + K_1 C_{H_2O_2}} \tag{5.4}$$

As discussed above, the H_2O_2 concentration was very high in our experiments $\left(K_1 C_{H_2O_2} \gg 1\right)$. Therefore; Eq. 5.4 can be simplified to first order rate law:

$$r = kC_Q \tag{5.5}$$

The proposed mechanism with its simplified rate equation (Eq. 5.5) was test in performance equation of plug flow reactor (Eq. 5.6) and integral analysis was used to develop linear relationship.

$$\frac{W}{F_{Q0}} = \int_0^{X_Q} \frac{dX_Q}{r} \tag{5.6}$$

$$\left(\frac{1}{C_{Q0}} ln \frac{1}{1 - X_Q}\right) = k\left(\frac{W}{F_{Q0}}\right) \tag{5.7}$$

Fig. 5.18a shows that both terms in parentheses have linear relationship at different temperature. These results indicate that Eley-Rideal mechanism is in good agreement with experimental data. The Eley-Rideal mechanism has also been reported by He et al. [2014] and Furman et al. [2009] during degradation of pollutants on chromium substituted magnetite and birnessite, respectively. The slopes of straight lines were used to determine the rate constants (k) and shown in Table 5.6. The highest value of rate constant for mineralization of quinoline was estimated to be 6.12 L h^{-1} Kgcat^{-1} at 80 °C. Activation energy (E$_a$) of mineralization of quinoline

was estimated using Arrhenius equation ($k = k_0 exp^{\frac{-Ea}{RT}}$, Fig. 5.18b) and found 23.21 KJ mol^{-1}. These kinetic parameters cannot be compared since no kinetic study has been reported for CWPO of any pollutant in continuous fixed bed reactor. Activation energy has been observed higher than diffusion limited reactions, which usually exist in range 10-13 kJ mol^{-1} [Lin et al. 1998].

Table 5.6: Kinetic parameters for mineralization of quinoline

Temperature (°C)	k	R^2	E_a (kJ mol^{-1})	R^2
40	2.22	0.97		
60	3.51	0.98	23.21	0.99
80	6.12	0.99		
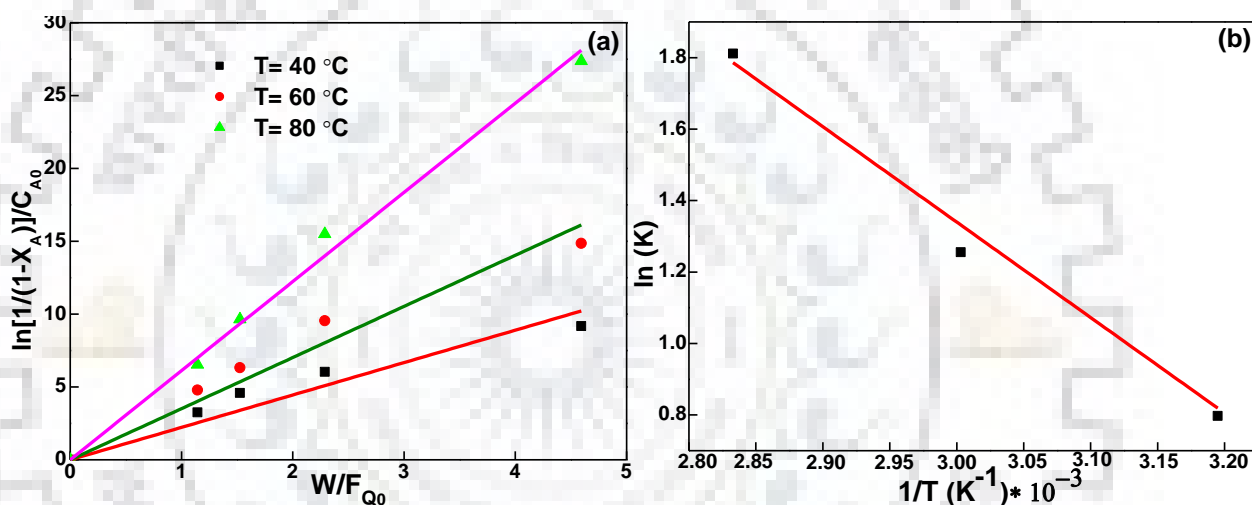
Fig. 5.18: Kinetic study of mineralization of quinoline

5.4. SUMMARY

Aqueous ion-exchange, wet-impregnation and precipitation-impregnation methods were used for the preparation of Cu/Zeolite Y catalysts and these catalysts were tested for continuous CWPO of recalcitrant quinoline. 5CuY$_{AIE}$ and 5CuY$_{IMP}$ manifested higher mineralization efficiencies in comparison to 5CuY$_{PI}$. The presence of isolated species, which exhibited high activity for H$_2$O$_2$ conversion into highly oxidizing HO* radical due to their properties of high mobility of charge carriers, was responsible for high removal efficiencies of 5CuY$_{AIE}$ and 5CuY$_{IMP}$. On the contrary, the lower (removal) efficiency of 5CuY$_{PI}$ was due to large crystallites of CuO, which promote decomposition of H$_2$O$_2$ to inactive O$_2$ and H$_2$O species. 5CuY$_{AIE}$ and 5CuY$_{IMP}$ were observed with high operational stability up to 250 h and found with high resistance towards copper leaching and carbon residues deposition. Because of high environmental benignity, greater control over copper

loading and comparable catalytic activity performance, the wet impregnation method has been selected as a better alternative to complex ion-exchange method. The parameters optimization reveals that the maximum catalytic performance are achieved under the following optimized condition: LHSV 4 h^{-1}, temperature 80 °C, Initial pH 7, H_2O_2 concentration of 185 mM, quinoline concentration of 3.87 mM and particle size 1.2-1.7 mm. This research showed that the Cu/zeolite Y synthesized by wet-impregnation can be a viable option for effective mineralization of a complex substrate. The chemical kinetics of CWPO of organic pollutant followed Eley-Rideal mechanism. This kinetic study can be used further for the development of CWPO process using fixed-bed reactor.

ULTRAFAST SONOCHEMICAL SYNTHESIS OF COPPER HYDROXYPHOSPHATE AND COPPER PHOSPHATE FOR CATALYTIC WET PEROXIDE OXIDATION OF ANILINE IN AQUEOUS SOLUTION

6.1. OVERVIEW

This chapter includes a detailed discussion on ultrafast sonochemical synthesis of copper hydroxyphosphate (Cu_2OHPO_4 (CHP)) and copper phosphate ($Cu_3(PO_4)_2$, (CP)) with controllable morphologies. The most common approach for the synthesis of CHP and CP has been the hydrothermal method which requires long reaction time of 6 h to 72 h. However, the sonochemical synthesis route took 1-2 h which is considerably shorter than the reaction time by any other reported methods. Different nano-architectures were prepared by adjustment of sonication energy and time, and characterized by XRD, N_2 sorption, FESEM, TEM and FT-IR. Copper hydroxyphospahte was obtained at pH 5, and copper phosphate was formed at pH = 3 and pH = 7 only in 2h. The as- synthesized materials were examined and compared in terms of catalyst activity and stability for the catalytic wet peroxide oxidation (CWPO) of aniline in batch reactor. Nanospindles-like hierarchical architecture shows the highest catalytic activity and stability for oxidative removal of aniline.

6.2. SONOCHEMICAL SYNTHESIS OF COPPER HYDROXYPHOSPHATE AND COPPER PHOSPHATE

The sonochemical synthesis of copper hydroxyphosphate and copper phosphate was strongly dependent upon pH. Nanoparticles of different sizes and morphologies were obtained through variation in sonication time and sonication energy. The mechanistic study show that $Cu_3(PO_4)_2$ come into existence initially *via* the reaction between Cu^{2+} and PO_4^{3-}, then get transformed to Cu_2OHPO_4 between 30-45 min depending upon the amplitude of sonochemical radiation. The samples are labeled as CHP-pH-A-t or CP-pH-A-t according to the initial pH of reaction solution, amplitude of sonochemical irradiation (A) and sonication time (t).

6.2.1. Structural characterization of CPs and CHPs

Fig. 6.1 shows the XRD pattern of samples prepared at different pH and sonication energy. The XRD patterns of CHP-5-20-2 and CHP-5-70-2 samples are similar to standard data of copper hydroxyphosphate or synthetic libethenite compound (PDF- 000360404). These samples have orthorhombic crystal system characterized with space group Pnnm and unit cell parameters a = 8.063 Å, b = 8.398 Å, and c = 5.887 Å. XRD patterns of CP-3-70-2 and CP-7-70-2 match with the

standard data of $Cu_3(PO_4)_2.3H_2O$ (PDF-000220548). No additional peaks of other phase have been found in XRD patterns, signifying the high purity of final products [He et al. 2015]. These results revealed that initial pH had strong effect on phase formation. The use of any alcohols (ethanol, glycerol, ethylene glycol) and organic precursors (copper acetate, etc.) led to the formation of $Cu_3(PO_4)_2$ even at pH = 5. A clear insight of this effect has been presented through mechanism of the ultra-sonication route in subsequent section.
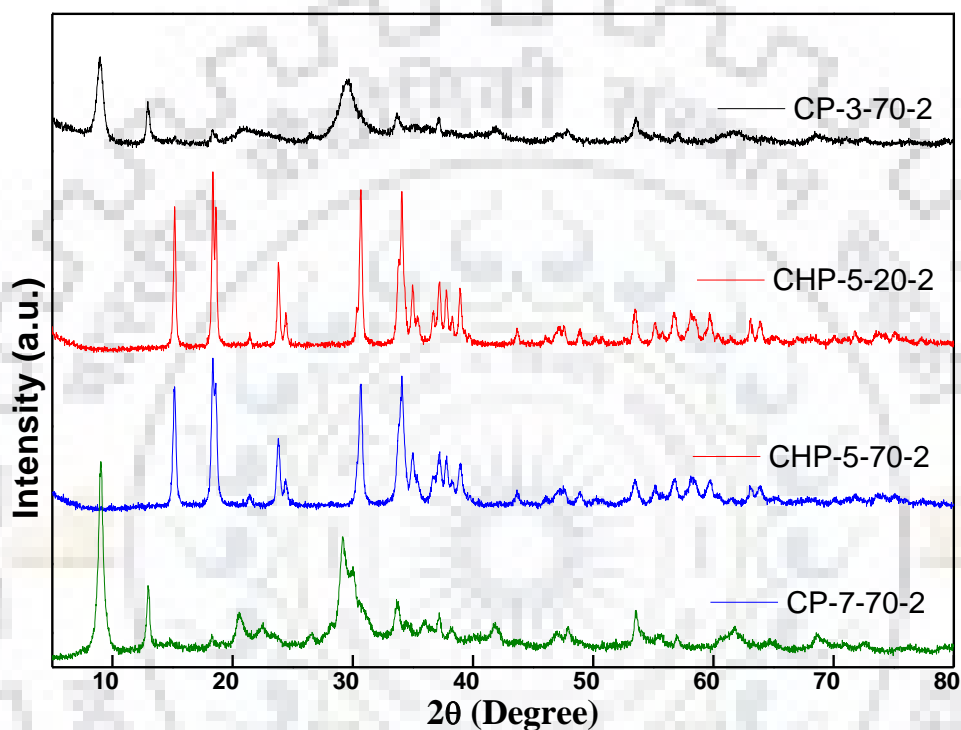
Fig. 6.1: X-ray diffraction pattern of $Cu_3(PO_4)_2$ and Cu_2OHPO_4 nanoarchitectures synthesized by sonochemical method

FTIR analysis was performed to further confirm the successful synthesis of CHP and CP framework (Fig. 6.2). The broad band in range 2700-3700 cm^{-1} and the sharp band at 3470 cm^{-1} indicates two different kinds of hydroxyl groups in CP and CHP samples. In CP-3-70-2 and CP-7-70-2 samples, the broad band existed due to stretching vibration of hydroxyl group of structural water in $Cu_3(PO_4)_2.3H_2O$. However, the characteristic sharp band at 3470 cm^{-1} in CHP-5-70-2 and CHP-5-20-2 samples can be indexed to stretching vibrations of hydroxyl group of copper hydroxy phosphate framework. The FTIR spectra of CHP-5-70-2 and CHP-5-20-2 samples were almost identical. In these samples, the band at 811 cm^{-1} is related to bending vibrations of hydroxyls group of copper hydroxy phosphate [Chen et al. 2015]. The presence of phosphate in these CHP

samples is evident by the band at 557, 610 and 644 cm^{-1} which correspond to ν_4 bending mode of phosphate [Zhao et al. 2015].
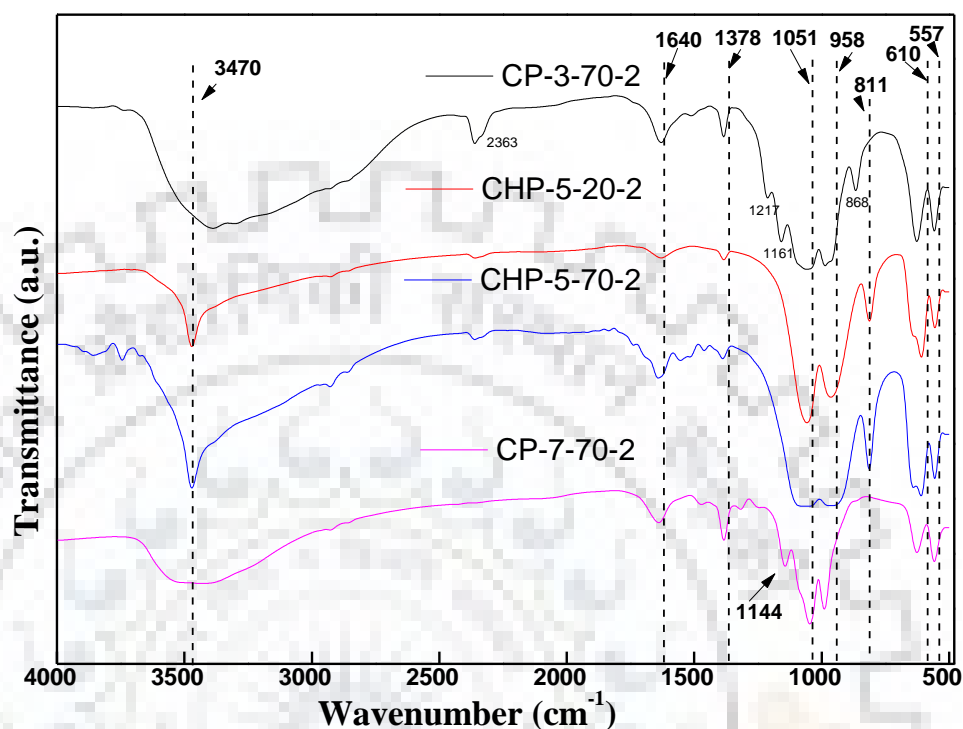
Fig. 6.2: FTIR spectra of Cu$_3$(PO$_4$)$_2$ and Cu$_2$OHPO$_4$ nanoarchitectures synthesized by sonochemical method

Table 6.1: Complete assignment of FTIR bands for Cu$_3$(PO$_4$)$_2$ and Cu$_2$OHPO$_4$ nanoarchitectures synthesized by sonochemical method

Samples	Wavenumber (cm^{-1})	Functional groups
CHP-5-70-2 and CP-5-20-2	557, 610, 644	Bending mode of phosphate
	811	Bending vibration of hydroxyls in framework
	958	Symmetric stretching of PO$_4^{3-}$
	1051	Asymmetric stretching of PO$_4^{3-}$
	1378	Stretching vibration of P=O
	3470	stretching vibrations of hydroxyls in framework
CP-3-70-2 and CP-7-70-2	557, 625	Bending mode of O-P-O bond in phosphate
	992	Symmetric stretching of PO$_4^{3-}$
	1051	Asymmetric stretching of PO$_4^{3-}$
	1144	Asymmetric stretching of PO$_4^{3-}$
	1378	Stretching vibration of P=O
	2700-3700	stretching vibration of hydroxyl group of structural

water

In all samples, the bands located at 958 and 1051 cm^{-1} can be attributed to symmetric (ν_1) and asymmetric (ν_3) stretching of PO_4^{3-}, respectively [He et al. 2015]. In addition, all samples exhibit bands at 1378 cm^{-1} which correspond to P=O stretching vibration. These results confirm the presence of hydroxyl and phosphate group in CHP samples. The bands located at 625 and 557 cm^{-1} in CP-3-70-2 and CP-7-70-2 can be assigned to ν_4 bending mode of O-P-O bond [Rong et al. 2017]. A weak band at 2363 cm^{-1} in all samples is attributed to the atmospheric CO_2. Complete assignments of the bands are given in Table 6.1.

6.2.2. Textural investigations of CPs and CHP

The N_2 sorption isotherms of CP-3-70-2, CHP-5-70-2 and CP-7-70-2 samples are shown in Fig. 6.3. The resulting isotherms of all specimens display IUPAC type-III isotherms with H3 hysteresis loop [Mosayebi et al. 2012]. This kind of hysteresis appears because of slit-like pores with non-uniform shape and/or size [Chowdhury et al. 2016]. The BJH pore size distributions (PSDs) estimated from desorption branch of isotherms are shown in Fig. 6.4.
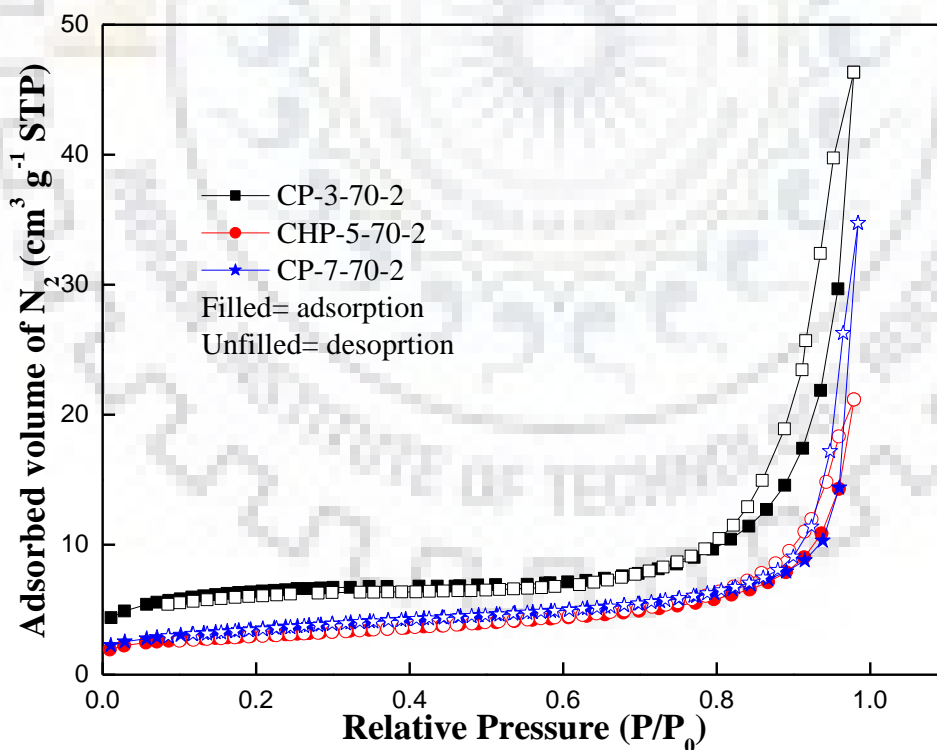
Fig. 6.3: N_2 sorption isotherms of $Cu_3(PO_4)_2$ and Cu_2OHPO_4 nanoarchitectures synthesized by sonochemical method
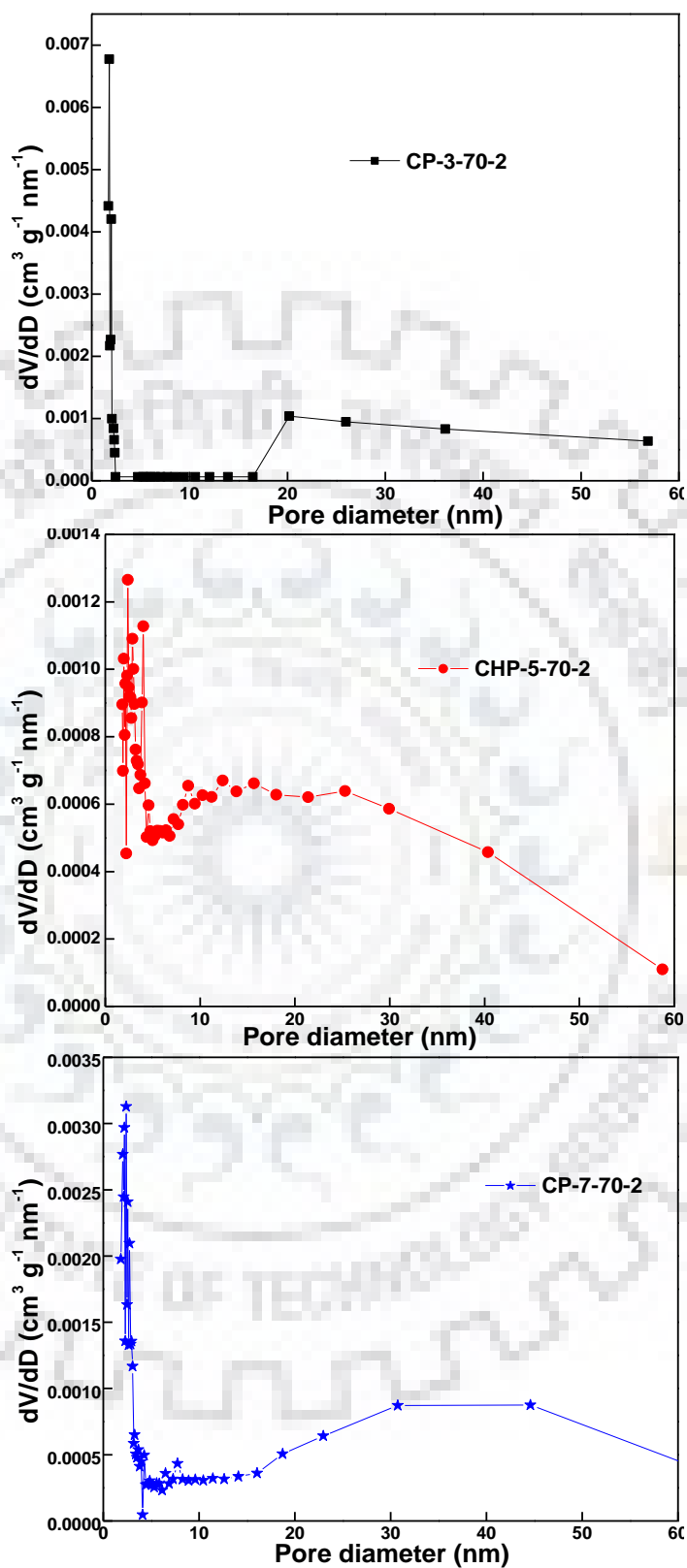
Fig. 6.4: BJH pore size distribution of Cu₃(PO₄)₂ and Cu₂OHPO₄ nanoarchitectures synthesized by sonochemical method

All samples exhibit wide PSD curves and this behavior confirms the presence of irregular size and shape of the pores. Both characteristics (type-III isotherm and PSD curves) suggest the coexistence of macropores and mesopores in samples. The textural properties (specific surface area, total pore volume and the average pore diameter) of all samples are summarized in Table 6.2.

The BET surface area and total pore volume increased in the order of CHP-5-20-2 < CHP-5-70-2 < CP-7-70-2 < CP-3-70-2 and observed higher for CP samples in comparison to CHP. These results indicate the higher porous structure of CP in comparison to CHP. Higher porosity of CP may also be attributed to its smaller pore size and particles size (*vide infra*). The smaller particles size causes higher interparticle porosity in $Cu_3(PO_4)_2$ in comparison to Cu_2OHPO_4 samples.

Table 6.2: Textural parameters of $Cu_3(PO_4)_2$ and Cu_2OHPO_4 nanoarchitectures synthesized by sonochemical method

Sample ID	S_{BET} [a]$(m^2\ g^{-1})$	V_p [b]$(cm^3\ g^{-1})$	D_{BJH} [c](nm)
CP-3-70-2	20.78	0.07	3.75
CHP-5-70-2	10.11	0.03	12.9
CHP-5-20-2	7.98	0.01	16.7
CP-7-70-2	12.17	0.05	5.67

[a] BET surface area, [b] Total pore volume, [c] Pore diameter using BJH method

6.2.3. FESEM/EDAX analysis of CPs and CHP

FESEM images shown in Fig. 6.5 depict the morphological characteristics of samples prepared by sonication method at different pH and sonication energy. The SEM image of CP-3-70-2 in Fig. 6.5a reveals the aggregations of thin nanoflakes of size 100-200 nm. The morphology of CHP-5-70-2 is shown in Fig. 6.5b. It can be clearly observed that small nanorods of size ~50 nm were self-assembled to larger nanospindles-like hierarchical architecture of size 500-700 nm. Additionally, at pH = 5, the change of sonication energy also affected the morphology of Cu_2OHPO_4. For illustration, when the sonication amplitude was decreased from 70% to 20%, the morphology of corresponding material changed from nanospindles-like hierarchical architecture to beautiful one dimensional nanorods of size 800-1200 nm (Fig. 6.5d). On the other hand, thick nanoflakes of size around 100-200 nm were generated for CP-7-70-2 at pH = 7 (Fig. 6.5c). XRD and FESEM results revealed that initial pH had important role on phase formation as well as morphologies of the final products.
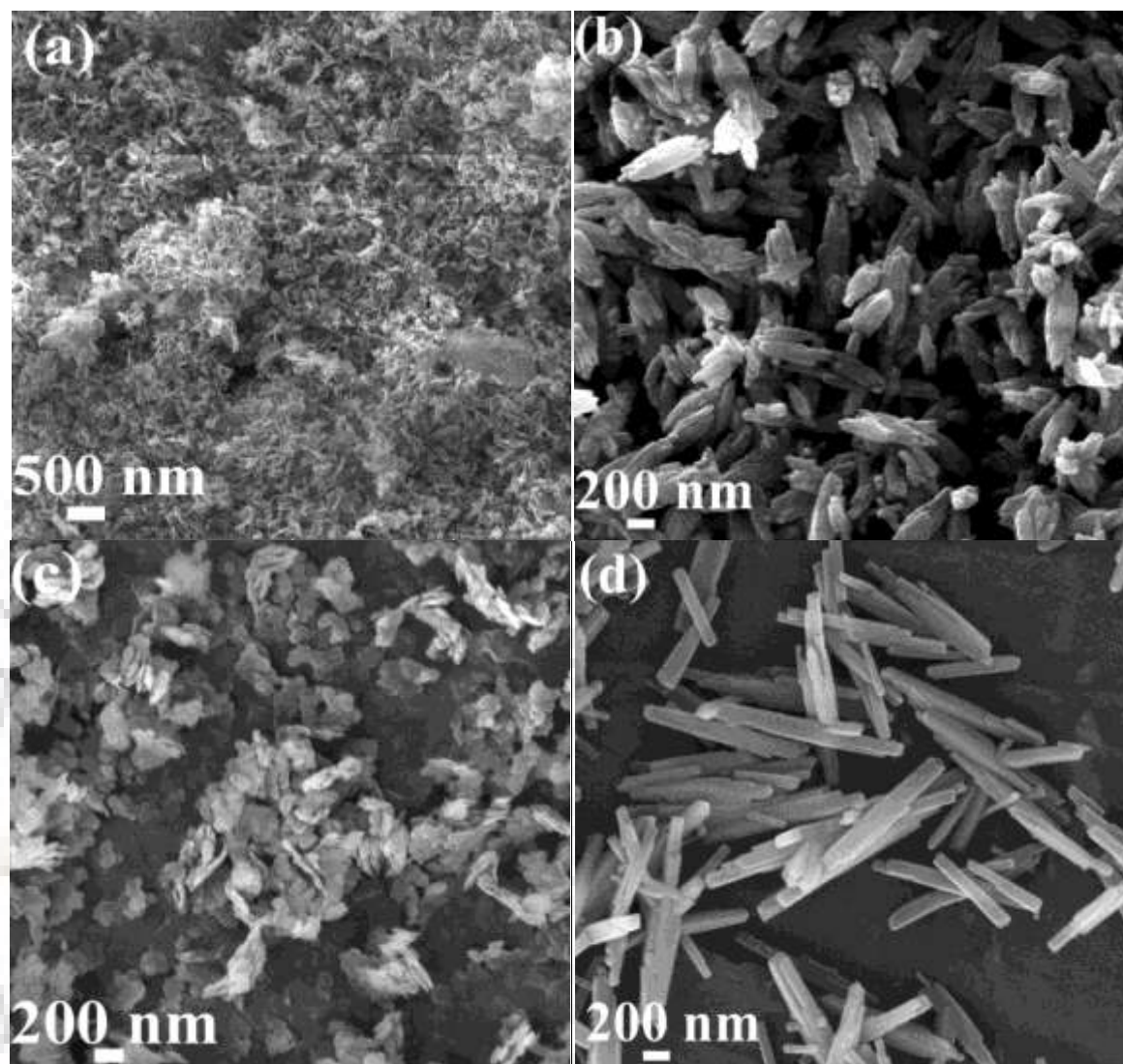
Fig. 6.5: FESEM images of (a) CP-3-70-2, (b) CHP-5-70-2, (c) CP-7-70-2 and (d) CHP-5-20-2

TEM images as shown in Fig. 6.6 further confirmed the morphology of different samples. Fig 6.6a shows TEM image of CP-3-70-2 sample which depicts the aggregation of flake-like nanocrystals of about 100-200 nm size. It could be clearly seen from Fig. 6.6b that CHP-5-70-2 is composed of nanospindles-like hierarchical architectures of size 500-700 nm. These hierarchical nanostructures were further composed of small 1D nanorods of size ~50 nm. These results corroborate the observation of small nanorods in CHP-5-70-2 sample through FESEM analysis. Fig. 6.6c shows the presence of individual one dimensional nanorods of size 800-1200 nm for CHP-5-20-2. The results are in good agreement with FESEM images. The selected area electron diffraction (SAED) pattern of CHP-5-70-2 sample shows clear diffraction spot array, which

indicates that each nanorod is single crystalline [Zhou et al. 2009]. The single crystalline nature can also be observed from clear lattice fringes.
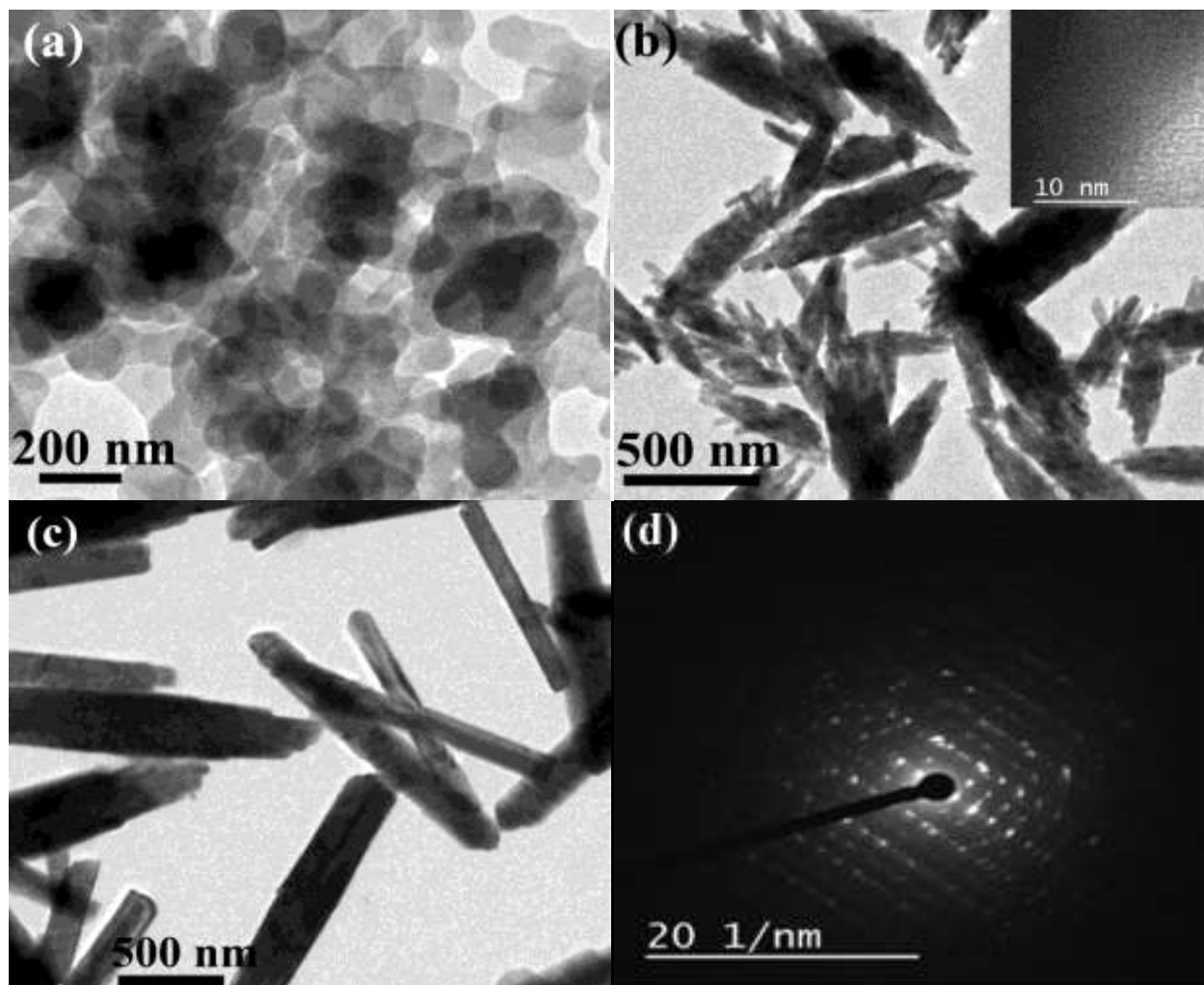
Fig. 6.6: TEM image of (a) CP-3-70-2, (b) CHP-5-70-2, (c) CHP-5-20-2, (d) SAED pattern of CHP-5-70-2. HRTEM image shows lattice fringes of CHP-5-70-2 in inset of Fig. 6.6(b)

6.2.4. Mechanism for the formation Cu_2OHPO_4

In order to understand the formation mechanism and morphological evolution of Cu_2OHPO_4 nanospindles-like hierarchical architecture, the growth stages were systematically studied by XRD and FESEM analysis. Fig. 6.7 depicts the XRD pattern of the samples prepared at different sonication time (t = 15, 30, 45, 90, and 120 min). After sonication time of 15 min, the diffraction peaks of synthesized sample can be indexed as $Cu_3(PO_4)_2.3H_2O$ (PDF-000220548). These peaks further become slightly sharp and narrow with increase in sonochemical time to 30 min, which

indicate the small increase in crystallite size. A complete transformation of $Cu_3(PO_4)_2$ to pure and highly crystalline Cu_2OHPO_4 was observed after sonication time of 45 min. These result suggest that $Cu_3(PO_4)_2$ is formed in the beginning and then transformed into the Cu_2OHPO_4. After sonication time of 45 min, the color of suspension becomes pale green and pure Cu_2OHPO_4 was generated. The peaks become broader and intensity decreased on further increase in the irradiation time, indicating decrease in the average crystallite size. On the contrary to hydrothermal method, the average crystallite size of Cu_2OHPO_4 reduces with increase in sonication time.
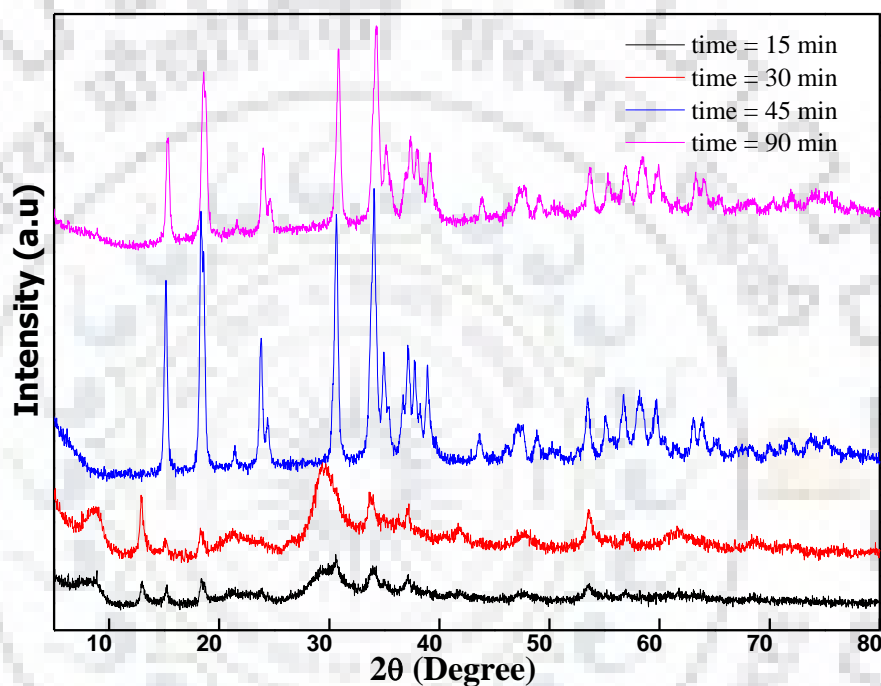
Fig. 6.7: X-ray diffraction pattern showing formation mechanism of Cu_2OHPO_4 nanoarchitectures as a function of time

The morphological evolution of nanospindle-like hierarchical architecture has been presented in Fig. 6.8. FESEM images were taken at low and high magnifications for the in-depth analysis of generated morphologies. Fig. 6.8 reveals that the sample $t = 15$ min consists of spheres of average diameter of 4μm. FESEM images at high magnification shows that these $Cu_3(PO_4)_2$ microspheres exhibit hierarchical structure and comprise of several self-assembly nanoflakes of uniform size ~ 200 nm. After 30 min of sonication time, the size of nanoflakes decreased to 100 nm. The sample generated after 45 min contains a mixture of nanospheres (diameter = 300-500 nm) and nanospindles (length = 800-1300 nm) of Cu_2OHPO_4. These nanospindles consist of oriented assembly of nanorods of size 200 nm. FESEM image at high magnification shows that nanospindles are obtained in large quantity with good uniformity after sonication period of 90 min.

The size of nanospindles decreases from 800-900 nm to 500-700 nm with an increase in sonication time from 90 to 120 min. This decrement in size occurs because of reduction in the size of self-assembled nanorods from 100-150 nm to 60-100 nm.
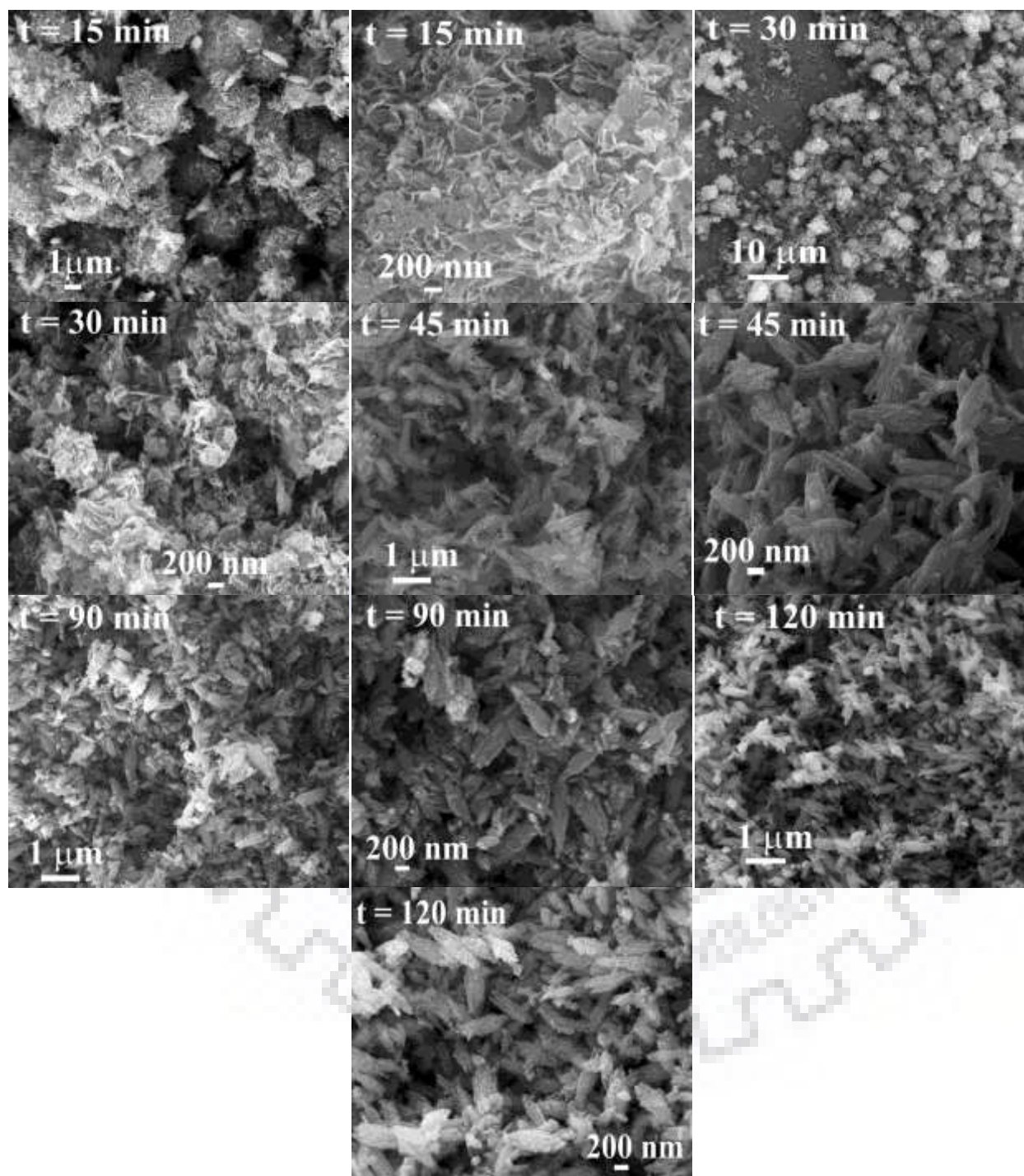
Fig. 6.8: Formation mechanism of Cu$_2$OHPO$_4$ nanoarchitectures as a function of time

As explained above, Cu$_3$(PO$_4$)$_2$ come into existence initially *via* the reaction between Cu^{2+} and PO$_4^{3-}$ under assistance of sonochemical irradiation. Ultrasonic irradiation of water generates

138

highly reactive *OH and H* species. These *OH radicals are thought to be responsible for transformation of $Cu_3(PO_4)_2$ into Cu_2OHPO_4 at pH = 5. These *OH radicals have a high affinity to react with organic compounds and can be easily quenched using alcohols. Therefore, the use of any alcohols (ethanol, glycerol, ethylene glycol) and organic precursors (copper acetate, etc.) lead to the formation of $Cu_3(PO_4)_2$ instead of Cu_2OHPO_4 even at pH = 5.

6.3. CATALYTIC ACTIVITY STUDIES

6.3.1. Screening tests

The catalytic activity of CP and CHP samples has been studied in this section. Fig. 6.9 shows the CWPO performances of these catalysts in terms of aniline degradation, TOC removal, H_2O_2 conversion and copper leaching. The catalytic activity increased in the order of CP-3-70-2 < CP-7-70-2 < CHP-5-20-2 < CHP-5-70-2. The CHP samples show higher catalytic activity than the CP samples, although CP-3-70-2 and CP-7-70-2 samples possess higher surface areas (Table 6.2). These results indicate that specific surface area is not a predominate factor for comparison of catalytic activities of CP and CHP samples. The higher catalytic activity of the CHP sample may be attributed to hydroxyl group attached with copper atoms in the framework. This hydroxyl group in crystalline structure increases redox activity and favors the generation of more hydroxyl radicals. These additional radicals further increase the degradation rate of pollutants. In addition, various researchers reported that hydroxyl group in framework favors the conversion of H_2O_2 to hydroxyl radicals [Meng et al. 2003; Zhao et al. 2015].

The CHP-5-70-2 exhibits slightly higher aniline removal (99.86%) in comparison to CHP-5-20-2 (98.67%) after 2 h. In addition, CHP-5-70-2 attains the higher TOC removal of 74.73% in comparison to 70.22% of CHP-5-20-2 after 6 h (Fig. 6.9b). Similarly, a higher H_2O_2 conversion of 68.84% was observed for former sample in comparison to 62.46% of the later. The higher overall catalytic activity of CHP-5-70-2 can be ascribed to the more compact architecture consisting of smaller nanorods and slightly higher surface area, which facilitate more active centers. These smaller nanorods provide high mobility of charge carriers within the CHP framework and improved redox activity. These properties are responsible for effective generation of highly reactive hydroxyl radicals (*OH) from hydrogen peroxide. The high conversion of H_2O_2 also confirms the high redox catalytic activity of CHP-5-70-2. As shown in Fig. 6.9b, all samples show high resistance for copper leaching. The minimum leached copper concentration of 0.8-1.4 mg L^{-1} was noticed for CHP samples after 6 h. Due to highest catalytic activity and stability, CHP-5-70-2

was selected as the best catalysts for CWPO of aniline and used for further studies for the optimization of operating parameters. During the run time, the color of slurry changed from its initial white color to lemon yellow and finally a transparent solution appeared after settling of catalyst slurry.

Fig. 6.9: Effect of CP and CHP samples on (a) aniline degradation, and (b) TOC removal, H$_2$O$_2$ conversion and leached copper concentration at pH = 7, H$_2$O$_2$ = 2.4 mL, catalyst = 1 g L^{-1}, T = 80 °C, and aniline = 1.07 mM

6.3.2. Effect of initial pH

The influence of initial pH was studied on degradation and mineralization of aniline in the range 5 to 11 and shown in Fig. 6.10. A complete removal of the aniline was noticed at pH$_0$ = 7 in 150 min. The aniline removals at pH 5, 9 and 11 are 98.67%, 97.72% and 94.34, respectively. At pH = 11, the rate of degradation was slower in comparison to other pH conditions. Similar trend was also observed for mineralization efficiency. Fig. 6.10b shows that the TOC removal increases from 70.65 to 74.73% with an increase in pH from 5 to 7. However, TOC removals decrease from 66.78% to 47.73% with an increase in pH from 9 to 11. Similar conclusions have been reported by other researchers from various studies using copper as active phase in oxidation of organic pollutants [Lin et al. 2005; Zhan et al. 2010]. The low catalytic activity at higher alkaline conditions has been described in *section 4.3.4 of Chapter IV* on the basis of involvement of various side reactions (*Eqs. 4.3 and 4.7 of Chapter IV*). As observed in previous studies, the catalyst manifests the maximum leaching in acidic condition i.e. at pH = 5. The concentration of leached

copper decreases from 5.4 to 0.6 mg L^{-1} with increase in initial pH from 5 to 11, respectively. As shown in Fig 6.11 the pH of solution decreases with time and the final pH of reaction solution is less than initial pH. This decrement of solution pH may be ascribed to the formation of low molecular weight organic acids and mineral acid such as HNO_3 formed due to oxidation of amino groups [Karkmaz et al. 2004]. In view of the high catalytic activity, high selectivity for generation of *OH radicals and low leaching of active phase, initial pH = 7 was selected as optimum condition and used in the subsequent studies.

Fig. 6.10: Effect of initial pH on (a) aniline degradation, and (b) TOC removal, H_2O_2 conversion and leached copper concentration at H_2O_2 = 2.4 mL, catalyst = 1 g L^{-1}, T = 80 °C, and aniline = 1.07 mM for CHP-5-70-2
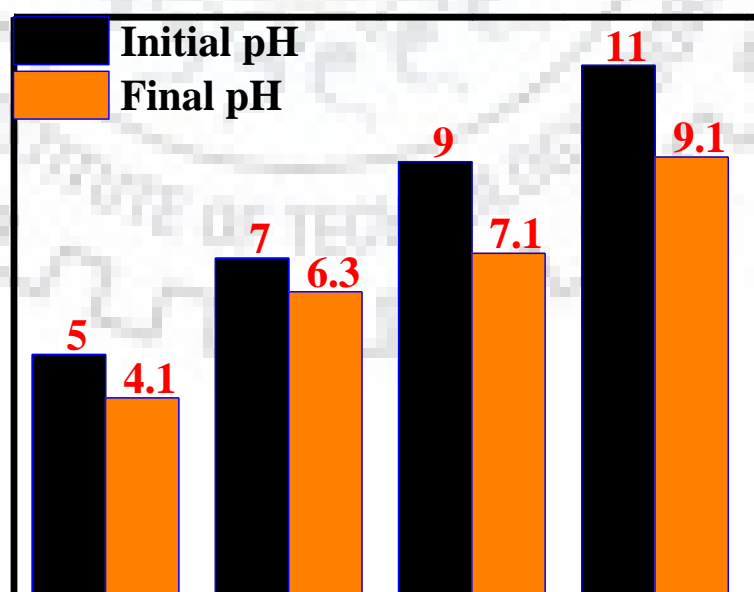
Fig. 6.11: Effect of initial pH of solution on final pH at t = 6 h

6.3.3. Effect of H₂O₂ amount

The effect of H_2O_2 amount on aniline degradation, TOC removal, H_2O_2 conversion and copper leaching is shown in Fig. 6.12. Since H_2O_2 act as a source of *OH radical and directly control its concentration, the H_2O_2 amount has a strong effect on the oxidation of pollutant. Fig. 6.12a shows that the aniline degradation increases from 90.43 to 99.89% with increase in H_2O_2 amount from 0.4 to 2.4 mL. Likewise, the TOC removal increases from 62.65 to 74.73% with an increase in H_2O_2 concentration from 0.4 to 2.4 mL. However, both response parameters decrease with further increase in H_2O_2 amount to 3.2 mL. This reduction in catalytic activity at higher amount of H_2O_2 can be attributed to undesirable quenching of *OH radicals with itself (*Eq. 4.4 of Chapter IV*) or by the excessive H_2O_2 (*Eq. 4.5 of Chapter IV*) [Zhan et al. 2010]. Thus, the H_2O_2 amount of 2.4 mL has been considered as optimum. As expected, the H_2O_2 conversion decrease from 82.43 to 48.52% with an increase in H_2O_2 amount from 0.4 to 3.2 mL. The leached copper concentration was also measured at different H_2O_2 amounts and it varies in the range of 1.2-1.7 mg L^{-1}, even after increasing H_2O_2 amount 8 times. As observed in our previous studies, almost negligible influence of H_2O_2 amounts on copper leaching was identified.
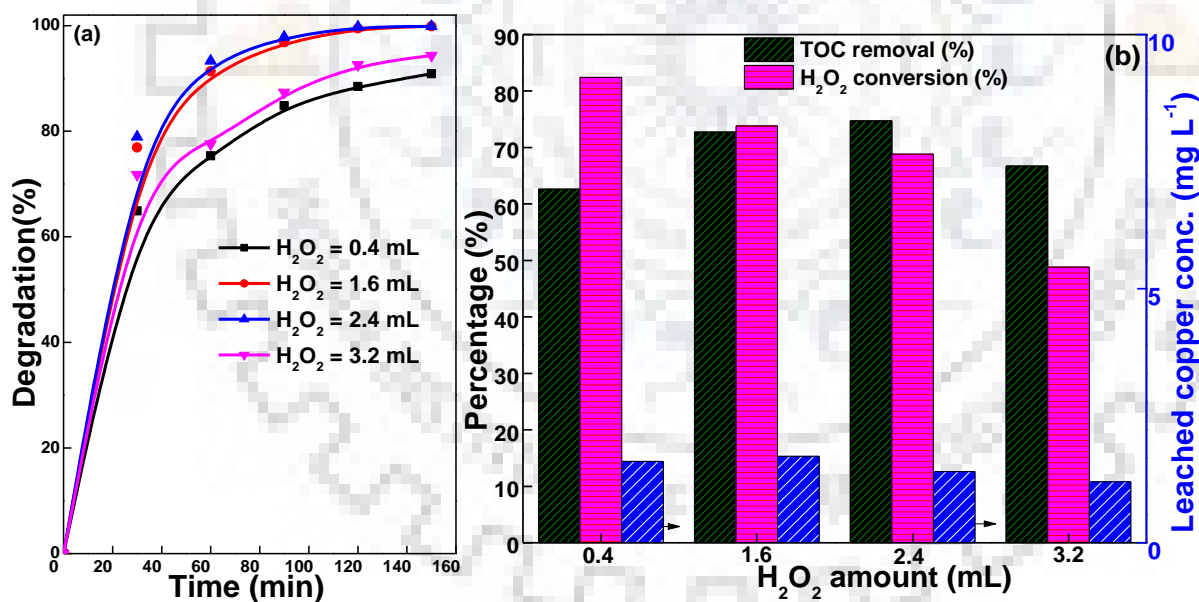
Fig. 6.12: Effect of H₂O₂ amount on (a) aniline degradation, and (b) TOC removal, H₂O₂ conversion and leached copper concentration at pH₀ = 7, catalyst = 1 g L⁻¹, T = 80 °C, and aniline = 1.07 mM for CHP-5-70-2

6.3.4. Effect of catalyst concentration

In order to explore the effect of catalyst concentration on catalytic activity, experiments were conducted with five different catalysts concentrations (0.3, 0.6, 1.0, 1.5 and 2.0 g L^{-1}). Fig. 6.13

shows the effect of catalysts concentration on aniline degradation, TOC removal, H_2O_2 conversion and copper leaching. It was observed that aniline degradation and TOC removal increased from 91.89 to 99.89% and 63.65 to 74.73%, respectively, with increase in catalyst concentration from 0.6 to 1.0 g L^{-1}. The catalytic activity improves because of increase in number of available active centers responsible for the transformation of H_2O_2 to *OH radicals [Ramirez et al. 2007]. However, both response factors decreased from 99.89 to 94.34% and 74.73 to 62.78%, respectively, on further increased of catalyst concentration from 1 to 2 g L^{-1}. This reduction in catalytic performance may be attributed to quenching of *OH radicals with excess Cu ions (*Eq. 4.6 of Chapter IV*) [Lyu et al. 2015]. Thus, catalyst concentration of 1 g L^{-1} was taken as optimum. As predicted, the leached copper concentration increased from 0.9 to 3.1 mg L^{-1} with increase in catalyst concentration from 0.6 to 2.0 g L^{-1}.
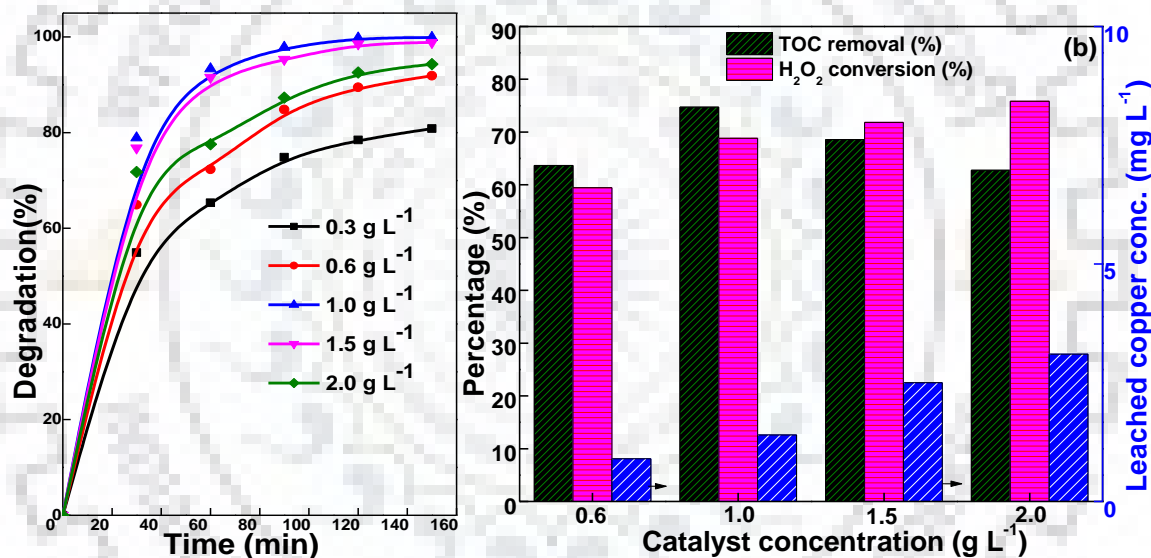
Fig. 6.13: Effect of catalyst concentration on (a) aniline degradation, and (b) TOC removal, H_2O_2 conversion and leached copper concentration at pH_0 = 7, H_2O_2 = 2.4 mL, T = 80 °C, and aniline = 1.07 mM

6.3.5. Effect of reaction temperature

Fig. 6.14 shows the aniline degradation and TOC removal as a function of temperature in the range of 25-80 °C, respectively. Aniline degradation of 76.55, 86.89, 92.67 and 99.89% were measured at temperature 25, 40, 60 and 80 °C, respectively. A significant influence of temperature was observed on degree of mineralization. TOC removals of 22.97, 46.73, 62.34 and 74.73% were observed at temperature 25, 40, 60 and 80 °C, respectively. Likewise, H_2O_2 conversion increase from 28.44 to 68.84% with increase in temperature from 25 to 80 °C. The sharp increase in catalytic performance can be attributed to higher conversion of H_2O_2 to highly reactive *OH

radicals with increase in temperature [Rusevova et al. 2014]. Surprisingly, copper leaching was not much affected in this range of temperature. In view of the high mineralization efficiency, all experiments were carried out at 80 °C.
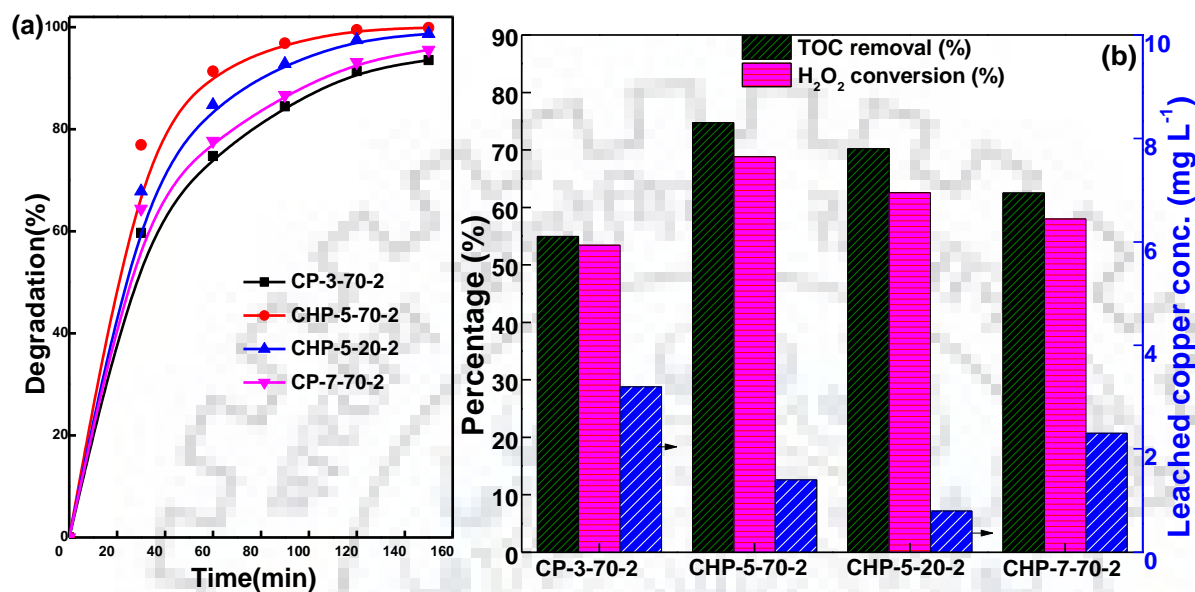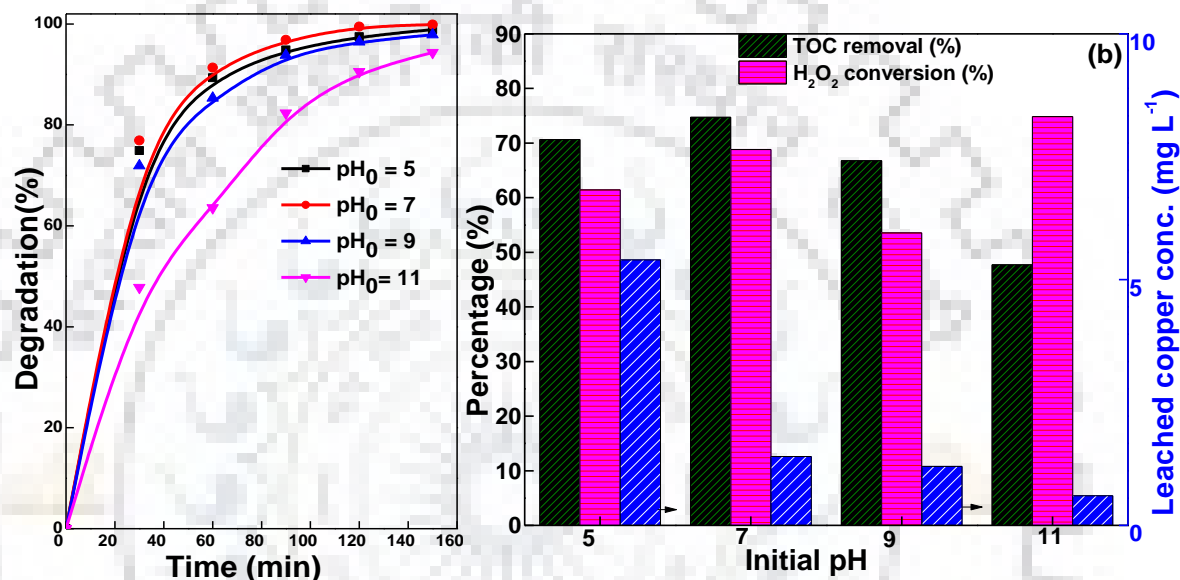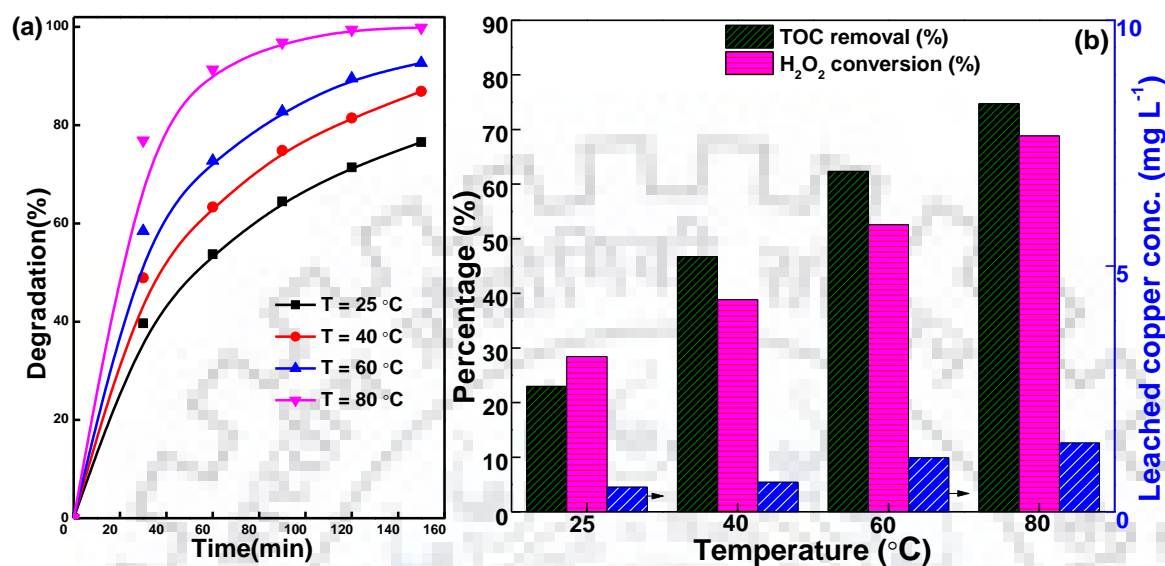

Fig. 6.14: Effect of reaction temperature on (a) aniline degradation, and (b) TOC removal, H₂O₂ conversion and leached copper concentration at pH₀ = 7, H₂O₂ = 2.4 mL, catalyst = 1 g L⁻¹ and aniline = 1.07 mM

6.3.6. Kinetic studies

Kinetic study for the CWPO of aniline was carried out by determining the aniline concentration as function of time. Many researchers reported that pollutants degradation follows the pseudo-first order model [Yan et al. 2016, Wei et al. 2017, Hammouda et al. 2017]. Assuming pseudo-first order model for degradation of aniline, the rate law can be expressed as:

$$-r = -\frac{dC_A}{dt} = kC_A \tag{6.1}$$

Integral analysis can be used to develop linear relationship as follows:

$$-\ln\frac{C_A}{C_0} = kt \tag{6.2}$$

$$\ln\frac{1}{(1-X_A)} = kt \tag{6.3}$$

Where, C_A is the concentration of aniline at any time t, X_A is fraction of aniline degradation and k is pseudo-first order rate constant. According to eq. (6.3), the k value can be estimated from the slope of linear plot of $\ln(1/(1-X_A))$ vs. time. The proposed pseudo-first model shown in Fig. 6.15a was best-fitted with CWPO profiles of aniline with high values of coefficient of

determination ($R^2 > 0.95$). Rate constants and fitting parameters (R^2) for both steps are shown in Table 6.3. The rate constant increases with increase in temperature and the maximum value of 0.0435 min^{-1} was obtained at 80 °C. Activation energy (E_a) for degradation of aniline was estimated using Arrhenius equation ($k = k_0 exp^{\frac{-Ea}{RT}}$, Fig. 6.15b) and found to be 21.58 KJ mol^{-1}.
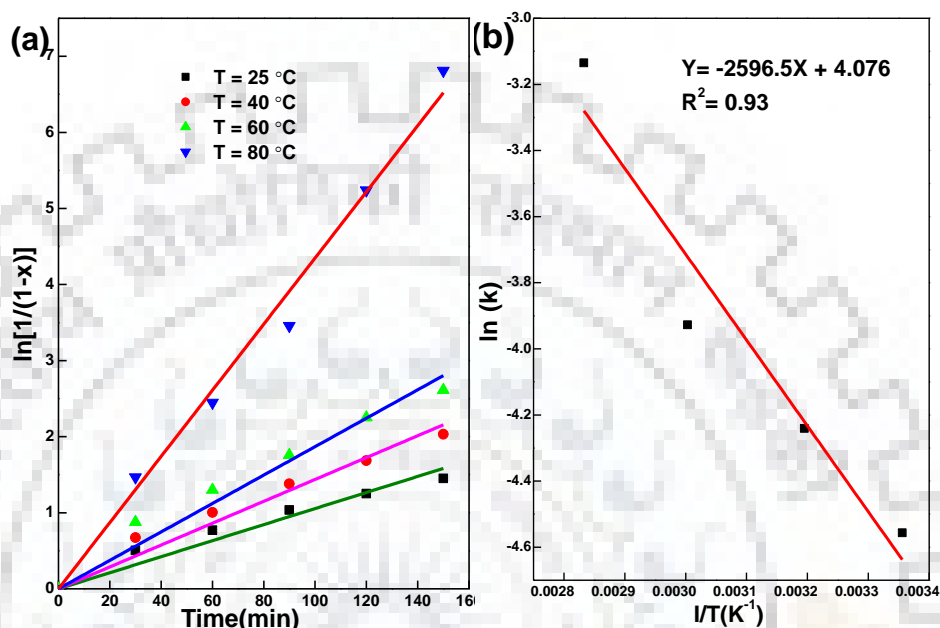
Fig. 6.15: Kinetic study plots for aniline degradation; (a) Pseudo-first model and (b) Activation energy plot

Table 6.3: Kinetic parameters for degradation of aniline at different temperatures

Temperature (°C)	k (min^{-1})	R^2	E_a (kJ mol^{-1})	R^2
25	0.0105	0.98		
40	0.0144	0.96	21.58	0.93
60	0.0197	0.96		
80	0.0435	0.99		

6.3.7. Reusability of catalyst

It is very much important to investigate the reusability of the catalyst as it is crucial parameter for an effective and economical application of catalyst. Reusability of the catalyst for CWPO process was investigated by performing five consecutive degradation cycles at optimized condition (Fig. 6.16). It is important to observe that degradation efficiency of 90.43% has been retained even after five consecutive cycles. In addition, TOC removal of 62.35% was observed after five cycle runs. Copper leaching was also measured in each cycle using AAS technique. Copper leaching was

always less than 1.4 mg L^{-1} which is much less than permissible limit of Indian Standards (3 mg L^{-1}) [CPCB 2018]. These results signify CHP applicability as a superior catalyst for degradation of aniline from industrial effluents.
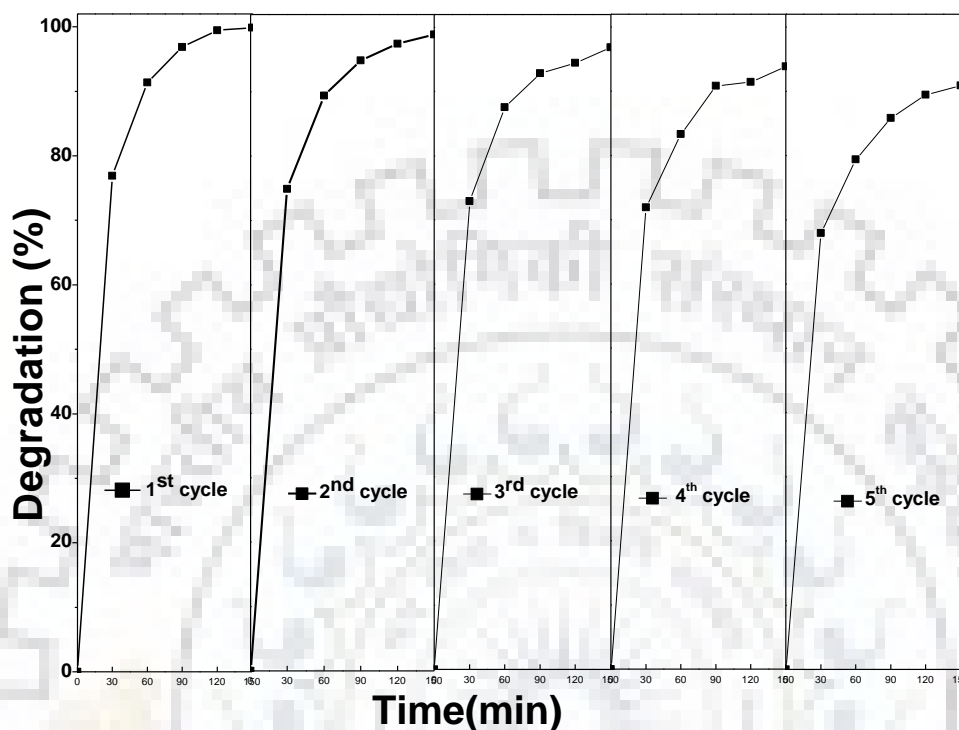
Fig. 6.16: Reusability test of CHP-5-70-2 catalyst at optimized condition

6.4. SUMMARY

An ultrafast sonochemical method has been developed for the synthesis of copper hydroxyphosphate and copper phosphate with controllable morphologies. Copper hydroxyphosphate (CHP) was synthesized at pH 5, and copper phosphate (CP) was formed at pH = 3 and pH = 7 in 2 h. The formation of pure phases and desired morphologies were characterized with the help of XRD, FTIR, N_2 sorption, FESEM, TEM and HRTEM techniques. The catalytic activity was strongly influenced by morphology of the catalyst. The maximum aniline degradation, TOC removal and H_2O_2 conversion of 99.86%, 74.73 and 68.42 were achieved for CHP-5-70-2. The optimum performance was observed at pH = 7, H_2O_2 amount = 2.4 mL, catalyst concentration = 1 g L^{-1} and T = 80 °C. The reaction kinetics was best fitted to pseudo-first order model. The recyclability up to five continuous cycles has shown remarkable operation stability.

CONCLUSIONS AND RECOMMENDATIONS

7.1. CONCLUSIONS

In the present work, Cu/zeolite Y samples were synthesized using wet-impregnation (IMP) and precipitation-impregnation (PI) routes as a better alternative to conventional aqueous ion-exchange (AIE) method and generation of mesoporosity in considerable extent. In addition, an ultrafast sonochemical route for the synthesis of Cu_2OHPO_4 (CHP) and $Cu_3(PO_4)_2$ (CP) nanostructures have been developed for the first time. The as-synthesized materials were characterized and tested for the catalytic wet peroxide oxidation (CWPO) of nitrogenous aromatic compounds, such as, Congo red, quinoline and aniline in batch and continuous fixed-bed reactors. The following conclusions are drawn on the basis of the result obtained:

- IMP and PI methods are better than the AIE in terms of control over copper loading. Both methods require low volume of solvent, less time, no filtration and no residual solvent.

- XRD study of CuY_{IMP} samples showed presence of well-dispersed copper species attached with Al sites (except $10\%CuY_{IMP}$). $10\%CuY_{IMP}$ contained small CuO particles in the pores of zeolites. The contraction of unit cell was observed with Cu loading ≤ 5 wt%; however, the unit cell size increased with further increase in copper loading.

- The textural properties of the samples were not affected up to 5wt% copper loading in CuY_{IMP} samples. Particularly at Cu loading of 7.5 wt%, the Langmuir surface area increased surprisingly from 567 to 667 $m^2 \, g^{-1}$ and the presence of H_4 type hysteresis loop in isotherm indicated the formation of mesopores. DFT model confirmed the generation of hierarchical porosity.

- FE-SEM images clearly depicted the smooth surface of HY and CuY_{IMP}, which indicates the uniform dispersion of copper species on zeolite surface. FTIR study confirmed the external linkage of Cu with zeolite framework.

- UV-vis DRS analysis suggests the presence of monovalent and divalent copper species in all samples. For $7.5\%CuY_{IMP}$ sample, the highest band intensity is associated with highly disperse copper species which strongly interacts with zeolite Y. Similar to UV-DRS analysis, XPS results also reveal coexistence of Cu^{1+} and Cu^{2+} states in $7.5\%CuY_{IMP}$ in equal extent. The shape of XPS spectrum confirmed that CuO crystallized out majorly for 10 wt% copper loading.

- The mechanistic study showed that degradation of Congo red occurred through synergetic effect of adsorption and heterogeneous catalysis. The maximum degradation, decolorization and mineralization of 93.58%, 95.34% and 79.52% were exhibited by Cu 7.5 wt% after optimum times of 2.5, 2 and 4 h, respectively. The optimized condition was observed at pH = 7, H_2O_2 concentration = 52.24 mM, catalyst concentration = 1 g L^{-1} and T = 60 °C.

- H_2O_2 had almost negligible effect on copper leaching. However, a strong influence of pH was noticed with maximum copper leaching of 13.85 mg L^{-1} at pH = 5. The kinetic studies revealed that the degradation and decolorization profiles for Congo red were well fitted with first-order kinetic model. Catalyst with 7.5 wt% copper loading showed reproducible activity up to 3rd cycle with good framework stability.

- In order to provide effective comparison of different synthesis routes, samples with copper loading of 5wt.% (equivalent to copper loading obtained by AIE method) were mainly focused. XRD analysis indicated that AIE for CuY_{AIE} promoted isolated species similar to CuY_{IMP}; however, large CuO crystallites of different sizes (4.7-6.1 nm) were present on the external surface of precipitation-impregnation (CuY_{PI}) catalysts depending upon the Cu loadings.

- N_2 sorption techniques revealed that framework of zeolite Y remain intact after AIE method. The comparison of sorption isotherms showed that higher extent of mesoporosity was generated by PI method as compared to IMP method. The Langmuir surface area and pore volume (V_p) increase surprisingly from 567 to 909 m^2 g^{-1} and 0.26 to 0.51 cm^3 g^{-1}, respectively, for $5CuY_{PI}$. The mesoporosity generation was due to synergetic effect of copper and base NaOH. The surface area and pore volume decreased on further increase in copper loading due to blockage of the pores by large CuO particles.

- FESEM images of $5CuY_{PI}$ sample clearly showed the clusters of CuO. However, copper species were dispersed uniformly on the surface of $5CuY_{AIE}$ sample.

- UV-vis DRS analysis indicates the higher extent of isolated Cu^{2+} species in $5CuY_{AIE}$ as compared to other preparation methods. Conversely, the isolated Cu^{2+} species and $(Cu-O-Cu)^{2+}$ dimers were absent for $5CuY_{PI}$. The main species were isolated Cu^{1+} and octahedrally coordinated CuO in $5CuY_{PI}$.

- The high intensity of XPS spectrum and low binding energy of $Cu2p_{3/2}$ core level for $5CuY_{PI}$ showed that major amount of copper was present on the surface. However, the lower intensity

and higher binding energy for $5CuY_{IMP}$ revealed that copper was present inside the pores. The relative amount of Cu^{2+}/Cu^{1+} for $5CuY_{PI}$ and $5CuY_{IMP}$ samples were 2.30 and 0.97, respectively. The generation of higher extent of mesoporosity in CuY_{PI} was result of higher desilication from zeolite framework due to synergetic effect of copper and NaOH.

- The catalytic activities of samples prepared by different synthesis routes were compared using quinoline as model pollutant in batch as well as continuous fixed-bed reactors. Almost comparable mineralization (61-65%) and H_2O_2 stoichiometric efficiencies (44.2-45.7%) were observed for CuY_{AIE} and CuY_{IMP} samples in continuous fixed-bed reactor. Higher catalytic activities of both catalysts in comparison to CuY_{PI} suggest that isolated sites are the most redox-active sites for H_2O_2 activation and play more important role than high surface area, i.e., for CuY_{PI}. The low catalytic activity of $5CuY_{PI}$ may be ascribed to the presence of large crystallites of CuO particles on the catalyst surface which promote non-selective decomposition of H_2O_2 to inactive O_2 and H_2O species. Due to comparable catalytic activity and controllable green synthesis, wet-impregnation was found better than aqueous ion-exchange method.

- CuY_{IMP} exhibited high operation stability for 250 h with >60% mineralization at LHSV = 4 h^{-1}, particle size = 1.2-1.7 mm, H_2O_2/quinoline = 48 and T = 80 °C. Copper leaching was majorly influenced by LHSV and particle size.

- The mechanistic view of quinoline degradation showed that *OH radical is the responsible species for the oxidation of quinoline. Quinoline was degrading into low molecular weight organic acids, and finally mineralized into CO_2, N_2, NH_3, NO_2^- and NO_3.

- The system followed Eley-Rideal mechanism and kinetic parameters were calculated using model based on this mechanism. The highest value of rate constant for mineralization of quinoline was observed as 6.12 L h^{-1} $Kgcat^{-1}$ at 80 °C.

- Copper hydroxyphospahte (CHP) was obtained at pH 5, and copper phosphate (CP) was formed at pH = 3 and pH = 7 in 2 h. XRD and FTIR analysis confirmed the successful synthesis of pure CHP and CP framework.

- The resulting isotherms of all specimens display IUPAC type-III isotherms with H3 hysteresis loop. This kind of hysteresis appears because of slit-like pores with non-uniform shape and/or size. The type-III isotherm and BJH pore size distribution curves suggest the coexistence of

macropores and mesopores in all the samples. The BET surface area and total pore volume increased in the order of CHP-5-20-2 < CHP-5-70-2 < CP-7-70-2 < CP-3-70-2 and observed higher for CP samples in comparison to CHP.

- The FE-SEM image of CP-3-70-2 reveals the aggregations of thin nanoflakes of size 100-200 nm. In CHP-5-70-2, small nanorods of size ~50 nm were self-assembled to larger nanospindles-like hierarchical architecture of size 500-700 nm. When the sonication amplitude was decreased from 70% to 20%, the morphology of corresponding material changed from nanospindles-like hierarchical architecture to beautiful one dimensional nanorods of size 800-1200 nm. On the other hand, thick nanoflakes of size around 100-200 nm were generated for CP-7-70-2 at pH = 7.

- TEM images further confirmed the morphology of different samples. SAED pattern and lattice fringes indicate that each nanorod is single crystalline.

- The formation mechanism indicates that the complete transformation of $Cu_3(PO_4)_2$ to pure and highly crystalline Cu_2OHPO_4 occurs after sonication time of 45 min. The *OH radicals generated through ultrasonic irradiation of water are thought to be responsible for transformation of $Cu_3(PO_4)_2$ into Cu_2OHPO_4 at pH = 5.

- The maximum aniline degradation, TOC removal and H_2O_2 conversion of 99.86%, 74.73% and 68.84% were achieved for CHP-5-70-2. The highest catalytic activity for oxidation of aniline may be attributed to smaller nanorods which provide high mobility of charge carriers and improved redox properties. The maximum performance was observed at pH = 7, H_2O_2 amount = 2.4 mL, catalyst concentration = 1 g L^{-1} and T = 80 °C.

- The reaction kinetics for CWPO profiles of aniline was best fitted with the pseudo-first order model. The recyclability up to five continuous cycles has shown a remarkable operational stability.

7.2. RECOMMENDATIONS FOR FUTURE WORK

On the basis of the present work, some areas were identified that are worthy of further study to provide more evidence to support the development of technology at industrial scale. The following recommendations are made for future studies:

- A detail explanation of oxidation mechanism is of great importance to improve the mineralization efficiency of CWPO process. The complete mechanism is still not clear. Density

functional theory (DFT) study should be used to understand the H_2O_2 activation and oxidation mechanism.

- Modelling and simulation of CWPO process has received less attention of researchers till now. Research should be carried out in this area for various reactor configurations (batch as well as continuous reactors).

- The by-products resulting from the oxidation processes may be more toxic than parent compounds. Therefore, toxicity of the treated effluent should be addressed more often in future studies.

- CWPO should be integrated with other AOPs to enhance the mineralization efficiency at ambient condition.
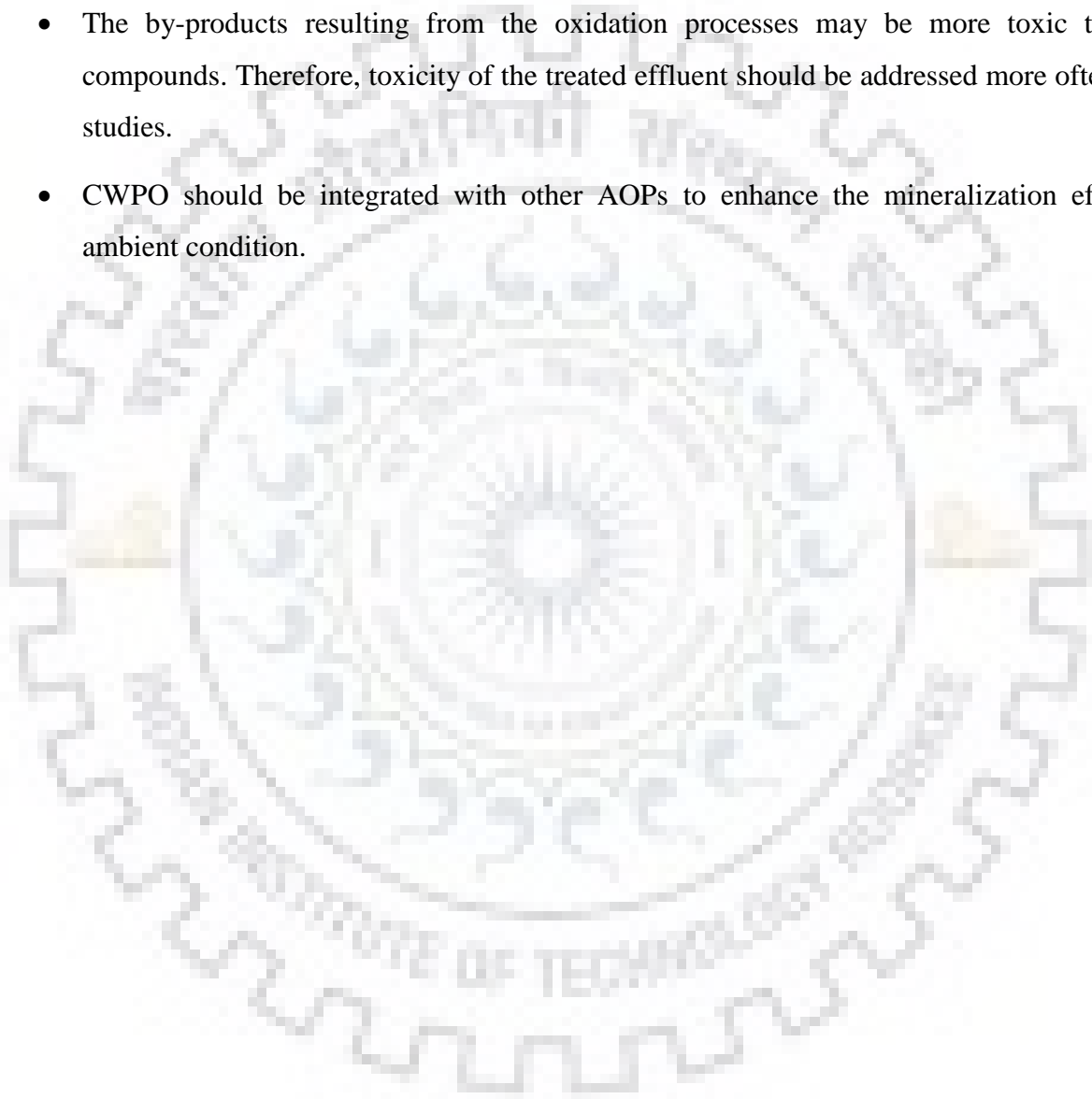
REFERENCES

- Acero, J. L.; Benitez, F. J.; Real, F. J.; Teva, F. Micropollutants removal from retentates generated in ultrafiltration and nanofiltration treatments of municipal secondary effluents by means of coagulation, oxidation, and adsorption processes, *Chem. Eng. J.* **289**, 48-58, 2016.

- Ahmadi, M.; Nambo, A.; Jasinski, J. B.; Ratnasamy, P.; Carreon, M. A. Decarboxylation of oleic acid over Pt catalysts supported on small-pore zeolites and hydrotalcite, *Catal. Sci. Technol.* **5**, 380-388, 2015.

- Ahmadi, S.; Mostafapour, F. K.; Bazrafshan, E. Removal of aniline and from aqueous solutions by coagulation/flocculation-flotation, *Chem. Sci. Int. J.* **18**, 1-10, 2017.

- Ahmed, Y.; Yaakob, Z.; Akhtar, P. Degradation and mineralization of methylene blue using a heterogeneous photo-Fenton catalyst under visible and solar light irradiation, *Catal. Sci. Technol.* **6**, 1222-1232, 2015.

- Aislabie, J.; Bej, A. K.; Hurst, H.; Rothenburger, S.; Atlas, R. M. Microbial degradation of quinoline and methylquinolines, *Appl. Environ. Microbiol.* **56**, 345-351, 1990.

- Ali, I.; Asim, M.; Khan, T. A. Low cost adsorbents for the removal of organic pollutants from wastewater, *J. Environ. Manage.* **113**, 170-183, 2012.

- Aljuboori, A. H. R.; Uemura, Y.; Osman, N. B.; Yusup, S. Production of a bioflocculant from *Aspergillus niger* using palm oil mill effluent as carbon source, *Bioresour. Technol.* **171**, 66-70, 2014.

- Alonso, F.; Arroyo, A.; Garcia, I. M.; Moglie, Y. Cross-dehydrogenative coupling of tertiary amines and terminal alkynes catalyzed by copper nanoparticles on zeolite, *Adv. Synth. Catal.* **357**, 3549-3561, 2015.

- Andas, J.; Adam, F.; Rahman, I. A. Heterogeneous copper-silica catalyst from agricultural biomass and its catalytic activity, *Appl. Surf. Sci.* **284**, 503-513, 2013.

- Anis, S. F.; Khalil, A.; Saepurahman, Singaravel, G.; Hashaikeh, R. A review on the fabrication of zeolite and mesoporous inorganic nanofibers formation for catalytic applications, *Microporous Mesoporous Mater.* **236**, 176-192, 2016.

- Anotai, J.; Lu, M. C.; Chewpreecha, P. Kinetics of aniline degradation by Fenton and electro-Fenton processes, *Water Res.* **40**, 1841-1847, 2006.

- Apul, O. G.; Karanfil, T. Adsorption of synthetic organic contaminants by carbon nanotubes: A critical review, *Water Res.* **68**, 34-55, 2015.

- Armengol, E.; Corma, A.; Fornes, V.; Garcia, H.; Primo, J. Cu^{2+}-phthalocyanine and Co^{2+}-perfluorophthalocyanine incorporated inside Y faujasite and mesoporous MCM-41 as heterogeneous catalysts for the oxidation of cyclohexane, *Appl. Catal. A: Gen*. **181**, 305-312, 1999.

- Arora, M. K.; Sahu, N.; Upadhyay, S. N.; Sinha, A. S. K. Activity of cadmium sulfide photocatalysts for hydrogen production from water: role of support, *Ind. Eng. Chem. Res.* **38**, 2659-2665, 1999.

- Ay, F.; Catalkaya, E. C.; Kargi, F. Advanced oxidation of Direct Red (DR 28) by Fenton treatment, *Environ. Eng. Sci.* **25**, 1455-1462, 2009.

- Ayed, L.; Achour, S.; Khelifi, E.; Cheref, A.; Bakhrouf, A. Use of active consortia of constructed ternary bacterial cultures via mixture design for Congo red decolorization enhancement, *Chem. Eng. J.* **162**, 495-502, 2010.

- Bai, Y.; Sun, Q.; Sun, R.; Wen, D.; Tang, X. Bioaugmentation and adsorption treatment of coking wastewater containing pyridine and quinoline using zeolite-biological aerated filters, *Environ. Sci. Technol*. **45**, 1940-1948, 2010.

- Barbier, J.; Oliviero, L.; Renald, B. Role of ceria-supported noble metal catalysts (Ru, Pd, Pt) in wet air oxidation of nitrogen and oxygen containing compounds, *Topics Catal*. **33**, 77-86, 2005.

- Baroi, C.; Mahto, S.; Niu, C.; Dalai, A. K. Biofuel production from green seed canola oil using zeolites, *Appl. Catal. A: General* **469**, 18-32, 2014.

- Barr, T. L. The nature of the relative bonding chemistry in zeolites: An XPS study, *Zeolites* **10**, 760-765, 1990.

- Bautista, P.; Mohedano, A. F.; Menendez, N.; Casas, J. A.; Rodriguez, J. J. Catalytic wet peroxide oxidation of cosmetic wastewaters with Fe-bearing catalysts, *Catal. Today* **151**, 148-152, 2010.

- Beckhoff, B.; Kanngießer, B.; Langhoff, N.; Wedell, R.; Wolff, H. *Handbook of practical x-ray fluorescence analysis*, Springer, Berlin, Heidelberg, 2006.

- Belik, A. A.; Koo, H. J.; Whangbo, M. H.; Tsujii, N., Naumov, P.; Takayama-Muromachi, E. Magnetic properties of synthetic libethenite Cu_2PO_4OH: a new spin-gap system, *Inorg Chem*. **46**, 8684-8689, 2007.

- Benaliouche, F.; Boucheffa, Y.; Starzyk, F. T. In situ FTIR studies of propene adsorption over Ag- and Cu-exchanged Y zeolites, *Microporous. Mesoporous. Mater.* **147**, 10-16, 2012.

- Bertin, E. P. *Introduction to X-Ray spectrometric analysis*, Springer, Boston, 1978.

- Bharate, J. B.; Vishwakarma, R. A.; Bharate, S. B. Metal-free domino one-pot protocols for quinoline synthesis, *RSC Adv.* **5**, 42020-42053, 2015.

- Bhargava, A.; Shukla, S.; Ohri, D. Chenopodium quinoa-An Indian perspective, *Ind. Crops Prod.* **23**, 73-87, 2006.

- Bhargava, S. K.; Tardio, J.; Prasad, J.; Föger, K.; Akolekar, D. B.; Grocott, S. C. Wet oxidation and catalytic wet oxidation, *Ind. Eng. Chem. Res.* **45**, 1221-1258, 2006.

- Bhatkhande, D. S.; Pangarkar, V. G.; Beenackers, A. A. C. M. Photocatalytic degradation for environmental applications - A review, *J. Chem. Technol. Biotechnol.* **77**, 102-116, 2002.

- Bisutti, I.; Hilke, I.; Raessler, M. Determination of total organic carbon - an overview of current methods, *Trends Analyt. Chem.* **23**, 716-726, 2004.

- Blum, P.; Sagner, A.; Tiehm, A.; Martus, P.; Wendel, T.; Grathwohl, P. Importance of heterocyclic aromatic compounds in monitored natural attenuation for coal tar contaminated aquifers: a review, *J. Contam. Hydrol.* **126**, 181-194, 2011.

- Bokare, A. D.; Choi, W. Review of iron-free Fenton-like system for activating H_2O_2 in advanced oxidation processes, *J. Hazard. Mater.* **275**, 121-135, 2014.

- Botas, J. A.; Melero, J. A.; Martínez, F.; Pariente, M. I. Assessment of Fe_2O_3/SiO_2 catalysts for the continuous treatment of phenol aqueous solution in a fixed bed reactor, *Catal. Today* **149**, 334-340, 2010.

- Brown, P. R.; Hartwick, R. A. *High performance liquid chromatography*, John Wiley & Sons, New York, 1989.

- Burgos, W. D.; Pisutpaisal, N.; Mazzarese, M. C.; Chorover, J. Adsorption of quinoline to kaolinite and montmorillonite, *Environ., Eng. Sci.* **19**, 59-68, 2004.

- Campos-Martin, J. M.; Guerrero-Ruiz, A.; Fierro, J. L. G. Changes of copper location in CuY zeolites induced by preparation methods, *Catal. Lett.* **41**, 55-61, 1996.

- Cao, Y.; Lan, L.; Feng, X.; Yang, Z.; Zou, S.; Xu, H.; Li, Z.; Gong, M.; Chen, Y. Cerium promotion on the hydrocarbon resistance of a Cu-SAPO-34 NH_3-SCR monolith catalyst, *Catal. Sci. Technol.* **5**, 4511-4521, 2015.

- Carreon, M. A. Book review of chemistry of zeolites and related porous materials: synthesis and structure, *J. Am. Chem. Soc.* **130**, 13184-13184, 2008.

- Carvalho, M. C. N. A. D.; Passos, F. B.; Schmal, M. The behavior of Cu/ZSM-5 in the oxide and reduced form in the presence of NO and methanol, *Appl. Catal. A: Gen.* **193**, 265-276, 2000.

- Central Pollution Control Board India, Standards for emission or discharge of environmental pollutants. http://cpcb.nic.in/effluent-emission/, 2018 (accessed 15.06.2018).

- Chakraborty, S.; Basak, B.; Dutta, S.; Bhunia, B.; Dey, A. Decolorization and biodegradation of Congo red dye by a novel white rot fungus *Alternaria alternata* CMERI F6, *Bioresour. Technol.* **147**, 662-666, 2013

- Chatterjee, S.; Lee, D. S.; Lee, M. W.; Woo, S. H. Enhanced adsorption of Congo red from aqueous solutions by chitosan hydrogel beads impregnated with cetyl trimethyl ammonium bromide, *Bioresour. Technol.* **100**, 2803-2809, 2009.

- Chen, C.; Zhou, Y.; Wang, N.; Cheng, L.; Ding, H. $Cu_2(OH)PO_4/g-C_3N_4$ composite as an efficient visible light-activated photo-Fenton photocatalyst, *RSC Adv.* **5**, 95523-95531, 2015.

- Cheng, B.; Le, Y.; Cai, W.; Yu, J. Synthesis of hierarchical $Ni(OH)_2$ and NiO nanosheets and their adsorption kinetics and isotherms to Congo red in water, *J. Hazard. Mater.* **185**, 889-897, 2011.

- Chowdhury, I. H.; Chowdhury, A. H.; Bose, P.; Mandal, S.; Naskar, M. K. Effect of anion type on the synthesis of mesoporous nanostructured MgO, and its excellent adsorption capacity for the removal of toxic heavy metal ions from water, *RSC Adv.* **6**, 6038-6047, 2016.

- Clemens, A. K. S.; Shishkin, A.; Carlsson, P. A.; Skoglundh, M.; Martínez-Casado, F. J.; Matěj, Z.; Balmes, O.; Härelind, H. Reaction driven ion exchange of copper into zeolite SSZ-13, *ACS Catal.* **5**, 6209-6218, 2015.

- Cui, Y.; Liu, X. Y.; Chung, T. S.; Weber, M.; Staudt, C.; Maletzko, C. Removal of organic micro-pollutants (phenol, aniline and nitrobenzene) via forward osmosis (FO) process: Evaluation of FO as an alternative method to reverse osmosis (RO), *Water Res.* **91**, 104-114, 2016.

- Daems, N.; Wouters, J.; Goethem, C. V.; Baert, K.; Poleunis, C.; Delcorte, A.; Hubin, A.; Vankelecom, I. F. J.; Pescarmon, P. P. Selective reduction of nitrobenzene to aniline over

electrocatalysts based on nitrogen-doped carbons containing non-noble metals, *Appl. Catal. B* **226**, 509-522, 2018.

- Dalai, A. K.; Rao, M. S.; Gokhale, K. Synthesis of NaX zeolite using silica from rice husk ash, *Ind. Eng. Chem. Prod. Res. Dev*. **24**, 465-468, 1985.

- Dantas, T. L. P.; Mendonça, V. P.; José, H. J.; Rodrigues, A. E.; Moreira, R. F. P. M. Treatment of textile wastewater by heterogeneous Fenton process using a new composite Fe_2O_3/carbon, *Chem. Eng. J.* **118**, 77-82, 2006.

- De M. A.; O'Connor O. A.; Kosson D. S. Metabolism of aniline under different anaerobic electron-accepting and nutritional condition, *Environ. Toxicol. Chem*. **13**, 233-239, 1994

- Demire, M.; Kayan, B. Application of response surface methodology and central composite design for the optimization of textile dye degradation by wet air oxidation, *Int. J. Ind. Chem.* **3**, 1-10, 2012.

- Devi, P.; Saroha, A. K. Utilization of sludge based adsorbents for the removal of various pollutants: A review, *Sci. Total Environ.* **578**, 16-33, 2017.

- Dong, Y.; He, K.; Yin, L.; Zhang, A. Catalytic degradation of nitrobenzene and aniline in presence of ozone by magnesia from natural mineral, *Catal. Lett*. **119**, 222-227, 2007.

- Duan, X.; Xiao, S.; Liu, Y.; Huang, H.; Wang, D.; Wang, L.; Liu, B.; Wang, T. Ionic liquid-assisted fabrication of copper hydroxyphosphate nanocrystals with exposed {100} facets for enhanced photocatalytic activity, *Nanotechnology* **26**, 031001 (1-7), 2015.

- Dükkanci, M.; Gündüz, G.; Yilmaz, S.; Prihodko, R. V. Heterogeneous Fenton-like degradation of Rhodamine 6G in water using CuFeZSM-5 zeolite catalyst prepared by hydrothermal synthesis, *J. Hazard. Mater.* **181**, 343-350, 2010.

- Dükkanci, M.; Gündüz, G.; Yılmaz, S.; Yaman, Y. C.; Prikhod'Ko, R. V.; Stolyarova, I. V. Characterization and catalytic activity of CuFeZSM-5 catalysts for oxidative degradation of Rhodamine 6G in aqueous solutions, *Appl. Catal. B: Environ.* **95**, 270-278, 2010.

- Duran, A.; Monteagudo, J. M.; Martin, I. S.; Merino, S. Photocatalytic degradation of aniline using an autonomous rotating drum reactor with both solar and UV-C artificial radiation, *J. Environ. Manage.* **210**, 122-130, 2018.

- El-Haloty, M. M.; Kamel, W. M.; Mohamed, Y. H. *Principles and applications of total organic carbon analyzer*, LAP Lambert Academic Publishing, Germany, 2013.

- Erdemoglu, S.; Aksu, S. K.; Sayilkan, F.; Izgi, B.; Asiltürk, M. Sayilkan, H. Frimmel, F.; Gucer, S. Photocatalytic degradation of Congo red by hydrothermally synthesized nanocrystalline TiO_2 and identification of degradation products by LC-MS, *J. Hazard. Mater.* **155**, 469-476, 2008.

- Erjavec, B.; Kaplan, R.; Djinović, P.; Pintar, A. Catalytic wet air oxidation of bisphenol A model solution in a trickle-bed reactor over titanate nanotube-based catalysts, *Appl. Catal. B: Environ.* **132**, 342-352, 2013.

- Espinos, J. P.; Morales, J.; Barranco, A.; Caballero, A.; Holgado, J. P.; González- Elipe, A. R. Interface effects for Cu, CuO, and Cu_2O deposited on SiO_2 and ZrO_2. XPS determination of the valence state of copper in Cu/SiO_2 and Cu/ZrO_2 catalysts, *J. Phys. Chem. B* **106**, 6921-6929, 2002.

- Esteves, B. M.; Rodrigues, C. S. D.; Boaventura, R. A. R.; Maldonado-Hodar, F. J.; Madeira, L. M. Coupling of acrylic dyeing wastewater treatment by heterogeneous Fenton oxidation in a continuous stirred tank reactor with biological degradation in a sequential batch reactor, *J. Environ. Manage.* **166**, 193-203, 2016.

- European Parliament, Directive 2000/60/EC of the European Parliament and of the council of 23 October 2000 establishing a framework for community action in the field of water policy, *Official Journal,* 22/12/2000, **L 327**, 0001-0073, 2000.

- Exposito, A. J.; Patterson, D. A.; Mansor, W. S. W.; Monteagudo, J. M.; Emanuelsson, E.; Sanmartin, I.; Duran, A. Antipyrine removal by TiO_2 photocatalysis based on spinning disc reactor technology, *J. Environ. Manage.* **187**, 504-512, 2017.

- Fan, J.; Guo, Y.; Wang, J.; Fan, M. Rapid decolorization of azo dye methyl orange in aqueous solution by nano scale zero valent iron particles, *J. Hazard. Mater.* **166**, 904-910, 2009.

- Faria, P. C. C.; Orfao, J. J. M.; Pereira, M. F. R. Activated carbon and ceria catalysts applied to the catalytic ozonation of dyes and textile effluents, *Appl. Catal. B: Environ.* **88**, 341-350, 2009.

- Fayer, M. D. Ultrafast infrared and raman spectroscopy, CRC Press, Boca Raton, USA, 2001.

- Felczak, A.; Zawadzka, K.; Lisowska, K. Efficient biodegradation of quinoline- Factors determining the process, *Int. Biodeterior. Biodegrad.* **96**, 127-134, 2014.

- Ferreira, L.; Aguiar, C. A.; Parpot, P.; Fonseca, A. M.; Neves, I. C. Preparation and assessment of antimicrobial properties of bimetallic materials based on NaY zeolites, *RSC Adv.* **5** 37188-37195, 2015.

- Fetzner, S.; Tshisuaka, B.; Lingens, F.; Kappl, R.; Hüttermann, J. Bacterial degradation of quinoline and derivatives - pathways and their biocatalysts, *Angew. Chem. Int. Ed.* **37**, 576-597, 1998.

- Fischer, A.; Weber, S.; Reineke, A. K.; Hollender, J.; Richnow, H. H. Carbon and hydrogen isotope fractionation during anaerobic quinoline degradation, *Chemosphere* **81**, 400-407, 2010.

- Fogler, H. S. Elements of chemical reaction engineering, Pearson Education Inc., 4th ed., 2006.

- Furman, O.; Laine, D. F.; Blumenfeld, A.; Teel, A. L.; Shimizu, K.; Cheng, I. F.; Watts, R. J. Enhanced reactivity of superoxide in water-solid matrices, *Environ. Sci. Technol.* **43**, 1528-1533, 2009.

- Gao, D. W.; Hu, Q.; Pan, H.; Jiang, J.; Wang, P. High-capacity adsorption of aniline using surface modification of lignocellulose-biomass jute fibers, *Bioresour. Technol.* **193**, 507-512, 2015.

- Gao, F.; Walter, E. D.; Washton, N. M.; Szanyi, J.; Peden, C. H. F. Synthesis and evaluation of Cu/SAPO-34 catalysts for NH_3-SCR 2: Solid-state ion exchange and one-pot synthesis, *Appl. Catal. B-Environ.* **162**, 501-514, 2015.

- Garcia, F. A. C.; Araujo, D. R.; Silva, J. C. M.; Macedo, J. L. D.; Ghesti, G. F.; Dias, S. C. L.; Dias, J. A.; Filho, G. N. R. Effect of cerium loading on structure and morphology of modified Ce-USY zeolites, *J. Braz. Chem. Soc.* **22**, 1894-1902, 2011.

- Garcia, J.; Gomes, H. T.; Serp, P.; Kalck, P.; Figueiredo, J. L.; Faria, J. L. Platinum catalysts supported on MWNT for catalytic wet air oxidation of nitrogen containing compounds, *Catal. Today* **102-103**, 101-109, 2005.

- Garcia, J.; Gomes, H. T.; Serp, Ph.; Kalck, Ph.; Figueiredo, J. L.; Faria, J. L. Carbon nanotube supported ruthenium catalysts for the treatment of high strength wastewater with aniline using wet air oxidation, *Carbon* **44**, 2384-2391, 2006.

- Garrido-Ramirez, E. G.; Theng, B. K. G.; Mora, M. L. Clays and oxide minerals as catalysts and nanocatalysts in Fenton-like reactions-A review, *Appl. Clay Sci.* **47**, 182-192, 2010.

- Ghosh, U. K.; Pradhan. N. C.; Adhikari, B. Synthesis and characterization of porous polyurethaneurea membranes for pervaporative separation of 4-nitrophenol from aqueous solution, *B. Mater. Sci.* **29**, 225-231, 2006.

- Ghuge, S. P.; Saroha, A. K. Catalytic ozonation of dye industry effluent using mesoporous bimetallic Ru-Cu/SBA-15 catalyst, *Process. Saf. Environ. Prot.* **118**, 125-132, 2018.

- Giordanino, F.; Vennestrom, P. N. R.; Lundegaard, L. F.; Stappen, F. N.; Mossin, S.; Beato, P.; Bordiga, S.; Lamberti, C. Characterization of Cu-exchanged SSZ-13: a comparative FTIR, UV-Vis, and EPR study with Cu-ZSM-5 and Cu-β with similar Si/Al and Cu/Al ratios, *Dalton Trans.* **42**, 12741-12761, 2013.

- Gomes, H. T.; Selvam, P.; Dapurkar, Figueiredo, J. L.; Faria, J. L. Transition metal (Cu, Cr, and V) modified MCM-41 for the catalytic wet air oxidation of aniline, *Microporous Mesoporous Mater.* **86**, 287-294, 2005.

- Gopinath K. P.; Sahib H. A. M.; Muthukumar K.; Velan M. Improved biodegradation of Congo red by using *Bacillus sp.*, *Bioresource Technol.* **100**, 670-675, 2009.

- Graef, M. D. *Introduction to conventional transmission electron microscopy*, Cambridge University Press, Cambridge, UK, 2003.

- Gregg, S. J.; Sing, K. S. W. *Adsorption, surface area and porosity*, Academic press, London, U.K., 1982.

- Guan, Y. H.; Ma, J.; Ren, Y. M.; Liu, Y. L.; Xiao, J. Y.; Lin, L. Q.; Zhang, C. Efficient degradation of atrazine by magnetic porous copper ferrite catalyzed peroxymonosulfate oxidation via the formation of hydroxyl and sulfate radicals, *Water Res.* **47**, 5431-5438, 2013.

- Gulce, H.; Eskizeybek, V.; Haspulat, B.; Sari, F.; Gulce, A.; Avci, A. Preparation of a new polyaniline/CdO nanocomposite and investigation of its photocatalytic activity: comparative study under UV light and natural sunlight irradiation, *Ind. Eng. Chem. Res.* **52**, 10924-10934, 2013.

- Gunale, T. L.; Mahajani, V. V. Studies in mineralization of aqueous aniline using Fenton and wet oxidation (FENTWO) as a hybrid process, *J. Chem. Technol. Biotechnol.* **82**, 108-115, 2007.

- Guo, J.; Al-Dahhan, M. Catalytic wet air oxidation of phenol in concurrent downflow and upflow packed-bed reactors over pillared clay catalyst, *Chem. Eng. Sci.* **60**, 735-746, 2005.

- Guo, N.; Liang, Y.; Lan, S.; Liu, L.; Zhang, J.; Ji, G.; Gan, S. Microscale hierarchical three-dimensional flowerlike TiO_2/PANI composite: synthesis, characterization, and its remarkable photocatalytic activity on organic dyes under UV-light and sunlight irradiation, *J. Phys. Chem. C* **118**, 18343-18355, 2014.

- Guo, X.; Guo, X.; Tao, W.; Chen, L.; Peng, L.; Ding, W. Inorganic nanotubes formation through the synergic evolution of dynamic templates and metallophosphates: from vesicles to nanotubes, *Chem. Commun.* **47**, 10061-10063, 2011.

- Gupta, A.; Garg, A. Degradation of ciprofloxacin using Fenton's oxidation: Effect of operating parameters, identification of oxidized by-products and toxicity assessment, *Chemosphere* **193**, 1181-1188, 2018.

- Guzmán-Vargas, A.; de la Rosa-Pineda, J. E.; Oliver-Tolentino, M. A.; Lima, E.; Ramírez - Rosales, D.; Flores-Moreno, J. L.; de J. Martínez-Ortiz, M. Stability of Cu species and zeolite structure on ecological heterogeneous Fenton discoloration-degradation of yellow 5 dye: Efficiency on reusable Cu-Y catalysts, *Environ. Prog. Sustain. Energy* **34** 990-998, 2015.

- Haber, J. IUPAC "Manual on catalyst characterization", *Pure and Appl. Chem.,* 1991, **63**, 1227-1246.

- Haine, M. E.; Cosslett, V. E. *The electron microscope*, Spon, London, UK, 1961.

- Halim, S. F. A.; Kamaruddin, A. H.; Fernando, W. J. N. Continuous biosynthesis of biodiesel from waste cooking palm oil in a packed bed reactor: optimization using response surface methodology (RSM) and mass transfer studies, *Bioresour. Technol.* **100**, 710-716, 2009.

- Hamilton, R. J.; Sewell, P. A. *Introduction to high performance liquid chromatography*, Springer, Netherlands, 1982.

- Hammouda, S. B.; Zhao, F.; Safaeia, Z.; Babu, I.; Ramasamya, D. L.; Sillanpää, M. Reactivity of novel Ceria-Perovskite composites CeO_2- $LaMO_3$ (MCu, Fe) in the catalytic wet peroxidative oxidation of the new emergent pollutant 'Bisphenol F': Characterization, kinetic and mechanism studies, *Appl. Catal. B: Environ.* **218**, 119-136, 2017.

- Han, H. J.; Zhuang, H. F. Heterogeneous catalytic ozonation of COD and quinoline from coal gasification wastewater secondary effluent with carbon supported copper oxides as catalyst, *Appl. Mech. Mater*. **316-317**, 379-382, 2013.

- Hanawalt, J. D.; Rinn, H. W.; Frevel, L. K. Chemical analysis by X-Ray Diffraction, *Ind. Eng. Chem. Anal. Ed*. **10,** 457-512, 1938.

- Hassan, H.; Hameed, B. H. Fe-clay as effective heterogeneous Fenton catalyst for the decolorization of reactive blue 4, *Chem. Eng. J.* **171**, 912-918, 2011.

- He, G.; Hu, W.; Li, C. M. Spontaneous interfacial reaction between metallic copper and PBS to form cupric phosphate nanoflower and its enzyme hybrid with enhanced activity, *Colloids Surf. B Biointerfaces* **135**, 613-618, 2015.

- He, J.; Yang, X.; Men, B.; Bi, Z.; Pu, Y.; Wang, D. Heterogeneous Fenton oxidation of catechol and 4-chlorocatechol catalyzed by nano-Fe_3O_4: Role of the interface, *Chem. Eng. J.* **258**, 433-441, 2014.

- Hernandez-Maldonado, A. J.; Yang, R. T. Desulfurization of liquid fuels by adsorption via π complexation with Cu(I)-Y and Ag-Y Zeolites, *Ind. Eng. Chem. Res.* **42**, 123-129, 2003.

- Herreros, B.; He, H.; Barr, T. L.; Klinowski, J. ESCA studies of framework silicates with the sodalite structure. 1. Comparison of purely siliceous sodalite and aluminosilicate sodalite, *J. Phys. Chem.* **98**, 1302-1305, 1994.

- Hidalgo, A. M.; Leon, G.; Gomez, M.; Murcia, M. D.; Bernal, M. D.; Ortega, S. Polyamide nanofiltration membranes to remove aniline in aqueous solutions, *Environ. Technol*. **35**, 1175-1181, 2014.

- Howie, A. J.; Brewer, D. B. Optical properties of amyloid stained by Congo red: History and mechanisms, *Micron* **40**, 285-301, 2009.

- Hu, C. 2014 Fe/CeO_2 catalysts for highly efficient degradation of congo red at low temperature, *Asian J. Chem.* **26**, 6431-6434, 2014.

- Hu, E.; Hu, Y.; Cheng, H. Performance of a novel microwave-based treatment technology for atrazine removal and destruction: Sorbent reusability and chemical stability, and effect of water matrices, *J. Hazard. Mater.* **299**, 444-452, 2015.

- Hu, Q.; Gao, D. W.; Pan, H.; Hao, L.; Wang, P. Equilibrium and kinetics of aniline adsorption onto crosslinked sawdust-cyclodextrin polymers, *RSC Adv.* **4**, 40071-40077, 2014.

- Hu, R.; Wang, X.; Dai, S.; Shao, D.; Hayat, T.; Alsaedi, A. Application of graphitic carbon nitride for the removal of Pb(II) and aniline from aqueous solutions, *Chem. Eng. J.* **260**, 469-477, 2015.

- Hu, X. X.; Zhao, L.; Zhao, S. Y.; Rong, L. I.; Xing, Y. J. Microwave-assisted preparation of copper hydroxyphosphate and characterization of photocatalysis under visible light, *J. Inorg. Mater.* **31**, 421-426, 2016.

- Hu, X.; Zheng, X. J.; Li, Y.; Zhang, J.; Ma, D. K. Cu_2PO_4OH: Controlled synthesis of various architectures and morphology-dependent 808 nm laser-driven photothermal performance, *J. Alloy Compd.* **695**, 561-566, 2017.

- Hu, Y.; Dong, L.; Shen, M.; Liu, D.; Wang, J.; Ding, W.; Chen, Y. Influence of supports on the activities of copper oxide species in the low-temperature NO + CO reaction, *Appl. Catal. B: Environ.* **31**, 61-69, 2001.

- Huang, S.; Zhang, J.; Wang, Y.; Chen, P.; Wang, S.; Ma, X. Insight into the tunable CuY catalyst for diethyl carbonate by oxycarbonylation: preparation methods and precursors, *Ind. Eng. Chem. Res.* **53**, 5838-5845, 2014.

- Huang, Y.; Wang, K.; Dong, D.; Li, D.; Hill, M. R.; Hill, A. J.; Wang, H. Synthesis of hierarchical porous zeolite NaY particles with controllable particles size, *Microporous Mesoporous Mater.* **127**, 167-175, 2010.

- Işik, M.; Sponza D. T. Effect of oxygen on decolorization of azo dyes by *Escherichia coli* and *Pseudomonas sp.* and fate of aromatic amines, *Process Biochem.* **38**, 1183-1192, 2003.

- Jadhav, A. J.; Srivastava, V. C. Adsorbed solution theory based modeling of binary adsorption of nitrobenzene, aniline and phenol onto granulated activated carbon, *Chem. Eng. J.* **229**, 450-459, 2013.

- Jenkins, R. *X-ray fluorescence spectrometry*, John Wiley & Sons, New Jersey, USA, 2nd Ed., 2012.

- Jianlong, W.; Xiangchun, Q.; Liping, H.; Yi, Q.; Hegemann, W. Microbial degradation of quinoline by immobilized cells of *Burkholderia pickettii*, *Water Res.* **36**, 2288-2296, 2002.

- Jiao, W.; Cheng, Y.; Zhang, J.; Che, R. Self-assembled 3D hierarchical copper hydroxyphosphate modified by the oxidation of copper foil as a recyclable, wide wavelength photocatalyst, *Langmuir* **33**, 13649-13656, 2017.

- Jin, Q.; Hu, Z.; Jin, Z.; Qiu, L.; Zhong, W.; Pan, Z. Biodegradation of aniline in an alkaline environment by a novel strain of the halophilic bacterium, *Dietzia natronolimnaea* JQ-AN, *Bioresour. Technol.* **117**, 148-154, 2012.

- Jing, J.; Li, J.; Feng, J.; Li, W.; Yu, W. W. Photodegradation of quinoline in water over magnetically separable Fe_3O_4/TiO_2 composite photocatalysts, *Chem. Eng. J.* **219**, 355-360, 2013.

- Jing, J.; Zhang, Y.; Li, W.; Yu, W. W. Visible light driven photodegradation of quinoline over TiO_2/graphene oxide nanocomposites, *J. Catal.* **316**, 174-181, 2014.

- Jing. J.; Liu, M.; Colvin, V. L.; Li, W.; Yu, W. W. Photocatalytic degradation of nitrogen-containing organic compounds over TiO_2, *J. Mol. Catal. A: Chem.* **351**, 17-28, 2011.

- Jones, S. M.; Watts, M. J.; Wickramasinghe, S. R.; A Nanofiltration decision tool for potable reuse: a new rejection model for recalcitrant CECs, *Water Environ. Res.* **89**, 1942-1951, 2017.

- Ju, K. S.; Parales, R. E. Nitroaromatic compounds, from synthesis to biodegradation, *Microbiol. Mol. Biol. Rev.* **74**, 250-272, 2010.

- Jurado-Sanchez, B.; Ballesteros, E.; Gallego, M. Occurrence of aromatic amines and N-nitrosamines in the different steps of a drinking water treatment plant, *Water Res.* **46**, 4543-4555, 2012.

- Kaduk, J. A.; Faber, J. Crystal structure of zeolite Y as a function of ion exchange, *Rigaku J.* **12**, 14-34, 1995.

- Karkmaz, M.; Puzenat, E.; Guillard, C.; Herrmann, J. M. Photocatalytic degradation of the alimentary azo dye amaranth mineralization of the azo group to nitrogen, *Appl. Catal. B: Environ.* **51**, 183-194, 2004.

- Karthikeyan, S.; Dionysiou, D. D.; Lee, A. F.; Suvitha, S.; Maharaja, P.; Wilson, K.; Sekaran, G. Hydroxyl radical generation by cactus-like copper oxide nanoporous carbon catalysts for microcystin-LR environmental remediation, *Catal. Sci. Technol.* **6**, 530-544, 2016.

- Khandegar, V.; Saroha, A. K. Electrocoagulation for the treatment of textile industry effluent-a review, *J. Enviro. Manage.* **128**, 949-963, 2013.

- Khataee, A. R.; Kasiri, M. B. Photocatalytic degradation of organic dyes in the presence of nanostructured titanium dioxide: Influence of the chemical structure of dyes, *J. Mol. Catal. A: Chem.* **328**, 8-26, 2010.

- Kim, J. K.; Martinez, F.; Metcalfe, I. S. The beneficial role of use of ultrasound in heterogeneous Fenton-like system over supported copper catalysts for degradation of p-chlorophenol, *Catal. Today* **124**, 224-231, 2007.

- Kim, K. H.; Ihm, S. K. Heterogeneous catalytic wet air oxidation of refractory organic pollutants in industrial wastewaters: A review, *J. Hazard. Mater.* **186**, 16-34, 2011.

- Kim, S. K.; Kim, K. H.; Ihm, S. K. The characteristics of wet air oxidation of phenol over $CuOx/Al_2O_3$ catalysts: effect of copper loading, *Chemosphere* **68**, 287-292, 2007.

- Kimura, M.; Matsui, Y.; Kondo, K.; Ishikawa, T. B.; Matsushita, T.; Shirasaki, N. Minimizing residual aluminum concentration in treated water by tailoring properties of polyaluminum coagulants, *Water Res.* **47**, 2075-2084, 2013.

- Kirk R. E.; Othmer D. F. *Encyclopedia of chemical technology*, Wiley-VCH, 4th ed., 1997.

- Klaas, J.; Schulz-Ekloff, G.; Jaeger, N. I. UV-Visible diffuse reflectance spectroscopy of zeolite-hosted mononuclear titanium oxide species, *J. Phys. Chem. B* **101**, 1305-1311, 1997.

- Komatsu, T.; Nunokawa, M.; Moon, I. S.; Takahara, T.; Namba, S.; Yashima, T. Kinetic studies of reduction of nitric oxide with ammonia on Cu^{2+}-exchanged zeolites, *J. Catal.* **148**, 427-437, 1994.

- Kondru, A. K.; Kumar, P.; Chand, S. Catalytic wet peroxide oxidation of azo dye (Congo red) using modified Y zeolite as catalyst, *J. Hazard. Mater.* **166**, 342-347, 2009.

- Kumar, A.; Mathur, N. Photocatalytic degradation of aniline at the interface of TiO_2 suspensions containing carbonate ions, *J. Colloid. Interface. Sci.* **300**, 244-252, 2006.

- Kustrowski, P.; Chmielarz, L.; Dziembaj, R.; Cool, P.; Vansant, E. F. Dehydrogenation of ethylbenzene with nitrous oxide in the presence of mesoporous silica materials modified with transition metal oxides, *J. Phys. Chem. A* **109**, 330-336, 2005.

- Laszlo, K.; Tombacz, E.; Novek, C. pH-dependent adsorption and desorption of phenol and aniline on basic activated carbon, *Colloids Surf. A Physicochem. Eng. Asp.* **306**, 95-101, 2007.

- Legube, B.; Leitner, N. K. V. Catalytic ozonation: a promising advanced oxidation technology for water treatment, *Catal. Today* **53**, 61-73, 1999.

- Lei, C.; Pi, M.; Jiang, C.; Cheng, B.; Yu, J. Synthesis of hierarchical porous zinc oxide (ZnO) microspheres with highly efficient adsorption of Congo red, *J. Colloid. Interface. Sci.* **490**, 242-251, 2017.

- Levi, R.; Milman, M.; Landau, M. V.; Brenner, A.; Herskowitz, M. Catalytic wet air oxidation of aniline with nanocasted Mn-Ce-Oxide catalyst, *Environ. Sci. Technol.* **42**, 5165-5170, 2008.

- Lewis R. J. SR.; *Sax's dangerous properties of industrial materials*, John Wiley & Sons, 11th ed., 2004.

- Li, J.; Liu, X.; Wang, S.; Du, Z.; Guo, Y.; Cheng, F. Synthesis and optimization of a novel poly-silicic metal coagulant from coal gangue for tertiary-treatment of coking wastewater, *J. Chem. Technol. Biotechnol.* **93**, 365-371, 2018.

- Li, J.; Ng, D. H. L.; Song, P.; Kong, C.; Song, Y.; Yang, P. Preparation and characterization of high-surface-area activated carbon fibers from silkworm cocoon waste for Congo red adsorption, *Biomass. Bioenergy.* **75**, 189-200, 2015.

- Li, J.; Wu, J.; Sun, H.; Cheng, F.; Liu, Y. Advanced treatment of biologically treated coking wastewater by membrane distillation coupled with pre-coagulation, *Desalination* **380**, 43-51, 2016.

- Li, M.; Cheng, Q.; Wittman, R. M.; Peng, X.; Chan, C. K. Electrochemical and photoelectrochemical properties of the copper hydroxyphosphate mineral libethenite, *ChemElectroChem* **1**, 663-672, 2014.

- Li, R.; Ning, X.; Sun, J.; Wang, Y.; Liang, J.; Lin, M.; Zhang, Y. Decolorization and biodegradation of the Congo red by *Acinetobacter baumannii YNWH 226* and its polymer production's flocculation and dewatering potential, *Bioresour. Technol.* **194**, 233-239, 2015.

- Li, Y.; Deng, J.; Song, W.; Liu, J.; Zhao, Z.; Gao, M.; Wei, Y.; Zhao, L. Nature of Cu species in Cu-SAPO-18 catalyst for NH_3-SCR: combination of experiments and DFT calculation, *J. Phys. Chem.* **120**, 14669-14680, 2016.

- Li, Y.; Wang, L.; Liao, L.; Sun, L.; Zheng, G.; Luan, J.; Gu, G. Nitrate-dependent biodegradation of quinoline, isoquinoline, and 2-methylquinoline by acclimated activated sludge, *J. Hazard. Mater.* **173**, 151-158, 2010.

- Liang, J.; Liang, Z.; Zou, R.; Zhao, Y. Heterogeneous catalysis in zeolites, mesoporous silica, and metal-organic frameworks, *Adv. Mater* **29**, 1701139 (1-21), 2017.

- Liang, X.; Zhong, Y.; He, H.; Yuan, P.; Zhu, J.; Zhu, S.; Jiang, Z. The application of chromium substituted magnetite as heterogeneous Fenton catalyst for the degradation of aqueous cationic and anionic dyes, *Chem. Eng. J.* **191**, 177-184, 2012.

- Liang, X.; Zhu, S.; Zhong, Y.; Zhu, J.; Yuan, P.; He, H.; Zhang, J. The remarkable effect of vanadium doping on the adsorption and catalytic activity of magnetite in the decolorization of methylene blue, *Appl. Catal. B: Environ.* **97**, 151-159, 2010.

- Liao, P.; Yuan, S.; Xie, W.; Zhang, W.; Tong, M.; Wang, K. Adsorption of nitrogen-heterocyclic compounds on bamboo charcoal: Kinetics, thermodynamics, and microwave regeneration, *J. Colloid. Interface. Sci.* **390**, 189-195, 2013.

- Lin, J.; Ye, W.; Baltaru, M. C.; Tang, Y. P.; Bernstein, N. J.; Gao, P.; Balta, S.; Vlad, M.; Volodin, A.; Sotto, A. P. Luis, Zydney, A. L.; der Bruggen, B. V. Tight ultrafiltration

membranes for enhanced separation of dyes and Na_2SO_4 during textile wastewater treatment, *J. Memb. Sci*. **514**, 217-228, 2016.

- Lin, Q.; Jianlong, W. Biodegradation characteristics of quinoline by *Pseudomonas putida*, *Bioresour. Technol.* **101**, 7683-7686, 2010.

- Lin, S. S.; Gurol, M. D. Catalytic decomposition of hydrogen peroxide on iron oxide: kinetics, mechanism, and implications, *Environ. Sci. Technol*. **32**, 1417-1423, 1998.

- Lin, T. Y.; Wu, C. H. Activation of hydrogen peroxide in copper(II)/amino acid/H_2O_2 systems: effects of pH and copper speciation, *J. Catal.* **232**, 117-126, 2005.

- Liu, H.; Lu, G.; Guo, Y.; Guo, Y.; Wang, J. Chemical kinetics of hydroxylation of phenol catalyzed by TS-1/diatomite in fixed-bed reactor, *Chem. Eng. J*. **116**, 179-186, 2006.

- Liu, M.; Lu, Z.; Chen, Z.; Yu, S.; Gao, C. Comparison of reverse osmosis and nanofiltration membranes in the treatment of biologically treated textile effluent for water reuse, *Desalination* **281**, 372-378, 2011.

- Liu, N.; Li, H.; Ding, F.; Xiu, Z.; Liu, P.; Yu, Y. Analysis of biodegradation by-products of nitrobenzene and aniline mixture by a cold-tolerant microbial consortium, *J. Hazard. Mater*. **260**, 323-329, 2013.

- Lousada, C. M.; Johansson, A. J.; Brinck, T.; Jonsson, M. Mechanism of H_2O_2 decomposition on transition metal oxide surfaces, *J. Phys. Chem. C* **116**, 9533-9543, 2012.

- Luca, C. D.; Massa, P.; Fenoglio, R.; Cabello, F. M. Improved Fe_2O_3/Al_2O_3 as heterogeneous Fenton catalysts for the oxidation of phenol solutions in a continuous reactor, *J. Chem. Technol. Biotechnol*. **89**, 1121-1128, 2014.

- Luo, M.; Bowden, D.; Brimblecombe, P. Catalytic property of Fe-Al pillared clay for Fenton oxidation of phenol by H_2O_2, *Appl. Catal. B: Environ*. **85**, 201-206, 2009.

- Lyu, L.; Zhang, L.; Wang, Q.; Nie, Y.; Hu, C. Enhanced Fenton catalytic efficiency of γ-Cu-Al_2O_3 by σ-Cu^{2+}-ligand complexes from aromatic pollutant degradation, *Environ. Sci. Technol.* **49**, 8639-8647, 2015.

- Macdonald, M. J.; Wu, Z.; Ruzicka, J. Y.; Golovko, V.; Tsang, D. C. W.; Yip, A. C. K. Catalytic consequences of charge-balancing cations in zeolite during photo-Fenton oxidation of formaldehyde in alkaline conditions, *Sep. Purif. Technol.* **125**, 269-274, 2014.

- Mackay, D.; Shiu, W. Y.; Ma, K. C.; Lee, S. C. *Physical-chemical properties and environmental fate and degradation handbook,* CRC Press, 2nd ed., 2006.

- Mohapatra, L.; Parida, K. A review on recent progress, challenges and perspective of layered double hydroxides as promising photocatalysts, *J. Mater. Chem. A.* **4**, 10744-10766, 2016.

- Maji, S., Pradhan, N. C., Banerjee, S. Separation of benzene/cyclohexane mixture using semifluorinated aromatic poly(ether amide) membranes with and without cardo unit in the main chain, *Sep. Purif. Technol.* **70**, 128-135, 2009.

- Martinez, F.; Melero, J. A.; Botas, J. A.; Pariente, M. I.; Molina, R. Treatment of phenolic effluents by catalytic wet hydrogen peroxide oxidation over Fe_2O_3/SBA-15 extruded catalyst in a fixed-bed reactor, Ind. Eng. Chem. Res. **46**, 4396-4405, 2007.

- Massa, P.; Ivorra, F.; Haure, P.; Fenoglio, R. Catalytic wet peroxide oxidation of phenol solutions over CuO/CeO_2 systems, *J. Hazard. Mater.* **190**, 1068-1073, 2011.

- Melero, J. A.; Calleja, G.; Martinez, F.; Molina, R.; Pariente, M. I. Nanocomposite Fe_2O_3/SBA-15: an efficient and stable catalyst for the catalytic wet peroxidation of phenolic aqueous solutions, *Chem. Eng. J.* **31**, 245-256, 2007.

- Mendes, F. M. T.; Schmal, M. The cyclohexanol dehydrogenation on $Rh-Cu/Al_2O_3$ catalysts Part 1. Characterization of the catalyst, *Appl. Catal. A: Gen.* **151**, 393-408, 1997.

- Meng, X.; Lin, K.; Yang, X.; Sun, Z.; Jiang, D.; Xiao, F. S. Catalytic oxidation of olefins and alcohols by molecular oxygen under air pressure over $Cu_2(OH)PO_4$ and $Cu_4O(PO_4)_2$ catalysts, *J. Catal.* **218**, 460-464, 2003.

- Mesquita, I.; Matos, L. C.; Duarte, F.; Maldonado-Hódar, F. J.; Mendes, A.; Madeira, L. M. Treatment of azo dye-containing wastewater by a Fenton-like process in a continuous packed-bed reactor filled with activated carbon, *J. Hazar. Mater.* **237**, 30-37, 2012.

- Mhamdi, M.; Khaddar-Zine, S.; Ghorbel, A. Influence of the cobalt salt precursors on the cobalt speciation and catalytic properties of H-ZSM-5 modified with cobalt by solid-state ion exchange reaction, *Appl. Catal. A-Gen.* **357**, 42-50, 2009.

- Miethling, R.; Hecht, V.; Deckwer, W. D. Microbial degradation of quinoline: kinetic studies with *Comamonas acidovorans* DSM 6426. *Biotechnol. Bioeng.* **42**, 589-595, 1993.

- Miladinovic, M. R.; Stamenković, O. S.; Veljković, V. B.; Skala, D. U. Continuous sunflower oil methanolysis over quicklime in a packed-bed tubular reactor, *Fuel* **154**, 301-307, 2015.

- Millemann, R. E.; Birge, W. J.; Black, J. A.; Cushman, R. M.; Daniels, K. L.; Franco, P. J.; Giddings, J. M.; McCarthy, J. F.; Stewart, A. J. Comparative acute toxicity to aquatic

organisms of components of coal-derived synthetic fuels, *Trans. Am. Fish. Soc.* **113**, 74-85, 1984.

- Mittal, A.; Mittal, J.; Malviya, A.; Gupta, V. K. Adsorptive removal of hazardous anionic dye "Congo red" from wastewater using waste materials and recovery by desorption, *J. Colloid Interface Sci.* **340**, 16-26, 2009.

- Mohamed, R. M.; Aazam, E. S. Effect of Sn loading on the photocatalytic aniline synthesis activity of TiO$_2$ nanospheres, *J. Alloy Compd*. **595**, 8-13, 2014.

- Mohite, R. G.; Garg, A. Performance of heterogeneous catalytic wet oxidation for the removal of phenolic compounds: Catalyst characterization and effect of pH, temperature, metal leaching and non-oxidative hydrothermal reaction, *J. Environ. Chem. Eng.* **5**, 468-478, 2017.

- Morshedi, D.; Mohammadi, Z.; Boojar, M. M. A.; Aliakbari, F. Using protein nanofibrils to remove azo dyes from aqueous solution by the coagulation process, *Colloids Surf. B Biointerfaces* **112**, 245-254, 2013.

- Mosayebi, Z.; Rezaei, M.; Hadian, N.; Kordshuli, F. Z.; Meshkani, F. Low temperature synthesis of nanocrystalline magnesium aluminate with high surface area by surfactant assisted precipitation method: Effect of preparation conditions, *Mater. Res. Bull.* **47**, 2154-2160, 2012.

- Moshoeshoe, M.; Nadiye-Tabbiruka, M. S.; Obuseng, V. A review of the chemistry, structure, properties and applications of zeolites, *Am. J. Mater. Sci.*, **7**, 196-221, 2017.

- Mouli, K. C.; Sundaramurthy, V.; Dalai, A. K. A comparison between ring-opening of decalin on Ir-Pt and Ni-Mo carbide catalysts supported on zeolites, *J. Mol. Catal. A: Chem.* **304**, 77-84, 2009.

- Munter, R. Advanced oxidation processes-current status and prospects, *Proc. Estonian Acad. Sci. Chem.* **50**, 59-80, 2001.

- Navalon, S.; Alvaro, M.; Garcia, H. Heterogeneous Fenton catalysts based on clays, silicas and zeolites, *Appl. Catal. B: Environ.* **99**, 1-26, 2010.

- Nawrocki, J.; Kasprzyk-Hordern, B. The efficiency and mechanisms of catalytic ozonation, *Appl. Catal. B: Environ.* **99**, 27-42, 2010.

- Nedoloujko, A.; Kiwi, J. Parameters affecting the homogeneous and heterogeneous degradation of quinoline solutions in light-activated processes, *J. Photochem. Photobiol. A: Chem.* **110**, 149-157, 1997.

- Nedoloujko, A.; Kiwi, J. Parameters affecting the homogeneous and heterogeneous degradation of quinoline solutions in light-activated processes, *J. Photochem. Photobiol. A: Chem.* **16**, 149-157, 1997.

- Nelms, S. M. *Inductively coupled plasma mass spectrometry handbook*, John Wiley & Sons, Chichester, U.K, 2009.

- Nezamzadeh-Ejhieh, A.; Salimi, Z. Solar photocatalytic degradation of o-phenylenediamine by heterogeneous CuO/X zeolite catalyst, *Desalination* **280**, 281-287, 2011.

- Nichela, D. A.; Berkovic, A. M.; Costante, M. R.; Juliarena, M. P.; Einschlag, F. S. G. Nitrobenzene degradation in Fenton-like system using Cu(II) as catalyst. Comparison between Cu(II)- and Fe(II)-based systems, *Chem. Eng. J.* **228**, 1148-1157, 2013.

- Nie, Y.; Hu, C.; Qu, J.; Zhao, X. Photoassisted degradation of endocrine disruptors over CuOx-FeOOH with H_2O_2 at neutral pH, *Appl. Catal. B: Environ.* **87**, 30-36, 2009.

- Ning X.; Yang C.; Wang Y.; Yang Z.; Wang J.; Li R. Decolorization and biodegradation of the azo dye Congo red by an isolated Acinetobacter baumannii YNWH **226**, *Biotechnol. Biproc. E.* 19, 687-695, 2014.

- Nitiss, J. L. DNA topoisomerase II and its growing repertoire of biological functions, *Nat. Rev. Cancer* **9(5)**, 327-337, 2009b.

- Nitiss, J. L. Targeting DNA topoisomerase II in cancer chemotherapy, *Nat. Rev. Cancer* **9(5)**, 338-350, 2009a.

- Olivares-Marín, M.; Fernándes-González, C.; Macías-García, A.; Gómez-Serrano, V. Preparation of activated carbon from cherry stones by chemical activation with $ZnCl_2$, *Appl. Surf. Sci.* **252**, 5967-5971, 2006.

- Orge, C. A.; Orfao, J. J. M.; Pereira, M. F. R.; Farias, A. M. D.; Fraga, M. A. Ceria and cerium-based mixed oxides as ozonation catalysts, *Chem. Eng. J.* **200-202**, 499-505, 2012.

- Oturan, M. A.; Aaron, J. J. Advanced oxidation processes in water/ wastewater treatment: principles and applications. A review, *Crit. Rev. Environ. Sci. Technol.* **44**, 2577-2641, 2014.

- Ou, X.; Pilitsis, F.; Xu, N.; Taylor, S. F. R.; Warren, J.; Garforth, A.; Zhang, J.; Hardacre, C.; Jiao, Y.; Fan, X. On developing ferrisilicate catalysts supported on silicon carbide (SiC) foam catalysts for continuous catalytic wet peroxide oxidation (CWPO) reactions. *Catal. Today*, 2018. https://doi.org/10.1016/j.cattod.2018.06.033.

- Ovejero, G.; Sotelo, J. L.; Rodriguez, A.; Diaz, C.; Sanz, R.; Garcia, J. Platinum catalyst on multiwalled carbon nanotubes for the catalytic wet air oxidation of phenol. *Ind. Eng. Chem. Res.* **46**, 6449-6455, 2007.

- Owen, T. *Fundamentals of modern UV-visible spectroscopy: A primer*, Hewlett-Packard, California, USA, 1996.

- Pachupate, N. J.; Vaidya, P. D. Catalytic wet oxidation of quinoline over Ru/C catalyst, *J. Environ. Chem. Eng.* **6**, 883-889, 2018.

- Padoley, K. V.; Mudliar, S. N.; Pandey, R. A. Heterocyclic nitrogenous pollutants in the environment and their treatment options -An overview, *Bioresour. Technol*. **99**, 4029-4043, 2008.

- Pandey, A.; Singh, P.; Iyengar, L. Bacterial decolorization and degradation of azo dyes, *Int. Biodeterior. Biodegr.* **59**, 73-84, 2007.

- Pardo, B.; Ferrer, N.; Sempere, J.; Gonzalez-Olmos, R. A key parameter on the adsorption of diluted aniline solutions with activated carbons: The surface oxygen content, *Chemosphere* **162**, 181-188, 2016.

- Park, C.; Baker, R. T. K. Modifications in the catalytic properties of nickel supported on different dielectric oxides, *Chem. Mater*. **14**, 273-280, 2002.

- Park, Y.; Na, Y.; Pradhan, D.; Min, B. -K.; Sohn, Y. Adsorption and UV/Visible photocatalytic performance of BiOI for methyl orange, Rhodamine B and methylene blue: Ag and Ti-loading effects, *CrystEngComm* **16**, 3155-3167, 2014.

- Patel, H.; Vashi, R. T. Removal of Congo red dye from its aqueous solution using natural coagulants, *J. Saudi. Chem. Soc*. **16**, 131-136, 2012.

- Pera-Titus, M.; Garcia-Molina, V.; Banos, M. A., Giménez, J.; Esplugas, S. Degradation of chlorophenols by means of advanced oxidation processes: A general review, *Appl. Catal. B: Enviro*. **47**, 219-256, 2004.

- Pereira, R.; Pereira, L.; van der Zee, F. P. and M. M. Alves, Fate of aniline and sulfanilic acid in *UASB* bioreactors under denitrifying conditions, Water Res., 2011, **45**, 191-200.

- Perkampus, Helmut, H. *UV-vis spectroscopy and its applications*, Springer-Verlag Berlin Heidelberg, 1992.

- Peter, A.; Mihaly-Cozmuta, L.; Mihaly-Cozmuta, A.; Nicula, C.; Indrea, E.; Tutu, H. Calcium- and ammonium ion-modification of zeolite amendments affects the metal-uptake of Hieraciumpiloselloides in a dose-dependent way, *J. Environ. Monit*. **14**, 2807-2814, 2012.

- Prajapati, K.; Sorokhaibam, L. G.; Bhandari, V. M.; Killedar, D. J.; Ranade, V. V. Differentiating process performance of various coagulants in removal of Congo red and Orange G dyes, *Int. J. Chem. React. Eng*. **14**, 195-211, 2016.

- Prajapati, S. M.; Patel, K. D.; Vekariya, R. H.; Panchal, S. N.; Patel, H. D. Recent advances in the synthesis of quinolines: a review, *RSC Adv*. **4**, 24463-24476, 2014.

- Qin, Z.; Shen, B.; Gao, X.; Lin, F.; Wang, B.; Xu, C. Mesoporous Y zeolite with homogeneous aluminum distribution obtained by sequential desilication-dealumination and its performance in the catalytic cracking of cumene and 1,3,5-triisopropylbenzene, *J. Catal*. **278**, 266-275, 2011.

- Rameshraja, D.; Srivastava, V. C.; Kushwaha, J. P.; Mall, I. D. Quinoline adsorption onto granular activated carbon and bagasse fly ash, *Chem. Eng. J*. **181-182**, 343-351, 2012.

- Ramirez, J. H.; Maldonado-Hodar, F. J.; Perez-Cadenas, A. F.; Moreno-Castilla, C.; Costa, C. A.; Madeira, L. M. Azo-dye Orange II degradation by heterogeneous Fenton-like reaction using carbon-Fe catalysts, *Appl. Catal. B: Environ*. **75**, 312-323, 2007.

- Ramirez, J. H.; Vicente, M. A.; Madeira, L. M. Heterogeneous photo-Fenton oxidation with pillared clay-based catalysts for wastewater treatment: A review, *Appl. Catal. B: Environ*. **98**, 10-26, 2010.

- Reddy, G. R.; Balasubramanian, S.; Chennakesavulu, K. Zeolite encapsulated Ni(II) and Cu(II) complexes with tetradentate N_2O_2 Schiff base ligand: catalytic activity towards oxidation of benzhydrol and degradation of rhodamine-B, *J. Mater. Chem. A* **2**, 15598-15610, 2014.

- Reddy, S. N.; Ravikumar, R. V. S. S. N.; Reddy, B. J.; Rao, P. S. Optical and EPR spectra of libethenite mineral, *Ferroelectrics* **166**, 55-62, 1995.

- Reemtsma, T.; Jekel, M. *Organic pollutants in the water cycle: properties, occurrence, analysis and environmental relevance of polar compounds*, John Wiley & Sons, New York, USA, 2006.

- Ribeiro, R. S.; Silva, A. M. T., Figueiredo, J. L.; Faria, J. L.; Gomes, H. T. Catalytic wet peroxide oxidation: a route towards the application of hybrid magnetic carbon

nanocomposites for the degradation of organic pollutants. A review, *Appl. Catal. B: Environ.* **187**, 428-460, 2016.

- Richter, M.; Fait, M. J. G.; Eckelt, R.; Schneider, M.; Radnik, J.; Heidemann, D.; Fricke, R. Gas-phase carbonylation of methanol to dimethyl carbonate on chloride-free Cu-precipitated zeolite Y at normal pressure, *J. Catal.* **245**, 11-24, 2007.

- Rodrigues, C. S. D.; Soares, O. S. G. P.; Pinho, M. T.; Pereira, M. F. R.; Madeira, L. M. *p*-Nitrophenol degradation by heterogeneous Fenton's oxidation over activated carbon-based catalysts, *Appl. Catal. B: Environ.* **219**, 109-122, 2017.

- Rodriguez, A.; Garcia, J.; Ovejero, G.; Mestanza, M. Wet air and catalytic wet air oxidation of several azodyes from wastewaters: the beneficial role of catalysis, *Water Sci. Technol.* **60**, 1989-1999, 2009.

- Rodriguez, A.; Ovejero, G.; Sotelo, J. L.; Mestanza, M.; J. Garcia, Heterogeneous Fenton catalyst supports screening for mono azo dye degradation in contaminated wastewaters, *Ind. Eng. Chem. Res.* **49**, 498-505, 2010.

- Romero, D.; Chlala, D.; Labaki, M.; Royer, S.; Bellat, J. P.; Bezverkhyy, I.; Giraudon, J. M.; Lamonier, J. F. Removal of toluene over NaX zeolite exchanged with Cu^{2+}, *Catalysts* **5**, 1479-1497, 2015.

- Rong, J.; Zhang, T.; Qiu, F.; Zhu, Y. Preparation of efficient, stable, and reusable laccase-$Cu_3(PO_4)_2$ hybrid microspheres based on copper foil for decoloration of Congo red, *ACS Sustainable Chem. Eng.* **5**, 4468-4477, 2017.

- Rouquerol, F.; Rouquerol, J.; Sing, K. *Adsorption by powders and porous solids: Principle, methodology and applications*, Academic press, London, U.K., 1999.

- Rusevova, K.; Köferstein, R.; Rosell, M.; Richnow, H. H.; Kopinke, F. D.; Georgi, A. $LaFeO_3$ and $BiFeO_3$ perovskites as nanocatalysts for contaminant degradation in heterogeneous Fenton-like reactions, *Chem. Eng. J.* **239**, 322-331, 2014.

- Saceda, J. J. F.; Leon, R. L. D.; Rintramee, K.; Prayoonpokarach, S.; Wittayakun, J. Properties of silica from rice husk and rice husk ash and their utilization for zeolite Y synthesis, *Quim. Nova* **34**, 1394-1397, 2011.

- Sadighi, A.; Faramarzi, M. A. Congo red decolorization by immobilized laccase through chitosan nanoparticles on the glass beads, *J. Taiwan Inst. Chem. Eng.* **44**, 156-162, 2013.

- Sagar, G. V.; Rao, P. V. R.; Srikanth, C. S.; Chary, K. V. R. Dispersion and reactivity of copper catalysts supported on Al_2O_3-ZrO_2, *J. Phys. Chem. B* **110**, 13881-13888, 2006.

- Saien, J.; Shafiei, H.; Amisama, A. Photo-activated periodate in homogeneous degradation and mineralization of quinoline: optimization, kinetic, and energy consumption, *Environ. Prog. Sustain. Energy* **36**, 1621-1627, 2017.

- Sajjad, A. K. L.; Shamaila, S.; Tian, B.; Chen, F.; Zhang, J. Comparative studies of operational parameters of degradation of azo dyes in visible light by highly efficient WO_x/TiO_2 photocatalyst, *J. Hazard. Mater.* **177**, 781-791, 2010.

- Samanta, S.; Bhunia, K.; Pradhan, D.; Satpati, B.; Srivastava, R. $NiCuCo_2O_4$ supported Ni-Cu ion-exchanged mesoporous zeolite heteronano architecture: an efficient, stable, and economical nonprecious electrocatalyst for methanol oxidation, *ACS Sustainable Chem. Eng.* **6**, 2023-2036, 2018.

- Samanta, S.; Khilari S.; Bhunia, K.; Pradhan, D.; Satpati, B.; Srivastava, R. Double-metal-ion-exchanged mesoporous zeolite as an efficient electrocatalyst for alkaline water oxidation: synergy between Ni-Cu and their contents in catalytic activity enhancement, *J. Phys. Chem. C* **122**, 10725-10736, 2018.

- Sanchez, l.; Peral, J.; Domenech, X. Aniline degradation by combined photocatalysis and ozonation, *Appl. Catal. B: Environ.* **19**, 58-65, 1998.

- Sangster, J. Octanol-water partition coefficients of simple organic compounds, *J. Phys. Chem. Ref. Data* **18**, 1111-1227, 1989.

- Santos, A.; Yustos, P. A. Quintanilla, G. Ruiz, Garcia-Ochoa, F. Study of the copper leaching in the wet oxidation of phenol with CuO-based catalysts: causes and effects, *Appl. Catal. B: Environ.* **61**, 323-333, 2005.

- Sassaroli, A.; Fantini, S. Comment on the modified Beer-Lambert law for scattering media, Phys. Med. Biol., 2004, **49**, N255-N257.

- Satishkumar, G.; Landau, M. V.; Buzaglo, T.; Frimet, L.; Ferentz, M.; Vidruk, R.; Wagner, F.; Gal, Y.; Herskowitz, M. Fe/SiO_2 heterogeneous Fenton catalyst for continuous catalytic wet peroxide oxidation prepared *in situ* by grafting of iron released from $LaFeO_3$, *Appl. Catal. B: Environ.* **138**, 276-284, 2013.

- Settle, F. A. *Handbook of instrumental techniques for analytic chemistry*, Prentice Hall, New Jersey, USA, 1997.

- Shang, M.; Wang, W.; Sun, S.; Ren, J.; Zhou, L.; Zhang, L. Efficient visible light-induced photocatalytic degradation of contaminant by spindle-like PANI/BiVO$_4$, *J. Phys. Chem. C* **113**, 20228-20233, 2009.

- Sharma, Y. C.; Uma; Sinha A. S. K.; Upadhyay S. N. Characterization and adsorption studies of Cocos nucifera L. activated carbon for the removal of methylene blue from aqueous solutions, *J. Chem. Eng. Data* **55**, 2662-2667, 2010.

- Sheydaei, M.; Aber, S.; Khataee, A. Preparation of a novel γ-FeOOH-GAC nano composite for decolorization of textile wastewater by photo Fenton-like process in a continuous reactor, *J. Mol. Catal. A-Chem.* **392**, 229-234, 2014.

- Shu, J.; Wang, Z.; Huang, Y.; Huang, N.; Ren, C.; Zhang, W. Adsorption removal of Congo red from aqueous solution by polyhedral Cu$_2$O nanoparticles: Kinetics, isotherms, thermodynamics and mechanism analysis, *J. Alloy Compd.* **633**, 338-346, 2015.

- Shwan, S.; Skoglundh, M.; Lundegaard, L. F.; Tiruvalam, R. R.; Janssens, T. V. W.; Carisson, A.; Vennestrom, P. N. R. Solid-state ion-exchange of copper into zeolites facilitated by ammonia at low temperature, *ACS Catal.* **5,** 16-19, 2015.

- Silverstein, R. M.; Webster, F. X.; Kiemle, D. J. *Spectrometric identification of organic compounds,* John Wiley & Sons, New Jersey, USA, 7th Ed., 2005.

- Singh, D. P.; Neti, N. R.; Sinha, A. S. K. and Srivastava, O. N. Growth of different nanostructures of Cu$_2$O (nanothreads, nanowires and nanotubes) by simple electrolysis based oxidation of copper, *J. Phys. Chem. C* **111**, 1638-1645, 2007.

- Singh, K.; Arora, S. Removal of synthetic textile dyes from wastewaters: a critical review on present treatment technologies, *Crit. Rev. Environ. Sci. Technol.* **41**, 807-878, 2011.

- Singh, L.; Rekha, P.; Chand, S. Cu-impregnated zeolite Y as highly active and stable heterogeneous Fenton-like catalyst for degradation of Congo red dye, *Sep. Purif. Technol.* **170**, 321-336, 2016.

- Sinha, B.; Ghosh, U. K.; Pradhan, N. C.; Adhikari, B. Separation of phenol from aqueous solution by pervaporation using modified polyurethaneurea membrane. *J. Appl. Polym. Sci.* **101**, 1857-1865, 2006.

- Sobalík, Z.; Dĕdecek, J.; Ikonnikov, I.; Wichterlova, B. State and coordination of metal ions in high silica zeolites incorporation, development and rearrangement during preparation and catalysis, *Microporous Mesoporous Mater.* **21**, 525-532, 1998.

- Song, H.; Wan, X.; Dai, M.; Zhang, J.; Li, F.; Song, H. Deep desulfurization of model gasoline by selective adsorption over Cu-Ce bimetal ion-exchanged Y zeolite, *Fuel Process. Technol.* **116**, 52-62, 2013.

- Sousa-Aguiar, E. F.; Camorim, V. L. D.; Zotin, F. M. Z.; Santos, R. L. C. D. A Fourier transform infrared spectroscopy study of La-, Nd-, Sm-, Gd- and Dy-containing Y zeolites, *Microporous Mesoporous. Mater.* **25**, 25-34, 1998.

- Stuart, B. *Infrared spectroscopy: Fundamentals and applications*, John Wiley & Sons, Chichester, UK, 2004.

- Su, C. C.; Pagaling, E. D.; Peralta, G. L.; Lu, M. C. Comparison of aniline degradation by Fenton and electro-Fenton reactor using plate and rod electrodes, *Environ. Prog. Sustain. Energy.* **32**, 1111-1117, 2013.

- Subbaramaiah, V.; Srivastava, V. C.; Mall, I. D. Catalytic activity of Cu/SBA-15 for peroxidation of pyridine bearing wastewater at atmospheric condition, *AICHE journal* **59**, 2577-2586, 2013.

- Suga, S.; Sekiyama, A. *Photoelectron spectroscopy: bulk and surface electronic structures*, Springer, Berlin, Germany, 2014.

- Sun, Q.; Bai, Y.; Zhao, C.; Xiao, Y.; Wen, D.; Tang, X. Aerobic biodegradation characteristics and metabolic products of quinoline by a *Pseudomonas* strain, *Bioresour. Technol* **100**, 5030-5036, 2009.

- Suresh, S.; Srivastava, V. C.; Mishra, I. M. Adsorptive removal of phenol from binary aqueous solution with aniline and 4-nitrophenol by granular activated carbon, *Chem. Eng. J.* **171**, 997-1003, 2011.

- Suwanprasop, S.; Eftaxias, A.; Stuber, F.; Polaert, I.; Julcour-Lebigue, C.; Delmas, H. Scale-up and modeling of fixed-bed reactors for catalytic phenol oxidation over adsorptive active carbon, *Ind. Eng. Chem. Res.* **44**, 9513-9523, 2005.

- Takahashi, A.; Yang, R. T.; Munson, C. L.; Chinn, D. Cu(I)-Y-zeolite as a superior adsorbent for diene/olefin separation, *Langmuir* **17**, 8405-8413, 2001.

- Tang, B.; Dai, W.; Sun, X.; Guan, N.; Li, L.; Hunger, M. A procedure for the preparation of Ti-Beta zeolites for catalytic epoxidation with hydrogen peroxide, *Green Chem.* **16**, 2281-2291, 2014.

- Tanhaei, B.; Chenar, M. P.; Saghatoleslami, N.; Hesampour, M.; Laakso, T.; Kallioinen, M.; Sillanpaa, M.; Manttari, M. Simultaneous removal of aniline and nickel from water by micellar-enhanced ultrafiltration with different molecular weight cut-off membranes, *Sep. Purif. Technol*. **124**, 26-35, 2014.

- Taran, O. P.; Yashnik, S. A.; Ayusheev, A. B.; Piskun, A. S.; Prihodko, R. V.; Ismagilov, Z. R.; Goncharuk, V. V.; Parmon, V. N. Cu-containing MFI zeolites as catalysts for wet peroxide oxidation of formic acid as model organic contaminant, *Appl. Catal. B: Environ.* **140**, 506-515, 2013.

- Teichert, A.; Schmidt, J.; Porzel, A.; Arnold, N.; Wessjohann, L. (Iso)-Quinoline alkaloids from fungal fruiting bodies of cortinarius subtortus, *J. Nat. Prod.* **71**, 1092-1094, 2008.

- Thomas, R. *Practical guide to ICP-MS: a tutorial for beginners*, CRC Press, Boca Raton, USA, 3rd Ed., 2013.

- Thommes, M.; Kaneko, K.; Neimark, A. V.; Olivier, J. P.; Reinoso, F. R.; Rouquerol, J.; Sing, K. S. W. Physisorption of gases, with special reference to the evaluation of surface area and pore size distribution (IUPAC Technical Report)*, Pure Appl. Chem*. **87,** 1051-1069, 2015.

- Tisa, F.; Raman, A. A. A.; Daud, W. M. A. W. Applicability of fluidized bed reactor in recalcitrant compound degradation through advanced oxidation processes: a review, J. *Environ. Manage*. **146**, 260-275, 2014.

- Tolstoy, V. P.; Chernyshova, I. V.; Skryshevsky, V. A. *Handbook of infrared spectroscopy of ultrathin films*, John Wiley & Sons, New Jersey, USA, 2003.

- Toma, A. C.; Pfohl, T. *Small-angle x-ray scattering (SAXS) and wide-angle x-ray scattering (WAXS) of supramolecular assemblies. Supramolecular chemistry: from molecules to nanomaterials*, John Wiley & Sons, Chichester, U.K., 2012.

- Tsuchiya, Y. Photon path distribution and optical responses of turbid media: Theoretical analysis based on the microscopic Beer-Lambert law, *Phys. Med. Biol.* **46**, 2067-2084, 2001.

- Tsuji, K.; Injuk, J.; Grieken, R. V. *X-ray spectrometry: Recent technological advances*, John Wiley & Sons, Chichester, UK, 2004.

- Ullah, R.; Dutta, J. Photocatalytic degradation of organic dyes with manganese-doped ZnO nanoparticles, *J. Hazard. Mater.* **156**, 194-200, 2008.

- United Nations, World Water Development Report, *Nature-based solutions for water*, 2018.

- USEPA, Proposed guidelines for carcinogen risk assessment, Notice, *Federal Register*, **61(79)**, 17960-18011, 1996.

- Uçar, S.; Erdem, M.; Tay, T.; Karagöz, S. Preparation and characterization of activated carbon produced from pomegranate seeds by $ZnCl_2$ activation, *Appl. Surf. Sci.* **255**, 8890-8896, 2009.

- Valkaj, K. M.; Katovic, A.; Zrnčević, S. Catalytic properties of Cu/13X zeolite based catalyst in catalytic wet peroxide oxidation of phenol, *Ind. Eng. Chem. Res.* **50** 4390-4397, 2011a.

- Valkaj, K.; Wittine, O.; Margeta, K.; Granato, T.; Katovic, A.; Zrnčević, S. Phenol oxidation with hydrogen peroxide using Cu/ZSM5 and Cu/Y5 catalysts, *Pol. J. Chem. Technol.* **13**, 28-36, 2011b.

- Venna, S. R.; Carreon, M. A. Microwave assisted phase transformation of silicoaluminophosphate zeolite crystals, *J. Mater. Chem.* **19**, 3138-3140, 2009.

- Verboekend, D.; Pérez-Ramírez, J. Design of hierarchical zeolite catalysts by desilication, *Catal. Sci. Technol.* **1**, 879-890, 2011.

- Verboekend, D.; Vile, G.; Ramirez, J. P. Hierarchical Y and USY zeolites designed by post-synthetic strategies, *Adv. Funct. Mater.* **22**, 916-928, 2012.

- Vico, L. I.; Acebal, S. G. Some aspects about the adsorption of quinoline on fibrous silicates and Patagonian saponite, *Appl. Clay Sci.* **33**, 142-148, 2006.

- Vijayaraghavan, G.; Shanthakumar, S. Performance study on algal alginate as natural coagulant for the removal of Congo red dye, *Desalin. Water Treat.* **57**, 6384-6392, 2016.

- Wada, S.; Ichikawa, H.; Tastsumi, K. Removal of phenols and aromatic amines from wastewater by a combination treatment with tyrosinase and a coagulant, *Biotechnol. Bioeng.* **45**, 304-309, 1995.

- Wagner, C. D.; Riggs, W. M.; Davis, L. E.; Moulder, J. E.; Mulenberg, G. E. *Handbook of X-ray photoelectron spectroscopy*, Perkin Elmer Corp., Minnesota, USA, 1979.

- Wang, C.; Ma, K.; Wu, T.; Ye, M.; Tan, P.; Yan, K. Electrochemical mineralization pathway of quinoline by boron-doped diamond anodes, *Chemosphere* **149**, 219-223, 2016.

- Wang, G.; Huang, B.; Ma, X.; Wang, Z.; Qin, X.; Zhang, X.; Dai, Y.; Whangbo, M. H. $Cu_2(OH)PO_4$, a near-infrared-activated photocatalyst, *Angew. Chem. Int. Ed.* **52**, 4810-4813, 2013.

- Wang, J.; Park, J. N.; Jeong, H. C.; Choi, K. S.; Wei, X. Y.; Hong, S. I.; Lee, C. W. Cu^{2+}-exchanged zeolites as catalysts for phenol hydroxylation with hydrogen peroxide, *Energy Fuels* **18**, 470-476, 2004.

- Wang, L.; Li, W.; Qi, G.; Weng, D. Location and nature of Cu species in Cu/SAPO-34 for selective catalytic shangreduction of NO with NH_3, *J. Catal.* **289**, 21-29, 2012.

- Wang, N.; Ji, S.; Zhang, G.; Li, J.; Wang, L. Self-assembly of graphene oxide and polyelectrolyte complex nanohybrid membranes for nanofiltration and pervaporation, *Chem. Eng. J.* **213**, 318-329, 2012.

- Wang, S.; Peng, Y. Natural zeolites as effective adsorbents in water and wastewater treatment, *Chem. Eng. J.* **156**, 11-24, 2010.

- Wang, X.; Liu, L.; Wang, L.; Jacobson, A. J. Hydrothermal synthesis and structures of the open-framework copper silicates $Na_2[Cu_2Si_4O_{11}](H_2O)_2$ (CuSH-2Na), $Na_2[CuSi_3O_8]$ (CuSH-3Na), $Cs_2Na_4[Cu_2Si_{12}O_{27}(OH)_2](OH)_2$ (CuSH-4NaCs), and $Na_2[Cu_2Si_5O_{13}](H_2O)_3$ (CuSH-6Na), *Solid State Sci.* **7**, 1415-1422, 2005.

- Wang, X.; Huang, X.; Zuo, C.; Hu, H. Kinetics of quinoline degradation by O_3/UV in aqueous phase, *Chemosphere* **55**, 733-741, 2004.

- Wang, Y.; Zheng, H.; Li, Z.; Xie, K. Investigation of the interaction between $Cu(acac)_2$ and NH_4Y in the preparation of chlorine-free CuY catalysts for the oxidative carbonylation of methanol to a fuel additive, *RSC Adv.* **5**, 102323-102331, 2015.

- Wei, X.; Wu, H.; He, G.; Guan, Y. Efficient degradation of phenol using iron-montmorillonite as a Fenton catalyst: Importance of visible light irradiation and intermediates, *J. Hazard. Mater.* **321**, 408-416, 2017.

- Weiss, J.; Shpigun, O. *Handbook of ion chromatography*, John Wiley & Sons, New Jersey, USA, 4th Ed., 2016.

- Wells, O. C. *Scanning electron microscopy*, McGraw-Hill, New York, USA, 1974.

- Welz, B. *Atomic absorption spectrometry*. Wiley, New York, USA, 941, 1999.

- Williams, D. B.; Carter, C. B. *Transmission electron microscopy: A textbook for materials science*, Springer, Berlin, Germany, 2009.

- Wischnitzer, S. *Introduction to electron microscopy*, Pergamon Press, New York, USA, 1962.

- Wu, C. K.; Yin, M.; O'Brien, S.; Koberstein, J. T. Quantitative analysis of copper oxide nanoparticles composition and structure X-ray photoelectron spectroscopy, *Chem. Mater*. **18**, 6054-6058, 2006.

- Wu, C.; Wang, Z.; Lei, H.; Zhang, W.; Duan, Y. Dual binding modes of Congo red to amyloid protofibril surface observed in molecular dynamics simulations, *J. Am. Chem. Soc.* **129**, 1225-1232, 2007.

- Wu, G. Q.; Zhang, X.; Hui, H.; Yan, J.; Zhang, Q. S.; Wan, J. L.; Dai, Y. Adsorptive removal of aniline from aqueous solution by oxygen plasma irradiated bamboo based activated carbon, *Chem. Eng. J.* **185-186**, 201-210, 2012.

- Xia, M., Long, M., Yang, Y., Chen, C., Cai, W., Zhou, B. A highly active bimetallic oxides catalyst supported on Al-containing MCM-41for Fenton oxidation of phenol solution, *Appl. Catal. B Environ*. **110**, 118-125, 2011.

- Xiao, F. S.; Sun, J.; Meng, X.; Yu, R.; Yuan, H.; Jiang, D.; Qiu, S.; Xu, R. A novel catalyst of copper hydroxyphosphate with high activity in wet oxidation of aromatics, *Appl. Catal. A: General* **202**, 267-271, 2001a.

- Xiao, F. S.; Sun, J.; Meng, X.; Yu, R.; Yuan, H.; Xu, J.; Song, T.; Jiang, D.; Xu, R. Synthesis and structure of copper hydroxyphosphate and its high catalytic activity in hydroxylation of phenol by H_2O_2, *J. Catal.* **199**, 273-281, 2001b.

- Xiao, G.; Long, L. Efficient removal of aniline by a water-compatible microporous and mesoporous hyper-cross-linked resin and XAD-4 resin: A comparative study, *Appl. Surf. Sci.* **258**, 6465-6471, 2012.

- Xiao, Y.; Gao, L.; Xiao, G.; Lv, J. Kinetics of the trans esterification reaction catalyzed by solid base in a fixed-bed reactor, *Energy Fuels*. **24**, 5829-5833, 2010.

- Xu, H.; Zhang, D.; Xu, W. Monitoring of decolorization kinetics of Reactive Brilliant Blue X-BR by online spect\rophotometric method in Fenton oxidation process, *J. Hazard. Mater.* **158**, 445-453, 2008.

- Xu, L.; Wang, J. A heterogeneous Fenton-like system with nanoparticulate zerovalent iron for removal of 4-chloro-3-methyl phenol, *J. Hazard. Mater.* **186**, 256-264, 2011.

- Xu, L.; Wang, J. Magnetic nanoscaled Fe_3O_4/CeO_2 composite as an efficient Fenton-like heterogeneous catalyst for degradation of 4-chlorophenol, *Environ. Sci. Technol.* **46**, 10145-10153, 2012.

- Xu, P.; Ma, W.; Han, H.; Hou, B.; Jia, S. Biodegradation and interaction of quinoline and glucose in dual substrates system, *Bull. Environ. Contam. Toxicol.* **94**, 365-369, 2015.

- Xu, Y.; Wang, C.; Yang, S. Uniform copper hydroxyphosphate microstructures with tunable size: Synthesis by a facile surfactant-free hydrothermal route and photocatalytic properties, *Mater. Lett.* **78**, 46-49, 2012.

- Yadav, B. R., Garg, A. Hetero-catalytic hydrothermal oxidation of simulated pulping effluent: Effect of operating parameters and catalyst stability, *Chemosphere* **191**, 128-135, 2018.

- Yadav, B. R.; Garg, A. Performance assessment of activated carbon supported catalyst during catalytic wet oxidation of simulated pulping effluents generated from wood and bagasse based pulp and paper mills, *RSC Adv.* **7**, 9754-9763, 2017.

- Yaman, Y. C.; Gündüz, G.; Dükkanci, M. Degradation of CI Reactive Red 141 by heterogeneous Fenton-like process over iron-containing ZSM-5 zeolites, Color. Technol., **129**, 69-75, 2013.

- Yan, H.; Yang, X.; Chen, J.; Yin, C.; Xiao, C.; Chen, H. Synergistic removal of aniline by carbon nanotubes and the enzymes of Delftia sp. XYJ6, *J. Environ. Sci. (China)* **23**, 1165-1170, 2011.

- Yan, Y.; Jiang, S.; Zhang, H. Catalytic wet oxidation of phenol with Fe-ZSM-5 catalysts, *RSC Adv.* **6**, 3850-3859, 2016.

- Yan, Y.; Jiang, S.; Zhang, H. Efficient catalytic wet peroxide oxidation of phenol over Fe-ZSM-5 catalyst in a fixed bed reactor, *Sep. Purif. Technol.* **133**, 365-374, 2014.

- Ye, Q.; Wang, L.; Yang, R. T. Activity, propene poisoning resistance and hydrothermal stability of copper exchanged chabazite-like zeolite catalysts for SCR of NO with ammonia in comparison to Cu/ZSM-5, *Appl. Catal. A: Gen.* **427**, 24-34, 2012.

- Zhan, Y.; Li, H.; Chen, Y. Copper hydroxyphosphate as catalyst for the wet hydrogen peroxide oxidation of azo dyes, *J. Hazard. Mater.* **180**, 481-485, 2010.

- Zhang, J.; Wu, Y.; Qin, C.; Liu, L.; Lan, Y. Rapid degradation of aniline in aqueous solution by ozone in the presence of zero-valent zinc, *Chemosphere* **141**, 258-264, 2015.

- Zhang, L.; Wang, X.; Xue, Y.; Zeng, X.; Chen, H.; Li, R.; Wang, S. Cooperation between the surface hydroxyl groups of Ru–SiO_2@$mSiO_2$ and water for good catalytic performance for hydrogenation of quinoline, *Catal. Sci. Technol.* **4**, 1939-1948, 2014.

- Zhang, N.; Zhou, X. F. Salen copper (II) complex encapsulated in Y zeolite: An effective heterogeneous catalyst for TCF pulp bleaching using peracetic acid, *J. Mol. Catal. A: Chem.*, **365**, 66-72, 2012.

- Zhang, S.; Li, A.; Cui, D.; Yang, J.; Ma, F. Performance of enhanced biological SBR process for aniline treatment by mycelial pellet as biomass carrier, *Bioresour. Technol.* **102**, 4360-4365, 2011.

- Zhang, T.; Zhang, J.; Liu, S.; Liu, Z. A novel and complete gene cluster involved in the degradation of aniline by *Delftia sp.* AN3, *J. Environ. Sci.* **20**, 717-724, 2008.

- Zhang, Y. G.; Ma, L. L.; Li, J. L.; Yu, Y. In Situ Fenton reagent generated from TiO_2/Cu_2O composite film: a new way to utilize TiO_2 under visible light irradiation, *Environ. Sci. Technol.* **41**, 6264-6269, 2007.

- Zhao, G.; Ma, F.; Wei, L.; Chua, H. Using rice straw fermentation liquor to produce bioflocculants during an anaerobic dry fermentation process, *Bioresour. Technol.* **113**, 83-88, 2012.

- Zhao, Y.; Teng, F.; Xu, J.; Liu, Z.; Yang, Y.; Zhang, Q.; Yao, W. Facile synthesis of Cu_2PO_4OH hierarchical nanostructures and their improved catalytic activity by a hydroxyl group, *RSC Adv.* **5**, 100934-100942, 2015.

- Zheng, J.; Li, Z.; Huang, L.; Wu, W.; Li, J.; Jiang, H. Palladium-catalyzed intermolecular aerobic annulation of o-alkenylanilines and alkynes for quinoline synthesis, *Org. Lett.* **18**, 3514-3517, 2016.

- Zhou L.; Wang W.; Xu H.; Sun S.; Shang M. Bi_2O_3 hierarchical nanostructures: controllable synthesis, growth mechanism, and their application in photocatalysis, *Chem. Eur. J.* **15**, 1776-1782, 2009.

- Zhou, B.; Song, J.; Zhou, H.; Wu, L.; Wu, T.; Liu, Z.; Han, B. Light-driven integration of the reduction of nitrobenzene to aniline and the transformation of glycerol into valuable chemicals in water, *RSC Adv.* **5**, 36347-36352, 2015.

- Zhu, H.; Han, Y.; Ma, W.; Han, H.; Ma, W. Removal of selected nitrogenous heterocyclic compounds in biologically pretreated coal gasification wastewater (BPCGW) using the catalytic ozonation process combined with the two-stage membrane bioreactor (MBR), *Bioresour. Technol.* **245**, 786-793, 2017.

- Zhu, H.; Ma, W.; Han, H.; Han, Y.; Ma, W. Catalytic ozonation of quinoline using nano-MgO: Efficacy, pathways, mechanisms and its application to real biologically pretreated coal gasification wastewater, *Chem. Eng. J.* **327**, 91-99, 2017.

- Zhu, S. N.; Liu, D. Q.; Fan, L.; Ni, J. R. Degradation of quinoline by *Rhodococcus* sp. QL2 isolated from activated sludge, *J. Hazard. Mater.* **160**, 289-294, 2008.

- Zhu, S.; Yang, X.; Yang, W.; Zhang, L.; Wang, J.; Huo, M. Application of porous nickel-coated TiO_2 for the photocatalytic degradation of aqueous quinoline in an internal airlift loop reactor, *Int. J. Env. Res. Public Health* **9**, 548-563, 2012.

- Zhuang, H.; Han, H.; Hou, B.; Jia, S.; Zhao, Q. Heterogeneous catalytic ozonation of biologically pretreated Lurgi coal gasification wastewater using sewage sludge based activated carbon supported manganese and ferric oxides as catalysts, *Bioresour. Technol.* **166**, 178-186, 2014.

- Zhuang, H.; Han, H.; Xu, P.; Hou, B.; Jia, S.; Wang, D.; Li, K. Biodegradation of quinoline by *Streptomyces* sp. N01 immobilized on bamboo carbon supported Fe_3O_4 nanoparticles, *Biochem. Eng. J.* **99**, 44-47, 2015.

- Zoha, K. D.; Stenstrom, M. K. Fenton oxidation of hexahydro-1,3,5-trinitro-1,3,5,-triazine (RDX) and octahydro-1,3,5,7-tetranitro-1,3,5,7-tetraazocine (HMX), *Water Res.* **36**, 1331-1341, 2002.